

# Ordering Phenomena in Transition-Metal-Oxide Heterostructures

vorgelegt von  
Alex Manuel Frano Pereira  
Tegucigalpa, Honduras

Von der Fakultät II - Mathematik und Naturwissenschaften  
der Technischen Universität Berlin  
zur Erlangung des akademischen Grades  
Doktor der Naturwissenschaften  
Dr.rer.nat.

genehmigte Dissertation

Promotionsausschuss:

Vorsitzender: Prof. Dr. rer. nat. Mario Dähne  
Gutachter: Prof. Dr. rer. nat. Stefan Eisebitt  
Gutachter: Prof. Dr. rer. nat. Bernhard Keimer  
Gutachter: Dr. habil. Eugen Weschke

Tag der wissenschaftlichen Aussprache:  
27.01.2014

Berlin 2014

D 83

# Abstract

## Ordering Phenomena in Transition-Metal-Oxide Heterostructures

This doctoral work presents a study of ordered ground states of transition metal oxide compounds and multilayers using resonant elastic soft x-ray scattering. The technique has developed over the last decades and become especially useful when sample sizes are limited like the case of nanometer-scale films and superlattices. By scattering with photon energies on resonance with the element's electronic transitions, it is an element-specific, sensitive tool providing a combination of spectroscopic and spatial information.

The thesis is divided into two central topics. The first part focuses on the investigation of perovskite-type, rare-earth nickelate heterostructures. X-rays tuned to the Ni  $L_3$ -edge were used to unveil unprecedented diffraction evidence of long range magnetic order in  $\text{LaNiO}_3\text{-RXO}_3$  ( $\text{RXO}_3 = \text{LaAlO}_3, \text{DyScO}_3$ ) superlattices. We report on the appearance of magnetic order in such systems with a propagation vector of  $\mathbf{Q}_{SDW} = (\frac{1}{4}, \frac{1}{4}, l)$  in pseudocubic notation, similar to bulk rare earth nickelates with  $R \neq \text{La}$ . With  $\text{LaNiO}_3$  being paramagnetic in its bulk form, the magnetic Bragg peak is only present in superlattices where the thickness of the  $\text{LaNiO}_3$  layers approaches the 2-dimensional limit. Besides the thickness dependence, the magnetic order was probed on samples grown on varying strain-inducing substrates. Azimuthal scans around  $\mathbf{Q}_{SDW}$  were done to determine the orientation of the spin spiral under these different conditions. We will explain how the reorientation of the spins can be understood by the magneto-crystalline anisotropy which is determined by the relative occupation of the Ni  $d$ -orbitals via spin-orbit coupling. First steps towards control of the spin spiral's orientation will be outlined, and along with the high remanent conductivity found in the magnetic spiral state, an outlook for metallic antiferromagnetic spintronics will be discussed.

The second part of this thesis will address the observation of charge density wave (CDW) order in single crystals of superconducting  $\text{YBa}_2\text{Cu}_3\text{O}_{6+\delta}$  (YBCO). With accumulating evidence of a Fermi surface reconstruction suggesting an underlying ordered ground state in underdoped YBCO, diffraction evidence of a CDW was found in  $\text{YBCO}_{6.6}$  single crystals during this PhD project. A thorough study of the energy, temperature, external magnetic field, and doping dependence was done to characterize the details of this ordered state. Together with results obtained on samples doped with non-magnetic Zn impurities, which locally slow the magnetic fluctuations, a competition between the CDW, the spin density wave, and superconducting phase

is proposed. Finally, the study extended to investigate the emergence of CDW in SLs comprising fully oxygenated YBCO, a doping level where CDW order eludes single crystals, and half-metallic  $\text{La}_{2/3}\text{Ca}_{1/3}\text{MnO}_3$  (LCMO). Our main finding is that the order originates at the YBCO interface due a charge transfer of electrons from LCMO. The temperature and magnetic field dependencies of the peak suggest a static, saturated phase in stark contrast to the single crystals' fluctuating order. Thus, this result demonstrates how oxide interfaces can act to nucleate metastable electronic phase transitions.

# Zusammenfassung in deutscher Sprache

## Ordnungsphänomene in Übergangsmetalloxid-Heterostrukturen

Thema der vorliegenden Arbeit ist eine Untersuchung geordneter Grundzustände in Übergangsmetalloxiden und deren Multilagen mit resonanter elastischer Streuung im weichen Röntgenbereich. Diese Methode ist eine Entwicklung der letzten Jahrzehnte und besonders dann von Vorteil, wenn kleine Probenmengen untersucht werden sollen, wie im Fall von nanoskaligen Filmen und Übergittern. Röntgenstreuung mit Photonenenergien im Bereich der Resonanz von elektronischen Übergängen ist eine sehr empfindliche, element-spezifische Methode, die die Spektroskopie mit Informationen über räumliche Korrelationen kombiniert.

Die Arbeit befasst sich mit zwei zentralen Themen. Der erste Teil konzentriert sich auf Heterostrukturen der Seltenerdnickelate, die als Volumen-Einkristalle eine Perowskitstruktur aufweisen. Röntgenstrahlen mit Energien im Bereich der Ni  $L_3$ -Kante wurden verwendet, um die magnetische Ordnung in Übergittern von  $\text{LaNiO}_3$  -  $\text{RXO}_3$  ( $\text{RXO}_3 = \text{LaAlO}_3, \text{DyScO}_3$ ) zu untersuchen. Obwohl Volumen-Einkristalle von  $\text{LaNiO}_3$  bei allen Temperaturen paramagnetisch sind, wurde in diesen Systemen magnetische Ordnung mit einem Wellenvektor von  $\mathbf{Q}_{SDW} = (\frac{1}{4}, \frac{1}{4}, l)$  (in pseudokubischer Notation) nachgewiesen, ähnlich wie bei anderen Seltenerd-Nickelaten mit  $R \neq \text{La}$ . Der magnetische Beugungsreflex wurde allerdings nur in Übergittern gefunden, bei denen sich die Dicke der  $\text{LaNiO}_3$ -Lagen dem 2-dimensionalen Grenzfall nähert. Zusätzlich zur Dickenabhängigkeit wurde diese magnetische Ordnung dann an Proben mit unterschiedlichen grenzflächeninduzierten Spannungen untersucht. Dazu wurden Heterostrukturen verwendet, die auf Substraten mit unterschiedlichen Gitterparametern gewachsen waren. Die azimutale Abhängigkeit der resonanten Streuung bei dem Wellenvektor  $\mathbf{Q}_{SDW}$  wurde benutzt, um die Momentenrichtungen in der Spinspirale unter diesen verschiedenen Bedingungen zu bestimmen. Wir erklären die Umorientierung der Spins durch die magnetokristalline Anisotropie, welche durch die relative Besetzung der Ni  $d$  Orbitale mittels Spin-Bahn Wechselwirkung bestimmt ist. Des weiteren zeigen wir erste Möglichkeiten zur Kontrolle der Orientierung der spiralen Spinstruktur auf, und diskutieren, zusammen mit der gefundenen remanenten Leitfähigkeit in diesem magnetischen Zustand eine mögliche Anwendung im Bereich der metallischen, antiferromagnetischen Spintronik.

Der zweite Teil der Arbeit befasst sich mit Ladungsdichtewellen in Einkristallen

und Heterostrukturen von supraleitendem  $\text{YBa}_2\text{Cu}_3\text{O}_{6+\delta}$  (YBCO). Während Hinweise auf eine Rekonstruktion der Fermifläche bereits auf einen geordneten Grundzustand in niedrig dotiertem YBCO hingedeutet hatten, konnte im Rahmen dieser Arbeit mit resonanter Röntgenbeugung der Nachweis einer Ladungsdichtewelle in  $\text{YBCO}_{6,6}$  geliefert werden. Weitere Details wurden anhand der Untersuchungen dieses geordneten Zustands als Funktion von Photonenenergie, Temperatur, externem Magnetfeld und Dotierung charakterisiert. Untersuchungen an YBCO, in dem Cu teilweise durch nichtmagnetisches Zn ersetzt ist, deuten auf eine gegenseitige Konkurrenz von Spinordnung, Ladungsordnung und supraleitendem Zustand hin. Die Studie wurde dann auf Übergitter von YBCO und halbmetallischem  $\text{La}_{2/3}\text{Ca}_{1/3}\text{MnO}_3$  (LCMO) erweitert. Das in diesen Übergittern verwendete YBCO ist vollständig mit Sauerstoff gesättigt, so dass aufgrund der Dotierung keine Ladungsdichtewelle erwartet wird. Das Hauptergebnis ist hier, dass trotzdem eine Ladungsdichtewelle in YBCO durch den Transfer von Elektronen an der YBCO/LCMO-Grenzfläche erzeugt werden kann. Die Temperatur- und Magnetfeldabhängigkeiten der Ladungsdichtewelle in den Übergittern deuten auf eine statische, stabile Phase hin - im Gegensatz zur fluktuierenden Ordnung in den Einkristallen. Dieses Ergebnis zeigt, wie durch Nukleation an Oxid-Grenzflächen metastabile elektronische Phasenübergänge unterstützt werden können.



# Table of Contents

<b>1</b>	<b>Introduction</b>	<b>1</b>
1.1	Scope of this thesis . . . . .	2
<b>2</b>	<b>The System: Transition Metal Oxides and their Heterostructures</b>	<b>3</b>
2.1	Transition metal oxides . . . . .	3
2.1.1	Crystal structure . . . . .	3
2.1.2	Electronic structure . . . . .	6
2.2	TMO heterostructures . . . . .	12
<b>3</b>	<b>The Technique: Resonant X-ray Scattering</b>	<b>17</b>
3.1	Introduction . . . . .	17
3.2	X-ray sources: synchrotron radiation . . . . .	18
3.3	Resonant scattering . . . . .	20
3.3.1	Basic principles of x-ray physics . . . . .	21
3.3.2	The interaction of light with matter . . . . .	23
3.3.3	XAS cross section . . . . .	24
3.3.4	Magnetic scattering: symmetry considerations . . . . .	29
3.3.5	Experimental access to reciprocal space . . . . .	34
<b>4</b>	<b>The Nickelates: A Spin Density Wave</b>	<b>41</b>
4.1	Properties of bulk RNO . . . . .	41
4.1.1	Electronic configuration and the Torrance phase diagram . . . . .	41
4.1.2	The MIT: charge disproportionation . . . . .	43
4.1.3	AFM order: noncollinear spiral . . . . .	45
4.1.4	A SDW-nested Fermi surface . . . . .	47
4.2	Properties of LNO SLs . . . . .	48
4.2.1	Reconstructing LNO . . . . .	48
4.3	Experimental results . . . . .	52
4.3.1	Structural details of LNO SLs . . . . .	52
4.3.2	Magnetic order in LNO . . . . .	59
4.3.3	Magnetic structure of RNO films . . . . .	65
4.3.4	Models: collinear vs. noncollinear spins . . . . .	68
4.4	Discussion and conclusions . . . . .	72
4.4.1	Orbital polarization altering the magnetic structure . . . . .	72
4.4.2	Remanent conductance in the SDW state and the question of concomitant CO . . . . .	74

---

<b>5</b>	<b>The Cuprates: A Charge Density Wave</b>	<b>79</b>
5.1	Properties of bulk YBCO . . . . .	79
5.2	CDW order in YBCO single crystals . . . . .	93
5.2.1	Discussion and conclusions . . . . .	101
5.3	CDW order in YBCO-LCMO heterostructures . . . . .	105
5.3.1	Properties of heterostructured YBCO . . . . .	105
5.3.2	Experimental results . . . . .	106
5.3.3	Discussion and conclusions . . . . .	116
	<b>Appendices</b>	<b>121</b>
A	The Kramers-Kronig Relations	123
B	Quantization of the Light Field	125
C	Fermi's Golden Rule	127
D	Mathematica script to analyze azimuthal dependencies	129
	<b>Bibliography</b>	<b>131</b>
	<b>List of Publications</b>	<b>145</b>
	<b>Acknowledgements</b>	<b>147</b>

# Chapter 1

## Introduction

A metal's Fermi surface, to which most of its macroscopic properties can be attributed, can become unstable at low temperatures to the formation of spin or charge density waves, superconductivity, or other collective electronic ordering phenomena. Full theoretical prediction and understanding of these ground states lies amongst the greater challenges in condensed matter physics. The dialogue between theory and experiment is vital to progress in this field, especially when techniques in detecting these ordered states are developing at rapid pace.

At center stage in this discussion are so-called strongly correlated materials, where the valence-state electrons can easily lose their mobility by feeling their mutual repulsion. Once these interactions become strong enough, the electrons' degrees of freedom become equally important. The lattice, the electron's charge, its spin, or its orbit can combine to build a rich array of properties ranging from metal-insulator transitions, superconductivity, ferro- and antiferromagnetism, etc. One of the most important classes of strongly correlated materials is composed of  $3d$ -transition metals and oxygen. These transition metal compounds exhibit half-empty  $d$  shells with enough spatial extent to overlap with the neighboring oxygen ions resulting in systems with electrons on the verge of localization. In this thesis, we will focus on  $3d$ -transition-metal oxides, where the intermediate extent of the valence shell leads to electronic bandwidths which can easily turn materials metallic to insulating, localize spins, and even glue electrons into Bosonic pairs with zero-resistance motion.

These interactions between the electrons' degrees of freedom can reshape the Fermi surface and lead to ordered states. Charge localization, for example, is largely responsible for the macroscopic transport properties which can be tuned between insulators and metals. Spin order, on the other hand, is responsible for the magnetic properties that many of today's hard drive storage exploit. With a strong intrinsic anisotropy, the orientation of ordered spins is yet another curious aspect which can range from collinear (anti-)parallel moments, to noncollinear spirals. These charge textures and spin spirals in TMO-materials can be studied using scattering techniques.

Along with the interest to understand these materials from a fundamental point of view, integrating them into modern electronic devices is of great interest. However, the structural complexity of these materials poses a considerable challenge and thus sample quality is greatly important. Growing single crystals of these materials is not always straightforward, let alone in doing so with extreme purity and high quality. Although the single crystals or powders available are important in discovering and understanding the physics, a new trend in growing these materials has developed during the last decade. In analogy to the semiconduc-

tor community's realization of the advantage of creating interfaces between two dissimilar materials, the growth of films, heterostructures, and superlattices comprising TMO layers has spawned an exciting approach to engineering new materials. Rapid advances in these growth techniques which include molecular beam epitaxy, pulsed laser deposition, etc., have lead to atomically sharp interfaces between layers of decreasingly small thickness, even down to single atomic layers. This geometry offers new perspectives which conventional solid state chemistry cannot, some of which will be discussed in the following chapter. However, the detection and control of the subtle spin- and charge-modulated structures resulting from Fermi surface instabilities in the atomically thin layers of such heterostructures remain challenging. This thesis will address the detection of sought-out spin and charge order in such materials using the technique of resonant x-ray scattering.

## 1.1 Scope of this thesis

**Chapter 2.** An outline of the most relevant physical properties of the systems investigated in this thesis is presented: transition metal oxides. Furthermore, the motivation of creating heterostructures of these materials will be presented, including recent theoretical proposals. Finally, a few words will be invested to describe the relevant growth and characterization techniques.

**Chapter 3.** This chapter will address the theoretical aspects and technical details of the experimental technique used in this thesis. X-ray scattering, in particular using resonant soft x-rays is a tool with a major importance in this field. First, a theoretical description of the technique's utility will be outlined. Furthermore, a depiction of the technical challenges and details that surround the experimental setup will be presented.

**Chapter 4.** In this section, the work done on nickelate heterostructures will be described. First, we will present an introduction to the class of materials, their phase diagram and their most relevant properties in their bulk state. Furthermore, a summary of results pertaining to superlattices comprising  $\text{LaNiO}_3$  over the last years will be made. Later, the results of this thesis will be presented, particularly focusing on the structural and magnetic properties.

**Chapter 5.** A major part of this PhD thesis was devoted to research on superconducting cuprates. The findings of this research will be outlined here, preceded by an introduction to the physics of these materials. The experimental findings include the discovery of a charge density wave state in both single crystal cuprates as well as its unexpected manifestation in cuprate-manganite heterostructures.

# Chapter 2

## The System: Transition Metal Oxides and their Heterostructures

Correlated electron systems like transition metal oxides (TMOs) attract special attention in modern solid state physics. They offer coupled charge, lattice, orbit, and spin degrees of freedom, which can be combined to achieve intriguing collective phases. Many of these phases can be tuned or explored by growing the materials into heterostructures. In this thesis, two classes of TMO compounds will be investigated which will be addressed in detail in each corresponding chapter. This chapter will present a summary of the general properties of TMO compounds and the motivation for creating artificially engineered materials via heterostructuring.

### 2.1 Transition metal oxides

TMOs are materials composed of metals with partially filled  $d$ -shell bonded to ligand oxygen ions. The following discussion will focus on the first row of these materials,  $3d$ -TMOs, collected from Ref.'s [1–8].

#### 2.1.1 Crystal structure

The basic structural building block of many TMO compounds is the  $\text{CaTiO}_3$  “perovskite” unit cell, whose essence is shown in Fig. 2.1. The transition metal ion, in this case  $\text{Ti}^{4+}$ , is coordinated by 6  $\text{O}^{2-}$  ions at the face centers. For a  $\text{ABO}_3$  material with cubic  $Pm\bar{3}m$  symmetry, where  $A$  is a rare earth metal and  $B$  the TM ion, the  $A$  ions corner a cube with  $a = b = c$  lattice constants. The most prominent of such compounds is  $\text{SrTiO}_3$  (STO), with lattice constants  $a = 3.905 \text{ \AA}$ , and is commonly used for substrates to grow heterostructures and other applications.

However, the full cubic symmetry is not easy to stabilize and only a few  $\text{ABO}_3$  compounds preserve  $Pm\bar{3}m$  symmetry. Instead, changing the size of the  $A$  or  $B$  ions will result in distorted unit cells. The most common ways of accommodating the electrostatic potential of different sized ions are by rotating the octahedron or distorting the octahedron’s shape, elongating/shrinking along favorable crystalline directions. The former is observed, for example, in the superconducting cuprates where an out-of-plane elongation leads to a

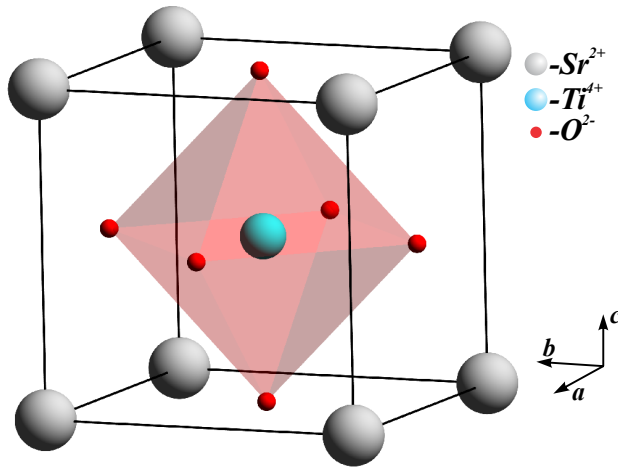


**Figure 2.1** The basic form of a perovskite unit cell, shown for cubic  $\text{SrTiO}_3$ .

quasi-2-dimensional system (Chapter 5). The latter, depicted in Fig. 2.2, is the case in rare-earth nickelate brethren (Chapter 4). The octahedral rotation can take place around any of the three cubic crystal axes. For each axis ( $x, y, z$ ), the corresponding rotations are labeled ( $\alpha, \beta, \gamma$ ).

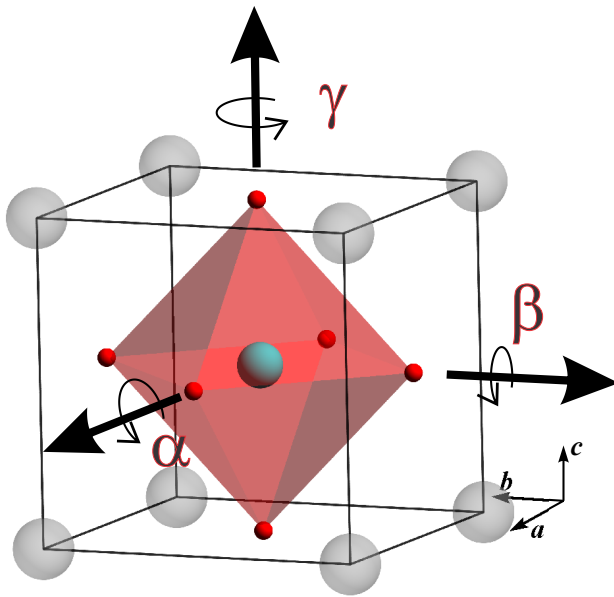


**Figure 2.2** The way perovskite unit cells adapt to differently sized ions, rotating the octahedra around any or all of the three formerly cubic axes.

The rotations of the octahedra can be different for each axis, and it can also be in- or out-of-phase. A rotation in phase around a certain axis implies that consecutive octahedra rotate in the same sense. An out-of-phase rotation occurs when subsequent octahedra rotate in opposite senses, giving rise to a doubled unit cell. An example of a  $\gamma$  rotation out of phase is depicted in Fig. 2.3. To consolidate the nomenclature, Glazer introduced the notation  $a^{+,-,0}b^{+,-,0}c^{+,-,0}$ , where each letter corresponds to the amount of rotation around the cyclic axes ( $\alpha, \beta, \gamma$ ), and the superscript determines whether the rotation around that axis is 0, in- (+), or out-of-phase (-) [7]. Below the cubic  $Pm\bar{3}m$  symmetry, the structure observed in TMOs with highest symmetry is  $R\bar{3}c$ , which has a Glazer notation pattern  $a^-a^-a^-$ . An example of such a system is  $\text{LaNiO}_3$  with  $\alpha = \beta = \gamma = 5.2^\circ$ , which will

be of major focus in later sections. A common distortion found in  $ABO_3$  TMOs is the so-called  $GdFeO_3$  distortion, named after the first compound discovered of the kind. This has a rotation pattern  $a^+b^-b^-$ . The space group is  $Pbnm$ , and is commonly found in other nickelates which will be of interest later on. These structures are shown in Fig. 2.4.

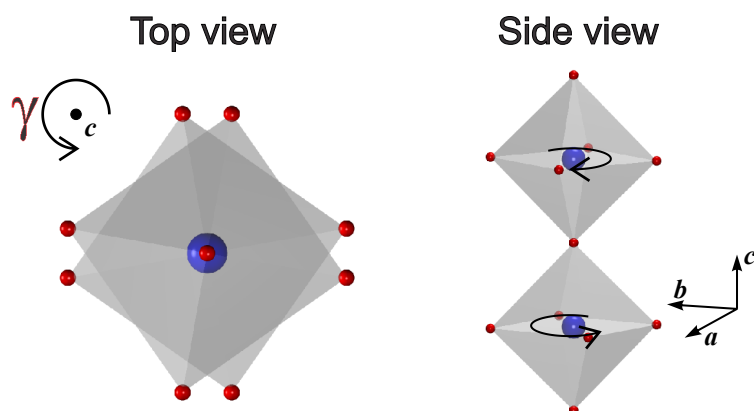


**Figure 2.3** An example of a rotation  $\gamma$  out of phase, as observed along the  $c$ -axis (left) and from the side (right).

Varying symmetries yielded by the rotation patterns lead to different diffraction selection rules, and thus can be monitored using scattering techniques. The crystal symmetries are commonly divided into space groups, consisting of both the point symmetry elements and the translations of the lattice. A complete list of the 230 space groups and their properties can be found in Ref. [9]. Formally speaking, once the cubic symmetry is abandoned the definition of the lattice requires the use of new indexing. However, the “pseudocubic” reference is commonly used particularly in heterostructures whose actual symmetry is hard to predict or measure. In that case, for example, the reflexes of a doubled, low-symmetry phase are indexed as  $(\frac{h}{2}, \frac{k}{2}, \frac{l}{2})$ . The details of space group symmetries is a much broader topic and will not be addressed further in this thesis. A much more thorough summary on these matters can be found in Ref.’s [7–11].

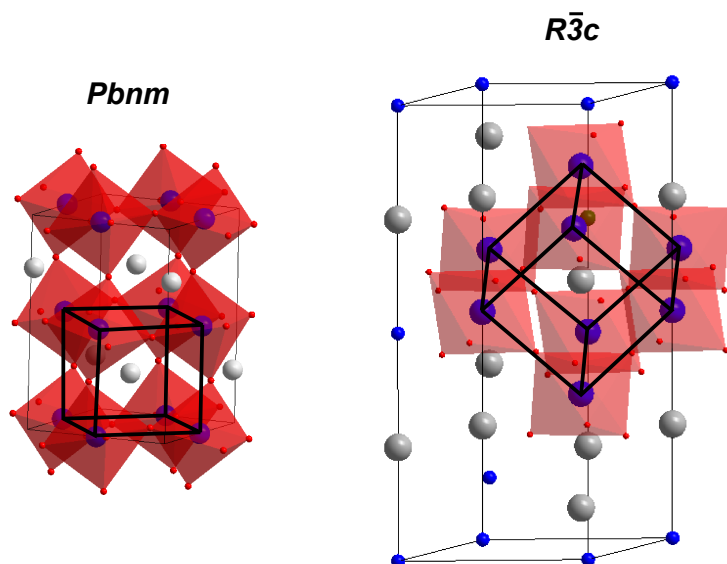


**Figure 2.4** (Left) A  $Pbnm$  and (right) a  $R\bar{3}c$  unit cell. In both cases, the pseudocubic unit cell is highlighted.

## 2.1.2 Electronic structure

The crystal structure in TMOs largely governs their electronic properties. In this section, we will survey the most relevant properties to the work done throughout this thesis.

### The $d$ orbitals

Once an electron is bound to an atom through the Coulomb interaction, the different energy levels of the orbitals yield wavefunctions with different real-space shapes. Beyond the spherical contour of the  $s$ -shell, higher energy orbitals have strong spatial anisotropy. The  $3d$  TMs of interest in this thesis have anisotropic, partially filled  $d$ -orbitals near the Fermi level and thus govern most of the characteristics of the materials.

The solution of the Schrödinger equation in the simple case of one atom yields five degenerate states with energy level  $n = 2$ , the  $d$  orbitals. The spatially anisotropic angular part of the wavefunction is shown in Fig. 2.5.

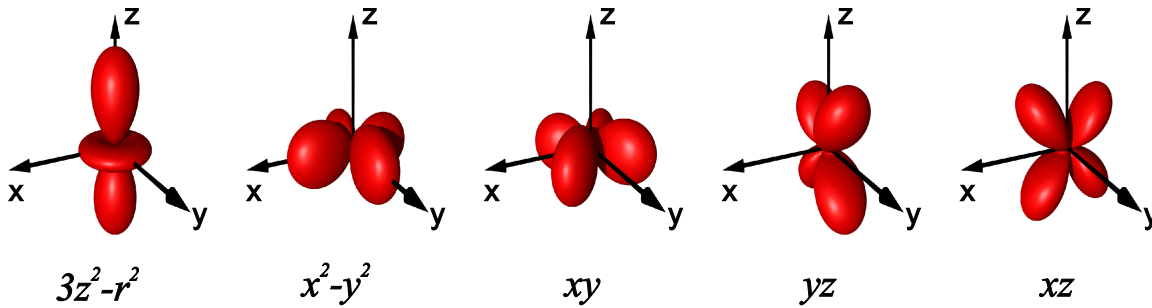


**Figure 2.5** The angular dependence of the five degenerate orbitals of the solution of the hydrogen-like orbitals for  $n = 2$ , i.e. the  $d$  orbitals

The spatial anisotropy of the orbitals becomes more significant when oppositely charged ions are placed around the TM ion, resulting in a lifting of the degeneracy of these levels. Consider the simple case of a TM ion inside a cubic octahedral environment as depicted in Fig. 2.1. The positional arrangement of the O ions along the  $x, y, z$  directions creates a field around the TM ion, known as the ligand field, which renders those orbitals which point towards the O ions energetically unfavorable. Thus, the  $d_{x^2-y^2}$  and  $d_{3z^2-r^2}$  orbitals, commonly referred to as the  $e_g$  levels, have higher energies. The orbitals with lower energy, known as the  $t_{2g}$  levels, point diagonal to the O ions. The splitting between the  $t_{2g}$  and  $e_g$  levels is known as the crystal field splitting, usually noted by  $\Delta_c$ , where the subscript indicates the type of symmetry the TM ion lives in. In the case of a tetragonally distorted octahedra, the splitting results in more levels. These two cases are shown in Fig. 2.6. In general, different crystal symmetries result in different level splitting schemes.

The way the  $d$ -electrons populate the available  $t_{2g}$  and  $e_g$  levels depends on details of the system. Consider a  $3d$  cubic perovskite system with four  $d$ -electrons, labeled  $3d^4$ . The first 3 electrons will find their way into the three  $t_{2g}$  levels with parallel spins due to Hund's rule, obeying Pauli's principle of exclusion. If the energy cost of placing the fourth electron in a singly occupied  $t_{2g}$  level is less than placing it in a  $e_g$  level, i.e.  $\Delta_c$ , then it will occupy a  $t_{2g}$  level. Pauli's principle will force it to have an antiparallel spin. The resulting electronic configuration will be  $t_{2g}^4 e_g^0$ . Because two of the four electrons have antiparallel spin, the state

is thus known as a “low spin” state. There are cases where Hund’s principle makes the occupation of a antiparallel  $t_{2g}$  state exceed the cost in energy of going up into the  $e_g$  level. The resulting electronic configuration is  $t_{2g}^3 e_g^1$ , with all spins parallel is known as a “high spin” state. Aside from details pertaining to different classes of systems, high and low spin states are usually governed by  $\Delta$ .

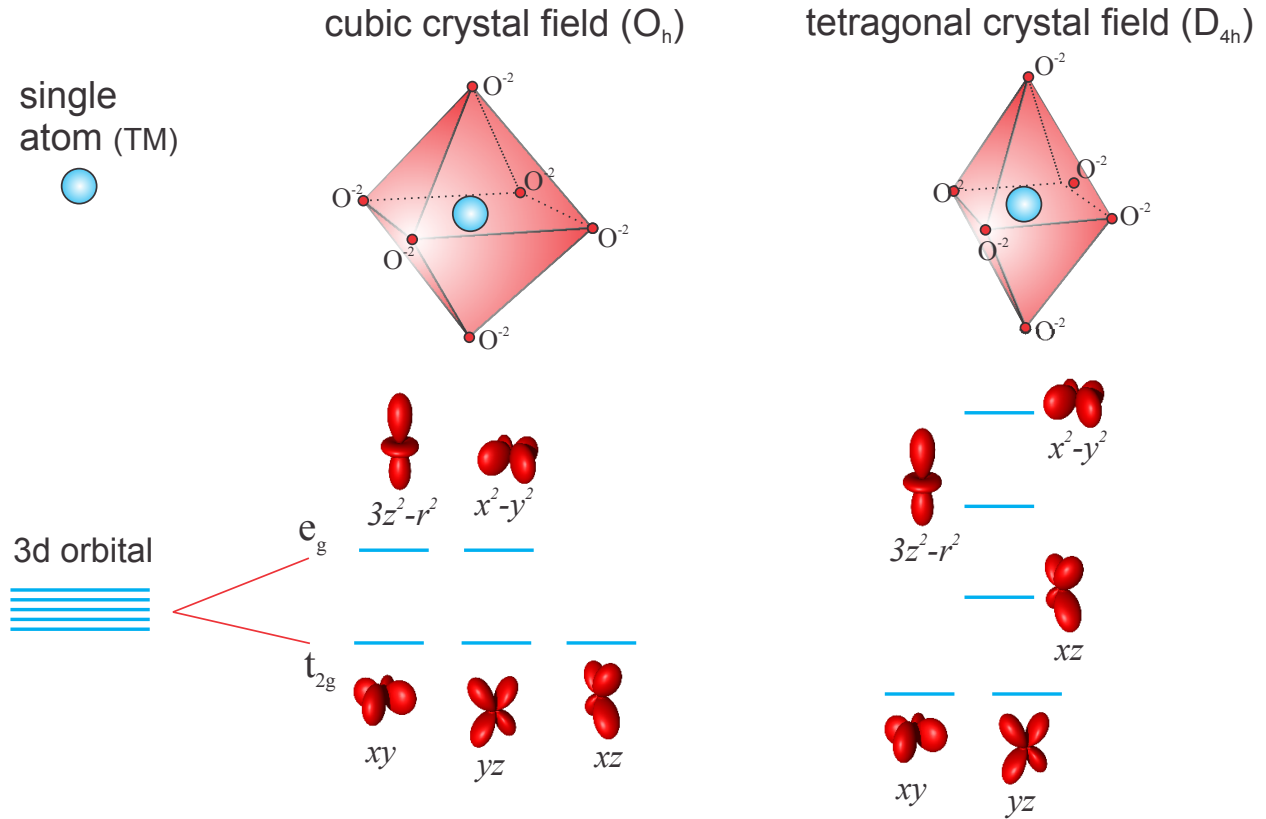


**Figure 2.6** The lifting of the degeneracy of the 5  $d$ -orbitals when placing the TM ion inside a regular octahedra with O ions at the corners (left) and a tetragonally distorted octahedra (right).

## Mott insulators

With an intermediate spatial extent of the  $3d$  wavefunction, the conduction electrons in some half-filled materials can localize once they feel the Coulomb interaction with other electrons. Thus, while expected by conventional band theory to be metallic, some of these materials undergo a metal to insulator transition (MIT). The energy of the electrons in such materials can be expressed as  $E = U - 2t$ , where  $t$  is the hopping amplitude obtained from the transfer integral of a tight binding model. It quantifies the probability of an electron occupying adjacent sites. The energy of a metal is dominated by this term. The term  $U$ , introduced into the Hamiltonian by Hubbard in 1963 [12], represents the essence of a Mott insulator. When this term  $U$  overpowers the hopping integral, the electrons tend to localize at corresponding sites, opening a gap of size  $U$  at the Fermi level. In other words, in an insulating ground state with electrons localized on every site, the energy cost of creating a doubly occupied site is  $U$ . Moreover, considering the intrinsic band width  $w$  of the  $d$ -level, which is governed by  $t$ , the effective band gap in a Mott insulator is  $U - w$ . This is shown

schematically in Fig. 2.7.

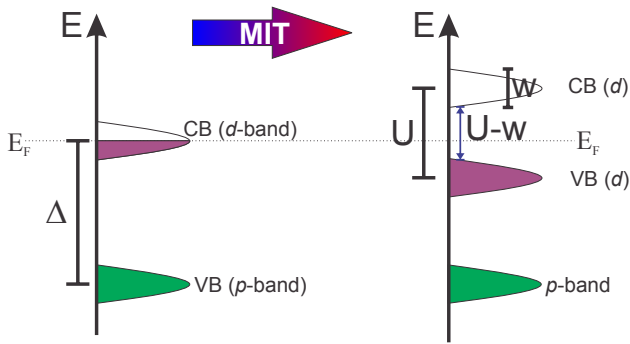


**Figure 2.7** Across a Mott transition, the half-filled conduction band (CB) above the valence band (VB) of a metal splits across the Fermi energy ( $E_F$ ) into two bands, with an energy difference governed by the interaction energy  $U$  and the width of the band  $w$ . Image reproduced from [5].

In TMOs, a covalent bond between the O and TM ions leads to hybridized states with energy close to that of the  $3d$  shell. The band below the  $d$ -level is the  $2p$  state of the ligand oxygens hybridized with the TM. The energy separation between these states is known as the charge transfer  $\Delta^1$ . A special class of interaction-driven insulators is that where  $\Delta$  is small. Upon crossing the MIT, the  $d$  band splits with a gap  $U$ , but the lower  $d$ -level leapfrogs the  $2p$ -level, leaving the  $p$ -band adjacent to the gap of value  $\Delta$ . These materials are known as “charge-transfer” insulators. Note that the mobility of electrons in these materials is allowed throughout the ligands, in contrast to a Mott insulator’s complete on-site localization. Such a classification was coined in the work of Ref. [13], and is depicted in Fig. 2.8. Generally speaking, the interaction term  $U$  increases for the heavier TM ions, thus making the early columns prone to a Mott insulating state, and the later ones like Cu and Ni compounds of charge transfer types.

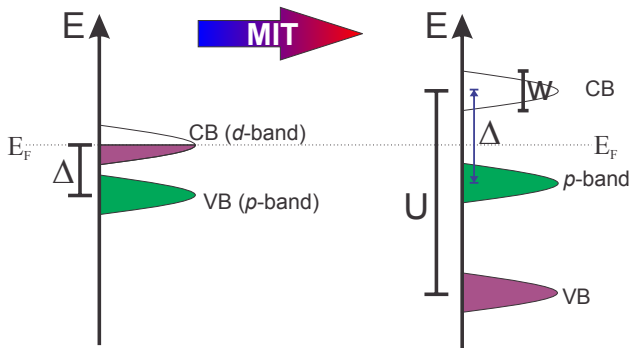


**Figure 2.8** Across a MIT in a charge-transfer insulator, the half-filled band of a metal splits across the Fermi energy ( $E_F$ ) into two bands, with an energy difference governed  $\Delta$  and the width of the band  $w$ . Image reproduced from [5].

## Charge and spin ordering

The localization of charge discussed above in a correlated insulator is not the only type of order that these materials can develop. Some materials display charge disproportionation (or charge order) between subsequent sites. In this case, the valence state of the TM ion varies from site to site in the form  $B^{3+\delta} - B^{3-\delta}$ , doubling the perovskite unit cell. Common cases of such materials are the manganites, discussed later in this chapter, and the nickelates, discussed in Chapter 4. The spin degree of freedom can concomitantly form ordered patterns which result in ferromagnetic (FM) and antiferromagnetic (AFM) systems. To describe a

<sup>1</sup>Not to be confused with the crystal field splitting which usually has a subscript to denote the symmetry.

simple ground state in a magnetically ordered system, a Hamiltonian is required that will couple adjacent spins based on the singlet-triplet energy splitting. Treating the case of a simple two-electron system with neighboring  $\vec{S}_1$  and  $\vec{S}_2$  and extending it to a lattice, the Hamiltonian reads

$$H_{spin} = - \sum_{ij} J_{ij} \vec{S}_i \cdot \vec{S}_j, \quad (2.1)$$

with  $J$  given by the singlet-triplet splitting. This simple Hamiltonian, commonly known as the Heisenberg Hamiltonian, at least qualitatively describes realistic systems and can be read more extensively in text books like Ref. [14]. Since the dot product changes with orientation of adjacent spins, the coupling constant  $J > 0$  ( $J < 0$ ) will favor parallel (antiparallel) spins.

Correlated materials of interest in this thesis commonly develop magnetic ordered states. Once including the magnetic term, the Hubbard Hamiltonian  $H$  of such a system, which we had discussed above without considering the spin channel, takes the general form

$$H_{Hub} = -t \sum_{\langle i,j \rangle \sigma} c_{j\sigma}^\dagger c_{i\sigma} + U \sum_i n_{i\uparrow} n_{i\downarrow}, \quad (2.2)$$

where  $\langle i, j \rangle$  implies adjacent sites and  $\sigma$  represents spin up or spin down states. The 4 possible states for a site  $i$  with two available states are: empty  $|\cdot, \cdot\rangle$ , one electron  $|\uparrow, \cdot\rangle$ , one electron  $|\downarrow, \cdot\rangle$ , two electrons  $|\uparrow, \downarrow\rangle$ . The second term above is diagonal in these terms, as it takes on a value  $U$  when site  $i$  is doubly occupied  $\uparrow\downarrow$ , and all other matrix elements are zero. This term will favor localized spin moments by nullifying the probability of a second electron to occupy a singly occupied site, recovering the discussion in the previous section. The first term in Eq. 2.2 is the kinetic energy, describing the annihilation of an electron with spin  $\sigma$  at site  $j$  and the creation at site  $i$ : moving the electron from site to site.

Mott insulators with large  $U$  are more prone to develop AFM order. Consider the case of half-filled metals, where the number of electrons equals the number of sites. For the case of negligible Coulomb repulsion ( $t \gg U$ ), the system is metal. However, when the repulsion is stronger ( $U \gg t$ ), the Hamiltonian of Eq. 2.2 can be treated to derive an expression analogous to Eq. 2.1, with  $J = -4t^2/U$ . In simple words, AFM alignment of spins is favored because it allows hopping of electrons to nearest sites.

### Fermi surface nesting

Ordered patterns are not exclusively driven by the same mechanism of the localized Mott insulators. Another kind of ordered ground state which can occur in itinerant metals is the formation of density waves [15,16]. These occur when conduction electrons self-organize into patterns of modulated charge or spin in the solid. The simplest case of a charge density wave (CDW) was first proposed by Peierls in the 1930's to explain how a 1-dimensional (1D) system cannot be metallic [15–18], summarized in Fig. 2.9. Consider the ground state of a 1D, half-filled array of atoms with spacing  $a$ . With a parabola-like dispersion of the electron energy, the system is filled up to the Fermi level  $E_F$  at  $k_F = \pi/2a$  and the electronic standing wave gap is formed at  $\pm\pi/a$  [14]. If the unit cell distorts in such a way as to double its size say by forming dimers, then the folded Brillouin zone boundary is at  $k_F = \pi/2a$  and a gap opens at  $E_F$ . The electronic energy of the system is reduced by lowering the energy of the states at  $k_F$ . In other words, if the gap opened at a smaller wavevector  $k_F - \delta$ , then some

electrons would raise to the higher band and others to the lower band. This yields no energy reduction. If the gap opened at  $k_F + \delta$ , the system would remain metallic with no change in total energy. Thus, opening a gap at  $k_F$  by forming dimers is a way for the system to find an energy minimum. Furthermore, Peierls showed that the elastic energy cost of this dimerization is paid at low temperatures by phonon-electron interactions. This results in a CDW with period  $2a$  shown in Fig. 2.9. Note that the electronic modulation of a CDW coexists with a lattice distortion introduced by the new periodicity.

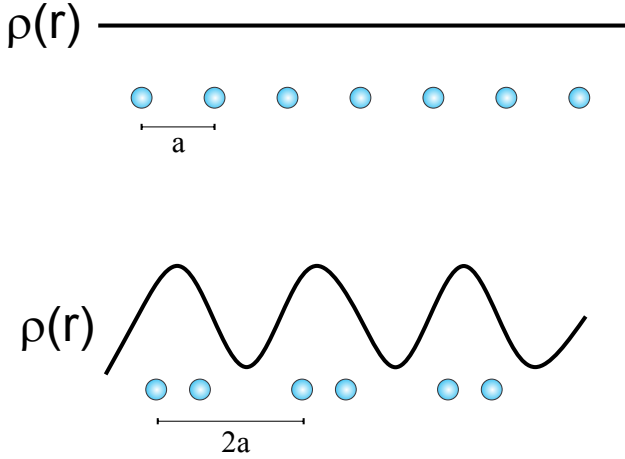


**Figure 2.9** The mechanism of a 1-dimensional Peierls transition. The regular lattice (top) yields an even density  $\rho(r)$ , while the distorted, doubled lattice (bottom) results in a sinusoidal charge density wave. Figure adapted from [15].

The vector of the new periodicity that caused an energy reduction is called a nesting vector. Let us take a close look at this definition, following [15, 16, 19]. Consider a perturbation  $H'$  in the form of a scattering process which adds momentum  $V = k - k'$  to a certain electron in state  $\phi(k)$ , coupling it to a hole above the Fermi level  $\phi(k')$ , shown in Fig. 2.10(top) as a yellow vector. Following quantum mechanical perturbation theory [20], the new states are linear combination of the unperturbed states  $\psi(k) \propto \phi(k) + C\phi(k')$  and  $\psi(k') \propto -C\phi(k) + \phi(k')$ , where  $C$  is a mixing term proportional to  $\langle \phi(k) | H' | \phi(k') \rangle$ . Two important observations can be made. First, treating the new state's density  $\psi(k)\psi^*(k)$ , as described in [19], shows that it is modulated by a term  $\cos(Vr)$ , where  $r$  is a vector of the lattice. This will yield a density wave, whose spin or charge character will depend on details of how the states  $\psi(k)$  and  $\psi(k')$  are occupied.

The second observation points to the peculiar case when  $\phi(k)$  and  $\phi(k')$  are degenerate. In that case, perturbation theory shows that the degeneracy is lifted by lowering and raising  $\psi(k)$  and  $\psi(k')$ , respectively, opening a gap between the levels. A system will thus find an efficient way to minimize the energy by scattering between degenerate states, i.e. states at the Fermi level. Fig. 2.10(bottom) shows how a 1-dimensional case with a parabolic dispersion will open a gap when scattering vector is  $V = 2k_F$ , shown as a red arrow. Once the gap is opened at  $E_F$ , the system ceases to be metallic.

In the 1D case, this definition is almost trivial because the vector that obeys the condition of opening a gap where the energy is lowered,  $2k_F$ , connects merely two points (hence the fact that such a system cannot be metallic). So let's extend the concept to 2D. Consider a periodic deformation with vector  $\vec{V}$ . A new periodicity will cut the Brillouin zone into parts, depending in size and orientation on  $\vec{V}$ . Moreover, we know from the 1D case that a deformation will also gap the FS at those values and lower the system's energy. The system will find an energy favorable condition when the FS lies at the edge of the cut made by

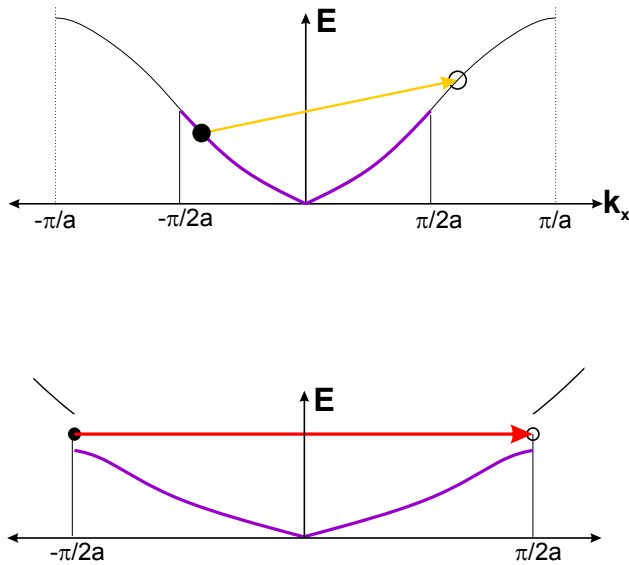


**Figure 2.10** The unstable case of a half-filled, 1-dimensional system. (top) The scattering process coupling an electron and a hole through a vector  $V$ , in yellow. (bottom) When the two states are degenerate, a gap opens.

$\vec{V}$ . So the tendency towards a nested case is the tendency to gain energy by introducing a modulation vector  $\vec{V}$ .

The more states at the FS lie at the edges produced by  $\vec{V}$ , the larger the energy reduction. Since Brillouin zone folding by  $\vec{V}$  is a flat cut, this condition is obeyed for a FS with flat regions, and  $\vec{V}$  is the vector connecting those flat regions. This can be seen in Fig. 2.11 for the case of 1D (always a flat Fermi “surface” in 2D), and for a flat FS in 2D. In this case, the FS shown in blue lies entirely at the edge of a folding cut (magenta lines) resulting from a vector  $\vec{V}$ , and the nesting vector is shown in red. Fig. 2.11 also shows a case with no nesting tendency for a circular FS. No flat cut can make the FS land on the edges. However, nesting is not exclusive to a flat FS. Since a nested FS lands on itself upon a translation by  $2\vec{V}$ , a curved FS can also nest. As shown in Fig. 2.11 by expanding outside of the first Brillouin zone, the red vector translates the FS invariantly and is therefore a nesting vector.

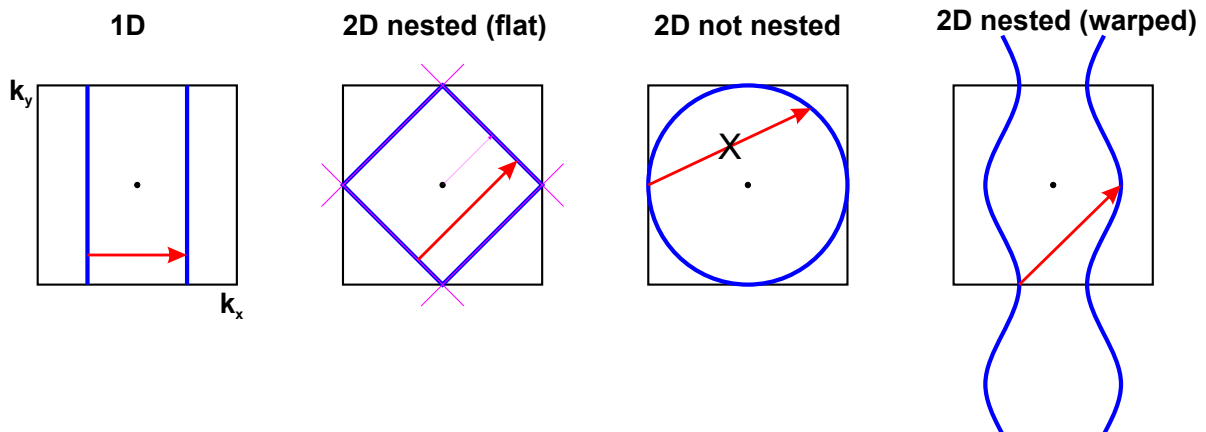


**Figure 2.11** Examples of Fermi surface (blue) nesting, highlighting the nesting vector (red), for 1D and 2D cases. While the former always has a nesting vector, the latter does not always have nesting (like in the circular case). It can do so when having a flat FS, or warped into special ways. The squares represent the first Brillouin zone. In the warped case the FS is extended for clarity.

In summary, the energy is lowered by connecting degenerate states through a scattering

process with momentum  $2\vec{V}$ . The degenerate states are at (and define) the FS so nesting occurs for metals only. The more states at the FS are connected by  $2\vec{V}$ , the more the system will gain in energy. So a system’s tendency to nest occurs when MANY states at the FS are connected by a vector  $2\vec{V}$ , occurring naturally in flat regions or in specially curved Fermi surfaces. However, it can also occur if the vector  $2\vec{V}$  connects points where many states accumulate, so-called “hot-spots”. Such a case is exemplified in Fig. 2.12 and may be responsible for the observed phenomenology of the high- $T_c$  cuprates (Chapter 5).

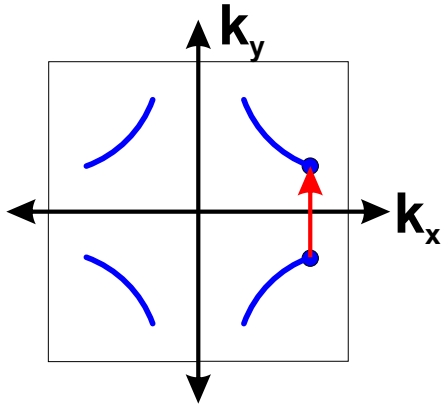


**Figure 2.12** A cartoon schematic of a nesting where a vector connects points at the edge of a FS with a large accumulation of states (blue circles).

The density waves that arise from scattering between states through a nesting vector can lead to organizing the electrons’ spin or charge. A spin state invariant under the scattering process yields a CDW, while a spin-flipping scattering process usually leads to a spin density wave (SDW) [19]. Experimentally, these result in pronounced changes in either the spin or charge susceptibilities [15] and can thus be detected using transport techniques. However, perhaps the most obvious manifestation of these density waves are the superstructure patterns that emerge. These patterns can be investigated using diffraction techniques addressed in Chapter 3.

## 2.2 TMO heterostructures

In this section, we turn from the single crystal attributes of TMOs to the case of materials grown on substrates into films, multilayers or superlattices (SLs): heterostructures of TMOs.

### Motivation

There are many ways to tune or investigate the wide range of properties of single crystal TMOs. Among these, and most prominently, strained films and superlattices (SLs) have become promising offers. First of all, some materials are hard to produce in large single crystals, so thin film research has provided insight to their physics. Secondly, endless combinations of straining, interfacing, and confining complex oxides provide the media to create unique metastable materials, with properties ranging from multiferroics to superconductors [21–24].

Heterostructured TMOs allow us, therefore, to manipulate the systems’ lattice, charge, orbital and spin degrees of freedom in ways that solid state chemistry cannot. There are several quintessential examples of novel phenomena at oxide interfaces. High electron mobility and the creation of a 2D electron gas at the interface between two band insulators

LaAlO<sub>3</sub>-SrTiO<sub>3</sub> (LAO-STO) was observed in 2004 [25] and has been extensively investigated thereafter. Amongst many other fascinating results, superconductivity was found at low temperatures [26]. Work done during this PhD period using non-resonant x-ray diffraction showed evidence of polar order driven by a gate voltage [27] and most recently evidence of FM order coexisting with SC was shown [28]. The superconducting, 2D LAO-STO interface has been recently compared to the high-T<sub>c</sub> cuprates, making analogies about the gap states [29].

While a lot of the effects taking place in LAO-STO are believed to be related to the charge reconstruction at the interface, oxide heterostructures allow more than manipulating the charge. This is where their potential surpasses conventional semiconductor based electronics. TMO systems offer the spin, which are made use of in spintronics, and orbital degree of freedom. Since these two are also coupled, they offer an infinite array of manipulation avenues [21–23], like in the case of the LAO-STO system [30,31].

### LNO-based superlattices

One of the most resounding proposals of engineering a new material in the last few years was the one made by Chaloupka and Khaliullin in 2008 [24]. First, the authors surveyed the properties of the superconducting cuprates which are widely accepted (more detail in Chapter 5). In such systems, the Cu ions are in a spin= 1/2 state with a singly (or vastly) occupied  $d_{x^2-y^2}$ . Furthermore, the Cu-electrons are isolated by blocking layers which confine them to a 2D space. Some of these characteristics can be reproduced in other TMO compounds, save one: the single occupation of the  $d_{x^2-y^2}$ -orbital. Without knowing exactly how the mechanism of superconductivity arises, the authors proposed a way to achieve all three aspects. They identified that a heterostructure comprising LaNiO<sub>3</sub> (LNO) and an isostructural band insulator like LaAlO<sub>3</sub> (LAO) could reproduce three essential features of the high-T<sub>c</sub> cuprates. Summarized in Fig. 2.13, imposing epitaxial strain that would elongate the NiO<sub>6</sub> octahedron in the plane as well as confining the electrons between blocking layers could substantially lift the orbital degeneracy. This proposal has sparked great interest and many groups today still investigate the growth of these SLs in search of a new superconductor. Although such a state has not been found, the material has displayed fascinating physics which will be addressed in Chapter 4.

### YBCO-LCMO superlattices

Another system which has attracted strong interest in the TMO heterostructure community is the YBa<sub>2</sub>Cu<sub>3</sub>O<sub>7</sub>-La<sub>2/3</sub>Ca<sub>1/3</sub>MnO<sub>3</sub> (LCMO). The former material is a conspicuous member of a class of superconducting cuprates, whose properties will be addressed in more detail in Chapter 5. LCMO is also a major player in TMO physics. It is a half-filled FM metal which has revealed an electrical conductance that can be increased by several orders of magnitude when applying an external magnetic field. This is known as colossal magnetoresistance (CMR), and despite intensive research remains to be fully explained theoretically or exploited technologically. A lot of literature has been written devoted to these materials, summaries of which can be found in Ref.'s [4,32–34].

The CMR manganites are found most commonly by doping the parent compound  $R\text{MnO}_3$ , which is a ABO<sub>3</sub> perovskite, by substituting the trivalent  $R$  site by divalent Ca or Sr ions.

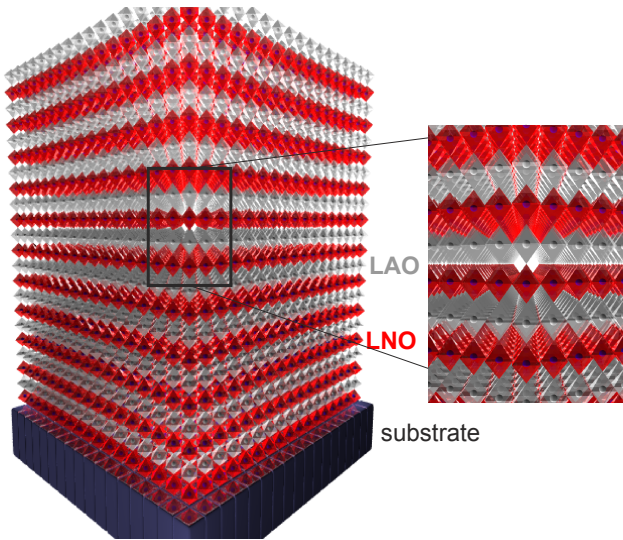


**Figure 2.13** A cartoon schematic of a LNO-LAO SL, proposed in Ref. [24].

The one mixture relevant to this thesis is taking  $R=La$  and substituting with Ca, with formula  $La_{1-x}Ca_xMnO_3$ . Substitution of Ca ions will change the carrier concentration, and thereby several ordered phases can be reached. These include charge ordered, AFM insulating, canted AFM, FM metal and FM insulating phases, all which are summarized in Fig. 2.14.

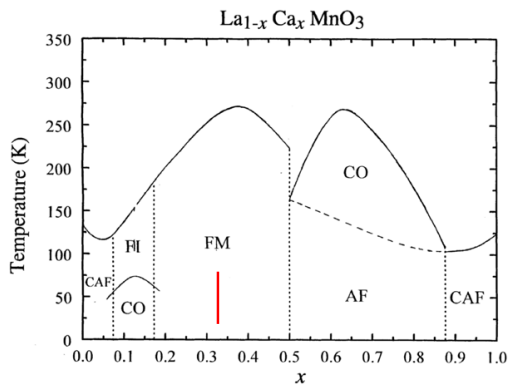


**Figure 2.14** The multiple phases of LCMO upon varying the Ca content, highlighting the FM-metal phase of interest to the present work. Figure taken from Ref. [34].

The parent perovskite  $LaMnO_3$  has a  $d^4 Mn^{3+}$  high spin state. When doped, lower lying  $(4-x)$   $d$  electrons will occupy the  $t_{2g}$  levels and  $(1-x)$  electron goes into a linear combination of the  $e_g$  levels. It turns out, hopping from site to site is favored when the  $e_g$  electron is FM aligned to the  $t_{2g}$ . This allows a FM metallic ground state. Some of the properties of these materials are believed to be strongly connected to the lattice, whether statically through the crystal structure or dynamically through phonons [34]. The region of the phase diagram of interest to this thesis is around  $x = 1/3$ . Shown in Fig 2.14 with a red line, the material turns from a paramagnetic insulator to a FM metal with an onset at about 250 K. With such a high transition temperature and a good conductivity in the magnetic state [33], these offer interesting potential applications in functional spin devices. As a half-metal, it provides a direct way of producing spin-polarized currents, that is most conduction electrons carry the same spin orientation. Furthermore, the properties of this and other manganites appear to be easily modified by growth into heterostructures [35].

Within the scope of exploring antagonistic order parameters, the interface between the

high- $T_c$  SC YBCO and half-metallic, ferromagnetic LCMO has become of prime interest. Driven by strong proximity effects [36–38], neutron reflectivity measurements [38, 39] evidenced an uncompensated magnetic moment in the SC YBCO layers, which was later confirmed using x-ray spectroscopic [40] and scattering tools [41]. Moreover, the superexchange coupling across the interface was partially attributed to a reconstruction of the Cu orbital occupation, which in turn leads to the transfer of electronic charge from the LCMO into the YBCO layers [42]. Anomalies in the Raman spectra of the LCMO layers upon entering the SC state expanded the discussion into the possible “engineering” of lattice dynamics aided by long range Coulomb interactions [43]. Such questions gave rise to a rich field of research which will be addressed in section 5.3.1, where further contributions were made in this doctoral work.

## Growth techniques

Several techniques to grow heterostructures of TMOs have been perfected since their promise has erupted in the last decade. Among these, most prominently are molecular beam epitaxy (MBE) and pulsed laser deposition (PLD). The former consists of heating different element sources until they evaporate and then condense on a substrate resulting in well-controlled heterostructures with extremely high quality surfaces and interfaces. It is deemed very useful in the growth of semiconductor film used in today’s common electronic devices. Its application to complex oxides was first introduced growing high- $T_c$  cuprates by Schlom, *et.al*, in Ref. [44]. It can also be used efficiently to grow high-purity heterostructures based on early TMs like Ti [45]. However, its application to other TMs, particularly ones which require high oxidation pressure remains a technical challenge pursued by many groups.

The technique more commonly used in complex oxide growth is PLD. All the samples investigated in this thesis were grown using it. PLD is a technique which allows environments with higher oxidation pressure, thus making it suitable to grow more complex oxides. It was first applied to grow films of the high- $T_c$  cuprates [46]. The technique itself is a very simple principle. Ablation is the process by which part of material is removed from its surface by exciting it through a high energy process. In PLD, this excitation is done by exposing the material to a pulsed, high-density laser. The high absorption of the material of the laser results in a very localized heating, which eventually evaporates the material creating a plasma plume. The material exposed to the laser is called the target, which is just a compressed powder pellet of the stoichiometric material wished to be grown. High laser fluxes induce nonequilibrium process whereby, with the choice of the right wavelength and for a given material, a vaporization process common to all cations of the material is produced. The ablated material travels through the chamber immersed in oxygen pressure, and eventually condenses on the substrate. By using the right oxidation pressure within the growth environment, the stoichiometry of the material (in particular the oxidation state) can be preserved all the way to the growth. Therefore, the ability to conserve the full chemical stoichiometry of targets with several elements on different substrates is an important advantage of PLD. The frequency and duration of the pulse regulate the growth rate of the material.

The process of PLD can be summarized as follows. A chamber is pumped to low air pressures in order to facilitate a large mean free path of the ablated material. Moreover, a reactive atmosphere of oxygen is introduced through gas inlets. A laser is generated by a UV

light source outside the chamber, then collimated using a lens. Once it strikes the target, which is simultaneously rotating to have the laser hit the sample on different positions, a plume of ablated plasma will travel perpendicular to the target surface and eventually reach the substrate. The latter is heated generically with a furnace or punctually by an additional laser, which enables the ablated material's reaction with the substrate. A schematic of a PLD chamber is shown in Fig 2.15. More thorough accounts on PLD can be found in Ref.'s [35,47] and others therein.

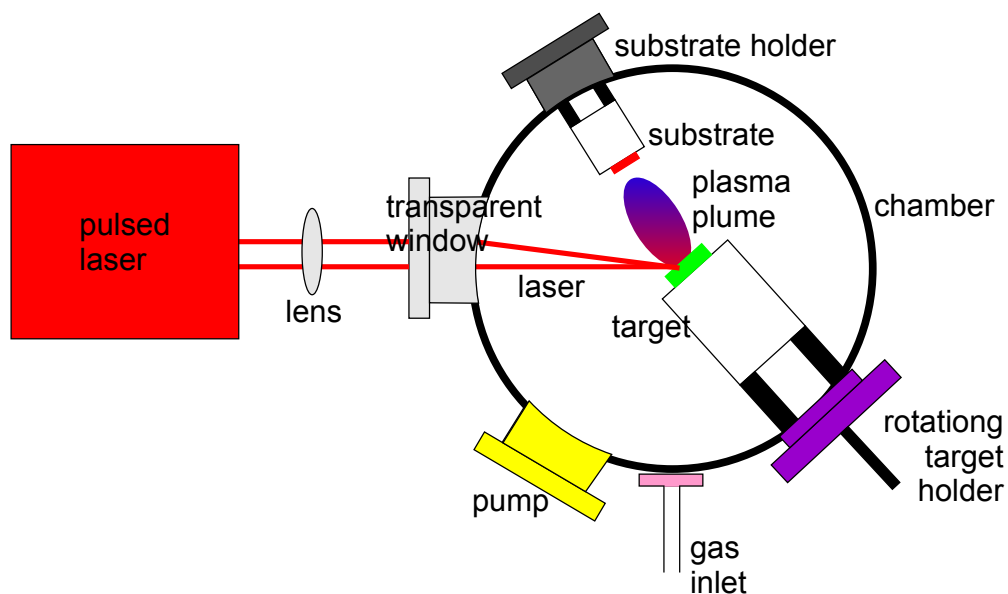


**Figure 2.15** A schematic of a PLD chamber. Figure adapted from Ref. [35].

# Chapter 3

## The Technique: Resonant X-ray Scattering

### 3.1 Introduction

The experimental technique used throughout this thesis to investigate the ordered states of the TMO heterostructures is resonant soft x-ray scattering (RSXS). In general, wave scattering techniques provide a non-destructive way to obtain correlation function information involving a large number of scattering entities. Non-resonant x-ray scattering served the framework for crystal structure determination when the tube source was developed. Later, other methods emerged including electron and neutron scattering, which with a charge or spin attribute, can interact with solid state matter and render precise location information about nuclear, ionic and magnetic scatterers. However, these can have limitations including non-element specificity, narrow penetration depths, low fluxes available, need for bulk samples, etc. Some of these limitations are overcome by the use of x-rays.

Resonant x-ray scattering (REXS) in general refers to a technique based on tuning the x-ray photon's energy to match the value required to excite an inner-shell electron into a valence state of the atom of interest. While non-resonant scattering can provide insight beyond structural origin, e.g. magnetic or orbital [48, 49], the cross sections involved are small, so detailed refinements remain a technical challenge. This is where the REXS technique is important to solid state physics. We will later show how the scattering cross section is dramatically enhanced by tuning the incoming photon energies to the absorption transitions. Thus, this class of experiments combines the x-ray absorption (XAS) with diffraction, i.e. a Fourier transform of spatial modulations sensitive to electronic details. However, tuning to any edge may not be sufficient to enhance the cross section into a detectable range. Instead, judiciously chosen dipole-allowed transitions into final states near the Fermi level can result in a larger cross section, which directly ties into the electrons responsible for the macroscopic physics of the material. For  $3d$ -TMOs, the appropriate dipole-allowed transition is  $2p \rightarrow 3d$ , the  $L_{2,3}$ -edges, which falls within the energy range of  $200 - 2000eV$ , the so-called soft x-rays. Although this wavelength range ( $\sim 1nm$ ) drastically limits the accessible reciprocal space region, some ordered superstructures in TMOs reach the nm-scale, making RSXS the tool of choice to investigate the details of possible spin, orbital, and charge order. For a review on recent developments of the technique, see Ref.'s [50, 51].

Despite its great assets, the RSXS method has its challenges and disadvantages. The wavelength scale is rather large, limiting the momentum transfer. In addition, due to the large absorption coefficient of air at these energies, sample environments must be held in vacuum. Moreover, generating the x-rays is not as simple as in non-resonant diffraction. This is where the progression of synchrotron based sources provided useful.

## 3.2 X-ray sources: synchrotron radiation

REXS and particularly RSXS are techniques closely connected to the development of synchrotron radiation light sources. The synchrotron emerged as an accidental discovery in particle accelerator physics [52–54], but has since developed into sources for modern x-ray techniques. The last five decades have spawned 4 generations of synchrotron light sources, all of which rely on the notion of accelerating a charged electron into relativistic speeds within curved paths. In the first 3 generations, an accelerator drives electrons into closed orbits by applying magnetic fields. The 3<sup>rd</sup> generation is characterized by the inclusion of straight “insertion devices” within the ring<sup>1</sup>. A schematic of a typical 3rd-generation synchrotron layout is shown in Fig. 3.1, whose components will be explained in the following.

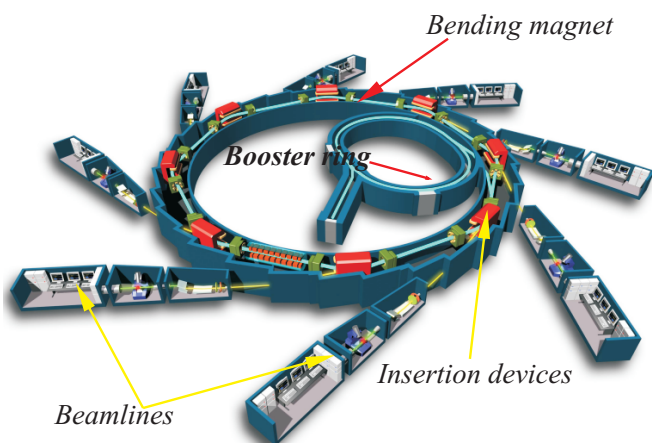


**Figure 3.1** A schematic of a synchrotron radiation source: electrons are injected through the booster ring, then accelerated along the bending magnets, and/or insertion devices. The radiation is collected for research at the beamline end-stations.

The electrons are first ramped into relativistic velocities in the booster ring. Then, the “storage rings” maintain the electrons in a high-energy orbit, replenishing their energy as they emit a special kind of light. This source kind is termed “bending magnet” radiation, and has several unique features like a high brilliance (a term defined to contain the degree of collimation, beam size, intensity, and spectral distribution), a broad and tunable emission energy range and a high degree of polarization of the light. These characteristics are a combined result of the relativistic movement of the electrons around a curved path and the relativistic Doppler effect. The conventional Doppler shift of an emitting electron has a spherical effect, where wavelength is increased when the moving object is going towards the viewer, and decreasing when moving away from it. The relativistic Doppler effect, on the

<sup>1</sup>The 4-th generation of these light sources are linear accelerators, or “free electron lasers”, which do not force the electrons in circular orbits but in linear paths.

other hand, and due to the Lorentz transformations, causes the radiation to be strongly blue-shifted and the direction of emittance is highly concentrated in the forward direction. The divergence of the beam under a relativistic Doppler blue-shift is roughly given by  $mc^2/E_e$ , where  $m$ ,  $E_e$ ,  $c$  are the mass and energy of the electron, and the speed of light in vacuum, respectively. A characteristic energy defined as  $\hbar\omega_c[keV] = 0.665E_e^2[GeV]B[Tesla]$  is given by the conditions of a bending magnet. For example, the BESSY synchrotron in Berlin, Germany operates at 1.7 GeV, optimized for the soft x-ray regimes. This quantity varies depending on the research focus of the synchrotron.

A large improvement in generating synchrotron light was achieved with the conception of insertion devices, which can offer more brilliance, sharp tunable energy spectra, partial temporal and spatial coherence, and full polarization control from the source. These are essentially arrays of alternating magnets which drive relativistic electrons into an oscillatory path. The two important parameters of an insertion device are the magnetic field  $B$  and the magnet period  $\lambda_u$ , as shown in Fig.3.2.

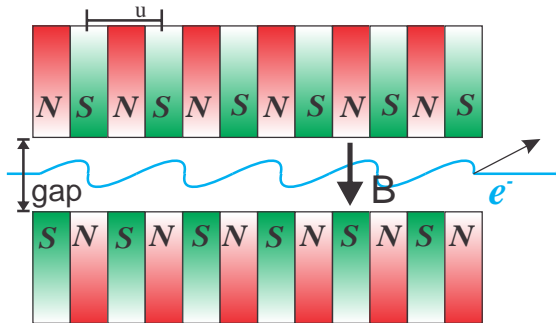


**Figure 3.2** The basic principle of an insertion device, where alternating magnetic dipoles accelerate the electrons in a oscillating path. These emit more intense radiation compared to the bending magnet. The oscillations occur outside the paper's plane.

A dimensionless parameter used to discern between insertion device types,  $K = \frac{eB\lambda_u}{2\pi\beta m_e c}$ , classifies the deflection path of the electron. There are two types of insertion devices: undulators ( $K \lesssim 1$ ) and wigglers ( $K \gg 1$ ). Wigglers operate with high magnetic fields with a large number  $N$  of period repetitions. They can be regarded as a superposition of bending magnet radiators, so the intensity becomes  $I \propto N$ . Undulators, on the other hand, produce a coherent superposition of the emitted light, so  $I \propto N^2$  but concentrated within a narrow energy range. The energy spectral range  $\Delta\omega/\omega$  of an undulator source can be several orders of magnitude reduced with respect to the bending magnet radiation, resulting in a much higher brilliance. Because of the sinusoidal nature of the electron's path, the energy an undulator produces from a single electron inherently comes in a discrete value, and its subsequent odd harmonics<sup>2</sup>. The expression for this energy is given by

$$E_n(eV) = n \frac{950E_e^2(GeV)}{\lambda_u(cm)(1 + K_{eff}^2/2 + \gamma^2\theta^2)}, \quad (3.1)$$

where  $\gamma$  is the relativistic factor of the electrons,  $K_{eff} = 0.934\lambda_u(cm)B(T)$ ,  $\theta$  is the polar angle from the undulator axis (Fig. 3.2), and  $n$  is the odd harmonic.

<sup>2</sup>However, the even harmonics do also exist in the off-axis radiation, that is, the radiation emitted at a small angle with respect to the tangential forward direction of the electron

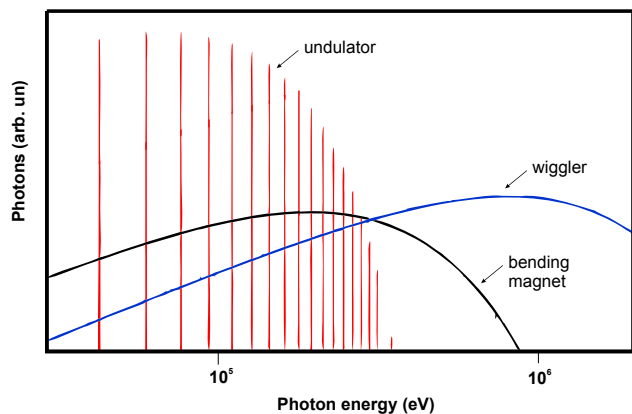


**Figure 3.3** A schematic of an undulator’s discrete spectrum compared to the continuous wiggler and bending magnet spectra. Image adapted from [55].

Undulators can change the gap between magnetic dipoles, modifying the magnetic field strength and thus  $K$ . This shifts the peaks in the energy spectra horizontally, optimizing the brightness for a certain energy range of interest. The resulting spectral brightness of an undulator compared to bending magnets and wigglers is shown in Fig.3.4. Furthermore, “helical undulators” allow to horizontally shift the magnetic dipoles inducing a spiral motion of the electron wave train. This can result in variable polarization of the emitted light, which can adopt linear (with any angle from vertical to horizontal) or elliptical (positive and negative) states.

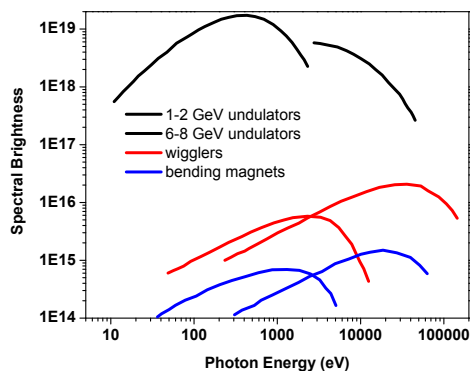


**Figure 3.4** A comparison between the spectral brightness of bending magnets, wigglers, and undulators.

### 3.3 Resonant scattering

The field of REXS emerged in the mid 1970’s, once the technical challenge of producing tunable, bright x-ray sources was overcome. It began with a discussion of so-called “anomalous scattering” [56], which was a term referring to finite intensities emerging around otherwise forbidden reflections when the photon energy neared an absorption edge. Subsequent seminal work on REXS included Hannon *et al.* [57], Carra and Thole [58], Hill and McMorrow [59], etc., which climaxed during the International Conference on Anomalous Scattering in Marlene, Germany, in 1992 [60]. During these stages, the importance of calculating resonant scattering factors was realized, so the theoretical framework to understand resonant XAS was developed alongside, which is summarized in papers like [61] and others. In this section, we will lay out the theoretical background of REXS, including a brief introduction to x-ray

physics, general remarks about the interaction of light and matter, the scattering factor, its connection to XAS, charge, magnetic and orbital scattering, and finalize with a description of realistic experimental aspects. This section was written collecting Refs. [50, 51, 57, 62–66] and others therein.

### 3.3.1 Basic principles of x-ray physics

The interaction of x-rays with solid state matter is a field with an enormous utility and widespread interest. While a thorough introduction can be found in [53], we begin our discussion with few words on absorption and diffraction. For non-resonant, elastic scattering from a single atom, the classical description serves a valid framework. The atom is modeled as an electron density of spherical symmetry  $\rho(\vec{r})$ . The unequal optical path lengths traveled by different wavefronts,  $\vec{q}_1 \cdot \vec{r}_1 \neq \vec{q}_2 \cdot \vec{r}_2$  (where the momentum transfer  $\vec{q} \equiv \vec{k} - \vec{k}'$ ), will result in a phase shift between waves, i.e. diffraction. The diffraction event will integrate over all waves scattered from each position  $\vec{r}_i$ :

$$f(\vec{q}) = \int r_0 \rho(\vec{r}) e^{i\vec{q} \cdot \vec{r}} d\vec{r}, \quad (3.2)$$

where we have introduced the atomic form factor  $f(\vec{q})$ . The full atomic form factor is, in general, energy dependent:

$$f^{full}(\vec{q}, \hbar\omega) = f(\vec{q}) + f'(\hbar\omega) + i f''(\hbar\omega), \quad (3.3)$$

where  $\hbar\omega$  is the photon energy.  $f'(\hbar\omega)$  accounts for ways that electrons with different binding energies respond to the incoming field, and the term  $i f''(\hbar\omega)$  arises from the binding energy which acts as a damping mechanism to the otherwise free electron density. The calculated values of the energy dependent terms for single atoms are tabulated [67]. These terms are relevant when doing REXS, where the quantum mechanical description is needed.

X-ray scattering in the solid state can benefit from the fact that the atoms are arranged in a periodic lattice. In doing so, each atom constitutes a scattering entity (as described above), but the contribution of each atom must be summed discretely, which yields the crystal structure factor  $F(\vec{q})$ , given by

$$F(\vec{q}) = \sum_{\vec{R}} f(\vec{q}) e^{i\vec{q} \cdot \vec{R}}; \vec{R} = n_1 \vec{a}_1 + n_2 \vec{a}_2 + n_3 \vec{a}_3 \quad (3.4)$$

where  $\vec{R}$  represents the position of an ion. The scattered intensity,  $|F|^2$ , takes on a large value when all the scattered waves scatter in phase. This condition is met if the scattering vector is such that  $\vec{q} \cdot \vec{R} = 2\pi m$ , where  $m$  is any integer, defining the **reciprocal lattice**, expressed as

$$\vec{a}_i^* = 2\pi \frac{\vec{a}_j \times \vec{a}_k}{\vec{a}_1 \cdot (\vec{a}_2 \times \vec{a}_3)} = 2\pi \frac{\vec{a}_j \times \vec{a}_k}{V}, \quad (3.5)$$

where the  $i, j, k$ -indices follow cyclic notation,  $V$  is the volume of the unit cell (from the scalar triple product). These reciprocal lattice vectors, defined as  $\vec{G} = h\vec{a}_1^* + k\vec{a}_2^* + l\vec{a}_3^*$ , where  $h, k, l$  are integers, also have a periodicity and thus a fundamental ‘unit cell’, known as the Brillouin zone. Therefore, Fourier-transforming the reciprocal lattice, measurable through

diffraction, will yield the real space lattice. In more complex systems with multiple ions in the real space unit cell, the structure factor becomes

$$F(\vec{q}, E) = \sum_{\vec{r}_j} f^{full}(\vec{q}, E) e^{i\vec{q}\cdot\vec{r}_j} \sum_{\vec{R}_n} e^{i\vec{q}\cdot\vec{R}_n}, \quad (3.6)$$

where  $J$  is the number of distinct atoms in the unit cell and  $N$  is all the unit cells in the crystal. In an ideally perfect scenario,  $N$  growing to infinity will render  $F(\vec{q})$  a Dirac delta function. In general, the maxima repeat every time  $\vec{q} = \vec{G}$ , although different crystal systems may render combinations of  $h, k, l$ -values which suppress the term  $e^{i\vec{q}\cdot\vec{R}_n}$ . These “selection rules” are very useful in non-resonant x-ray scattering, i.e. serve to identify the crystal symmetry. However, Templeton and Templeton [56] as well as Finkelstein *et al.* [68] first observed forbidden reflections appearing close to resonance. This spawned the notion that anisotropic crystals can distort the electronic wave function, and the form factor takes on a highly non-trivial matrix form when approaching the resonant condition. In general, the form of  $f^{full}(\vec{q}, \hbar\omega)$  in Eq. 3.3 describes the essence of REXS. In the following sections, specific aspects of this form factor will be derived.

Finally, ordering phenomena in crystals can change the lattice periodicity and be detected by diffraction. A crystal with a real space lattice defined in Eq. 3.6 will yield diffraction peaks when  $\vec{q} = \vec{Q}$ , i.e. integer values of  $h, k, l$  governed by their selection rules. In general, however, an ordered state of any kind (charge, spin, orbital) might change the symmetry of the crystal, and thus call for a new lattice definition. For example, take a simple 1-dimensional system of non-magnetic ions, whose period is defined as  $a$ , so  $Q = 2\pi/a$ . If the system were to take on AFM order, this will yield a new unit cell double in size to the original, setting  $a' = 2a$  and  $Q' = \pi/a$ . In this case, the Brillouin zone defined before will reduce into half. This is shown in Fig. 3.5, which can easily be extended to 3-dimensions. However, instead of redefining the set of reciprocal lattice vectors  $\vec{Q}'$ , non-integer  $(h, k, l)$ -values are commonly used within the preceding reciprocal lattice definition  $\vec{Q}$ . For general ordered state, where different periodicities can be induced in all three crystallographic directions, the labeling  $(\frac{h}{n_1}, \frac{k}{n_2}, \frac{l}{n_3})$  takes a frequent use, where the integers  $n_i$  refer to the manifold multiplication of the unit cell along the axis  $i$ . However, some ordered states can create charge and/or spin textures which are not commensurate with the crystal lattice. For such a case, not even a new definition of integer  $(h, k, l)$ -values would yield a simple description of the system. Therefore, the use of  $(\frac{h}{n_1}, \frac{k}{n_2}, \frac{l}{n_3})$ , with non-integer  $n_i$ , is required. These kinds of order are known as *incommensurate*, and we will see a manifestation of it in Chapter 5.

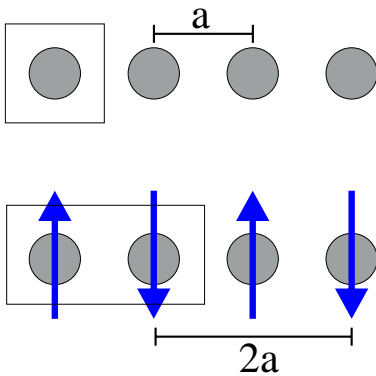


**Figure 3.5** When a chain of ions with lattice spacing  $a$  (upper panel) enters a AFM phase, the unit cell (area enclosed by a square) doubles (lower panel), which results in reciprocal space folded into half.

### 3.3.2 The interaction of light with matter

In general, light and matter interaction serve a very important tool in condensed matter research. A medium exposed to an external electromagnetic wave will drive the system out of equilibrium through the duration of the interaction. Some properties of the system will couple to the external field and thus be altered in a specific way. For the case of low excitation fields, the change that the external field exerts on the system is proportional to that field, and this proportionality constant is known as the linear response function. Examples in other fields of such a function are specific heat, magnetic susceptibility, compressibility, etc. This section will describe the process of x-ray absorption and elastic scattering within the framework of linear response theory. In other words, a system's reaction to an x-ray perturbation can be used to extract information about it. This will lead to an expression which corresponds to  $f^{full}(\vec{q}, E)$  in Eq. 3.3.

Consider an oscillating electron perturbed by a time-dependent external field. The Hamiltonian for such a scenario looks like  $H = H_0 + H_{ext}$ , where  $H_0$  is the unperturbed, equilibrium state, and  $H_{ext}$  is the perturbation field, in this case the electromagnetic wave  $\equiv \vec{E}_{in}$ . For small perturbations  $H_{ext}$ , as is the case in most particle scattering experiments, the polarization vector of the electron responds linearly to the field:

$$\vec{P} = \chi \vec{E}_{in}(t), \quad (3.7)$$

where  $\chi$  is defined as the electric susceptibility of the electron, a quantity describing how easily the system can be polarized. For an electromagnetic wavefield,  $\vec{E}_{in}(t) = \hat{\epsilon} E_0 e^{-i(\omega t - \vec{k} \cdot \vec{r})}$ , where  $\hat{\epsilon}$  is a unit vector along the polarization of the wave which is complex (circular light),  $E_0$  is the amplitude of the field, and  $\omega$  its frequency. The velocity and acceleration of the electron are:

$$\vec{j} \equiv \frac{\partial \vec{P}}{\partial t} = -i\omega \chi \vec{E}_{in}(t) \quad (3.8)$$

and

$$\vec{a} \equiv \frac{\partial \vec{j}}{\partial t} = \omega^2 \chi \vec{E}_{in}(t) \quad (3.9)$$

where the latter quantity implies a radiated field, i.e.  $\vec{a} \propto \vec{E}_{out}$ . The absorption process can be viewed as the damping of the oscillatory motion of the electron as it dissipates energy from  $\vec{E}_{in}(t)$ . This is equal to the power it absorbs, which is given by the time-averaged work done by the oscillator:

$$W = \frac{1}{T} \int_0^T \vec{F} \cdot \vec{j} dt = \langle \vec{E}_{in} \cdot \vec{j} \rangle = \frac{1}{2} \text{Re}[\vec{E}_{in}^* \cdot (-i\omega \chi) \vec{E}_{in}], \quad (3.10)$$

where the later step involves simple complex number algebra. Introducing the conductivity  $\sigma(\hbar\omega) = \omega \chi$ , we obtain a simple expression for the absorption process:

$$I_{XAS}(\hbar\omega) = \frac{1}{2} \text{Im}[\hat{\epsilon}^* \cdot \sigma(\hbar\omega) \cdot \hat{\epsilon}]. \quad (3.11)$$

We note at this point, that  $\sigma$  is not necessarily a scalar quantity, so generally it is referred to as the *conductivity tensor*. It has a real and imaginary part, which arise from the solution to the differential equation of a damped oscillator. Thus, it follows that these two components

of  $\sigma$  are Kramers-Kronig related<sup>3</sup>. Therefore, this quantity can be connected to the term  $f^{full}(\vec{q}, E)$  in Eq. 3.3, as follows

$$\sigma(\hbar\omega) \propto f'(\hbar\omega) + if''(\hbar\omega), \quad (3.12)$$

which directly links the conventional notion that  $f''(\hbar\omega)$  is related to the XAS process.

Detecting a scattering process, moreover, is a quantification of the radiated field of the accelerated electron. It is the squared norm of the radiated field divided by the squared norm of the incoming field. Using the definitions above, this comes down to

$$I_{REXS}(\hbar\omega) = \frac{|\vec{E}_{out}|^2}{|\vec{E}_{in}|^2} \propto |\hat{\epsilon}_{out}^* \cdot \sigma \cdot \hat{\epsilon}_{in}|^2. \quad (3.13)$$

Equations 3.12 and 3.13 reveal that the conductivity tensor  $\sigma$  holds the pertinent information about the system, showing the connection between absorption and scattering of x-rays in analogy to the optical description.

### 3.3.3 XAS cross section

The development of the XAS cross section begins with quantum mechanical, first-order perturbation theory. In this case, the system is described by a time-dependent Hamiltonian  $H = H_0 + H_{ext}$ . The term  $H_0$  refers to the unperturbed system, in this case the ion or cluster to consider, with eigenstates  $H_0|\varphi_0\rangle = E_n|\varphi_0\rangle$ , and  $H_{ext}$  arises from the potential field of the light,  $\vec{A}(\vec{r}, t)$ , and the canonical transformation of the momentum. The time-dependent part of the Hamiltonian is  $H_{ext}$ . For a light-matter interaction, the full Hamiltonian contains the terms [20]:

$$\begin{aligned} H_1 &= \frac{e^2}{2m} \vec{A}^2 \\ H_2 &= -\frac{e}{mc} \vec{p} \vec{A} \\ H_3 &= -\frac{e\hbar}{mc} \vec{s} (\nabla \times \vec{A}) \\ H_4 &= -\frac{e\hbar}{2m^2c^3} \vec{s} \left( \frac{\partial \vec{A}}{\partial t} \times \frac{e}{c} \vec{A} \right). \end{aligned} \quad (3.14)$$

The term  $H_1$  is responsible for so-called Thomson scattering, involves the field potential interacting with itself so it is left out of the REXS process. The term  $H_4$ , on the other hand, is quadratic in  $\vec{A}$  and describes the non-resonant magnetic scattering process, which we will not discuss in this section. The terms  $H_2$  and  $H_3$  describe the resonant process, and thus their inspection is needed. The term  $H_3$  is related to the spin, but the higher order terms of the Taylor expansion of the exponential (see below) can be regrouped with high-order multipole terms of  $H_2$  and will thus not be considered further. We will see, moreover, how the magnetic terms can later be incorporated into  $\sigma$ . It is therefore from the term  $H_{ext} = H_2$  that we will derive the connection between  $\sigma$  and the transition rate matrix. Also known as Fermi's Golden Rule, this matrix is an important quantity in experimental spectroscopy.

<sup>3</sup>The connection between a damped oscillator and the Kramers-Kronig relations is given in Appendix A.

We begin by expressing the momentum operator  $\vec{p} = im[H, \vec{r}]$ , which can be derived from the canonical commutation relations. Thus,  $H_{ext}$  can be expressed as

$$H_{ext} = \frac{ie}{m^2}[H, \vec{r}] \cdot \vec{A}. \quad (3.15)$$

The photon field potential  $\vec{A}$  has the form of a traveling wave, i.e.

$$\vec{A} = A_0 \hat{e} e^{-i(\omega t + \vec{k} \cdot \vec{r})} + A_0 \hat{e}^* e^{i(\omega t + \vec{k} \cdot \vec{r})} = 2A_0 \hat{e} \cos(\omega t + \vec{k} \cdot \vec{r}). \quad (3.16)$$

Using the gauge transformations  $\vec{E} = -\frac{\partial \vec{A}}{\partial t}$ , the last term can be expressed in terms of the electric field as  $\vec{E} = 2i\omega A_0 \hat{e} \sin(\omega t + \vec{k} \cdot \vec{r})$ . So  $H_{ext}$  becomes

$$H_{ext} = \frac{eE_0}{2m^2\omega}[H, \vec{r}] \cdot \hat{e} e^{i\vec{k} \cdot \vec{r}}, \quad (3.17)$$

where  $E_0 = 2i\omega A_0$ .

Fermi's Golden Rule, on the other hand, is a way to calculate the rate of transition into a certain state, given a perturbation acting on the system. In other words,

$$I_{XAS} = \sum_f |\langle f | H_{ext} | i \rangle|^2 (\delta(\omega + E_i - E_f) + \delta(\omega - E_i + E_f)), \quad (3.18)$$

where the initial and final states of the transition are labeled  $i$  and  $f$ , and the delta functions appear to enforce energy conservation.<sup>4</sup> Having a useful expression for  $H_{ext}$ , we turn to calculate the matrix element:

$$\begin{aligned} \langle f | H_{ext} | i \rangle &= \langle f | \frac{e}{2m^2\omega} [H, \vec{r}] \cdot \hat{e} e^{i\vec{k} \cdot \vec{r}} | i \rangle \\ &= \frac{eE_0}{2m^2\omega} (E_f - E_i) \langle f | \vec{r} \cdot \hat{e} e^{i\vec{k} \cdot \vec{r}} | i \rangle. \end{aligned} \quad (3.19)$$

When the photon's energy matches the transition,  $\omega \propto E_f - E_i$  we obtain an expression for  $I_{XAS}$ :

$$I_{XAS} = \frac{eE_0^2}{2m^2} \sum_f |\langle f | \vec{r} \cdot \hat{e} e^{i\vec{k} \cdot \vec{r}} | i \rangle|^2 (\delta(\omega + E_i - E_f) + \delta(\omega - E_i + E_f)). \quad (3.20)$$

In real physical experiments, Dirac functions are replaced by Lorentzian functions, which can be done mathematically through the transformation

$$\delta(x) = -Im\left(\lim_{\Gamma \rightarrow 0} \frac{1}{\pi(x + i\Gamma/2)}\right), \quad (3.21)$$

where  $\Gamma$  is the width. Developing an expression for  $I_{XAS}$ :

$$I_{XAS} = \frac{eE_0^2}{2m^2} \sum_f |\langle f | \vec{r} \cdot \hat{e} e^{i\vec{k} \cdot \vec{r}} | i \rangle|^2 (\delta(\omega + E_i - E_f)) \quad (3.22)$$

---

<sup>4</sup>More details on the derivation of Fermi's Golden Rule can be found in Appendix C.

$$\begin{aligned}
&= -\frac{eE_0^2}{2m^2} Im \sum_f \left( \lim_{\Gamma \rightarrow 0} |\langle f | \vec{r} \cdot \hat{\epsilon} e^{i\vec{k} \cdot \vec{r}} | i \rangle|^2 \frac{1}{\pi(\omega + E_i - E_f + i\Gamma/2)} + \frac{1}{\pi(\omega - E_i + E_f + i\Gamma/2)} \right) \\
&= -\frac{eE_0^2}{2m^2} Im \sum_f \lim_{\Gamma \rightarrow 0} \langle i | (\vec{r} \cdot \hat{\epsilon} e^{i\vec{k} \cdot \vec{r}})^\dagger | f \rangle \left( \frac{1}{\pi(\omega + E_i - E_f + i\Gamma/2)} \right. \\
&\quad \left. + \frac{1}{\pi(\omega - E_i + E_f + i\Gamma/2)} \right) \langle f | (\vec{r} \cdot \hat{\epsilon} e^{i\vec{k} \cdot \vec{r}}) | i \rangle \\
&= -\frac{eE_0^2}{2m^2} Im \lim_{\Gamma \rightarrow 0} \langle i | (\vec{r} \cdot \hat{\epsilon} e^{i\vec{k} \cdot \vec{r}})^\dagger \left( \frac{1}{\pi(\omega + E_i - H + i\Gamma/2)} \right. \\
&\quad \left. + \frac{1}{\pi(\omega - E_i + H + i\Gamma/2)} \right) (\vec{r} \cdot \hat{\epsilon} e^{i\vec{k} \cdot \vec{r}}) | i \rangle.
\end{aligned} \tag{3.23}$$

Using the Taylor expansion of the exponential, the first approximation simplifies  $H_{ext} \rightarrow \hat{\epsilon} \cdot \vec{r}$ , yielding the dipole approximation (E1) which is useful to model most scattering processes. Mentioned for completeness, the linear term of the expansion is the so-called quadrupole term (E2), with an interaction Hamiltonian that looks like  $\hat{\epsilon} \cdot \vec{k} \vec{r} \cdot \vec{r}$ .

Finally, comparing Eqs. 3.11 and 3.23, a useful expression for  $\sigma$  can be written as

$$\sigma = \frac{e}{2\pi m^2} \langle i | \vec{r} \left( \frac{1}{\omega + E_i - H + i\Gamma/2} + \frac{1}{\omega - E_i + H + i\Gamma/2} \right) \vec{r} | i \rangle. \tag{3.24}$$

The process can be described as follows: the Hamiltonian  $H$  acts twice on the system, driving the system into an intermediate state, also known as the core-hole state, and returning it to its initial state. Thus, knowing the eigenvalues of the Hamiltonian  $H$  in the core-hole state will suffice to calculate the conductivity tensor  $\sigma$ , and all the cross sections needed for scattering experiments. The resonant enhancement to the scattered intensity is evident from the divergence of the denominators with photon energies tuned to the right transitions. In practice, for 3d TMOs,  $L_{2,3}$ -edge enhancements can reach up to several orders of magnitude.

Finally, we turn to derive rules for the transition to take place with non-zero probability. For this purpose, we make use of the spherical harmonic expression of the wave functions and the photon field. Consider the case of linear polarization along  $\vec{z}$ , the dipole term can be expressed as  $r \cos(\theta) \propto r Y_0^1(\theta, \phi)$ . The case for circular polarization is  $\propto r Y_{\pm 1}^1(\theta, \phi)$ , indicating that the angular part of the integral  $\langle l'm' | Y_m^1(\theta, \phi) | lm \rangle$  will yield selection rules for the transition process. For linear polarized light, the rules are  $\Delta l = \pm 1$  and  $\Delta m = 0, \pm 1$ .

The studies presented in this thesis involve  $L_{2,3}$ -edges of 3d TMOs. In this case, the transition corresponds to  $2p \rightarrow 3d$ . Since the electronic states of interest, close to the Fermi level, are around the 3d-level, this transition is the key one to investigate these systems. Furthermore, spin-orbit coupling splits the 2p core-hole state into two:  $2p_{3/2}$  and  $2p_{1/2}$ . These states are separated by  $\sim 10$  eV for these systems. This yields two available transitions, which are usually called  $L_3$  ( $2p_{3/2} \rightarrow 3d$ ) and  $L_2$  ( $2p_{1/2} \rightarrow 3d$ ). The final state 3d, moreover, also has several features which can be probed using x-rays. The real-space orbitals that were outlined in Chapter 2,  $t_{2g}$  and  $e_g$ , and their occupation number are useful quantities that we will discuss later. A schematic of a transition of electrons into the 3d shell is shown in Fig. 3.6, which illustrates a process that represents the fundamental backbone of resonant x-ray physics in TMOs.

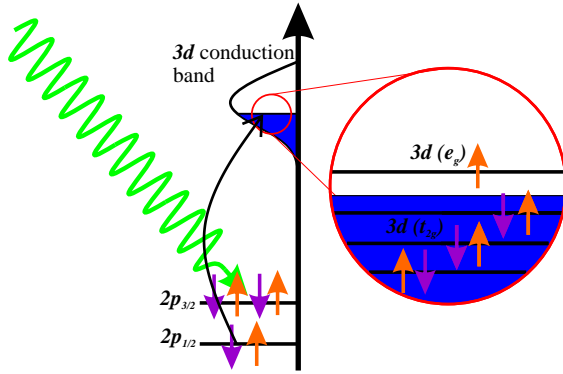


**Figure 3.6** A schematic of a photon inducing a  $2p \rightarrow 3d$  transition. This example portrays a  $3d^7$  system with crystal field separating the  $t_{2g}$  and  $e_g$  into a low spin state.

### A two level system

We proceed to calculate the conductivity tensor  $\sigma$  for the simple case of a system with two levels, which also serves a realistic approach because REXS experiments are taken in the vicinity of one absorption edge, i.e. one transition element. We take a transition  $|s\rangle \rightarrow |p\rangle$ , and we define the difference in energy between the two states as  $\omega_0$ . In that case, we can evaluate the expression 3.24, and obtain

$$\sigma = \frac{e}{2\pi m^2} \left( \frac{1}{\omega + \omega_0 + i\Gamma/2} + \frac{1}{\omega - \omega_0 + i\Gamma/2} \right). \quad (3.25)$$

Fig. 3.7 shows the resulting projections of  $\sigma$  on the imaginary and real axes, taking the values of  $\omega_0$  and  $\Gamma$  listed in the caption, which resemble the Kramers-Kronig related response of the damped oscillator.

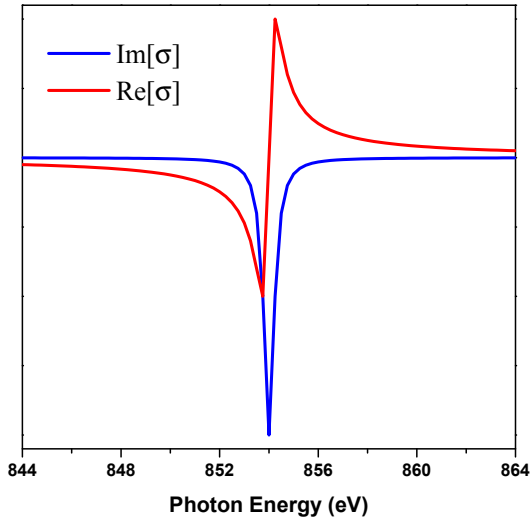


**Figure 3.7** A plot of the real and imaginary part of  $\sigma$ , taking  $\omega_0 = 854 \text{ eV}$ , and the broadening  $\Gamma = 0.5 \text{ eV}$ .

Furthermore, the tensor character of  $\sigma$  can generally be expressed in matrix form as follows:

$$\sigma(\omega) = \begin{pmatrix} \sigma_{xx} & \sigma_{xy} & \sigma_{xz} \\ \sigma_{yx} & \sigma_{yy} & \sigma_{yz} \\ \sigma_{zx} & \sigma_{zy} & \sigma_{zz} \end{pmatrix}. \quad (3.26)$$

In this general case, the symmetry of the final state will be represented in the (in)equivalency of the terms  $\sigma_{ij}$ . For example, a final state with  $|p\rangle$ -character will yield a matrix of the form

$$\sigma_{s \rightarrow p}(\omega) = \begin{pmatrix} \sigma_{s \rightarrow p_x} & \sigma_{s \rightarrow p_{xy}} & \sigma_{s \rightarrow p_{xz}} \\ \sigma_{s \rightarrow p_{yx}} & \sigma_{s \rightarrow p_y} & \sigma_{s \rightarrow p_{yz}} \\ \sigma_{s \rightarrow p_{zx}} & \sigma_{s \rightarrow p_{zy}} & \sigma_{s \rightarrow p_z} \end{pmatrix}.$$

where off-diagonal elements will be projections of the  $|p_{x,y,z}\rangle$  states off the cartesian axes. Consider, a  $|p\rangle$ -state in cubic symmetry, where  $|p_x\rangle \equiv |p_y\rangle \equiv |p_z\rangle$ , then the terms  $\sigma_{ii}$  are all equal, and the off-diagonal  $\sigma_{ij} = 0$ . For the case of tetragonal symmetry, which is one commonly considered in TMO heterostructures, epitaxial strain usually distorts the lattice in-plane. This might introduce an energy separation between otherwise degenerate orbitals (like  $p$  or  $d$ ), and so the conductivity tensor becomes,

$$\sigma^{tetragonal}(\omega) = \begin{pmatrix} \sigma_{xx} & 0 & 0 \\ 0 & \sigma_{xx} & 0 \\ 0 & 0 & \sigma_{zz} \end{pmatrix}.$$

Recalling Eq. 3.11, taking the coordinates of the light polarization in the linear, cartesian basis, a conductivity tensor of this form will yield inequivalent spectra when the polarization of the incoming light is in- or out-of-plane. This phenomenon, called natural linear dichroism (LDIC), can be very useful to determine the occupation of non-degenerate  $e_g$  orbitals, as can be visualized in Fig. 3.8. In that case, depicting a typical measurement geometry available in heterostructures grown on a tetragonal substrate, the light with polarization in-plane ( $\hat{\epsilon}_{ab}$ ) will couple with the terms  $\sigma_{xx}$ . Similarly, the light with perpendicular linear polarization will have a component on the  $c$  axis, so  $\hat{\epsilon}_c$  can couple into the states  $\sigma_{zz}$ . In  $3d$  systems like the ones investigated in this thesis, the character of  $\sigma_{xx}$  and  $\sigma_{zz}$  can be directly related to the occupation of the  $e_g$  orbitals. A prime example of an application of such linear dichroism in TMO heterostructures can be found in Refs. [42, 69–71]. Later, we will see how this plays a role in the magnetic properties of RNO heterostructures. We note that other crystal symmetries result in different relations between  $\sigma_{ij}$ , with the triclinic system with lowest symmetry rendering 6 unequal matrix elements (3 different diagonal elements, and 3 more obeying the condition  $\sigma_{ij} = \sigma_{ji}$ ).

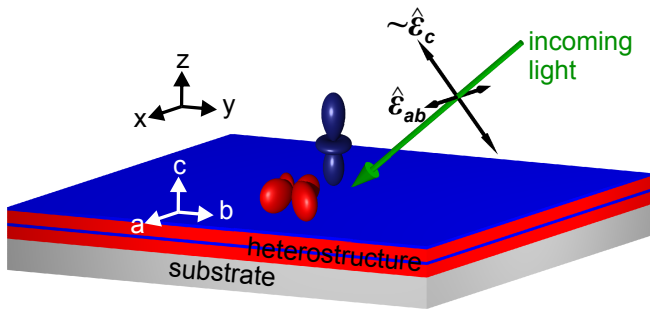


**Figure 3.8** A schematic of a LD experiment of a heretostructure grown on a substrate. The polarization vectors are either in-plane ( $\hat{\epsilon}_{ab}$ ) or have a component out-of-plane ( $\hat{\epsilon}_c$ ). The former couples into states with  $x^2 - y^2$  symmetry (red orbitals), and the latter to  $3z^2 - r^2$  states (purple orbitals). Thus, this measurement can probe the unbalance of occupation of such states.

In summary, we derived and discussed the importance of the scattering tensor  $\sigma$ , which contains the information about the system under investigation. It holds the key for the interpretation of XAS, especially when considering symmetries which can manifest in dichroism

effects. Because of the relation between  $\sigma$  and the scattered signal given by Eq. 3.13, these symmetry details will reappear, and sometimes more effectively, in the scattered signal. Eq. 3.26 shows the general form of the conductivity tensor.

Finally, to lead in to the following section, we briefly discuss the basic form of a magnetic conductivity tensor. Consider a cubic system with a net magnetization along the  $\hat{z}$ -direction. Classically, the magnetic field will create a Lorentz force which creates a Hall current in the  $xy$ -plane, modifying the electric permittivity into  $\vec{D} = \hat{\epsilon}\vec{E} = \epsilon'\vec{E} + \imath\vec{g} \times \vec{E}$ , where  $\vec{g}$  is the gyromagnetic ratio. This results in the well-known off-diagonal, imaginary terms in  $\sigma$ , which lead to the magneto optical phenomena like the Kerr and Faraday effect. Quantum mechanically, spin-orbit coupling and time-reversal symmetry breaking causes the tensor to take on imaginary off-diagonal elements. The cubic system described above results in a tensor like

$$\sigma_z^{magnetic}(\omega) = \begin{pmatrix} \sigma_{xx} & \imath\sigma_{xy} & 0 \\ -\imath\sigma_{xy} & \sigma_{xx} & 0 \\ 0 & 0 & \sigma_{zz} \end{pmatrix}.$$

### 3.3.4 Magnetic scattering: symmetry considerations

We now turn to discuss in more detail the different forms that  $\sigma$  can take in the presence of a magnetic moment, and the implications it has in the scattered signal. This will provide the tools needed for magnetic structure determination using RSXS. The majority of this section's scope was obtained from Refs. [57, 59, 64] and others therein.

We begin by considering the general form of the scattering tensor in for any crystal symmetry to consider:

$$F(\omega) = \begin{pmatrix} F_{xx}(\omega) & F_{xy}(\omega) & F_{xz}(\omega) \\ F_{yx}(\omega) & F_{yy}(\omega) & F_{yz}(\omega) \\ F_{zx}(\omega) & F_{zy}(\omega) & F_{zz}(\omega) \end{pmatrix},$$

where we make use of Cartesian coordinates highlighting that even in the presence of a randomly oriented magnetic moment, the strong energy dependence of  $F(\omega)$  can be projected to the principal axes which are in turn aligned with the crystal axes. Note that taking high crystal symmetries and its set of symmetry operations  $\Gamma$  without a moment will simplify the form of  $F(\omega)$ . Furthermore, consider now the presence of a magnetic moment along a random orientation. It is easy to visualize that any operation  $\Gamma$  will break the symmetry by inevitably rotating the moment, leaving only the identity operation as valid. Thus, a new symmetry operation  $\Gamma'$  will require first a rotation of the whole system,  $\Gamma$ , and then a rotation of the magnetic moment back. That is, we will treat the moment and the system it lies in separately, defining  $F(\omega) \equiv F_1(\omega, \hat{\epsilon})F_2(\vec{M})$ , where one part depends only on the energy and polarization of the light and the other term holds the magnetic moment's identity. This can be achieved by expanding the terms of  $F(\omega)$  in spherical harmonics on the unit sphere, that is

$$F(\theta, \phi, \omega) = \sum_{k=0}^{\infty} \sum_{m=-k}^k \begin{pmatrix} F_{xx}^{km}(\omega) & F_{xy}^{km}(\omega) & F_{xz}^{km}(\omega) \\ F_{yx}^{km}(\omega) & F_{yy}^{km}(\omega) & F_{yz}^{km}(\omega) \\ F_{zx}^{km}(\omega) & F_{zy}^{km}(\omega) & F_{zz}^{km}(\omega) \end{pmatrix} Y_{km}(\theta, \phi), \quad (3.27)$$

where  $\theta, \phi$  define the moment's direction in spherical coordinates from

$$\vec{M} = \begin{pmatrix} m_x \\ m_y \\ m_z \end{pmatrix} = \begin{pmatrix} |\vec{M}| \cos(\phi) \sin(\theta) \\ |\vec{M}| \sin(\phi) \sin(\theta) \\ |\vec{M}| \cos(\theta) \end{pmatrix},$$

and  $Y_{km}$  are the spherical harmonics. The  $F_{ij}(\omega)$ 's are the components of the scattering tensor on the basis of linear polarized light projected on the crystal system, that is  $\hat{\epsilon} \equiv (\epsilon_x, \epsilon_y, \epsilon_z)$ . Now, to calculate the set of allowed coefficients of the expansion, the same set of symmetry operations considerations will be taken, that is  $\Gamma'F = F$ . In other words,  $F(\omega)$  must fulfill the symmetry of the system. The simplest operation to consider is a 4-fold rotation along the  $z$ -axis ( $C_4(z)$ ), which implies rotating the system and the magnetic moment by  $-\pi/2$ , and then rotating  $F(\omega)$  back:

$$\begin{pmatrix} 0 & 1 & 0 \\ -1 & 0 & 0 \\ 0 & 0 & 1 \end{pmatrix} \cdot \sum_{k=0}^{\infty} \sum_{m=-k}^k \begin{pmatrix} F_{xx}^{km} & F_{xy}^{km} & F_{xz}^{km} \\ F_{yx}^{km} & F_{yy}^{km} & F_{yz}^{km} \\ F_{zx}^{km} & F_{zy}^{km} & F_{zz}^{km} \end{pmatrix} Y_{km}(\theta, \phi) \cdot \begin{pmatrix} 0 & -1 & 0 \\ 1 & 0 & 0 \\ 0 & 0 & 1 \end{pmatrix} = \\ \sum_{k=0}^{\infty} \sum_{m=-k}^k \begin{pmatrix} F_{yy}^{km} & -F_{yx}^{km} & F_{yz}^{km} \\ -F_{xy}^{km} & F_{xx}^{km} & -F_{xz}^{km} \\ F_{zy}^{km} & -F_{zx}^{km} & F_{zz}^{km} \end{pmatrix} Y_{km}(\theta, \phi - \pi/2)$$

which gives a set of rules to evaluate the coefficients  $F_{ij}$ .

The first, simplest, and perhaps most useful system to consider is the case of spherical symmetry. In this case, the  $\phi$ -dependent part of the function can be integrated out, and the properties of the remaining Legendre polynomials ( $\int P_m(\cos \theta) d \cos \theta = 0$  unless  $m = 0$ ) reduce the summation over  $m$  to one term. In addition, following the triangular truncation procedure, the summation on  $k$  is only taken for  $k \in \{0, 1, 2\}$ . So we can easily see the rules the coefficients must follow:

$$\begin{aligned} \sum_{k=0}^2 F_{yx}^{k0} Y_{k0}(\theta, \phi) &= - \sum_{k=0}^2 F_{xy}^{k0} Y_{k0}(\theta, \phi - \pi/2), \\ \sum_{k=0}^2 F_{zz}^{k0} Y_{k0}(\theta, \phi) &= \sum_{k=0}^2 F_{zz}^{k0} Y_{k0}(\theta, \phi - \pi/2), \\ \sum_{k=0}^2 F_{xx}^{k0} Y_{k0}(\theta, \phi) &= \sum_{k=0}^2 F_{yy}^{k0} Y_{k0}(\theta, \phi - \pi/2), \end{aligned}$$

and all other coefficients are 0. After some algebra, we arrive at the expression for a magnetic moment along the  $\vec{z}$ -direction, i.e. setting  $\theta = \pi/2$ :

$$F_{\vec{z}}^{mag} = \begin{pmatrix} F^{(0)} - \frac{1}{3}F^{(2)} & -F^{(1)} & 0 \\ F^{(1)} & F^{(0)} - \frac{1}{3}F^{(2)} & 0 \\ 0 & 0 & F^{(0)} + \frac{2}{3}F^{(2)} \end{pmatrix}. \quad (3.28)$$

More realistic scenarios, however, will not have the magnetic moment along such a high symmetry direction. Indeed determining the direction of the moment is a problem that

REXS is viable to address. For that reason, we turn to develop an expression for  $F^{mag}$  with a random orientation. This is done simply by taking the tensor  $F_z^{mag}$  and rotating it to a random direction:  $F^{mag} = RF_z^{mag}R^T$ , where the rotation matrix defining the spherical angles  $(\phi, \theta)$  is given by

$$R = \begin{pmatrix} \cos(\phi) & -\sin(\phi) & 0 \\ \sin(\phi) & \cos(\phi) & 0 \\ 0 & 0 & 1 \end{pmatrix} \cdot \begin{pmatrix} \cos(\theta) & 0 & \sin(\theta) \\ 0 & 1 & 0 \\ -\sin(\theta) & 0 & \cos(\theta) \end{pmatrix}.$$

This yields the general form of  $F^{mag}$  in spherical symmetry:

$$F^{mag} = \begin{pmatrix} F^{(0)} + (x^2 - \frac{1}{3})F^{(2)} & -zF^{(1)} + xyF^{(2)} & yF^{(1)} + xzF^{(2)} \\ zF^{(1)} + xyF^{(2)} & F^{(0)} + (y^2 - \frac{1}{3})F^{(2)} & -xF^{(1)} + yzF^{(2)} \\ -yF^{(1)} + xzF^{(2)} & xF^{(1)} + yzF^{(2)} & F^{(0)} + (z^2 - \frac{1}{3})F^{(2)} \end{pmatrix}. \quad (3.29)$$

In magnetic diffraction experiments, the quantity  $I_{REXS}$  of Eq. 3.13 must contain the phase shift of the diffracted wave. In other words

$$I_{mag} = \left| \sum_i e^{i(\vec{k}_{in} - \vec{k}_{out}) \cdot \vec{r}_i} \hat{\epsilon}_{out}^* \cdot F_i^{mag} \cdot \hat{\epsilon}_{in} \right|^2, \quad (3.30)$$

where  $\hat{\epsilon}_{in,out}$  represent the polarization vectors of in- and out-coming light, and likewise  $\vec{k}_{in,out}$  represent the wave vectors of both light states, which are set by the requirement of fulfilling the Bragg condition.  $\vec{r}_i, F_i^{mag}$  represent the position and scattering tensor of the  $i$ -ion, and the summation runs over the sample size, but the phase information is entirely encoded by running the summation over the magnetic unit cell. In a practical experiment, the polarization vectors can be tuned using the parameters of the undulator (Section 3.2) between circular left and right, and linear vertical and horizontal. The latter two define the most useful set of coordinates as follows. Let  $\boldsymbol{\pi}$  be the linear polarization state parallel to the scattering plane, and  $\boldsymbol{\sigma}$  the one perpendicular, as in Fig. 3.9<sup>5</sup>.

We express now the light wave propagation vectors  $\vec{k}_{in,out}$  in the cartesian coordinate system we have defined. Let  $\hat{q} \equiv \{q_x, q_y, q_z\}/|\vec{q}|$ , and  $\hat{q}_\perp$  any vector perpendicular to it, which will be needed to define the scattering plane in these coordinates. Now, let  $\psi$  be the angle between  $\hat{q}_\perp$  and the scattering plane. The angle between  $\vec{k}_{in}$  and  $\hat{q}$ , related to the Bragg angle, we call  $\theta$ . So now we can define all the needed vectors in the crystal coordinates, as follows:

$$\begin{aligned} \vec{k}_{in} &\parallel \sin(\theta)[\cos(\psi)\hat{q}_\perp + \sin(\psi)(\hat{q}_\perp \times \hat{q})] + \cos(\theta)\hat{q}, \\ \vec{k}_{out} &\parallel \sin(\theta)[\cos(\psi)\hat{q}_\perp + \sin(\psi)(\hat{q}_\perp \times \hat{q})] - \cos(\theta)\hat{q}, \\ \boldsymbol{\sigma}_{in} = \boldsymbol{\sigma}_{out} &\equiv \boldsymbol{\sigma} = (\vec{k}_{in} \times \vec{k}_{out})/\sin(2\theta), \\ \boldsymbol{\pi}_{in} &= (\vec{k}_{in} \times \boldsymbol{\sigma}), \\ \boldsymbol{\pi}_{out} &= (\vec{k}_{out} \times \boldsymbol{\sigma}). \end{aligned} \quad (3.31)$$

Finally, the polarization vectors  $\hat{\epsilon}_{in,out}$  can be written as linear combinations of the vectors  $\boldsymbol{\sigma}$  and  $\boldsymbol{\pi}$ . So now we define the four experimental quantities that can, in principle, be measured in experiment at a fixed angle:  $F_{ij}$ , where  $ij \in \{\sigma, \pi\}$ . For example, one of the four channels

<sup>5</sup>Not to be confused with the conductivity tensor  $\sigma$ , shown in non-bold typeface in this work

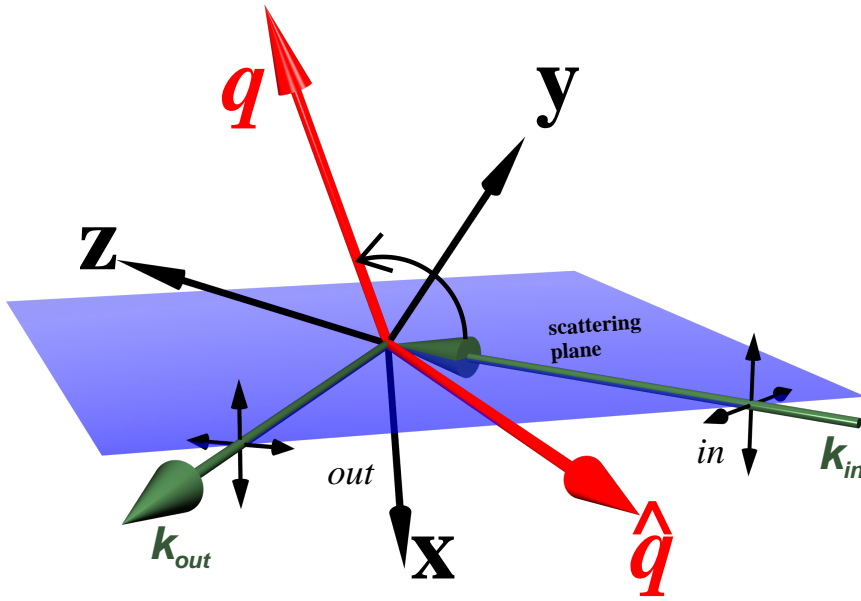


**Figure 3.9** The definition of the vectors used in the description of the scattering process in the main text, combining the visualization in the crystal frame and in the experimental scattering frame. The crystal axes lie in an arbitrary position, determined by the position in  $q$ -space where the Bragg peak of interest lies. The figure does not show the direction of the magnetic moment, which will be determined later.

can be  $F_{\sigma\sigma} \equiv (\boldsymbol{\sigma} \cdot \mathbf{F} \cdot \boldsymbol{\sigma})$ , so the four channels are  $F_{\sigma\pi}$ ,  $F_{\sigma\sigma}$ ,  $F_{\pi\sigma}$ ,  $F_{\pi\pi}$ . Completely discerning the polarization state of the outgoing light is possible using a polarization analyzer of the scattered beam, which is not always available, especially in the soft x-ray regime. However, measuring four linear-independent spectra ( $\boldsymbol{\sigma}$ ,  $\boldsymbol{\pi}$ ,  $\boldsymbol{\sigma} + \boldsymbol{\pi}$ ,  $\boldsymbol{\sigma} + i\boldsymbol{\pi}$ , the latter two being linear  $45^\circ$  rotated and circular light) yields enough information to map out the scattering tensor on the basis of  $\boldsymbol{\sigma}$ ,  $\boldsymbol{\pi}$ . In many cases, enough information about the scattering tensor can be obtained by measuring only the two states  $\boldsymbol{\sigma}$ ,  $\boldsymbol{\pi}$ , provided the azimuthal dependence can be measured. Then, the two measurable channels are given by

$$\mathbf{I}_\pi = I_{\pi\sigma} + I_{\pi\pi}; \mathbf{I}_\sigma = I_{\pi\sigma}, \quad (3.32)$$

where we will show later how the channel  $I_{\sigma\sigma}$  goes to 0. Finally, we turn to express  $F^{mag}$  in terms of the experimentally accessible vectors  $\hat{\epsilon}_{in,out}$ , evaluating the expression 3.29 and carrying out some algebra leads to:

$$F^{mag} = F^{(0)}(\hat{\epsilon}_{out}^* \cdot \hat{\epsilon}_{in}) + F^{(1)}(\hat{\epsilon}_{in} \times \hat{\epsilon}_{out}^*) \cdot \hat{m} + F^{(2)}(\hat{\epsilon}_{out}^* \cdot \hat{m})((\hat{\epsilon}_{in} \cdot \hat{m})), \quad (3.33)$$

which is the result obtained by Hannon *et al.* [57], a long-standing and widely used expression for magnetic scattering in spherical symmetry. Note that in their approach, the magnetic Hamiltonian,  $H_3$  in Eq. 3.14, was the starting point to calculate the scattered intensity. In the approach described here, the magnetic moment information is contained in the scattering tensor we have defined. From Eq. 3.33, it can now be seen which terms will be needed to interpret the scattered intensity of a AFM system.  $F^{(0)}$  has no term proportional to the magnetic moment and is usually disregarded in magnetic scattering. The term  $F^{(1)}$  is linear in  $\hat{m}$  and will give rise to the first harmonic of an AFM. This term is indeed related to the

magnetic circular dichroism ( $\Delta m_j = \pm 1$ ). The term proportional  $F^{(2)}$  also has magnetic influence, but it is quadratic in  $\hat{m}$ , so it will be blind to an AFM system, canceling the antiparallel spin directions. If the AFM system is a spiral, then it will give rise to second harmonics, which require twice the momentum transfer to access the corresponding Bragg peak. A quintessential example of such a spiral system was studied in films of Holmium metal [72] and in manganites [73]. A visualization of this consequence can be seen in Fig. 3.10.

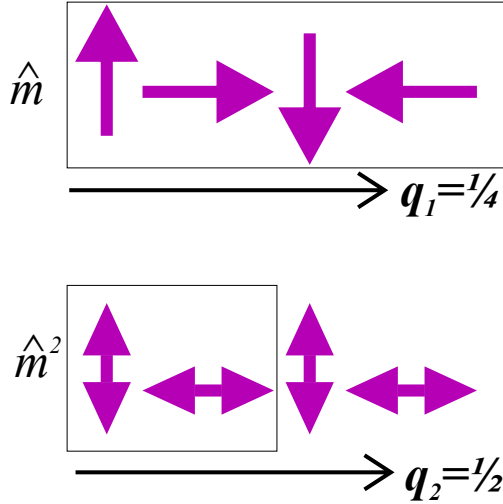


**Figure 3.10** In a spiral, the term quadratic in  $\vec{m}$  will give rise to second harmonics of the first Bragg peak, which are double in momentum transfer.

Therefore, the intensity of magnetic scattering is proportional to the terms containing  $F^{(1)}$ , which can be expressed in spherical symmetry as:

$$F^{mag} = \begin{pmatrix} 0 & -m_z & m_y \\ m_z & 0 & -m_x \\ -m_y & m_x & 0 \end{pmatrix}. \quad (3.34)$$

From this expression, it can be seen that for any vector  $\vec{v}$ ,  $\vec{v} \cdot F^{mag} \cdot \vec{v} = 0$ . Therefore, knowing that vector  $\sigma$  remains unchanged during the scattering event (from Eq. 3.31 and Fig. 3.9),  $F_{\sigma\sigma} = 0$  for resonant magnetic scattering. This expression also yields a valuable piece of information: the components of the magnetization direction  $m_i$  are encoded in the tensor  $F^{mag}$ , and they can be determined by measuring azimuthal scans around the Bragg condition  $\hat{q}$ , as shown in Fig. 3.11. For simplicity, the figure is represented in the laboratory frame of reference, as opposed to Fig. 3.9 which is in the crystal frame. Both are equivalent and advantageous depending on the discussion. In this thesis, the latter will be used, and we can arrive at expressions of the diffracted intensity as a function of the azimuthal angle. For example, the channel  $F_{\sigma\pi}$  for a simple AFM system looks like:

$$F_{\sigma\pi} = (\vec{k}_{out} \times \sigma) \left( e^{i0} \begin{pmatrix} 0 & -m_z & m_y \\ m_z & 0 & -m_x \\ -m_y & m_x & 0 \end{pmatrix} + e^{i\pi} \begin{pmatrix} 0 & m_z & -m_y \\ -m_z & 0 & m_x \\ m_y & -m_x & 0 \end{pmatrix} \right) (\vec{k}_{in} \times \vec{k}_{out}) / \sin(2\theta),$$

where the phase of  $\vec{q} = \frac{1}{2}$  was taken, and the sum runs over two sites. Note that the second matrix in  $F$  represents a spin oriented antiparallel to the first. The terms  $\vec{k}_{in,out}$  and  $\sigma$  contain the geometry information, including the azimuthal angle  $\psi$ . It is important to define here the reference frame, that is  $\psi = 0^\circ$  and the sense of rotation. This is achieved by

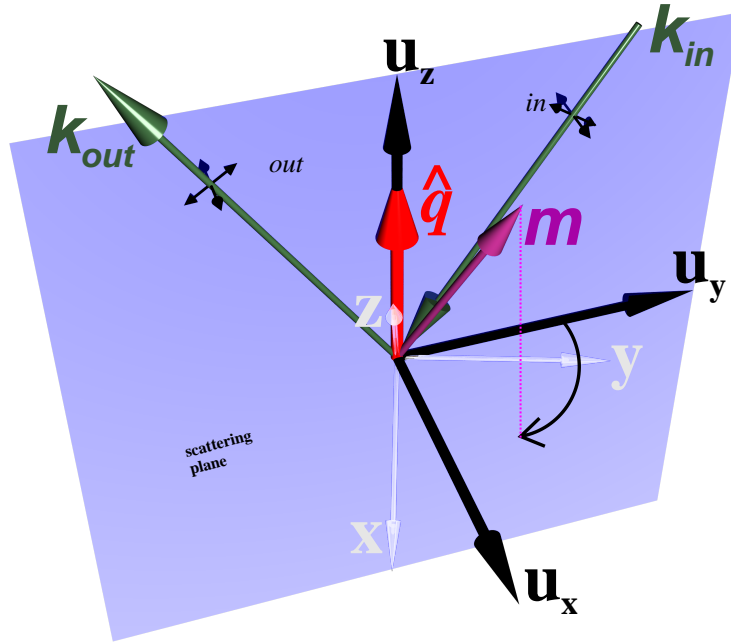


**Figure 3.11** The way the direction of a magnetic moment  $\vec{m}$  can be determined by doing azimuthal scans around the diffraction vector  $\hat{q}$ . Axes in this figure are defined in the laboratory reference frame, where the direction of the crystal axes  $(x, y, z)$  can be rather skew.

carefully defining  $\hat{q}_\perp$  at the value of  $\psi = 0^\circ$ , while the rotation around  $\hat{q}$  is defined as right handed.

Finally, for completeness, it is noted that the form of  $F^{mag}$  can change when considering systems beyond spherical symmetry. Although that was not the case during this thesis, there are systems which deviate substantially from spherical symmetry, and their scattering tensor must be considered accordingly. In our treatment, the different symmetries will arise from carrying out the summation over the spherical harmonics of Eq. 3.27. A full description of this effect can be found in Ref. [64].

### 3.3.5 Experimental access to reciprocal space

The theoretical framework presented so far will now be brought to the experimental realm, discussing typical RSXS experimental setups. To this effect, let us begin by visualizing the translation between a real space context of a diffraction experiment and its reciprocal space counterpart. Fig. 3.12 shows on the left, and incident ray of x-rays into a sample (of tetragonal nature, common to the heterostructures investigated in this thesis). The light that has penetrated to the sample is eventually scattered following Eq. 3.6 in many different directions. The task of a diffraction experiment is to align the detector in such a way as to pick up the scattered signal. However, in systems of single orientation (single crystals and heterostructures), accessing a desired reflection requires more than just moving the detector: it involves moving the incident angle of the beam, i.e. rotating the sample with respect to the incoming beam. Moreover, the beam which is scattered in directions underneath the sample surface, the sample horizon, will be absorbed by the sample. The relationship given

by Eq. 3.6 will yield information about the Bragg planes. Whether they be of structural or electronic origin, Bragg planes will result in points in reciprocal space. Their layout is shown on the right of Fig. 3.12. The reciprocal space vectors ( $\vec{q}_x, \vec{q}_y, \vec{q}_z$ ) are defined by the crystal axes ( $\vec{a}, \vec{b}, \vec{c}$ ), and the points below the sample horizon are shown as faded. They are accessible in tilted geometries, as described below. Finally, the momentum transfer  $\vec{q} = (\vec{k}_{in} - \vec{k}_{out})$  is limited by the wavelength of the incoming x-rays. This limitation is also known as the Ewald sphere. For soft x-rays, the Ewald sphere is in the order of  $0.1\text{\AA}^{-1}$ , which is sufficient to probe Bragg planes with separation of at least  $\sim 10\text{\AA}$ .

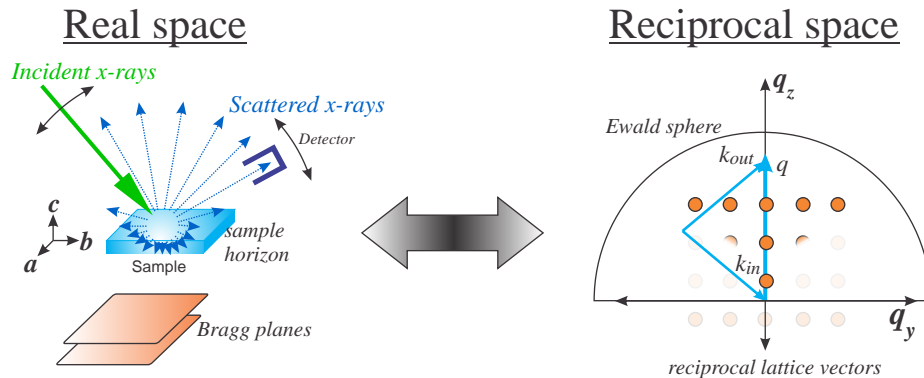


**Figure 3.12** The translation between real space (the experimental setup and the probed atomic positions) and reciprocal space, where the x-ray's provide the means to obtain the Fourier-transform of the Bragg planes. Navigating in reciprocal space corresponds therefore to scanning different combinations of the direction of incident beam, detector position.

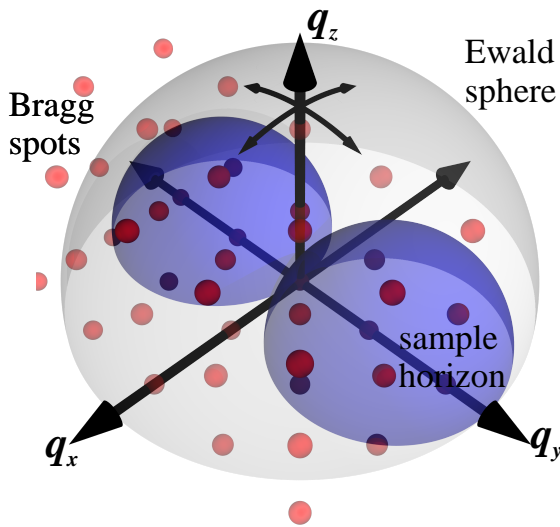
### Navigating in reciprocal space

Any position in  $\vec{q}$ -space can be reached by adjusting a set of angles in real space, essentially the angle of incidence and exit. In a multiple circle diffractometer, a direct translation between the angles and the position in  $\vec{q}$ -space can be calculated using the so-called orientation matrix [74]. For RSXS, where normally there is no structural Bragg peak within the Ewald sphere, the orientation matrix is defined in “virtual” terms. That is, the crystal systems are previously aligned and the angular directions are known. The heterostructures investigated throughout this thesis have the advantage of withholding the overall substrate tetragonal symmetry. Even for cases when the systems are relaxed, the  $(a, b, c)$  directions are well-defined with respect to the macroscopic sample. Epitaxially grown heterostructures, however, cannot be polished along different crystal directions which can make accessing Bragg peaks below the sample horizon difficult.

Figure 3.13 shows a 3-dimensional pictograph of reciprocal space. The sample-horizon-blocked areas are shown by shaded blue spheres, as is the entire Ewald sphere (gray). Peaks of the kind  $(0, 0, l)$  are reached by adjusting  $(\omega, 2\theta)$  with the constraint  $\omega = 2\theta/2$ . Furthermore, there are essentially two ways to access a reciprocal lattice point with in-plane component  $(0, k, l)$ . First, setting  $2\theta$  to the value of  $\theta$  given by Bragg's law. Then, an angular offset is introduced to the angle  $\omega$  ( $\chi$ ) to introduce the value along  $k$  ( $h$ ). The offset is given by

$$\alpha = \arccos \frac{(0, 0, l) \cdot (0, k, l)}{|(0, k, l)| |(0, 0, l)|} \quad (3.35)$$

## Diagonal view



## Side view

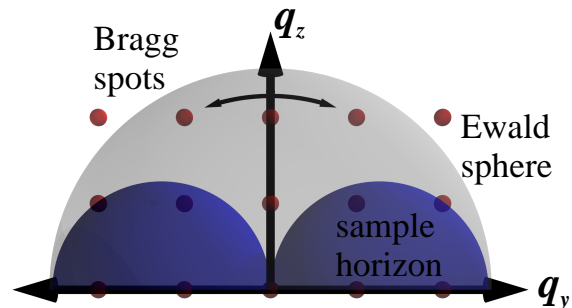


**Figure 3.13** (left) 3-dimensional pictograph of scans in reciprocal space. The in-plane directions can be accessed by offsetting  $\omega$  or  $\chi$ , while rotating  $\varphi$  and a combination of  $\omega$  and  $\chi$  will access positions of the kind  $(h, k, l)$ . (right) A typical sample horizon schematic when using the flat scattering geometry.

This schematic is outlined in Fig. 3.13. The geometry in which the offset is introduced in  $\omega$  is *flat*, because the sample surface normal is in the scattering plane. On the other hand, placing the offset in  $\chi$  yields a *tilted* scattering geometry. Fig. 3.13 also shows that in a flat geometry, a  $\varphi$ -rotation of  $90^\circ$  (rotation about  $q_z$ ) will invert the roles of  $\omega$  and  $\chi$ . Finally, to access reflexes of the kind  $(h, k, l)$ , a combination of all three angles  $\omega, \chi$  and  $\varphi$  is required. For example, accessing the  $(1, 1, 1)$  direction, as we will see in later chapters, involves offsetting  $\chi \rightarrow 55^\circ$  and  $\varphi \rightarrow 45^\circ$ . When doing this, the vector of interest  $(h, k, l)$  is placed into the scattering plane, but more importantly, that vector is now perpendicular to the  $\varphi$ -rotatable disc. This means that rotating  $\varphi$  will now rotate around  $(h, k, l)$ . However, the tilted geometry will have a disadvantage. As we will see in Chapter 4, this tilt will restrict the access to rotation around  $(h, k, l)$ .

The shape of Bragg reflex in RS can be visualized using the technique of reciprocal space mapping (RSM). Any diffraction measurement involves a scan of  $\vec{q}$ -values in RS. The method of RSM is essentially cutting several adjacent lines in RS in such a way as to record a 2-dimensional intensity map around the vicinity of a certain Bragg peak. This is discussed at length in Ref.'s [75, 76].

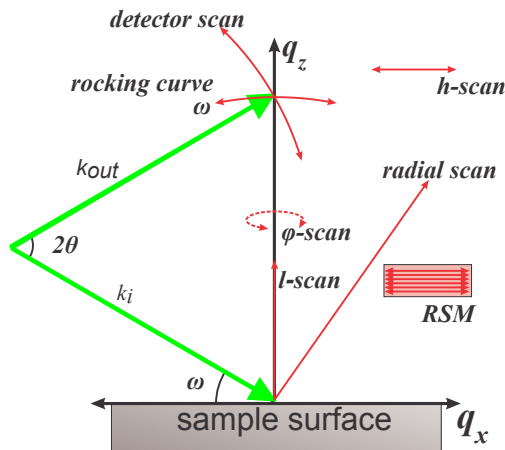


**Figure 3.14** A schematic of how certain angular movements translate into RS, as well as some definitions of linear scans in defined directions. A RSM consists in an array of adjacent linear scans to map a 2D region in RS.

### Bragg reflex topology

In practice, the rules given by Eq. 3.6 are relaxed for different values of  $(h, k, l)$ . In other words, real conditions of the sample and the experiment will give rise to broadened peaks. The main mechanisms of elongation common in heterostructures are mosaicity (mostly finite in-plane correlation), truncation rods, resolution of the experiment, and strong absorption. The latter is a consequence of the reduction of scatterers when the penetration depth is reduced. Strongly enhanced on resonance, quantifying a Bragg reflex's width as function of energy across a resonance can yield absorption coefficients in absolute units [77]. The experimental resolution is the smallest effect in many of today's sources.

Mosaicity arises when different portions of the sample are slightly misaligned with respect to others. In heterostructures, this can easily occur during the growth process. Introducing small misalignments of the unit cell with respect to the substrate implies the scattering in different directions at a given incident angle. Since the magnitude of  $\vec{q}$  is the same, the other scattering directions will all be along a centered at the origin, with radius  $\sqrt{q_x^2 + q_y^2 + q_z^2}$ . Scanning  $\omega$ , also known as a rocking curve, is a common method of quantifying the degree of mosaicity in a sample. The angular width of a rocking curve corresponds to the amount of mosaicity in the sample. In heterostructures, the term mosaicity is commonly associated with the in-plane correlation length. That is, it refers to the size of laterally spaced domains with the same crystal orientation. The concept is shown visually in Fig. 3.15.

Heterostructures always possess a marked surface along  $z$ , which leads to an important inherent property: the crystal truncation rod. Taking the Fourier-transform of the product of the infinite (and periodic)  $\rho(\vec{r})$  with a Heaviside function  $h(z)$ , one convolutes the Fourier-transforms of those functions. The Fourier transform of a step function like  $h(z)$  is  $i/q_z$ , and thus the intensity is proportional to  $1/q_z^2$ . Combining this result with the delta functions of Eq. 3.6, one obtains streaks of intensity along the surface normal. This effect is shown visually in Fig. 3.15. Moreover, this effect is also present in any truncated crystal system, like the superconducting cuprates, as we will discuss in Chapter 5.

### The experimental setup

The actual scattering geometry commonly used in RSXS is shown in Fig. 3.16. First of all, due to the large absorption cross section of air for x-rays of this wavelength [67], these experiments can only be done with operating pressures below  $10^{-4}$  mbar. Thus, the entire

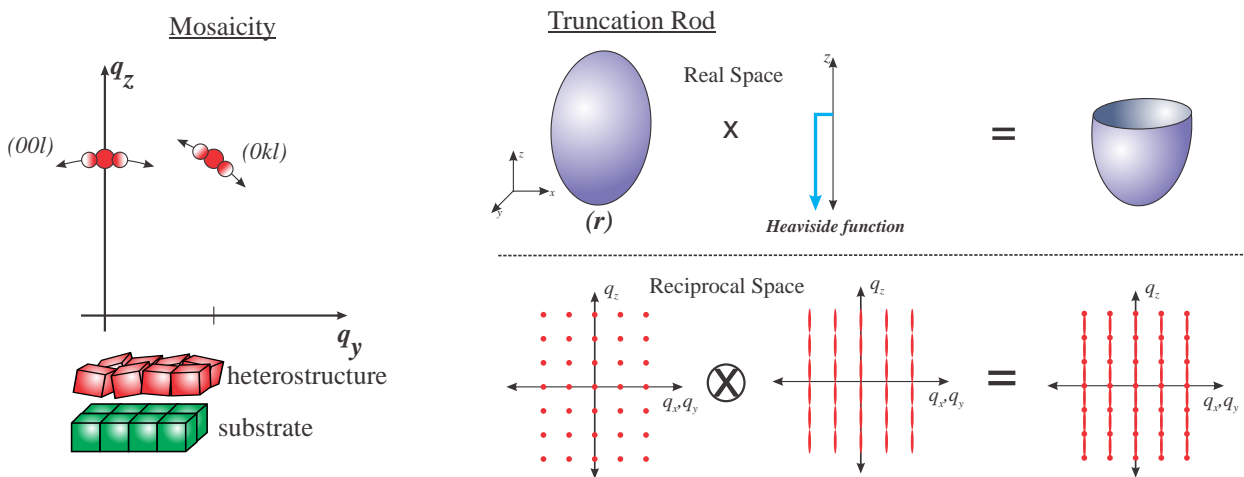


**Figure 3.15** (left) The concept of mosaicity involves domains of equal crystal orientation, which gives rise to a broadening along the  $\omega$  direction. (right) A long broadening along the  $l$ -direction arising from the surface truncation.

experiments are enclosed in vacuum chambers. The simplest kind of diffraction setup offers 2 automated motors: the sample and detector rotation. Additionally, the setup can offer the option of mounting the sample on a rotatable disc (highlighted yellow in Fig. 3.16), which allows rotation around a vector perpendicular to the holder's back surface in the scattering plane.

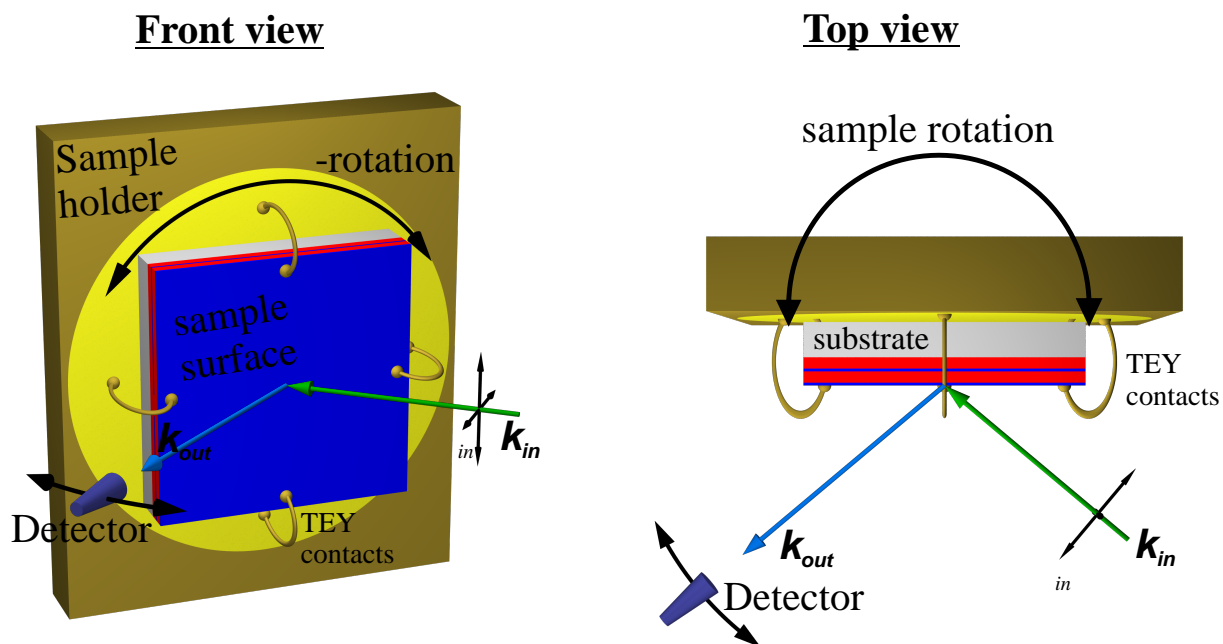


**Figure 3.16** A schematic of the two-circle diffractometer used in throughout this thesis.

When scattering in the flat geometry of Fig. 3.16, this corresponds to a  $\varphi$ -rotation. The measurement of the XAS is done by grounding the sample from the heterostructure to the

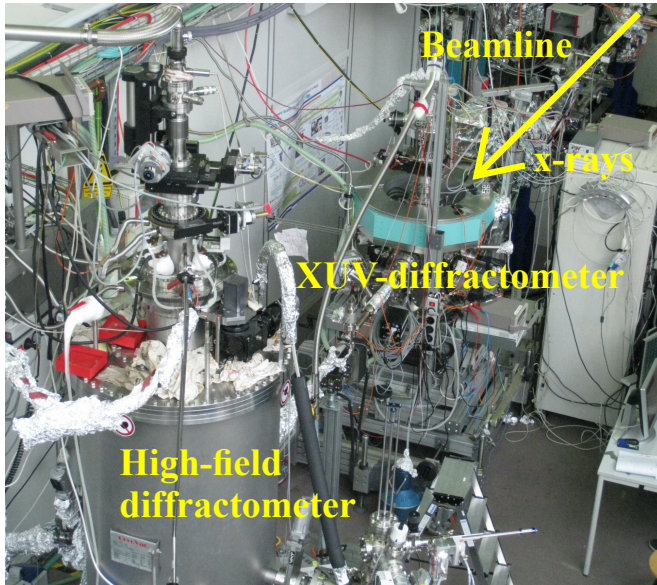


**Figure 3.17** The setup of the the UE46-PGM1 beamline at BESSY, in Berlin, Germany. The beamline operates two chambers: one predominantly for diffraction which Fig. 3.16 depicts, and one for magnetic circular dichroism (XMCD) experiments.

holder, as indicated in Fig. 3.16 by wires connecting the sample surface<sup>6</sup>. Then, when the light strikes the samples and releases photoelectrons, the grounded sample will replenish the exited electrons and register a current. This current measurement is normally called a “drain current” or total electron yield (TEY) signal.

The RSXS experiments of this thesis were done using the setup of the UE46-PGM1 beamline at BESSY in Berlin, shown in Fig. 3.17. The undulator at this beamline generates x-rays with variable polarization and energies in the range 200-1900 eV with a bandwidth of  $\leq 1$  eV. The beamline operates two end-stations, which can be run independently. The first one is an ultra-high vacuum diffraction chamber. It operates at pressures of around  $10^{-10}$  mbar and is equipped with a continuous flow He cryostat. The temperature ranges that can be achieved are 10-350K, although certain conditions can even allow lower temperatures (down to 3K). Inside the chamber, there is a 2-circle diffractometer like the one depicted in Fig. 3.16. The sample motor ( $\omega$ ) and detector motor ( $2\theta$ ) rotations are essentially independent, with wide angular ranges accessible ( $-30^\circ < \omega < 160^\circ$ ,  $-50^\circ < 2\theta < 180^\circ$ ). The diffractometer, which is built on a very stable mount, has motorized movement in all three directions of the sample stage, and so allows maximum precision when measurement small samples. The  $\varphi$ -rotation of the sample is not motorized, in order to reach temperatures below 30K. This rotation is done manually using a screw driver installed behind the sample holder. The precision of this rotation is about  $\sim 5^\circ$ . The drain signal is measured independently from the scattered signal.

The second end-station operating at UE46-PGM1 is a high-magnetic field chamber. A rotatable, superconducting magnetic coil can generate fields of up to 7T in any direction with respect to the sample surface. Whilst most of the experiments carried out in this end-station are XAS measurements of magnetic circular dichroism (XMCD), the chamber does possess a very unique feature. The chamber has rotatable sample and detector motors ( $\omega$  and  $2\theta$ ). This permits scattering experiments in high magnetic fields, albeit with certain limitations due to the rotatable magnet. Fixed slits provide windows in  $2\theta$  of  $0^\circ < 2\theta < 66^\circ$

<sup>6</sup>The substrates used to grow TMO heterostructures are insulating, so the grounding cannot be done through the substrate.

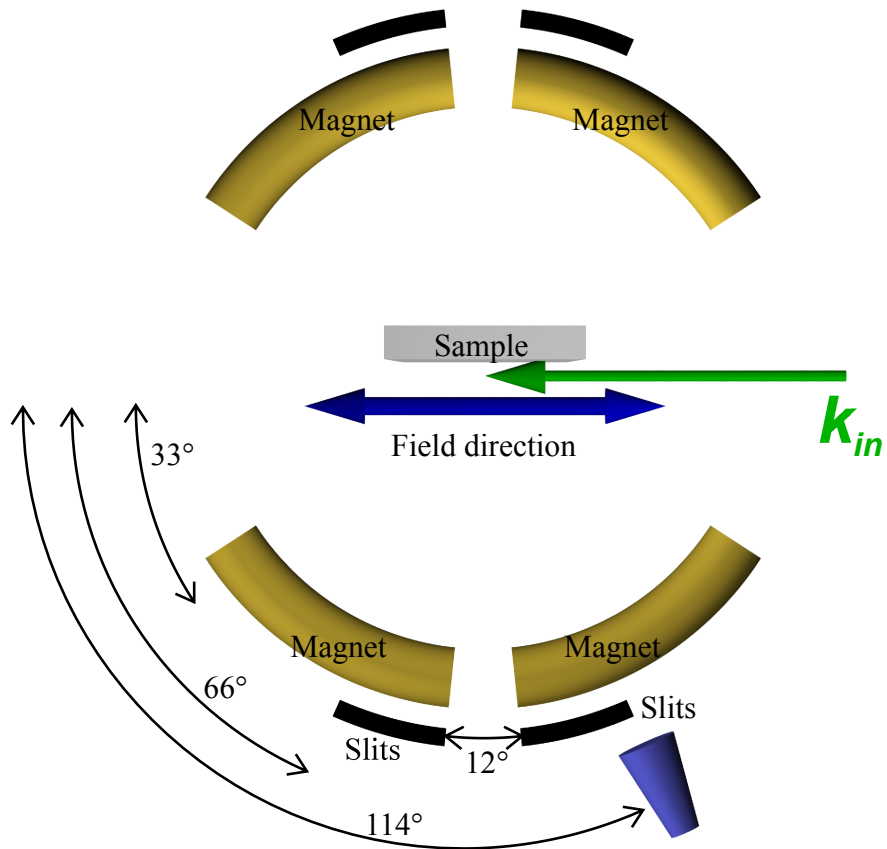


**Figure 3.18** A schematic of the scattering geometries available with applied magnetic field at the high-field station of the the UE46-PGM1 beamline at BESSY. The field direction rotates with the magnet.

and  $84^\circ < 2\theta < 96^\circ$ . A schematic of the available scattering geometries under applied field with the magnet set at  $0^\circ$  is shown in Fig. 3.18.

# Chapter 4

## The Nickelates: A Spin Density Wave

Engineering new electronic and structural phases by combining complex materials into heterostructures is a task taken on with widespread enthusiasm around the world. Amongst others, heterostructures comprising 113-rare-earth nickelates  $R\text{NiO}_3$  (RNO), where  $R$  is any rare earth metal in the Lanthanum line, have become very popular. In the bulk, the RNO family of materials display a phase diagram which reflects the complexity of TMOs. It has several electronic phases which are accessible by small structural changes. In this Chapter, we will review some of the most relevant aspects of the RNO family, spanning research done over more than a decade. In the end of this summary, we will outline theories of how the ground state of these materials can be described, motivating the study of this PhD. In the experimental part, we will present evidence of a novel kind of magnetic order in  $\text{LaNiO}_3$  (LNO)-based superlattices (SLs), as well as in RNO films grown under epitaxial strain, using RSXS. We will attempt in the discussion to connect these findings to a spin density wave (SDW) instability in the FS of these materials.

### 4.1 Properties of bulk RNO

To summarize the properties of 113 rare-earth nickelate family, the following section was collected from body of literature developed between 1992 to the present, including most prominently Ref.'s [78–82].

#### 4.1.1 Electronic configuration and the Torrance phase diagram

We begin the discussion of the properties of bulk RNO with a brief description of its electronic configuration shown in Fig. 4.1(left). Formally, the  $\text{Ni}^{3+}$  ion inside a perovskite building block is in a  $3d^7$  valence electron configuration. The lower-lying  $t_{2g}$ -levels are all full with six antiparallel electrons. This leaves one electron occupying the states of the higher energy  $e_g$ -levels with a spin =  $\frac{1}{2}$ . This electron interacts with the crystal field environment, which is expected to split the degeneracy of the  $e_g$  levels via a Jahn-Teller distortion. Such a distortion has been suggested for the low temperature phase of the heavy rare-earths (Lu, Y, Ho), where a segregation into two sites with subsequent octahedral environments with covalent and ionic bonds was proposed [81]. In the lighter elements (Nd, Pr, La), a structural distortion of this kind has not been observed and is presumed to be dynamic rather than

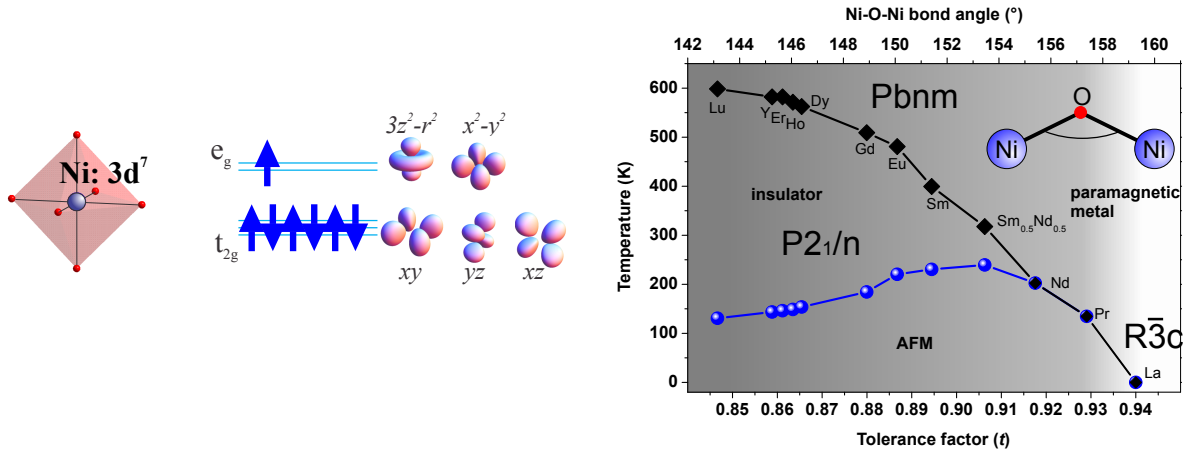


**Figure 4.1** (left) Formally, the Ni ion in a perovskite unit is in a  $3d^7$  state with low-spin configuration, leaving one electron in the  $e_g$ -level. (right) The phase diagram of the 113-RNO family, comprising temperature driven metal-to-insulator transitions and paramagnetic-AFM transitions with different onset temperatures depending on rare-earth ion.

static [81]. The main focus of this thesis are RNO materials with  $R=\text{Nd,Pr,La}$ , where the  $e_g$ -level bandwidths exceed any remanent splitting.

Fig. 4.1(right) contains the temperature vs rare-earth ion phase diagram that fully summarizes the most important properties of the RNO family, known as the ‘‘Torrance Phase Diagram’’, in honor of the substantial contribution of Ref. [78]. It displays the transition temperatures across a metal-insulator transition (MIT) and a paramagnetic-AFM transition for all the different rare-earth ions across the Lanthanide row, except for Lanthanum. While an ideal perovskite retains the cubic symmetry, the rare-earth ions of the RNO family are not large enough to accommodate the cubic lattice. Therefore, they result in lower symmetry structures, as discussed in section 2.1.1. As these ions shrink in size while they grow in weight across the periodic table, the resulting structure can distort up to a strongly orthorhombic  $Pbnm$  lattice. To quantify this structural distortion upon changing the rare-earth ion, two quantities serve useful. First, the angle between two adjacent Ni ions, passing through a ligand oxygen will decrease as the rare-earth size shrinks. Second, the ratio of the distances between the R-O and the Ni-O ions, known as the *tolerance factor*, defined as  $t \equiv D_{R-O}/\sqrt{2}D_{Ni-O}$ . These are the horizontal axes of the Torrance Diagram of Fig. 4.1, which connects the electronic phase transitions to the deviations of the perovskite structure upon the chemical pressure of larger R-ions.

The heavier R-ions result on the left exhibit highly distorted  $Pbnm$  lattices, with Ni-O-Ni angles well away from  $180^\circ$  and correspondingly low tolerance factors. The gray scale of phase diagram in Fig. 4.1 quantifies the  $Pbnm$  distortion as it weakens when approaching the Pr ion. Ultimately, the LNO has such a smaller distortion that it results in a rhombohedral  $R\bar{3}c$  structure (white). Remarkably, the electronic phases throughout the diagram show a close behavior to the structure. For the heavy R-ions, the onset temperature of the MIT ( $T_{MIT}$ ) starts from about 600 K and drops to about room temperature for Samarium. Moreover, a solid solution mixing two adjacent R-ions will result in a  $T_{MIT}$  right between the two pristine materials, as observed in for the  $\text{Sm}_{1/2}\text{Nd}_{1/2}$  case. In the insulating phase, below  $T_{MIT}$  the materials enter a Néel state below  $T_N$ , with AFM order discovered by neutrons in the seminal work of References [83–85], which will be addressed in detail in upcoming sections.

In the more intriguing cases of the larger Nd, Pr compounds,  $T_{MIT}$  and  $T_N$  coincide at around 200 and 120 K, respectively. For these materials, the  $Pbnm$  distortion is rather small and they are very close to a metallic ground state. For LNO the distortion is the smallest and the straighter Ni-O-Ni bonds allow hopping and conductivity of a metal down to lowest temperature. In the bulk, this material has never shown any sign of magnetic order. Work done in this thesis will show the properties of RNO can be changed by heterostructuring and that magnetic order emerges.

### 4.1.2 The MIT: charge disproportionation

The mechanism which drives the MIT has been discussed extensively in the past years. Aside from being strongly connected to the material's bulk structure as previously discussed, the insulating state is believed to be strongly connected to a charge density wave, or charge order (CO). Although the CO results only in a minimal change in the unit cell's (u.c.) volume, it is very easily observed in the case of the heavier R-ions (Y, Lu, Ho), as it results in a structural transition from  $Pbnm$  to a low-temperature  $P2_1/n$  monoclinic phase [82, 86, 87], which doubles the pseudocubic u.c.. In the lighter R's, this structural transition is too small to be detected from conventional structural refinements, as discussed in Ref.'s [86, 87].

The case of  $\text{NdNiO}_3$  (NNO) was thus investigated with an alternate technique in the seminal work of Reference [88]. In that study, evidence of a different low-temperature "structural" phase was observed by doing resonant hard x-ray diffraction. Since the doubling of the pseudocubic u.c. results in peak of the kind  $\mathbf{Q}_{CO}=(\frac{h}{2}, \frac{k}{2}, \frac{l}{2})$ , the  $L$ -edge wavelength's insufficient momentum transfer precludes from doing RSXS experiments at  $\mathbf{Q}_{CO}$ . Therefore, the study required x-rays tuned to the Ni  $K$ -edge which is around 8340 eV. The electronic transition that corresponds to this edge is between  $1s \rightarrow 4p$ , which as we discussed in Chapter 3, does not enter into a state close to the Fermi level for the  $3d$  TMOs. So these experiments do not directly probe the  $d$ -electrons as RSXS does, but can still be sensitive to the local environment of the Ni ion. In certain cases, a "resonant" lineshape can arise from details that alter the scattering tensor. For other examples and reviews on  $K$ -edge resonant diffraction experiments, see Ref.'s [89–91].

The study by Staub *et al.* [88] was performed on NNO films grown using PLD on substrates of (001)-oriented  $\text{NdGaO}_3$  substrates, which are also  $Pbnm$ . We note here that the advance in film growth was crucially important to this investigation, and later ones as well, as the RNO materials cannot be grown into large single crystals. Previous neutron studies were done on powder samples, and it was difficult to assign reciprocal lattice peaks given the multi-domain patterns. So the studies performed after 2002 were done mostly on films. This, of course, questions whether the bulk properties are actually being measured or whether epitaxial strain already modifies the system. However, in the work by Staub *et al.* the data confirmed the film to be of  $Pbnm$  structure, i.e. like the bulk.

A  $Pbnm$  structure has a distorted pseudocubic u.c. (Fig. 2.4) which results in peaks of the kind  $(\frac{h}{2}, \frac{k}{2}, \frac{l}{2})$  in pseudocubic notation. Thus, distinguishing their origin as structural or electronic is a task which involves resonant x-ray diffraction. However, not all the half-order peaks are structurally allowed. Some of these forbidden  $Pbnm$  peaks become allowed in the low-temperature phase, so their mere appearance serves a solid clue of a phase transition. The main findings that lead to the CO picture in NNO are summarized in Fig. 4.2. First of all, panel (a) shows the two reflections the study focused on. Note that the  $hkl$ -indexing

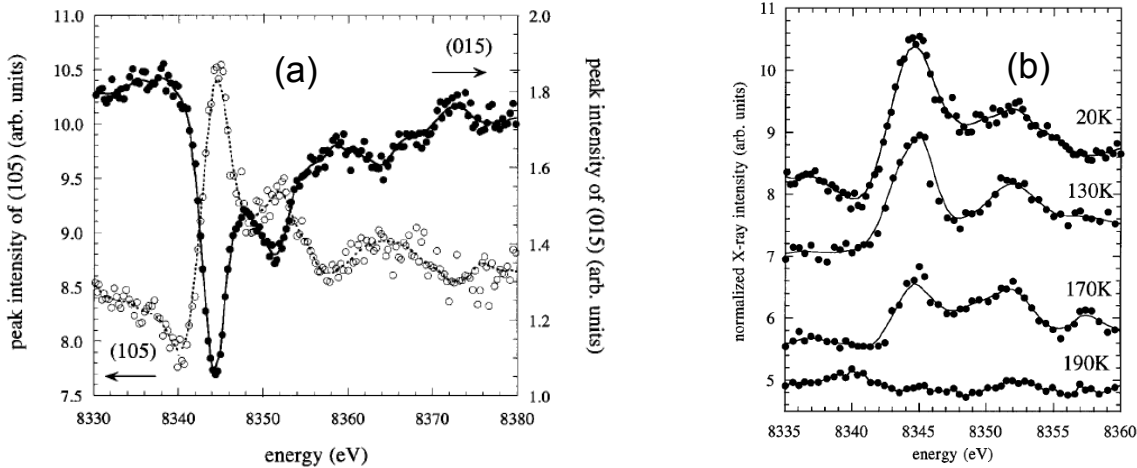


**Figure 4.2** (left) The energy dependence of the scattered intensity of certain reflexes which are sensitive to the CO phase. (right) The temperature dependence of these energy lineshapes shows a connection of the CO to the MIT observed in the transport measurements. Both panels taken from [88].

is in  $Pbnm$  notation. The conversions to the PC system are  $(105)_{Pbnm} \equiv (\frac{5}{2}, \frac{1}{2}, \frac{1}{2})_{PC}$  and  $(015)_{Pbnm} \equiv (\frac{5}{2}, \frac{1}{2}, \frac{1}{2})_{PC}$ . In both cases, intricate lineshapes arise in the low temperature phase, suggesting the increasing role of the Ni contribution in the structure factor. The  $(\frac{5}{2}, \frac{1}{2}, \frac{1}{2})$  peak is structurally allowed in  $Pbnm$ , so the lineshape resembles that of an “anti-resonance”: the effect of reducing the scattered intensity as the penetration depth decreases across a resonance. In this case, the structure factor is dominated by ions other than Ni, and the lineshape across the Ni  $K$ -edge is an “inverse” of the Ni’s XAS contribution.

The  $(\frac{5}{2}, \frac{1}{2}, \frac{1}{2})$ , on the other hand, is not allowed in  $Pbnm$ , so its appearance in the low-temperature phase can only arise from a structural phase transition: one where the structure factor takes on strong contributions from the Ni ions (see Eq. 3.6). Fig. 4.2(b) shows how the energy lineshape of the  $(\frac{5}{2}, \frac{1}{2}, \frac{1}{2})$  peak changes with different temperatures. The resonant lineshape, and the peak itself, vanishes upon warming above  $T_{MIT}$ , as compared to transport measurements done on the same film.

Although, the “wiggly” lineshape observed in Fig. 4.2(a) appears to be of electronic origin, the phenomenon that the x-ray experiments are detecting is more a structural one. The CO, assuming for simplicity to localize charge only on the Ni sites, will alter the valence state from  $3d^7$  to a modulated  $3d^{7+\delta}-3d^{7-\delta}$  wave. The propagation vector of this CDW is the  $(111)$ , resulting in a rock salt type of pattern. Assuming at first approximation the valence bond sum model holds, which connects the valence state of the Ni and ligand ions to the structure, the dissimilar Ni sites will yield disproportionate bond lengths. We note here that these conclusions do not assert which of these effects is precursor and which is consequence. Most likely they both occur in a lockstep fashion. Each Ni site will have a different core potential, shifting the position of the edge jump in the XAS (and in the real part of  $\sigma$ ). So XAS measurement will only measure the average of the two sites:  $XAS \propto \Im(\sigma_{Ni_1} + \sigma_{Ni_2})$ , which will wash out any possible difference between them into a slightly broader spectrum. A diffraction experiment, on the other hand, will be sensitive to the difference between the two sites. In other words, by introducing the phase shift of the x-ray wavefront, the two  $\sigma$ ’s will interfere into a complex lineshape, with the real and imaginary part simultaneously

playing a role in the scattered intensity. Thus, by shifting both the real and imaginary parts of the two sites, and then diffracting them at the right  $\mathbf{Q}_{CO}$ , the authors of Reference [88] were able to estimate a charge  $\delta$  in the order of  $\sim 0.2$ . A visual summary of this interpretation is shown in Fig. 4.3.

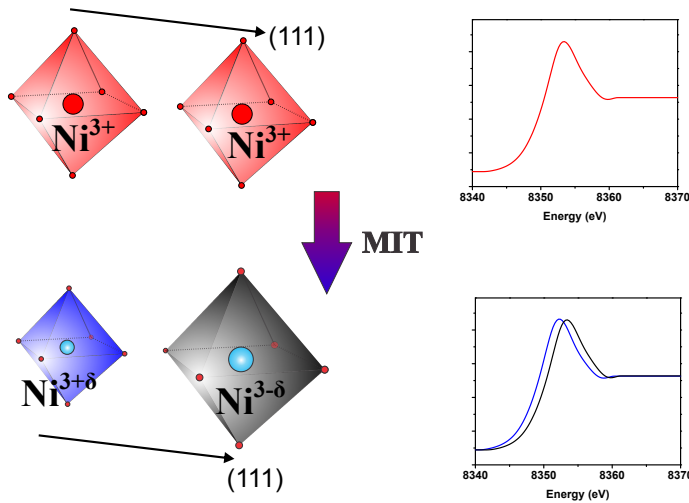


**Figure 4.3** A schematic of the charge disproportionation taking place in NNO upon cooling across the MIT, following the discussion of Ref. [88]. In the CO state, a rock salt pattern of smaller-larger sites yielded from different valence state of the Ni ion will give rise to different reflexes as compared to the high-temperature, metallic phase. This yields a shift between the  $K$ -edge of each Ni site, exemplified in the right panel comparing the XAS.

### 4.1.3 AFM order: noncollinear spiral

The magnetic ordered phase of the RNO materials is a rather intricate one. As discussed on page 8, perovskite-type oxides tend to form AFM order via the next-nearest neighbor superexchange interaction. This would result in a doubling of the u.c. and peaks similar to  $\mathbf{Q}_{CO}$ . However, neutrons first determined that this is not the case for the RNO materials. In Ref.'s [84, 85], authors García-Muñoz *et al.* discovered an unusual ( $\uparrow\uparrow\downarrow\downarrow$ ) quarter-fold spin density wave propagating along the PC (111) direction in the more itinerant NNO and PrNiO<sub>3</sub> (PNO) compounds. This resulted in peaks of the kind  $\mathbf{Q}_{SDW}=(\frac{1}{4}, \frac{1}{4}, \frac{1}{4})$ . The size of the moment is  $\sim 0.9\mu_B$ , indicating a low-spin ( $S = \frac{1}{2}$ ) Ni<sup>3+</sup> configuration. Other studies like [92] confirmed the same type of magnetic ordering present in all the RNO's (except La).

To explain the mechanism behind the magnetic order, García-Muñoz *et al.* proposed an orbital superlattice where  $d_{x^2-y^2}$  and  $d_{3z^2-r^2}$  orbitals are staggered with the same periodicity as the magnetic moments, thus also contributing to  $\mathbf{Q}_{SDW}$ . A schematic of the magnetic u.c., with a simple ( $\uparrow\uparrow\downarrow\downarrow$ ) structure as well as the orbital superlattice suggested are shown in Fig. 4.4. Despite the discoveries made by neutron scattering, the fact that the samples were polycrystalline powders precluded a magnetic structure determination. The direction of the spins was left largely unaddressed. This spurred the discussion between collinear ( $\uparrow\uparrow\downarrow\downarrow$ ) and non collinear ( $\uparrow\rightarrow\downarrow\leftarrow$ ) models, which remained unanswered for several years.

To address these open questions regarding the origin and details of the unique magnetic structures of the RNO materials, Valerio Scagnoli *et al.* contributed substantial knowledge in their work of Ref.'s [93, 94]. Once again, to circumvent the problem of polycrystalline samples the authors investigated films of NNO. In contrast to the work done to qualify the CO scenario, these were (111)-oriented NdGaO<sub>3</sub> substrates, whose similar lattice parameters and  $Pbnm$  symmetry did not alter NNO's bulk structure. The orientation was chosen to allow to reach  $\mathbf{Q}_{SDW}$  inside a RSXS chamber and measure a full azimuthal dependence of

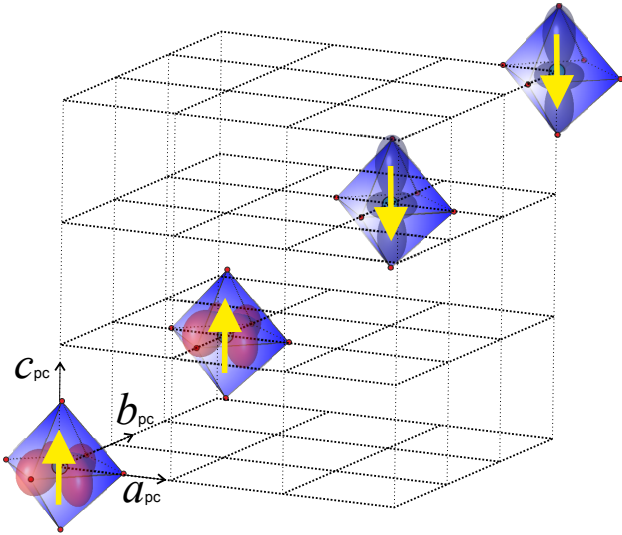


**Figure 4.4** A schematic of the four-fold magnetic ( $\uparrow\uparrow\downarrow\downarrow$ ) u.c. in PC reference, propagating along the  $(111)_{PC}$  direction. The orbital superstructure of alternating  $d_{x^2-y^2}$  and  $d_{3z^2-r^2}$  orbital occupation proposed by García-Muñoz *et al.* in Ref.'s [84, 85] is also superimposed.

the scattered intensity. The experiments were performed at the Ni  $L_{2,3}$ -edges, utilizing the resonance enhancement and sensitivity we elaborated on Chapter 3.

In those studies, the authors were able to disentangle the ambiguity between a combined magnetic/orbital scattering and a purely magnetic ordered state. By looking at the azimuthal dependencies at both the  $L_3$ - and  $L_2$ -edges, which would be different in the case of two ordered states living at  $\mathbf{Q}_{SDW}$ , they noticed only one origin of the scattering: magnetic order. By ruling out the orbital superlattice picture, the consensus of CO mechanism driving the concomitant MIT rose. In addition, the authors exploited the formalism discussed under the context of Eq. 3.33 on page 32. Thus, by performing the azimuthal scans of the scattered intensity, they directly determined the orientation of the spins.

The results of their azimuthal investigation are reproduced in the left panel of Fig. 4.5. First of all, we discuss the vertical axis of their plot. In conventional RSXS chambers, a full polarization analysis of the scattered intensity is difficult to achieve. Therefore, the authors measured the scattered intensity for  $\sigma$ - and  $\pi$ -polarized incident photons, so that the two channels  $\pi \equiv I_{\pi\sigma} + I_{\pi\pi}$  and  $\sigma \equiv I_{\sigma\pi}$  were distinguished.<sup>1</sup> Moreover, because of the large wavelength of the soft x-rays, there is no Bragg reflex accessible for signal normalization. Therefore, the authors present the data as the ratio  $\frac{\pi}{\sigma}$ , which heals out experimental effects like sample position, beam shape/size, etc., that can alter the absolute intensities.

In their calculations, the authors considered two magnetic models shown in Fig. 4.5. On the one hand, they considered a collinear ( $\uparrow\uparrow\downarrow\downarrow$ ) model, with all spins parallel/antiparallel to the  $(110)_{PC}$  direction, as suggested by neutron scattering. In addition, they considered a noncollinear ( $\uparrow\rightarrow\downarrow\leftarrow$ ) period-4 spin spiral. In that case, the first and third spins are parallel/antiparallel to the  $(111)$ -direction and the second and fourth spins point along the  $(\bar{1}\bar{1}2)$  direction. Fig. 4.5 shows that the experimental data fits fairly well to the spiral ruling out the collinear model.

At this point, a notation which will be extensively used throughout this thesis is introduced, shown in the panels below the spin structures on the right of Fig. 4.5. Using the PC cartesian reference frame, each figure shows the first and second spin sublattices. The third and fourth spins are the negative counterparts of the first two.

<sup>1</sup>Recall that the channel  $I_{\sigma\sigma}$  is not active in magnetic scattering

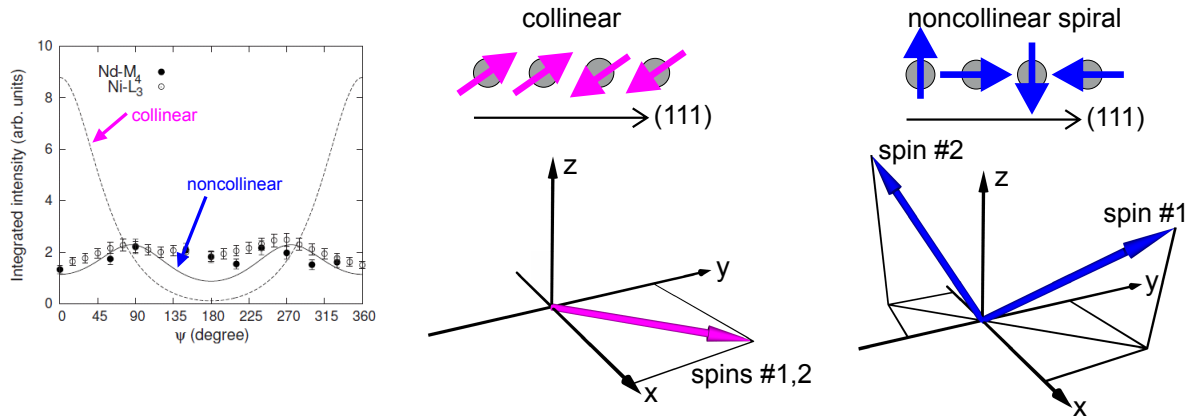


**Figure 4.5** (left) The azimuthal dependence of the  $\frac{\pi}{\sigma}$  ratio, shown for a collinear and spiral, along with the actual data for NNO (from Ref. [94]). (right, top) Schematics of the collinear and non-collinear (spiral) spin orientation along the (111) direction. (right, bottom) The nomenclature to be used throughout this thesis, where first two spin sublattices are shown in the PC reference. The other two are just the corresponding negative vectors.

#### 4.1.4 A SDW-nested Fermi surface

After the intensive research carried out between the 1990’s and early 2000’s on the nickelates, details of the ground state properties were discussed in terms of charge and spin order. However, a close look at the Torrance phase diagram has recently motivated a revisiting of the ground state. Except for the cases of Nd and Pr, with  $T_{MIT}=T_N$ , in the rest of the phase diagram the magnetic ordering is apparently independent from the MIT. The onset of the magnetization is a first order transition when  $T_{MIT}=T_N$  and second order when  $T_{MIT}>T_N$  [95]. In fact, an extrapolation of an order-parameter like temperature behavior of the magnetization in NNO and PNO suggests that the magnetic order onset temperature would actually be higher than the  $T_{MIT}$  [95]. These open questions call for particular attention to the lighter Nd and Pr systems, since for them  $T_{MIT}=T_N$ , and the question of whether the ionic, localized picture truly corresponds to these rather itinerant systems. The coincidence of both onset temperatures further puts into doubt whether the CO is a precursor to the AFM order.

In a resurgent interest to address these questions, several new theories including modern ones addressing nickelate heterostructures have emerged in the last years [96–98]. Despite the increasing accuracy of the tools to develop these theories, widespread consensus is not yet reached. A recent proposal by Lee *et al.* used a framework based on a phenomenological Landau theory [99] founded upon semi-microscopic Hartree-Fock calculations [100]. In their theory, the structure of the  $e_g$  levels near the Fermi level, as calculated by their microscopic theory, yield a nesting-unstable Fermi surface (FS), which addressed under a Landau formalism will reproduce the observed properties of NNO and PNO. The authors find a peak in the spin susceptibility, which suggests the proneness to spin order driven by the nesting. The fermiology, moreover, seems to show a nesting vector very similar to  $\mathbf{Q}_{SDW}$ . This is summarized in Fig. 4.6, taken from [99]. The authors also suggest that under certain geometrical modifications of the RNO systems which might be accessible via heteroepitaxial growth like layered confinement and strain, the CO could be “turned off”, resulting in a pure SDW material: an AFM metal.

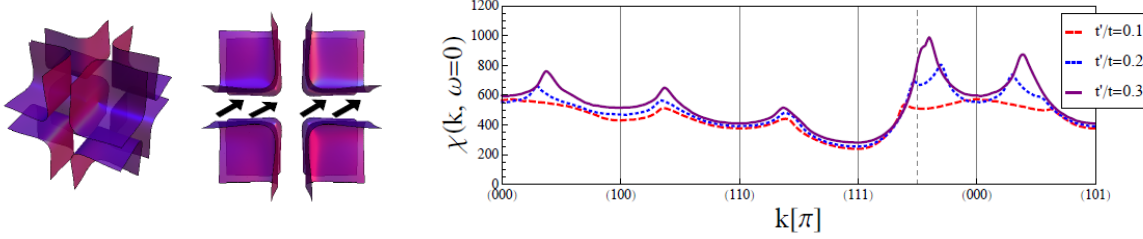


**Figure 4.6** (left) The FS for the RNO's calculated in Ref.'s [99,100] with a nesting vector close to  $\mathbf{Q}_{SDW}$ . (right) The spin susceptibility peaking at  $\mathbf{Q}_{SDW}$ , strongly suggesting a SDW instability which would explain the robust magnetic ordered state of the RNO's. Both figures taken from [99].

## 4.2 Properties of LNO SLs

Despite bulk LNO not undergoing phase transitions, the resurgent interest in nickelates during the last  $\sim 5$  years arose from LNO-based superlattices. Spawned by the theory discussed on page 13, we will turn now to briefly discuss the most recent results in the field of exploring LNO-based superlattices.

### 4.2.1 Reconstructing LNO

Elaborated on page 13, the motivation of constructing LNO-based superlattices (SLs) is based on the idea of potentially creating a system with three ingredients which we know from the superconducting cuprates (for more, see Chapter 5): a spin- $\frac{1}{2}$  system with strong AFM correlations, charge carriers confined to a 2-dimensional plane, and a FS with a pronounced  $d_{x^2-y^2}$  character.

The question around the orbital reconstruction has sparked an interesting dialogue between the theoreticians. Some have supported the feasibility of altering the orbital occupations using strain and confinement [101,102] or by varying the counter-ion across the interface between LNO and the blocking layer [103]. Other studies have oppositely suggested that the covalency with the oxygen ligand will effectively make altering the orbital occupation impossible [104]. The answers to these open questions have been experimentally addressed exploring natural linear dichroism (LDIC) using polarization dependent XAS measurements. As depicted and described in Fig. 3.8 on page 28, x-rays polarized linearly can be projected onto two different orthogonal directions with respect to the PC cartesian reference. In this way, the measurement will probe the symmetry of the available end-states of the system. For example, when the system has one hole in the  $d_{x^2-y^2}$  orbital like in  $\text{Cu } 3d^9$ , the XAS intensity will be suppressed when the x-ray's polarization is orthogonal to the plane. Motivated by the reconstruction of the valence states near the Fermi level, results of this kind have been shown in nickelates grown on epitaxial strain in Ref.'s [69–71, 105]. In all these cases, the orbital polarization, the amount of imbalance in the occupation of the otherwise degenerate  $e_g$  levels, is defined as:

$$P = \frac{n_{x^2-y^2} - n_{3z^2-r^2}}{n_{x^2-y^2} + n_{3z^2-r^2}}, \quad (4.1)$$

where  $n_{x^2-y^2}$  represents the number of electrons in the  $d_{x^2-y^2}$  orbital. To connect the latter to the quantities experimentally accessible via XAS: the number of holes or empty states,

so-called sum rules for linear dichroism are utilized, namely:

$$X \equiv \frac{n_{3z^2-r^2}}{n_{x^2-y^2}} = \frac{3I_{E\parallel z}}{4I_{E\parallel x} - I_{E\parallel z}}, \quad (4.2)$$

where  $I_{E\parallel z}$  would represent the XAS intensity of x-rays polarized along the  $z$ -axis. These sum rules are thoroughly addressed in Ref.'s [69, 106, 107].

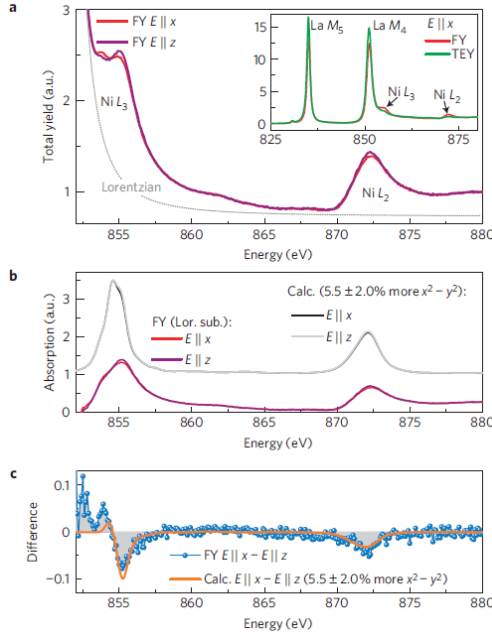


**Figure 4.7** The way that LDIC is probed in LNO systems. The vicinity of the La  $M_4$ -line to the Ni  $L_3$ -edge makes the analysis intricate. A very careful background subtraction is required. Image reproduced from Ref. [69].

In the first paper addressing this issue experimentally, XAS was combined to x-ray reflectivity to quantify not only the orbital polarization of LNO-LAO SLs on STO to be in average of  $\sim 5\%$  (Fig. 4.7), but to map a spatial profile of orbital polarization across the LNO layers [69]. These results were disputed later on by other groups relying only on XAS data. In a more simplistic case, the authors of Ref. [70] studied single films of LNO on both compressive and epitaxial strain: LaSrAlO<sub>4</sub> (LSAO) and STO, to find that while compressive strain results in a level splitting and a preferred occupation of the  $d_{3z^2-r^2}$  orbital, the case of tensile strain does not simply reverse the sign of the effect. The authors claim no  $e_g$ -level splitting and no LDIC is clear for the film on STO, although ruling this out completely seems difficult, as there is at least a little dichroic signal evident in their data. When studying more intricate systems, built from LNO-LAO SLs, authors Freeland *et al.* also suggest an asymmetric response in the splitting of the orbital levels with compressive and tensile strain [71], albeit they did see an orbital polarization arising in SLs on tensile strain. In both of these papers, they propose that SLs under tensile strain show a distortion which could act as a precursor to a charge disproportionation. The close lying La  $M_4$ -line ( $\sim 852$  eV) compels a careful background subtraction to quantify details of the Ni  $L_3$ -edge (see Fig. 4.7).

In a detailed experimental survey, we recently addressed a possible answer to these open questions. By investigating SLs with several different compositions and amount of epitaxial strain, we found a symmetric response of the lattice to the orbital modifications and the effect of confinement were comprehensively laid out [105, 108]. In summary, these results show that

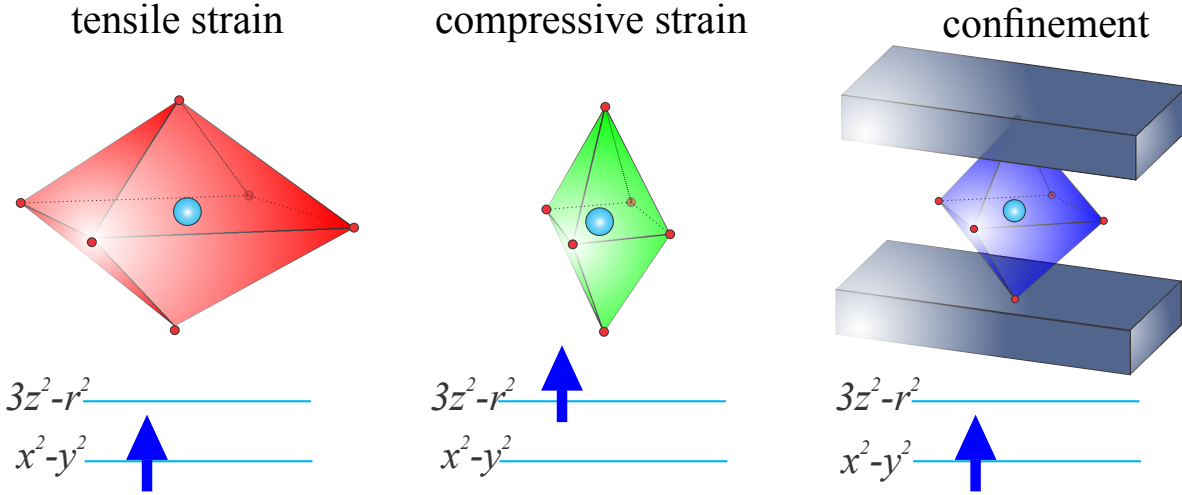


**Figure 4.8** A summary of the results of Ref.'s [69, 71, 105, 108], showing orbital polarizations in nickelate heterostructures depending on strain and confinement. Tensile strain splits drives a preferential occupation of the  $d_{x^2-y^2}$  level, while pure compressive strain shows preferential  $d_{3z^2-r^2}$ . Pure confinement results in a preferred  $d_{x^2-y^2}$  orbital.

SLs on compressive strain show a  $e_g$ -level splitting which lowers the  $d_{3z^2-r^2}$  orbital. The effect is countered by layer confinement which results in a zero net orbital polarization. The results also show that for tensile strain the situation is reversed with increasing  $e_g$ -level splitting and preferential occupation of the  $d_{x^2-y^2}$ . Moreover, epitaxial strain's ability to distort the lattice was identified as the more viable road towards a  $d_{x^2-y^2}$ -like band structure. These results are summarized in Fig. 4.8. The trend will later on be connected to the behavior of the magnetic structure with epitaxial strain.

The effect of confining Ni electrons on the ground state properties of LNO has attracted widespread interest. Ref.'s [109–111] are among the most important experimental results. Despite differing details about which thickness of LNO is a critical one, the results show that when reducing LNO to  $\lesssim 5$  u.c. in SLs or thin films, the system undergoes changes in the electrical conductivity at low temperatures. Instead of a temperature-independent metallic behavior as observed for bulk LNO, MIT's are observed using  $dc$ -conductance probes [110, 111] or optical probes [109], the latter of which serve a more reliable experiment as it is not sensitive to misfit dislocations which may alter the absolute values of conductance.

The results of Ref. [109] are summarized in Fig. 4.9. In the top panels, the data of the optical response  $\epsilon_1^*$  as function of sample temperature shows that a SL with 4 u.c. behaves metallic down to lowest temperature, just like bulk LNO. But when the SL only contains 2 u.c. of LNO, the real part of the dielectric permittivity shows an upturn at temperatures around 120 K. This behavior is confirmed by noticing a spectral weight shift in the optical conductivity from low frequencies to energies above  $\sim 0.4$  eV, which suggest a loss of Drude weight due to the partial gapping of the FS. While the onset temperature of this “pseudogap” differs between substrates, the fact that it occurs independent of the substrate's strain and only dependent on the layer thickness suggests that confinement is the only driving force behind the phenomenon.<sup>2</sup> We note here that despite the fact that a full gap does not open in the low temperature phase, we label the upturn in the temperature dependence of  $\epsilon_1^*$  a

<sup>2</sup>These results also rule out the phase transition of STO [112] as driving the transition.

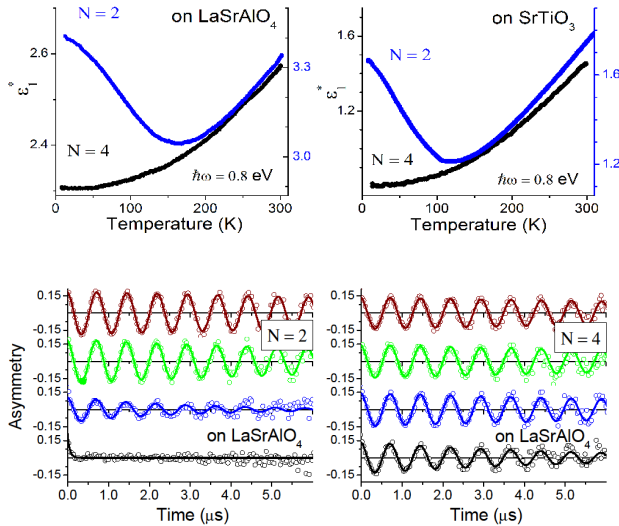


**Figure 4.9** (Top) The optical response as function of temperature for LNO-LAO SLs with  $N=2$  and 4 u.c. of LNO, grown on compressive (left) and tensile strain (right). (Bottom) The slow  $\mu\text{SR}$  asymmetry spectrum, revealing the presence of ordered moments in the SLs with  $N=2$  of LNO. Image reproduced from Ref. [109].

“MIT”.

Most reports approximately converge upon the fact that LNO’s conductance approaches that of a MIT at low temperatures when confined to sufficiently small systems. However, only one paper has addressed the magnetic ground state of LNO by low-energy muon relaxation under these conditions; Ref. [109] (lower panels in Fig. 4.9). In such experiments [113], the sample is placed into a beam of spin-polarized muons at low temperatures in an applied magnetic field transversal to the muon spin polarization. Muons, which carry a spin =  $\frac{1}{2}$  magnetic moment, will precess about the transverse field direction with a cyclotron frequency proportional to the applied field strength.

When penetrating into a magnetic sample, the muons interact with the local magnetic fields. Within microseconds, muons decay into  $\mu^+ \rightarrow e^+ + \nu_e + \bar{\nu}_\mu$ , with the positron forward motion along the direction of the muon spin. The experiment detects these emitted positrons in a spatially discerning way. This way, the precession frequency of the muon can be determined by detecting the asymmetry of positrons that decay in a given direction. So in a paramagnet, the frequency of the precession will be given only by the external field. However, in a magnetized sample, the precession frequency will be much higher given by the strong local interaction between the muon and the magnetically ordered electron spin. The lower panel of Fig. 4.9 shows that a 4 u.c. SL of LNO (on both cases of strain) have a response oscillating equal to the cyclotron frequency of the applied field even at lowest temperatures. On the other hand, SLs with 2 u.c. of LNO show that at low temperatures all the muons precess at a much faster frequency, well above the experiment’s resolution. These findings strongly suggest the presence of a magnetic ordered state. Although the technique does not serve to say which kind of magnetic order, which element is involved, etc., the findings served the motivation to understand the newly found magnetic ground state of LNO-LAO SLs.

Other groups investigated the magnetic characteristics of related LNO-based SLs. In the work by Gibert *et al.* [114] on LNO- $\text{LaMnO}_3$  SLs, with  $\text{LaMnO}_3$  a ferromagnetic insulator, the authors found the effect of exchange bias when confined to ultrathin LNO layers. This indicates a magnetic ordered state evolving in LNO, presumably an AFM state, although other scenarios like a spin glass or SDW were suggested. We note here that these results have also motivated the research done in this thesis, although these SLs are different than

the ones we have investigated: grown on substrates cut in the (111)-direction and containing a ferromagnetic insulator  $\text{LaMnO}_3$  instead of a band-gap insulator like LAO. These findings were also studied using XAS, in particular XMCD [115].

Work done in this thesis was carried out to study the magnetic order in LNO-based SLs by RSXS to address the following questions: is it a spin glass state? Is it true AFM order? If so, what kind? Could it be related to the FS nesting vector proposed in Ref.s [99,100]? If so, by confining the system are we altering the FS of LNO and bringing it closer to its unstable nested case? These questions have motivated the research described in the upcoming section.

## 4.3 Experimental results

Now we turn to the experimental results obtained in the investigation of nickelate heterostructures and their magnetic properties. As in many TMOs, the structure of the system is of crucial importance. Therefore, before discussing the magnetic properties, we will go through some structural details observed in LNO-based heterostructures. At this point we introduce the notation to be used throughout this section of this thesis. A SL with  $X$  u.c. of LNO and  $Y$  of RMO material repeated  $N$  times will be labeled  $(X//Y)\times N$ . The  $hkl$ -indexing of the reciprocal lattice points will be done in the pseudocubic (PC) notation.

### 4.3.1 Structural details of LNO SLs

The structure of the films and SLs we have investigated were probed using non-resonant hard x-ray diffraction. The basic principle of diffraction was described on page 21. Moreover, a more thorough account of the technique employed here of reciprocal space mapping (RSM) is available on page 35 and Ref. [76]. For the structural characterization, experiments were performed at the MPI-MF Surface Diffraction beamline of the ANKA light source of the Karlsruhe Institute of Technology in Germany, using X-rays of  $10\text{keV}$  to access a large Ewald sphere. A linear array of 1280 reverse-biased silicon diodes was used as a detector (each  $50\mu\text{m}$  wide), which allowed recording of high-precision mapping of  $(q_y, q_z)$ -planes. The same detector was used to record maps along the  $(q_x, q_y)$ -plane, with a 10 pixel region of interest.

We divide the following study into the case of tensile and compressive strain, focusing primarily on the latter. The case of tensile strain was investigated in Ref. [76] and is summarized in Fig. 4.10, for a  $(4//4)\times 10$  LNO-LAO SL on STO.

Each sub-figure of Fig. 4.10 shows black solid lines which indicate the lateral position of the substrate peak, and can be used to identify the relaxation amount. Pink solid lines show the values for a cubic lattice. The position of the bulk LNO and LAO are also indicated. The dashed black lines indicate the mosaicity direction, which is  $q$ -dependent. It is evident that the elongation of the SL peak is due to mosaicity. The extracted lattice constants are  $a, b = 3.852 \pm 0.001\text{\AA}$ ,  $c = 3.789 \pm 0.001\text{\AA}$ , resulting in a  $(57 \pm 0.1)\%$  relaxation. The same partially relaxed behavior was observed for all samples on STO. Other cases of tensile strain result in fully strained systems, as shown in Table 4.1.

The case for LNO-LAO SLs grown on LSAO, i.e. compressive strain, is much more intricate and we thus elaborate on it further. The structure of LSAO is tetragonal ( $I4/mmm$ ), with parameters  $c = 12.636\text{\AA}$  and  $a = b = 3.756\text{\AA}$  so it applies differing values of com-

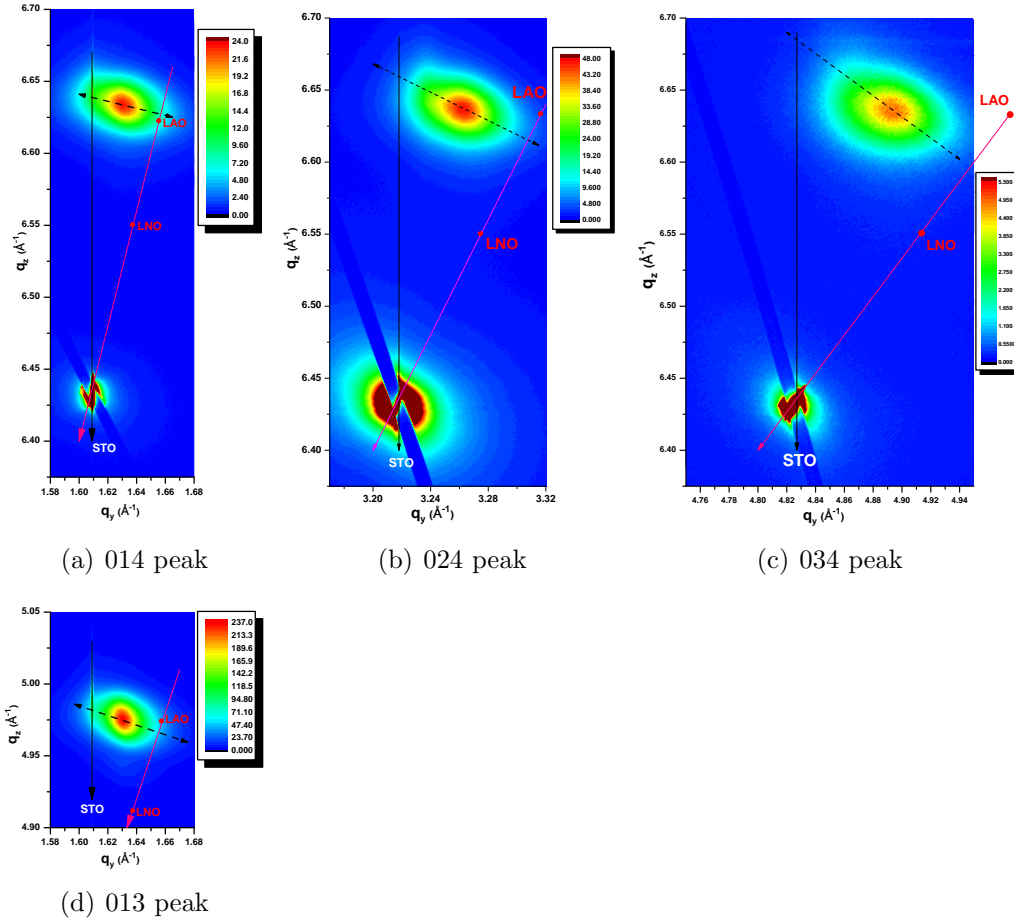


**Figure 4.10** RSM's of the labeled reflexes of a  $285 \pm 20 \text{ \AA}$  SL grown on STO (LNO-LAO-BE53). Pink lines point towards the origin, black-solid lines indicate the lateral position of the substrate peaks, and dashed-black lines denote the mosaicity direction.

pressive strain to both LNO and LAO, which have lattice constants of  $3.837$  and  $3.789 \text{ \AA}$ , respectively. The SL bilayer periodicities and total thicknesses ( $T$ ) were obtained from specular X-ray diffraction patterns, as described in [76]. First of all, we discuss SLs with total thickness  $T = 30 \text{ nm}$ .

Fig. 4.11 exemplifies representative RSMs slicing the  $(q_y, q_z)$ -plane around the (015) and (025) reflexes. Around the (015) peak, recorded intensity peaks at  $(1.671, 8.104) \text{ \AA}^{-1}$  revealing a structure with in-plane lattice constant matching LSAO (shown as a white solid line) and a  $c$ -axis lattice constant of  $3.874 \text{ \AA}$ . This behavior was realized for all samples with similar  $T$  and bilayer periodicities ranging between 2 and 4 u.c.'s. Furthermore, we searched for diffracted intensity at all accessible half-order positions. Following the Glazer approach [7, 10, 116], their extinction rules served to determine the oxygen octahedra rotation pattern. All samples with thickness  $T < 400 \text{ \AA}$  exhibited half-order peaks at all  $(\frac{h}{2}, \frac{k}{2}, \frac{l}{2})$  values except  $(\frac{h}{2} = \frac{k}{2} = \frac{l}{2})$  ( $h, k$ , and  $l$  are odd integers) [8]. These selection rules are consistent with octahedral rotations of the kind  $a^-a^-c^-$ : equal rotation angles along  $a$  and  $b$  and different rotation around  $c$ , all anti-phase [7]. This results in a monoclinic space group  $C2/c$ , in agreement with LNO films and SLs [117, 118]. Within our experimental resolution no peak splitting is observed, so the monoclinic angle  $\gamma$  deviates only minimally from  $90^\circ$ .

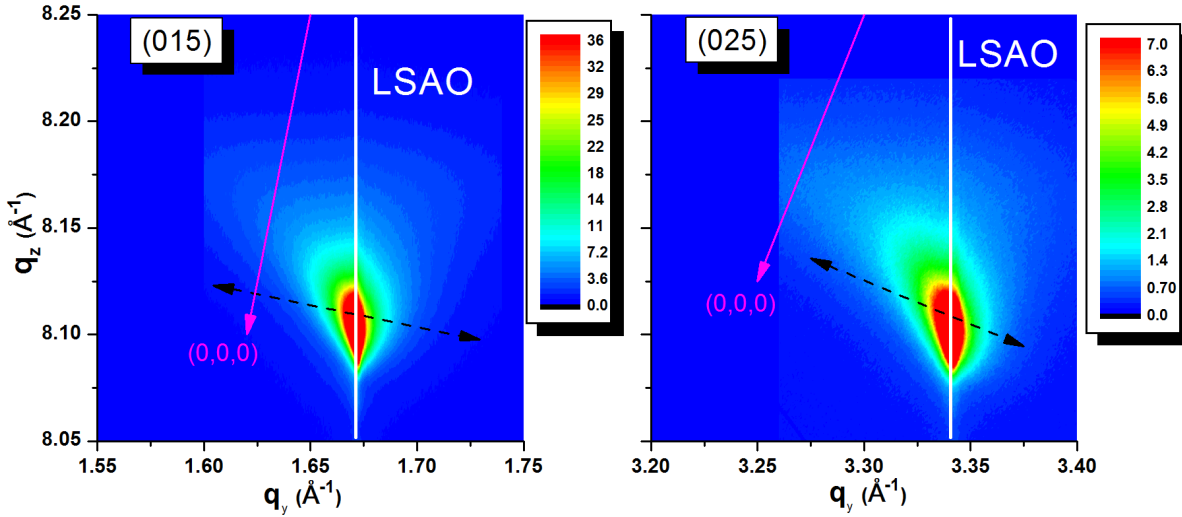


**Figure 4.11** The behavior of a LNO-LAO SL  $(3//3)\times 13$ , i.e.  $T = 30$  nm, grown on LSAO, measuring RSMs near the (015) and (025) reflections of the SL. A high degree of strain is evident from the match of the SL to the substrate lattice (indicated as vertical streaks). The black dotted lines indicate the mosaicity direction.

Furthermore, equivalent peaks like  $(\frac{h}{2}, \frac{k}{2}, \frac{l}{2})$  and  $(-\frac{h}{2}, \frac{k}{2}, \frac{l}{2})$  show similar intensity, suggesting equal occupation of all four possible orientational domains. In this structure, the cation sublattices essentially preserves the tetragonal symmetry imposed by the substrate, with octahedral tilts allowing to accommodate the lattice mismatch. We stress that because a single peak characterizes the system, growth of a two-component SL with total thickness  $T < 40$  nm results in a single structure, epitaxially strained to the substrate.

A striking difference is observed when investigating samples with total thickness of about 100 nm. A pronounced change in the structure is observed for  $40 < T < 100$  nm, exemplified in Fig. 4.12. The  $(q_y, q_z)$ -maps covering the same range as for thin samples reveal now a multiple peak structure. Despite the multiple peaks, a feature at  $q_z = 8.133\text{\AA}^{-1}$  resembles the in-plane lattice parameters of thin SLs, likewise showing no splitting in any direction. This single feature was also characterized at half-integer positions, showing the same extinction rules as the previous case, i.e. a  $C2/c$  space group.

Furthermore, around integer  $k$ -values two additional peaks appear at  $q_z = 8.172\text{\AA}^{-1}$ , split  $0.06\text{\AA}^{-1}$  along the  $q_y$ -direction. To understand the pattern, we recorded  $(q_x, q_y)$ -maps around several Bragg reflections at  $q_z = 8.172\text{\AA}^{-1}$ , shown in Fig. 4.13(a), where the  $(h, k)$ -grid is referenced to the substrate index. First, it confirms the peak multiplet around every Bragg spot to be 4-fold. A constant  $q_x(q_y)$  separation for all values of  $h(k)$  indicates a twinned structure rather than a system composed of distinct structures with different lattice parameters, while a growing  $q_x(q_y)$  splitting for increasing  $l$  (not shown) would evidence a twin-domain structure without in-plane periodicity. No out-of-plane splitting was observed, i.e. all peaks share the value of  $l$  for a given  $(hkl)$ -index. From individual peak widths we estimate the size of the domains to be  $\sim 30$  nm. The average in-plane lattice constant, taken from the center-of-mass of the peak multiplet, is  $a, b = 3.80\text{\AA}$ , indicating a partial relaxation of the system.

A similar instance of non-periodic, in-plane splitting was observed in 88-nm-thick man-

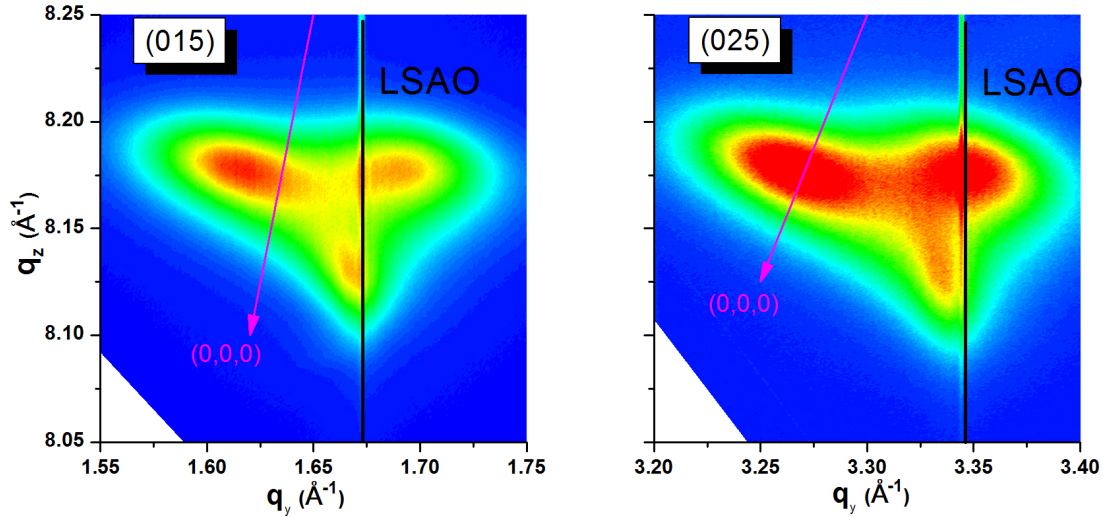


**Figure 4.12** The behavior of a LNO-LAO SL  $(2/2) \times 66$ , i.e.  $T \sim 100$  nm, grown on LSAO, measuring RSMs near the (015) and (025) reflections of the SL.

ganite films [116] and was ascribed to twin domains with (001)-planes tilted along (100) and (010). In contrast, our data shows splitting along the face-diagonals hence a different structural description is needed. On Fig. 4.13(b), comparatively laid out over the measured RS regions of Fig. 4.13(a), is the calculated Bragg spot layout resulting from the real-space structure proposed in Fig. 4.13(c-d), color coded to four equivalently occupied  $(x, y)$  domains. The cation sublattice is distorted by pulling the  $a, b$ -vectors along the face diagonal and shifting along the  $z$ -axis, leaving the  $c$ -vector unaffected. Vertical planes remain vertical, ensuring no  $l$ -splitting. Then, the primitive  $PC$  vectors for one domain can be written as

$$\begin{aligned}\vec{a} &= (a, \delta_x, \delta_z), \\ \vec{b} &= (\delta_x, b, \delta_z), \\ \vec{c} &= c(0, 0, 1).\end{aligned}$$

where  $\delta_x = 0.00675$ ,  $\delta_z = 0.0045$  were obtained to quantitatively match the observed splitting pattern. The resulting unit cell angles are  $\alpha = \beta = 89.74^\circ$ ,  $\gamma = 89.22^\circ$ . Furthermore, we characterized the reflections at half-order values, and again registered intensity at all  $(h, k, l)$ -half-integer numbers except when  $h = k = l$ . These selection rules indicate a monoclinic distortion in the  $ab$  plane which would be consistent with space group  $I2/m$  (standard setting  $C2/m$ , No. 14) ( $a^-a^-a^0$ ). However, this space group is not a subgroup of the bulk LNO  $R\bar{3}c$  ( $a^-a^-a^-$ ) and is not compatible with the monoclinic space group  $C2/c$  ( $a^-a^-c^-$ ) found from the full structural refinement we performed for the 30 nm thick SLs [8].

To understand the details of the structure in the thick LNO-LAO SLs grown on LSAO, we performed a corresponding control study on single films of LNO and LAO grown on LSAO with 100 nm total thickness. Fig. 4.14 compares RSMs for the two films around the (005) and (015) reflexes, respectively. Fig. 4.14(d), a  $(q_x, q_y)$ -map around (005), reveals the lattice of the LNO films to have a peak structure similar to the one found in LNO/LAO SLs, with the exception that the LNO film exhibits *only* the distorted rhombohedral structure and no sublattice strained to the substrate. An inspection of the intensity at half-order  $h, k, l$ -values

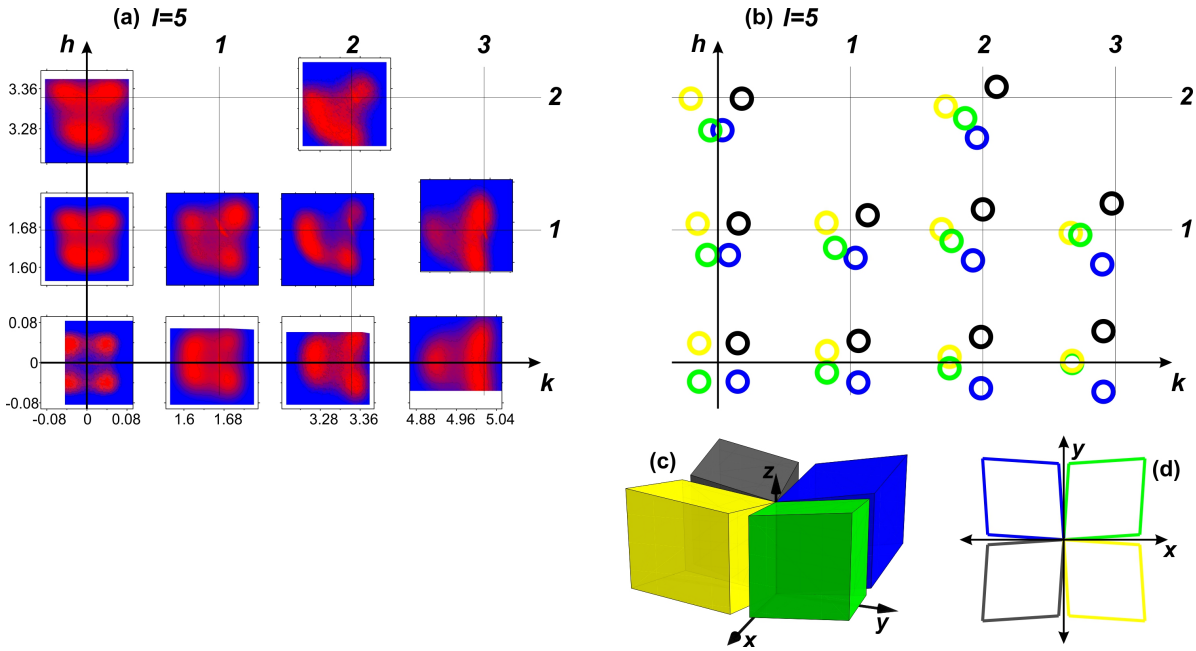


**Figure 4.13** (a) Layout of measured Bragg reflexes at  $q_z = 8.172\text{\AA}^{-1}$  ( $l = 5$ ) gridded to the  $(hk)$ -units of LSAO. (b) Color-coded Bragg spots calculated from the four equivalent distorted lattices shown in (c). (d) the in-plane projection of the PC  $a$  and  $b$  axes. Distortions are enhanced for clarity.

yielded the same extinction rules as the sublattice of LNO-LAO SLs. With wider peak splitting, the distortion is slightly more enhanced, yielding values  $\delta_x = 0.018$ ,  $\delta_z = 0.012$ , and  $\alpha = \beta = 89.31^\circ$ ,  $\gamma = 87.93^\circ$ , but it preserves the same symmetry and twin domain sizes. Fig. 4.14(c), a  $(q_y, q_z)$ -map around (015), shows it has an average in-plane lattice constant of  $3.84\text{\AA}$ , indicating a relaxed state throughout the entire film. In contrast, the LAO film, represented in Fig. 4.14(b):(005) and (a):(015), shows a single peak for all  $h, k, l$ -values. These data confirm the lattice constants to be strained to the LSAO substrate. Measurements of the half-order peaks yielded the rotation pattern  $a^-a^-c^-$  with space group  $C2/c$ . This comparison provides understanding of how the materials LNO and LAO naturally relax to the lattice mismatch of LSAO.

To support our X-ray diffraction data, we carried out TEM studies on the same samples. Fig. 4.15 compares high-resolution TEM images of SLs with thicknesses of  $T = 30$  nm (a) and  $T = 100$  nm (b-d), along with respective zoom-ins. The thin SL reveals a single structure, with epitaxial growth conditions preserved for all distinguishable (La, Ni, Al) atoms. These results are consistent with single Bragg spots strained to LSAO, inset (a). Thicker SLs exhibit a different scenario. In this case, an alternating array of homogeneous (LAO) and fuzzy (LNO) layers is evident, matching the periodicity of the SL (in this case each bilayer has 4 unit cells). However, diffraction patterns and  $Z$ -contrast TEM images (not shown) confirm that the epitaxy is preserved for both layers, LAO and LNO. We attribute the fuzziness of the LNO layers in the high-resolution, phase-contrast images to twin boundaries in LNO which lead to phase changes of the electron wave.

Before we turn to discuss scenarios explaining the observed SL data, we make a few remarks about the relaxation mechanisms that single-compound films are known to exhibit.

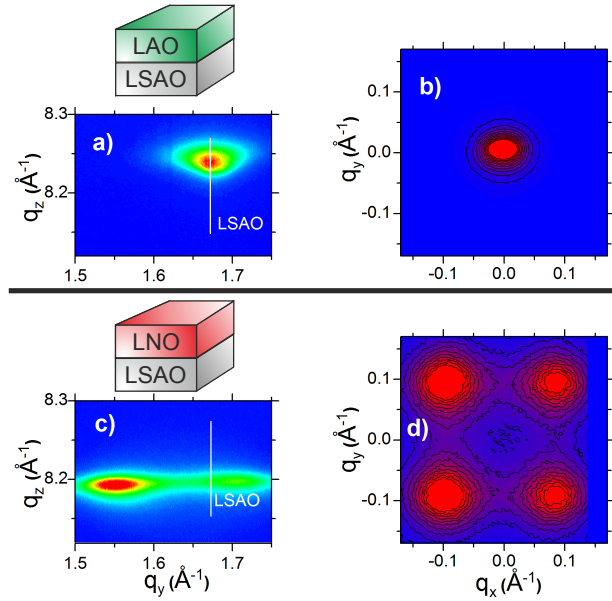


**Figure 4.14** RSMs around (a):(015) and (b):(005) for an LNO film compared to (c):(015) and (d):(005) for an LAO film, both with 100 nm thickness.

Ref. [119] reports examples of relaxation gradients in semiconductor heterostructures, which maintain a strained lattice close to the substrate interface and relax continuously as the thickness increases. In a different reported scenario, the entire semiconductor film undergoes a structural transition beyond a certain critical thickness. Films of  $\alpha$ -Sn, for example, exhibit a thickness and temperature dependent phase transformation from a metastable to a stable polymorph [120]. For oxides with more complex structures, similar instances of thickness-driven structural changes have been reported [121, 122]. In addition, perovskite cells tend to accommodate lattice mismatches with octahedral tilts, and their resulting low-symmetry structure is prone to minimize the strain energy by twinning, as was observed in manganite films [116].

The RSM of the thick SL (Fig. 4.12) exhibits a distinct set of reflections and is thus incompatible with the relaxation-gradient scenario. While we cannot fully exclude an inhomogeneous relaxation depth profile, the data renders it unlikely: The only conceivable scenario would be one with two distinct layers, a nearly strained one at the substrate, yielding the single peak at low  $q_z$ , and a fully relaxed one above, yielding the fourfold split peaks at higher  $q_z$ . This, however, is incompatible with the TEM results: First, the two sets of diffraction peaks are clearly split, implying a rather abrupt transition with high misfit dislocation density between the two layers, which we do not observe with TEM. Second, the TEM image indicates that the LNO layers are twinned throughout the entire sample, down to the substrate. Finally, if we were to identify the fourfold split set of peaks with both the LNO and LAO layers of the upper part of the film, both constituents would need to be twinned, which is not supported by TEM.

These observations substantiate the notion of a thickness-driven structural transition of LNO throughout the entire thickness of the SLs. It is immediately evident for our LNO film, Fig. 4.14(a,b), where no trace of a strained portion can be detected, and is the most likely scenario for the SLs. The comparison between Fig.'s 4.11 and 4.12 exposes that independent

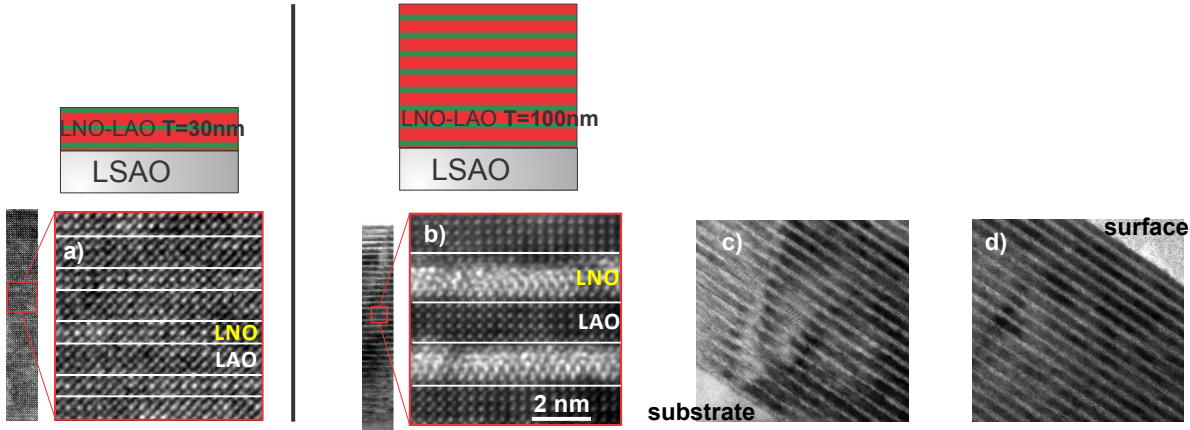


**Figure 4.15** A comparison of TEM micrographs between a LNO-LAO SL with  $T = 30$  nm (a) and one with  $T = 100$  nm (b-d).

of their bilayer periodicity, LNO-LAO SLs grown on LSAO develop from a single structure system into a system in which the LNO and LAO sublattices exhibit different crystallographic structures. This change takes place when growing beyond a total SL thickness of the order of  $\sim 50$  nm. A close look at Fig. 4.12 reveals that the sublattices are incommensurate both with respect to the substrate and to each other. The structural similarities of each sublattice to corresponding films of LNO and LAO along with our TEM data suggest a scenario in which the nanometer-scale LNO and LAO layers comprising the SL exhibit different structures across the entire SL: Each compound develops into its natural state, leaving LAO nearly strained while LNO alters into a twinned, distorted rhombohedral structure. The incommensurability of the two sublattices is manifest at every interface, in intriguing analogy to bulk structures built out of distinct units with different natural lattice parameters, like the Bi-based superconducting cuprates [123] or cobaltites [124]. These incommensurate crystal structures result in additional modulations (commensurate or not) that require a higher-dimensional space group formalism to be described [125]. In analogy to our case, it is the twin domain walls which serve to compensate the incommensurability. The resulting structure with alternating space groups may originate from the out-of-plane Coulomb interactions existing in oxide heterostructures, giving rise to so-called “Madelung strain” (see Ref. [126]). Despite the lattice and symmetry mismatch of the components, the layer connectivity is enhanced through the condition that the distorted rhombohedrons preserve vertical planes (and  $c$ -axes). The SL will thus switch between the two structural analogues, favored energetically by an alternating material. In conclusion, we have demonstrated SLs comprising LNO and LAO on compressive epitaxial strain exhibit a strong thickness dependent relaxation mechanism. As the SL grows beyond a certain critical thickness, it morphs into an alternating array of differing structural distortions. Such a strain relaxation mechanism proves how even under the violent, non-equilibrium conditions triggered by laser ablation growth techniques, oxide SLs can heal into self-organized arrays of constituents with differing properties.

Sample Name	Periodicity (N//N)×M	Total overlayer thickness (Å)	Substrate (lattice parameter Å)	In-plane lattice parameter
LNO-LAO-BE36	(2//2)×66	1000±30	LSAO (3.756)	3.80(2)
LNO-LAO-BE118	(2//2)×46	700±30	LSAO (3.756)	3.77(1)
NNO film	-	300±30	LSAO (3.756)	3.79(1)
LNO-LAO-BE48	(2//2)×66	1000±50	STO (3.905)	3.852(1)
LNO-LAO-BE125	(2//2)×46	700±30	LSAT (3.87)	3.860(2)
LNO-DSO-BE36	(2//2)×15	230±20	DSO (3.95)	3.951(2)
PNO film	-	400±30	LSAT (3.87)	3.840(5)

**Table 4.1** Summary of the properties of the samples used in this work.

### 4.3.2 Magnetic order in LNO

The promise of controlling spin-ordered ground states in TMO heterostructures is equalled by the challenge to probe the details of these magnetic states. Neutron and x-ray diffractometry have been colossal tools to examine these features, but have hitherto only monitored bulk or films with strong magnetic moments [127]. In recent years, new techniques like low-energy muon relaxation to study magnetism in thin films even with weak moments have been developed, but they are rarely available [113], not element specific, and provide limited information about the magnetic structure. While there exist methods to indirectly probe spin-related macroscopic properties, these usually pose more questions along the way.

Although avenues to drive metal to insulator transitions in systems with ultrathin slabs of LNO have been discussed, their magnetic ordered ground state has proven difficult to observe [109, 114], let alone manipulate. Understanding and tailoring the details of the LNO's magnetic structure, and perhaps therefore of its ground state, is paramount to the field. In this chapter, we will present resonant soft x-ray scattering (RSXS) experiments carried out at the Ni  $L_3$ -edge to reveal sought-out diffraction evidence of magnetic order in (001)-oriented, ultrathin LNO SLs. We will discuss the details of the SDW polarization and point out first steps towards controlling it.

#### Alignment and Q-dependence

The search for magnetic order in LNO based superlattices was guided originally by the magnetic order observed in NNO and the proximity to a FS at  $\mathbf{Q}_{SDW}$  suggested in previous references [99, 100]. The samples investigated in this work are listed and described in Table 4.1. The substrates used are LSAO,  $(\text{LaAlO}_3)_{0.3}(\text{Sr}_2\text{AlTaO}_6)_{0.7}$  (LSAT), STO, and  $\text{DyScO}_3$  (DSO), whose in-plane lattice constants are listed in Table 4.1 as well. Against the natural lattice constants of NNO (3.807 Å), PNO (3.815 Å) and LNO (3.837 Å) [82], these substrates then apply different amounts of tensile and compressive strain. Growing a fully strained heterostructure on large amounts of epitaxial strain is difficult, as discussed in the previous section. Thus, the actual lattice constants should be measured using the technique of RSM, described above and on page 35. The obtained lattice constants are listed in Table 4.1, which still confirms different degrees of strain. Finally, reference films of NNO and PNO were measured for comparison, and their properties are also listed in Table 4.1.

In order to provide the right epitaxial strain geometry to manipulate the occupation of

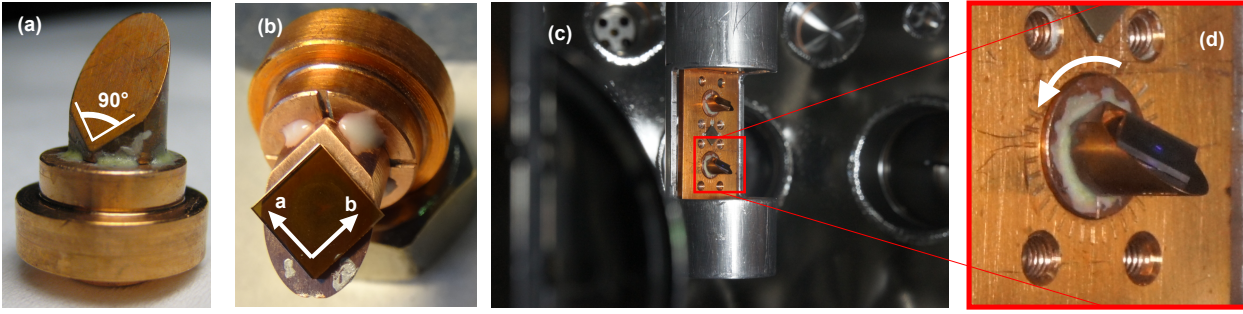


**Figure 4.16** (a) The wedges designed for the experiment of this section, with a marked right angle at the bottom of the wedge to guide the mounting of the samples (highlighted by white lines). These were glued to the conventional disc mounts of the diffractometer at UE46-PGM1 using silver paste and further supported by epoxy-like Torr Seal glue. (b) A sample was glued to the wedge using silver paste, with the diagonal facing up. (c-d) Finally, the sample was mounted on the diffractometer for measurements. The solid white line shows the azimuthal rotation, and the marks on the disc and diffractometer mount serve as guide for the quantitative rotation. The beam spot's fluorescence is seen on the sample, confirming the good alignment.

the  $e_g$  orbitals, all the substrates used in this investigation have surfaces along pseudocubic (001)-direction. (111)-oriented substrates, on the other hand, distort the lattice in oblique directions, possibly altering the  $e_g$ -splitting in a different way (and have shown intriguing magnetic properties as well [114]). However, the (001)-geometry incommodes the search for a magnetic Bragg reflection along the (111)-direction at  $\mathbf{Q}_{SDW}$ , given the limitation of the  $\chi$ -angle inside the RSXS chamber at UE46-PGM1, as discussed on page 37. Therefore, to access the (111)-direction, samples had to be mounted on wedges tilted  $55^\circ$  from the vertical mount of the chamber. Shown in Fig. 4.16, these wedges were designed to fit on the conventional sample holders of the UE46-PGM1 setup. Since the samples have edges along the crystallographic  $a$  and  $b$  axes, their alignment along the in-plane diagonal was guided by the lower edges of the wedge, which were cut at a  $90^\circ$  angle, as shown in Fig. 4.16(a-b). Later, the samples were mounted into the chamber, which allows 2 sample discs to be mounted simultaneously, shown in Fig. 4.16(c). The azimuthal rotation allowed in such setup is depicted in Fig. 4.16(d), which shows the marks carved on the sample holder and mount. The latter are  $10^\circ$  apart, yielding an error in the azimuthal angle of  $\sim 5^\circ$ . With (111) in the scattering plane, the axis of this rotation is  $\mathbf{Q}_{SDW}$ , as desired for the azimuthal dependencies which will be addressed later on.

A more detailed schematic of the scattering geometry using the pre-cut wedges is shown in Fig. 4.17, which is a scattering mode known in the field as “bisecting mode” or  $2\omega = 2\theta^\circ$ . In panel (a), which corresponds to our definition of  $\psi = 0^\circ$ , the crystal axes of the SL and their relative orientation in the experimental setup are shown in detail. The incoming and scattering angle are both the same,  $\sim 55^\circ$  (hence the name of the scattering mode), as shown by the green arrows. The sense of rotation around  $\mathbf{Q}_{SDW}$  we have defined as left handed. The two linear polarizations that define the ratio  $\frac{\pi}{\sigma}$  are also shown.

The strongest limitation imposed by this scattering geometry is shown in panels (b-c) of Fig. 4.17. When the azimuthal angles approach  $\pm 90^\circ$ , the take-off and incoming angles falls right below the horizon of the sample surface. Therefore, as the azimuthal angles approach these values, the diffracted intensity is reduced usually below our detection limit. This situation is worsened at  $\psi = 90^\circ$ , as a normal incident beam penetrates deeper into

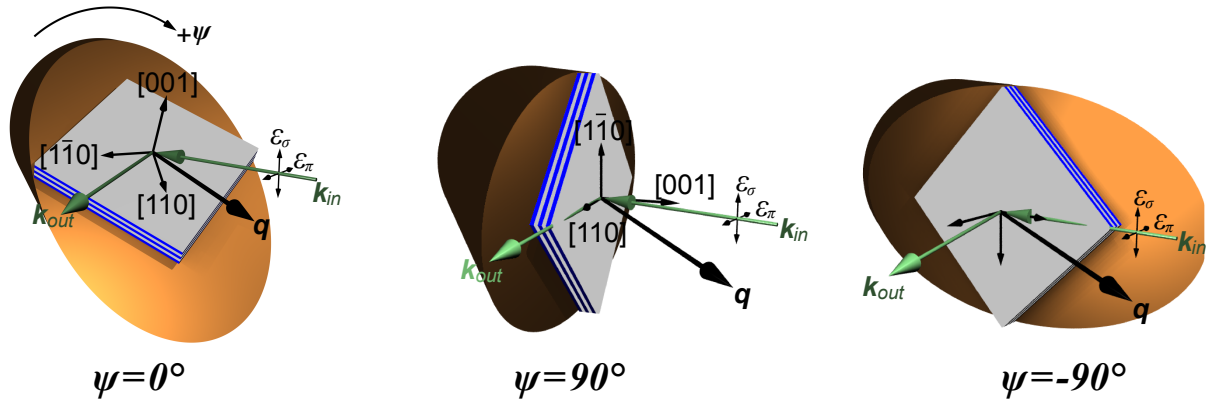


**Figure 4.17** A schematic of the wedge alignment indicating the incoming light beams and their polarization vectors, the direction of  $\mathbf{Q}_{SDW}$ , the crystal axes, and the azimuthal rotation, for the three labeled values of  $\psi$ .

the sample, making the grazing scattered beam travel through more material and suffer from absorption effects which dramatically reduce the overall intensity. In conclusion, the azimuthal angles  $40 < \psi < 130^\circ$  are impossible to measure.

Perhaps the most important result of this investigation is illustrated in Fig. 4.18. Panel (a) shows representative scans around  $\mathbf{Q}_{SDW}$  for LNO-LAO SLs which contain 2, 3 and 4 u.c. per slab. While the latter two cases show no Bragg peak, consistent with paramagnetic system, the sample with 2 u.c. shows a clear peak at  $\mathbf{Q}_{SDW}$ . This undoubtedly confirms the presence of long range, AFM order in LNO for the first time, at a position predicted by theory [99, 100]. We note here how remarkably sensitive the technique of RSXS is, making slabs of 2 u.c. scatter enough intensity to be detected.

To rule out the possible influence of strain on the newly discovered AFM ground state of LNO, we investigated (2//2) samples grown on different substrates. While the precondition of confining LNO to 2 u.c. still holds true for all substrates, the magnetic peak at  $\mathbf{Q}_{SDW}$  is observed in all cases. The overall intensities of all cases are comparable, albeit with different widths possibly pertaining to different structural details of the SL. We note that  $\sim 15$  repetitions  $M$  suffice to generate a detectable intensity, as was the case for the LNO-DSO sample. The absolute intensity of the peak, in the units of the detecting system of the UE46-PGM1 setup, was  $\sim 2$  pA.

The problem of scattering at  $\mathbf{Q}_{SDW}$  when mounted on the  $55^\circ$  wedge described above can be partially circumvented by using an alternate scattering geometry. In the so-called “asymmetric mode”, the incoming and take-off angle are not equal  $2\omega \neq 2\theta^\circ$ . The sample in this mode is not mounted on the wedge, but instead flat on the disc. Still, the in-plane diagonal is placed into the scattering plane, as shown in Fig. 4.19(a). Similar to the cases described in section 3.3.5, this allows certain ranges in RS to be scanned, but is strongly limited by the sample horizon. For this system’s lattice constants at the Ni  $L_3$  edge, the peak at  $\mathbf{Q}_{SDW}$  falls below the horizon, as shown by a red spot in Fig. 4.19(b). However, there is still a region of RS with slightly higher  $l$ -values which can be measured. The result of this RSM is shown in Fig. 4.19(c), which confirms a rod along the out-of-plane direction. Such an elongated peak is consistent with a truncation rod, as described on page 37, and/or the quasi 2-dimensional nature of the ultrathin slabs of LNO. The latter case would yield period-2 oscillations (2 u.c. layers) which can unfortunately not be verified in the limited

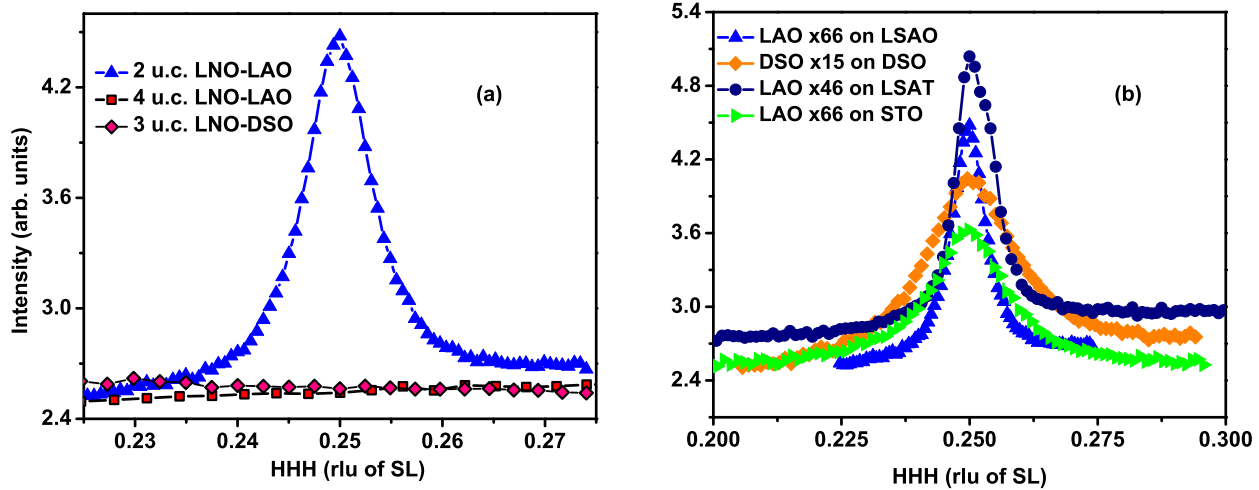


**Figure 4.18** (a) Scans around  $\mathbf{Q}_{SDW}=(\frac{1}{4}, \frac{1}{4}, \frac{1}{4})$  for SLs with  $N = 2$  consecutive LNO unit cells show a magnetic Bragg reflection, while those with  $N = 3, 4$  do not. (b) Scans for different  $(2/2) \times N$  SLs with compositions and substrates as shown in the legend consistently show a peak at  $\mathbf{Q}_{SDW}$ .

scanning range available.

In a relevant note, we point out here that the tail measured at  $(\frac{1}{4}, \frac{1}{4}, l)$  corresponds to the azimuthal angle  $\psi = 90^\circ$ , while the region around  $(-\frac{1}{4}, -\frac{1}{4}, l)$  corresponds to  $\psi = -90 = 270^\circ$ . Estimating the  $\frac{\pi}{\sigma}$ -ratio around these points will be crucial later on to help discern between magnetic structures.

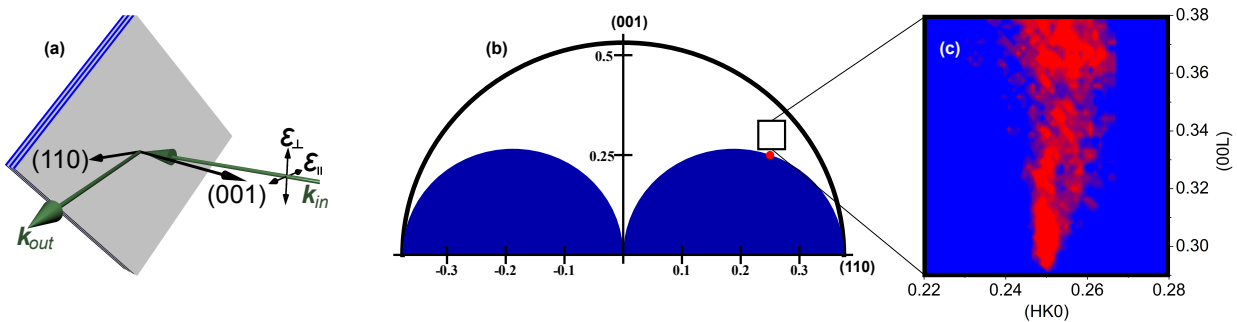


**Figure 4.19** (a) The alternative geometry used to access the vicinity of  $\mathbf{Q}_{SDW}$  without the wedge. (b) In RS, the latter geometry translates into areas blocked by the sample horizon, with the peak at  $\mathbf{Q}_{SDW}$  already at critical angles (red dot). However, slightly above it there is a small portion accessible for scanning, shown as a black square. (c) The results of scans of the LNO-LAO SL on LSAO in the area labeled previously, showing a rod-like shape.

## Energy and temperature dependencies

The origin of the peak at  $\mathbf{Q}_{SDW}$  observed in LNO-based SLs with 2 u.c. slabs is experimentally investigated by observing the temperature and energy dependence. To carry out the experiments, the sample height was scanned at every temperature to certify that despite the thermal contraction of the cryostat upon warming and cooling, the same position of the sample was scanned. This is particularly crucial when scattering off a wedge since movements of

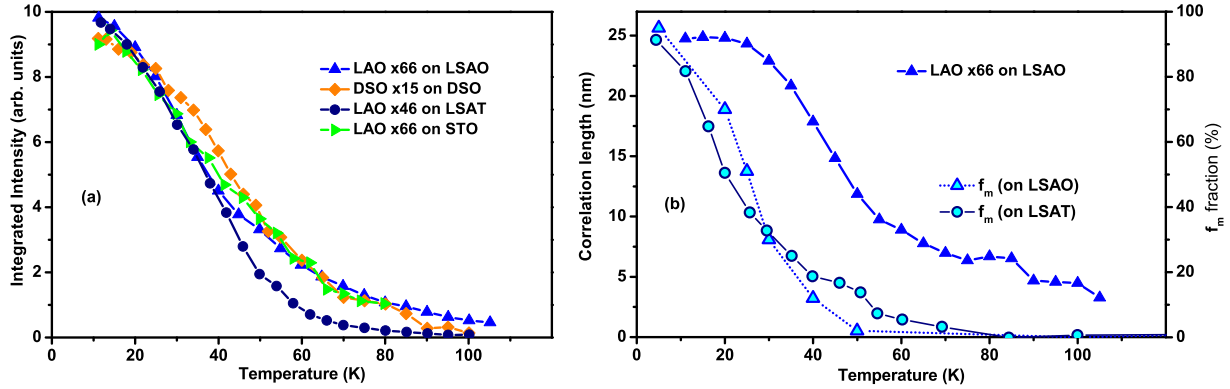


**Figure 4.20** (a) The temperature dependence of the peak’s integrated intensity at  $\mathbf{Q}_{SDW}$  of all the SLs investigated here, as labeled in the legend. (b) The correlation length extracted from the widths of the peak as function of temperature. For comparison, the temperature dependence of the magnetic volume fraction  $f_m$  as measured by slow  $\mu$ SR (SL on LSAO is taken from Ref. [109]).

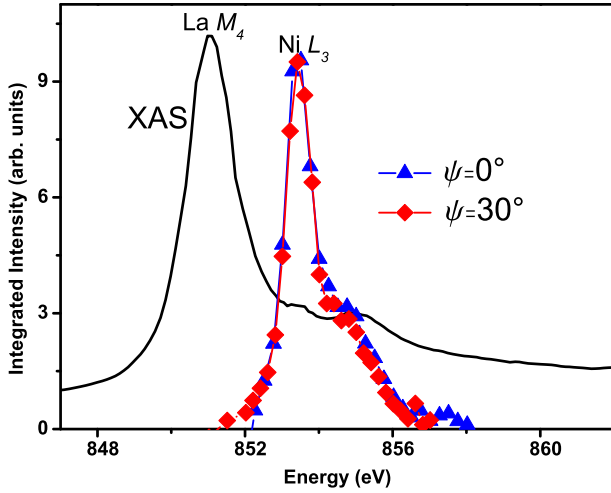
the sample height result in strong misalignment. Fig. 4.20(a) shows the dependence of the peak upon sample temperature for all the SLs investigated in this work. The data indicate magnetic phase transitions with Néel temperatures in the range  $T_N = 50 - 100$  K for all samples. The sharp onset is smeared out by a somewhat rounded temperature dependence, as commonly observed in quasi-2-dimensional antiferromagnets as a consequence of critical scattering [128].

Fig. 4.20(b) shows the temperature dependence of the peak width for a representative LNO-LAO SL on LSAO. The widths of the Bragg reflections saturate at low temperatures corresponding to a magnetic domain size of  $\sim 25 \pm 5$  nm<sup>3</sup>, identical (within the error) to the structural domain size inferred from non-resonant x-ray diffraction using RSM. Along with muon spin rotation measurements on the same sample [109] as well as on LSAT (shown as well in Fig. 4.20(b)), this indicates that the magnetically ordered state comprises the entire sample volume.

The latter data suggests that the origin of the peak at  $\mathbf{Q}_{SDW}$  is magnetic, at least partially. To discern whether the peak originates from an additional scattering entity like orbital ordering, we have carried out measurements to quantify the peak’s dependence on incoming photon energy. These measurement involve scanning rocking curves at each photon energy to subtract out the fluorescent background. The results are shown in Fig. 4.21. First of all, the XAS spectrum measured as TEY is shown for comparison, which is usually dominated by the neighboring  $M_4$ -line of Lanthanum, as was shown already in Fig. 4.7. The magnetic Bragg reflex, however, only resonates at the Ni L-edge. Thus, the magnetic order originates only from the Ni-ions.

The latter energy profiles of the peak at  $\mathbf{Q}_{SDW}$  were taken at different azimuthal positions, yielding identical lineshapes. A close look at Eq. 3.13 indicates that if the peak had several intrinsic origins, for example magnetic ( $\sigma_{mag}$ ) and orbital ( $\sigma_{orb}$ ), living at  $\mathbf{Q}_{SDW}$ , then the two scattering tensors which presumably have different symmetries would produce different lineshapes at different azimuthal angles. The fact that all azimuthal angles yield identical lineshapes indicates that only one ordered state, i.e. one  $\sigma_{mag}$ , lives at  $\mathbf{Q}_{SDW}$ , ruling out

<sup>3</sup>From the expression  $Corr. Length = \frac{a(nm)}{\pi \times FWHM}$



**Figure 4.21** The energy dependence of the scattered intensity at  $\mathbf{Q}_{SDW}$ , taken at two different azimuthal values. Superimposed is the XAS spectrum measured by the TEY.

any possible ordered state coexisting.

In the study of Ref. [94], the magnetic order at  $\mathbf{Q}_{SDW}$  was also found induced in the Nd ( $4f^3$ ) ions. By measuring the azimuthal dependence of the scattered intensity at the Nd  $M_4$ -edge, the authors found the same magnetic spiral in the Nd sublattice. In the case of LNO-LAO, this bears no influence because the La ions ( $5d^0$ ) are non-magnetic. The case of the LNO-DSO SL is different. DSO has a Dy $^{3+}$  ion in a  $4f^9$  configuration across the interface, with AFM order reported below 3.1 K [129]. Therefore, measurements were done to test whether there is a magnetic coupling across the interface between neighboring LNO and DSO layers. Scans at 10 K around  $\mathbf{Q}_{SDW}$  at the Dy  $M_5$ -edge are shown in Fig. 4.22, indicating magnetic order also in the Dy ions due to the presence of the AFM order of LNO. Further investigating the properties of this intriguing phenomenon remains part of the outlook of this thesis.

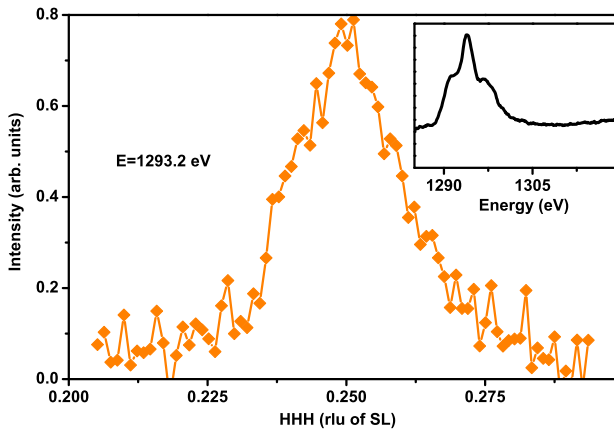


**Figure 4.22** Scattered intensity was also observed at the Dy  $M_5$ -edge at  $\mathbf{Q}_{SDW}$ . The inset shows the XAS spectrum as measured by fluorescence, to identify the edge position.

### Azimuthal dependence

Once the peak has been identified as a novel AFM ground state of LNO, the next step is to carry out measurements in search of the details of how the spins are oriented. The measurements were carried out by scanning rocking curves for both light polarizations at

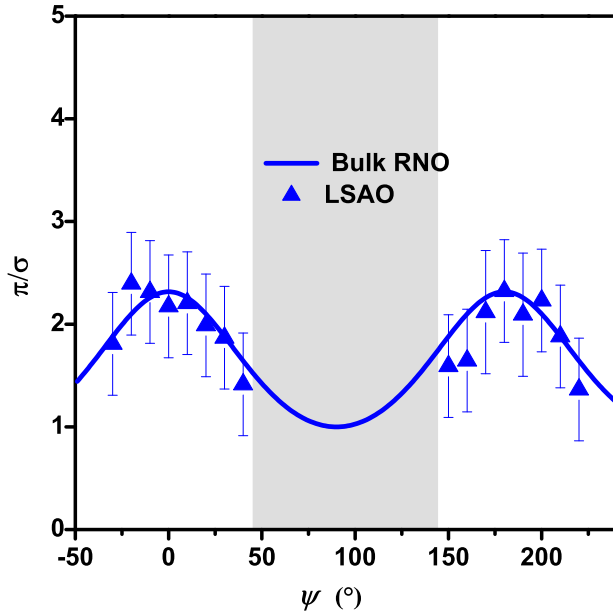


**Figure 4.23** The azimuthal dependence of the  $\frac{\pi}{\sigma}$ -ratio for a (2//2) LNO SL grown on LSAO which applies compressive strain to the LNO lattice, along with the magnetic spiral model of Ref. [94] (solid blue line).

all accessible azimuthal angles. The scans were later analyzed by subtracting a polynomial to the background shown in Fig. 4.18, and the peak intensity was quantified by its integral. The lack of a structural reflex for signal normalization is enhanced when scattering off a tilted wedge. Rotating the azimuth results in inequivalent projections to the sample surface (see Fig. 4.17). Therefore, we focus on the  $\frac{\pi}{\sigma}$ -ratio of the peak intensity.

The first result is shown in Fig. 4.23 which plots the  $\frac{\pi}{\sigma}$ -ratio obtained for a LNO-LAO SL grown on compressive strain (LSAO), along with the model identified in Ref.'s [93, 94]. Despite the areas where measurements cannot be done marked by a gray area, the information is sufficient to yield an acceptable agreement with the model. Note that the error bars arise from the peak analysis which suffers from systematic errors ranging from the background subtraction to the fitting procedure, and does not correspond to the statistical error of a standard counting experiment.

A very different situation was observed for all other LNO-based SLs. Recalling Table 4.1, these samples were grown with different amounts of tensile strain, taken from their measured lattice parameters. Fig. 4.24 displays the azimuthal dependence of all these samples, compared to the model found previously. The data for all samples on tensile strain deviates substantially from the previous model, especially when approaching  $\psi = 90^\circ$ , where the  $\frac{\pi}{\sigma}$ -ratio grows to values between 4 and 5. We note that remarkably, within the error bars, all samples show the same azimuthal dependence despite the differing lattice constants.

### 4.3.3 Magnetic structure of RNO films

To shed more light on the surprising behavior observed in the azimuthal dependence of the LNO-based SLs under tensile strain, we will turn to investigate films of RNO materials whose magnetic order exists already in the bulk. For this reason, films of PNO and NNO were grown on LSAT and LSAO, respectively. They serve reference points for the corresponding strain cases of the LNO study previously described.

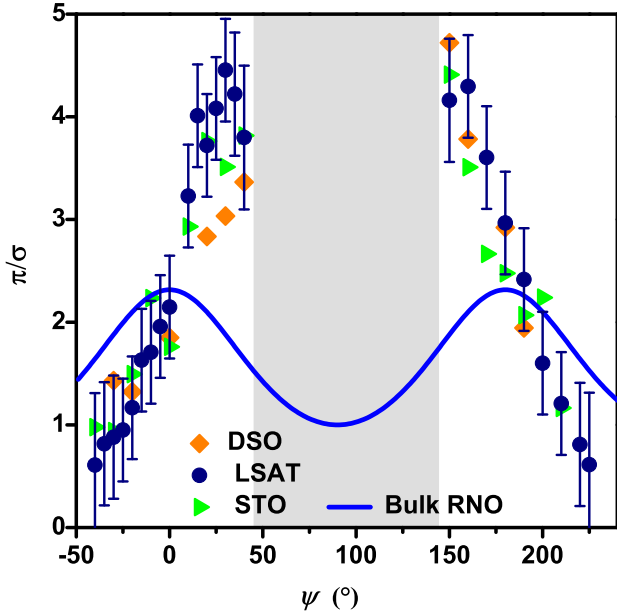


**Figure 4.24** The azimuthal dependence of the  $\frac{\pi}{\sigma}$ -ratio for LNO SLs with 2 u.c. of LNO, grown on the labeled substrates which apply varying amounts of tensile strain to the LNO lattice. Also shown is the magnetic spiral model of Ref. [94] (solid blue line).

In what comes as no surprise, first we set to reproduce the magnetic ordered state observed in bulk NNO and RNO. Fig. 4.25 confirms the peak observed in these systems, resulting in 2-3 orders of magnitude more intensity than the ones observed in LNO. Later we will attempt to discuss the reduction of intensity in the LNO system. Fig. 4.25(a) shows the onset of such magnetic order for both systems. While the PNO film shows an onset temperature in agreement with the bulk data [80], the NNO film on LSAT shows a reduced transition. Similar reports of NNO on compressive strain show that strain yields a fully metallic/paramagnetic state [80, 130, 131]. In this case, the partially relaxed lattice of NNO (as shown in Table 4.1) yields a AFM with an onset temperature reduced to  $\sim 100$  K, well below its reported bulk value of  $\sim 190$  K [93]. The energy dependence of the peak is also shown for the representative PNO film on LSAT in Fig. 4.25(b).

The first of the two azimuthal dependencies to compare with the LNO system is shown in Fig. 4.26(a), which is the case of PNO on tensile strain. It shows azimuthal dependence in agreement with LNO under different amounts of tensile strain. This result implies the observed trend in distorting the magnetic structure such as to yield a noticeably different magnetic structure does not pertain exclusively to the novel case of AFM in LNO. Instead, it seems to affect PNO in similar fashion when applying tensile strain.

With the former suggestion of epitaxial strain affecting already the bulk RNO system, we turn to investigate a NNO film under a slight amount of compressive strain. The result of such measurement is shown in Fig. 4.26(b), which yields yet another remarkably different azimuthal dependence. Instead of symmetrically turning upwards around  $\psi = 90^\circ$ , the  $\frac{\pi}{\sigma}$ -ratio reverses by turning upwards away  $\psi = 90^\circ$  and hovers around 1 around that point. Finally, we note here that the more intense peaks allows a reliable estimate of the point corresponding to  $\psi = 90^\circ$ , which we have carried out using the  $\omega \neq 0^\circ$  scattering geometry, described earlier. The data points are included in these plots already along with their error bars, and will be addressed in more detail in the following section.

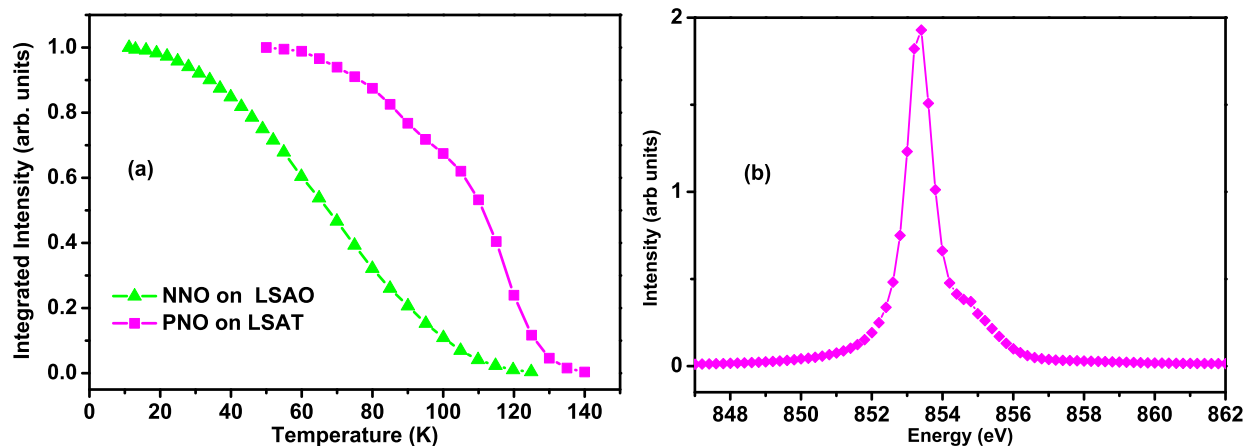


**Figure 4.25** (a) The temperature dependence of the peak's integrated intensity at  $Q_{SDW}$  of all the RNO films investigated here, as labeled in the legend. (b) A representative energy dependence of the PNO film on LSAT.

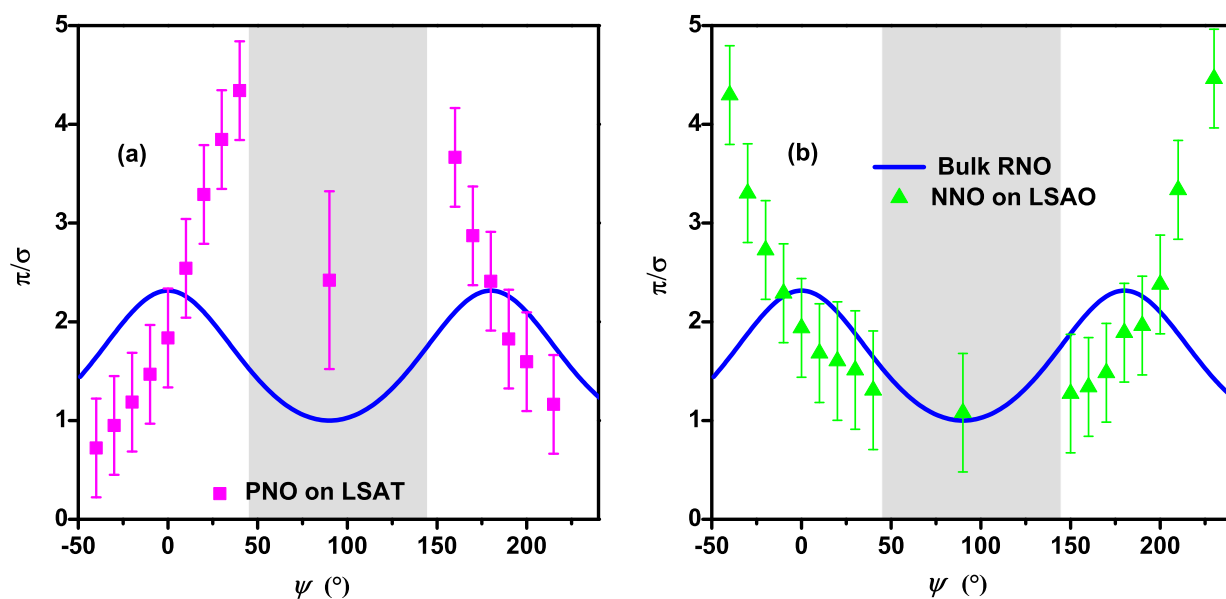


**Figure 4.26** (a) The azimuthal dependence of the  $\frac{\pi}{\sigma}$ -ratio for a PNO film grown on LSAT. (b) The azimuthal dependence of the  $\frac{\pi}{\sigma}$ -ratio for a NNO film grown on LSAO, In both cases, the solid blue line corresponds to the magnetic spiral model of Ref. [94].

### 4.3.4 Models: collinear vs. noncollinear spins

The different azimuthal dependencies observed for different RNO systems so far calls for a magnetic structure model beyond the one found for bulk NNO and for LNO SL on LSAO. In this section, we will go through the different magnetic models that are physically significant and show which one best fits the data for each case. To analyze the data, we used the following procedure in order to set up the formalism of Eq. 3.30. First, we build a magnetic cell containing 4 spins from the periodicity of  $\mathbf{Q}_{SDW}$ . This yields a system with different  $F^{mag}$ 's with the general form of Eq. 3.34, namely

$$F_i^{mag} = \begin{pmatrix} 0 & (-m_z)_i & (m_y)_i \\ (m_z)_i & 0 & (-m_x)_i \\ (-m_y)_i & (m_x)_i & 0 \end{pmatrix} \quad (4.3)$$

where  $i$  runs from 1 to 4. After, we setup Eq. 3.30 considering the phase 4 positions in the phase shift of  $\mathbf{Q}_{SDW}$  ( $0, \pi/2, -\pi, 3\pi/2$ ), Eq. 3.31 is taken using  $(1, 1, 1) = \hat{q}$ ,  $(1, \bar{1}, 0) = \hat{q}_\perp$  and the angle  $\theta = 35^\circ$  (notice Eq. 3.30 is based on  $\theta$  with respect to  $\hat{q}$ , i.e.  $(90 - 55)^\circ$ ). With those definitions, we can now calculate the  $\frac{\pi}{\sigma}$ -ratio as explained on page 32. We have left the directions of the spins  $(m_{x,y,z})_i$  as the adjustable parameter, applying the constraint:  $\vec{S}_1 = -\vec{S}_3$  and  $\vec{S}_2 = -\vec{S}_4$ , which defines AFM order with  $(\frac{1}{4}, \frac{1}{4}, \frac{1}{4})$  periodicity. The Mathematica<sup>®</sup> script used to model the data is given in Appendix D.

Fig. 4.27 shows the results of this analysis for the case of samples on tensile strain, which require only one solution as all systems display the same behavior within our error. Four magnetic structures are displayed alongside their corresponding azimuthal dependence of the  $\frac{\pi}{\sigma}$ -ratio. Panel (a) shows a system with both spin sublattices symmetrically tilted from the  $c$ -axis by  $28 \pm 2^\circ$ , coplanar with the blue arrows of the bulk model. A spiral with out-of-plane moments  $\sim 2$  times larger than  $[110]$  moments is shown in panel (b). This model yields an azimuthal dependence identical to the one of panel (a), but it would imply a charge disproportionation which will be addressed later on. Finally, collinear models are shown in panels (c-d). The first of these, in cyan color, represents spins along  $(\bar{1}\bar{1}2)$  (perpendicular to  $(111)$ ) whose calculated  $\frac{\pi}{\sigma}$ -ratio clearly deviates from the data. This also holds for all 3 directions perpendicular to  $(111)$  (not shown). Models with moments directed close to the  $c$ -axis yield reasonable agreement with the data in the ranges  $-40^\circ < \psi < 40^\circ$  and  $150^\circ < \psi < 230^\circ$ . However, the data point at  $\psi = 90^\circ$  obtained as described above clearly rules out this model, as shown in Fig. 4.27(d) for moments tilted  $\sim 13^\circ$  away from the  $c$ -axis. In the case of moments directed straight along  $c$ , the  $\sigma$  channel reaches 0 at  $\psi = 90^\circ$ , making the  $\frac{\pi}{\sigma}$ -ratio diverge.

The same analysis was carried out for the NNO film on compressive strain. Adjusting spin orientations, the solid green line is the solution which best describes the data. Fig. 4.28(a) illustrates the corresponding magnetic structure with solid green arrows. In this case, the first spin sublattice lies along the  $(110)$  diagonal while the second sublattice is perpendicular to  $(110)$ . Similarly, we outline a possible description of the azimuthal dependence of the NNO film under compressive strain in terms of a collinear ordering pattern. Fig. 4.28(b) shows such a solution, which has moments parallel to  $(110)$  (magenta color). Although the solution reproduces the increase of  $\pi/\sigma$  as  $\psi \rightarrow -90^\circ$  and  $\psi \rightarrow 270^\circ$ , the data point at  $\psi = 90^\circ$  again allows us to rule out this collinear state.

The collinear states discussed above were difficult to rule out without estimating the

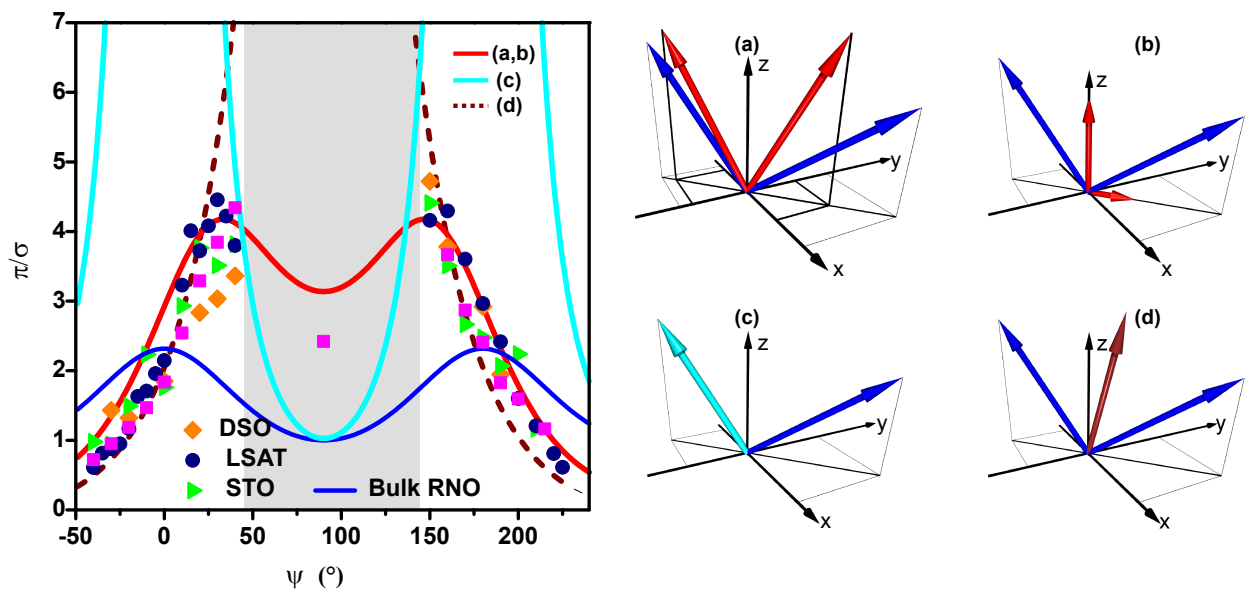


**Figure 4.27** The azimuthal dependence of different models considered for the case of samples on tensile strain, color coded to the arrows as follows: (a) a system with both spin sublattices symmetrically tilted from the  $c$ -axis by  $28 \pm 2^\circ$ , coplanar with the blue arrows. (b) A system with spins along the (001) and (110) with the former twice in magnitude as the latter. (c) A collinear system with spins along the  $(\bar{1}, \bar{1}, 2)$ -direction, perpendicular to  $\mathbf{Q}_{SDW}$ . (d) A collinear spin with spins pointing  $\sim 13^\circ$  away from the  $c$ -axis.

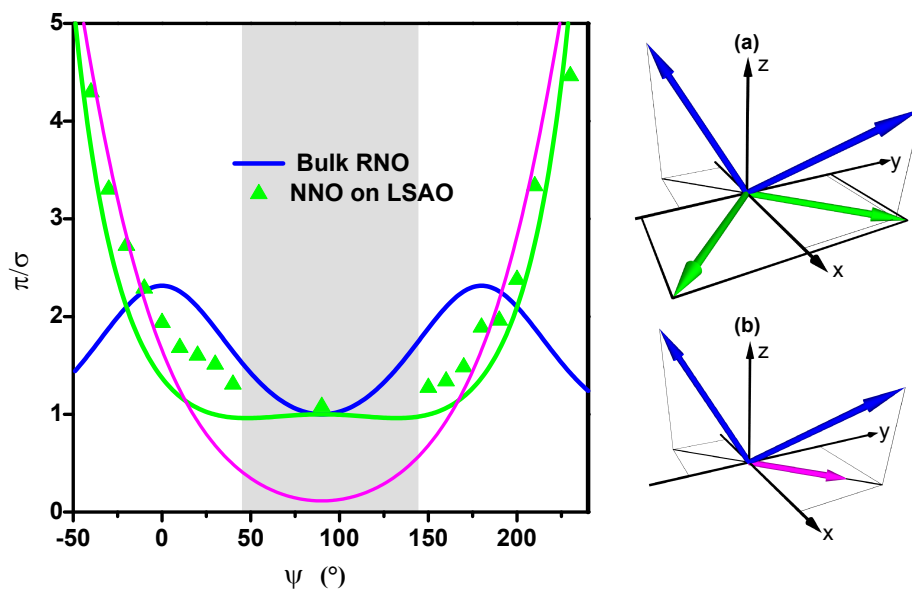


**Figure 4.28** The azimuthal dependence of different models considered for the case of NNO on LSAO, color coded to the arrows as follows: (a) a system with perpendicular spin sublattices in the  $a, b$ -plane. (b) A collinear system with spins along the (1, 1, 0)-directions.

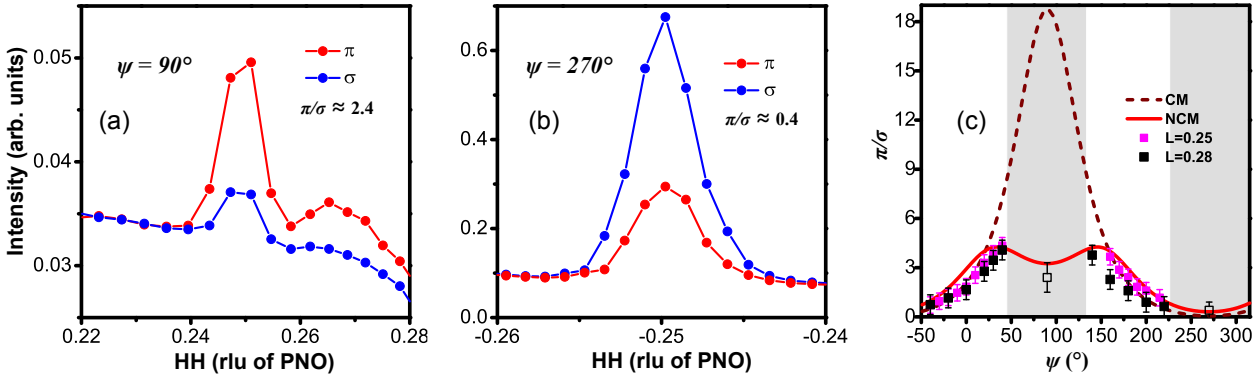


**Figure 4.29** *Tensile strain.* (a-b) The scans obtained using the non-tilted geometry at  $\psi = 90^\circ$  and  $270^\circ$ . (c) A comparison of the azimuthal scans obtained using wedges with differing tilt angles, which yield the shown  $l$ -values. The data points in open squares are measured in the non-tilted geometry.

point at  $\psi = 90^\circ$ . Therefore, we turn to discuss details of the acquisition of this data point. As explained previously, this data point was obtained using the  $\omega \neq 0^\circ$  geometry and thus not measured at  $\mathbf{Q}_{SDW}$ , but at a higher  $l$ -value, namely  $(\frac{1}{4}, \frac{1}{4}, 0.28)$  ( $\psi = 90^\circ$ ) and  $(-\frac{1}{4}, -\frac{1}{4}, 0.28)$  ( $\psi = 270^\circ$ ). By varying the incoming light polarization, we can estimate the  $\frac{\pi}{\sigma}$ -ratio. The actual data is shown in Fig. 4.29(a-b) for the case of tensile strain, and Fig. 4.30(a-b) for the case of NNO on compressive strain.

Technically speaking, the azimuthal dependence at  $\mathbf{Q}_{SDW}$  must not be identical to the one measured at  $(\frac{1}{4}, \frac{1}{4}, 0.28)$ . To validate the estimated value of the ratio measured at a slightly different  $\mathbf{q}$ -value, we carried out the experiment using wedges of different angles measuring the azimuthal dependence at overlapping angular regions. The resulting data for tensile strain are shown in Fig. 4.29(c), and for compressive strain in Fig. 4.30(c). The two data sets are equivalent within the experimental accuracy. This suggests a non-collinear magnetic structure rather than a collinear one for heterostructures on tensile strain as well as for the NNO sample on compressive strain.

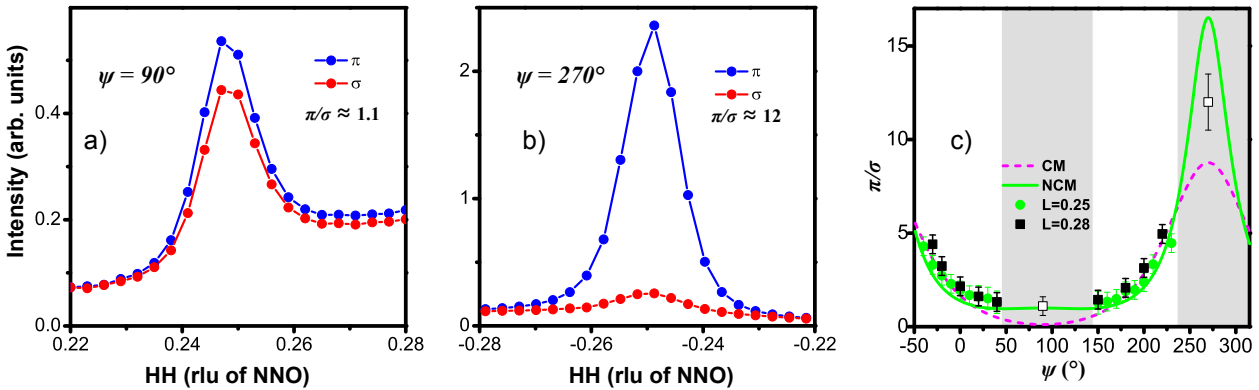


**Figure 4.30** *Compressive strain.* (a-b) The scans obtained using the non-tilted geometry at  $\psi = 90^\circ$  and  $270^\circ$ . (c) A comparison of the azimuthal scans obtained using wedges with differing tilt angles, which yield the shown  $l$ -values. The data points in open squares are measured in the non-tilted geometry.

A final test to verify the point extracted at these two critical angles  $\psi = 90, 270^\circ$  was done

by fixing  $(-\frac{1}{4}, -\frac{1}{4}, 0.28)$  and scanning the polarization of the light. This feature is unique to modern undulators, as discussed on page 18. A schematic of such a measurement is shown in Fig. 4.31, viewing the wedge and sample from the  $\vec{k}_{in}$  perspective. In this case, instead of rocking the sample or detector, the setup is fixed while the incoming light's polarization is moved from  $\pi$  to  $\sigma$ , whose angle we call  $\phi$ . Note that the extreme values of  $\phi$  correspond to the original  $\pi$  and  $\sigma$  channels.

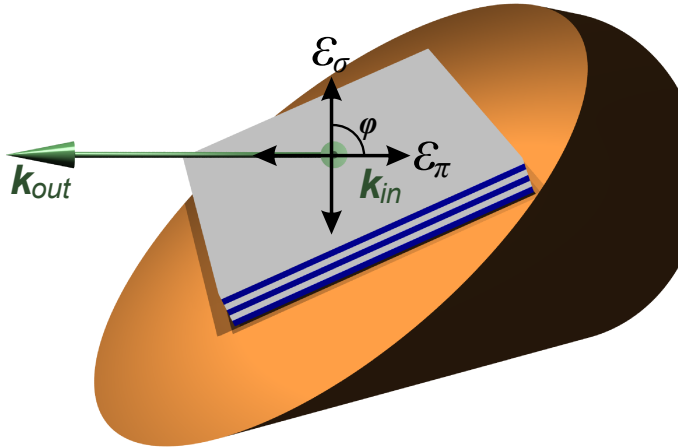


**Figure 4.31** The definition of the light rotation scans, as viewed from the direction of the incoming light. The diffraction condition remains fixed, while the incoming light polarization is rotated from  $\pi$  to  $\sigma$ , with a rotation angle we call  $\phi$ . Data points follow Fig. 4.26 and solid lines show the calculated behavior.

The results of such scans are shown in Fig. 4.32, for both tensile and compressive strain, along with model calculations of the polarization rotation scans using the noncollinear models that were obtained in the previous sections. Once again, the agreement between the data and the model calculations is acceptable, yielding solid proof in favor of the noncollinear models proposed before.

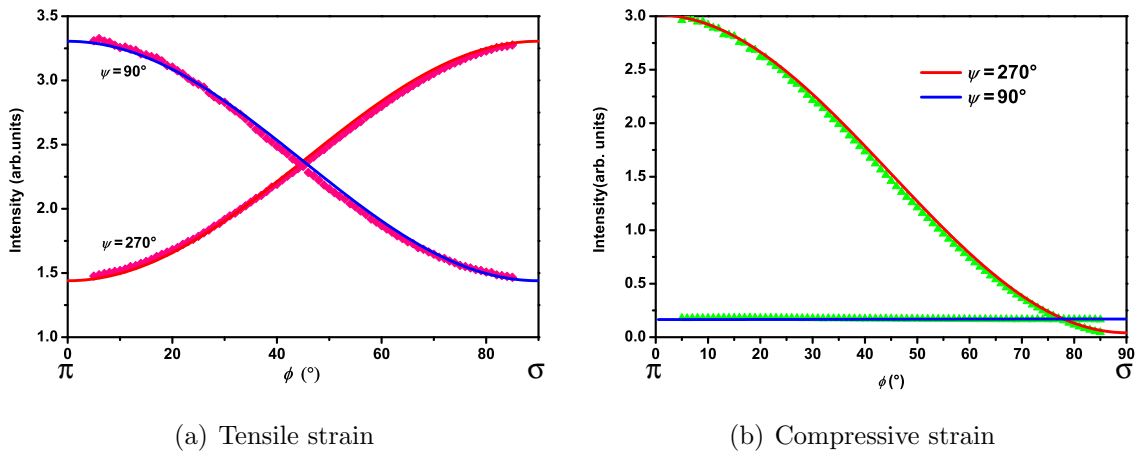


**Figure 4.32** Light rotation scans performed for the case of (a) tensile strain, (b) compressive strained NNO, along with the calculated intensities using the noncollinear models discussed in the previous section.

## 4.4 Discussion and conclusions

Finally, we turn to discuss the main conclusions and potential outlook around the results pertaining to the discovery a magnetic ground state in LNO-based SLs. The discovery itself of AFM order with a period 4 unit cell, analogous to the bulk magnetic order in other members of the RNO family is perhaps the most resounding result of this investigation. Although much effort had been invested in exploring the changes in the transport properties of LNO upon confinement in a SL geometry, the magnetic properties had remained relatively overlooked. In this thesis, following up on the work we did in Ref. [109], the first diffraction evidence of an AFM order in otherwise paramagnetic LNO was reported. As astonishing as it appears, we were able to use the powerful technique of RSXS to identify magnetic order in slabs of LNO with only 2 u.c., as depicted in Fig. 4.33, which summarizes the main findings of this investigation. The study lead in addition to identify a new state in the spin spiral that forms in these systems, whose mechanism we now attempt to explain.

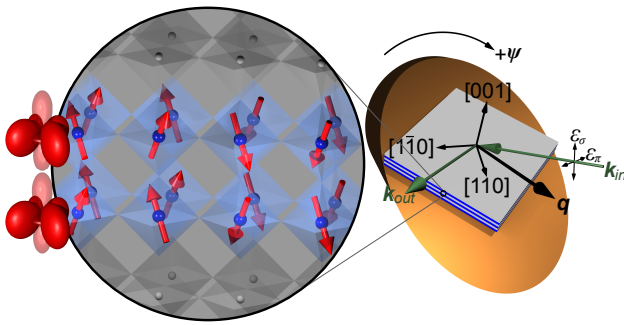


**Figure 4.33** The main conclusions of this investigation, where magnetic order was found in SLs containing 2 u.c. layers of LNO, a material otherwise paramagnetic.

### 4.4.1 Orbital polarization altering the magnetic structure

The pattern observed of different SDW polarizations, both in and out of the  $a, b$ -plane, must be understood by accounting for known effects that epitaxial growth has on these systems. The first candidate is the crystal lattice. Structurally, in-plane strain is known to affect oxygen octahedra rotations in inequivalent ways for tensile and compressive strain [8, 117, 118]. We have carried out our own extensive structural characterization which reveals similar Glazer rotation patterns for all samples under tensile strain, with subtle differences in the magnitudes of the rotations [8, 11]. Within our sensitivity, these samples exhibit the same SDW polarization which could thus arise from such strain driven structural distortions. However, these fail to account for the systematics pertaining to compressive strain. In such case, similar Glazer rotation patterns are expected for both the strained NNO film and the LNO-LAO SL, while distinguishable magnetic structures are observed. Thus, a purely structural origin of the magnetic structure's response to strain can be ruled out.

Another property that strain is known to modify is the orbital occupation of the  $e_g$  levels. In the more itinerant bulk NNO, PNO and LNO, all  $3d^7$  systems in low spin state, a single electron occupies the degenerate  $e_g$  level. As discussed previously on page 50, STO's tensile strain and confinement of LNO in a SL geometry induces an average polarization of  $\sim 5\%$  favoring the  $d_{x^2-y^2}$  orbital [69]. Single films of LNO under compressive strain, where the  $c$ -axis expands at the expense of in-plane contraction, have slightly more occupation of  $d_{z^2-r^2}$  [70]. Equivalent behavior is observed for a compressed NNO film. However,

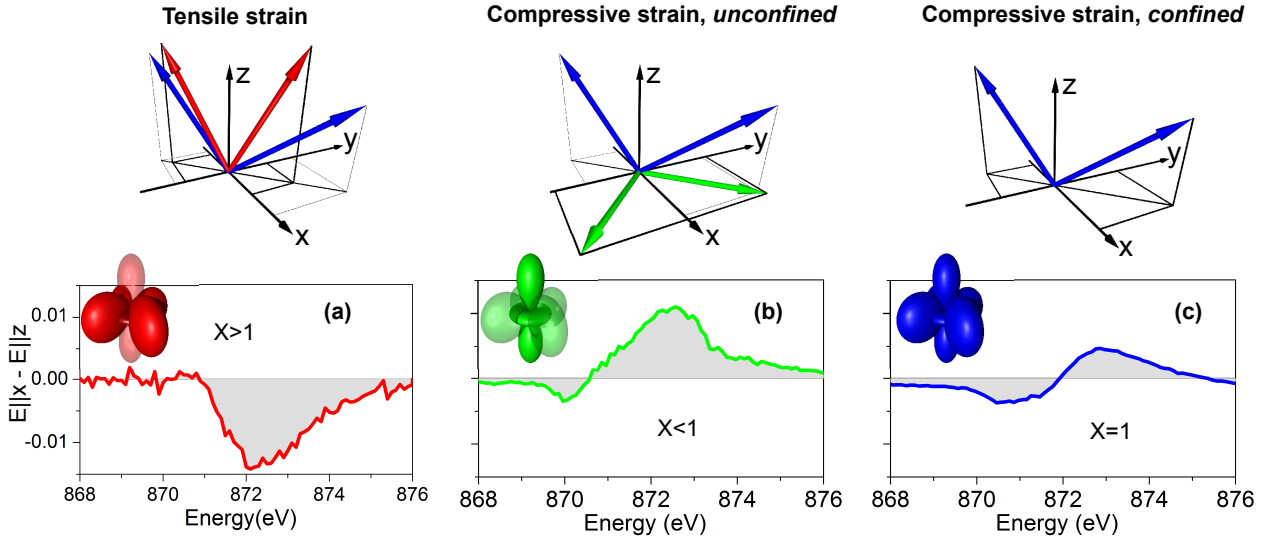


**Figure 4.34** Linear dichroism around the Ni  $L_2$ -edge from XAS signals with incoming light polarization in and out of plane for (a) LNO-DSO on DSO, (b) NNO on LSAO, (c) LNO-LAO on LSAO. The sum-rule derived  $e_g$  orbital occupations are given and schematized by color coded solid and semitransparent lobes.

heterostructured LNO under compressive strain is less straightforward to interpret. As we reported in Ref. [105] and discussed on page 50, the competition between the confinement and compressive strain will result in an orbitally degenerate system.

To test these ideas and their connection to the magnetic structure changes observed, we measured XAS with linearly polarized x-rays near the Ni  $L_2$ -edge to determine the occupation of the Ni  $d$ -orbitals. Fig. 4.34 displays the difference of the absorption spectra for photons polarized parallel and perpendicular to the heterostructure plane for three representative samples. The derivative-like lineshape of the spectra in panels (b-c) arises from an energy splitting between  $d$ -orbitals of  $3z^2 - r^2$  and  $x^2 - y^2$  symmetry due to the non-cubic crystal-field, as described in Fig. 4.8 and Ref. [105]. With the aid of the sum rule for linear dichroism, the energy-integral of the dichroic difference spectra can be converted into the ratio of hole occupation numbers, as shown in Eq. 4.2. The SLs and films grown under tensile strain show  $X > 1$ , corresponding to an enhanced electron occupation of the  $d_{x^2-y^2}$  orbital (red lobe in the case of tensile strain in Fig. 4.34). Lifting this degeneracy and occupying more  $d_{x^2-y^2}$  results in a finite  $d_{m_z}$  state with finite orbital moment along  $z$ . Therefore, the experimentally observed canting of the spin moments towards this direction is a natural consequence of the intra-atomic spin-orbit coupling. Conversely, the preferential  $d_{3z^2-r^2}$  occupation ( $X < 1$ ) found in the compressively strained NNO film (middle Fig. 4.34) accounts for the observed spin polarization in the  $x, y$ -plane. In the compressively strained LNO-LAO SL, our data show that the equal population of  $d_{x^2-y^2}$  and  $d_{3z^2-r^2}$  found in bulk nickelates is restored. In contrast to the long-range effect of epitaxial strain, the orbital polarization due to dimensional confinement is more effective at the interface with a blocking layer, thus affording an independent means of controlling the SDW polarization.

#### 4.4.2 Remanent conductance in the SDW state and the question of concomitant CO

Finally, we turn now to carefully examine the conductivity of the LNO SLs in the AFM state and discuss the possible suppression of CO justifying the usage of the term SDW. The main observation of this context is summarized in Fig. 4.35, which compares the onset of the magnetic Bragg peak detected by RSXS to a representative resistance curve of a LNO-LAO SL on LSAO. Two important trends are observed: First, the change of slope of the resistance occurs at around the same temperature as the onset of the AFM state, suggesting that the two are connected. Second, the absolute values of the resistance at the lowest temperatures are still quite low, defying the term “insulator”. This is consistent with a SDW that leaves some segments of the Fermi surface ungapped [99, 100], and with experimental results on other SDW systems [15, 132].

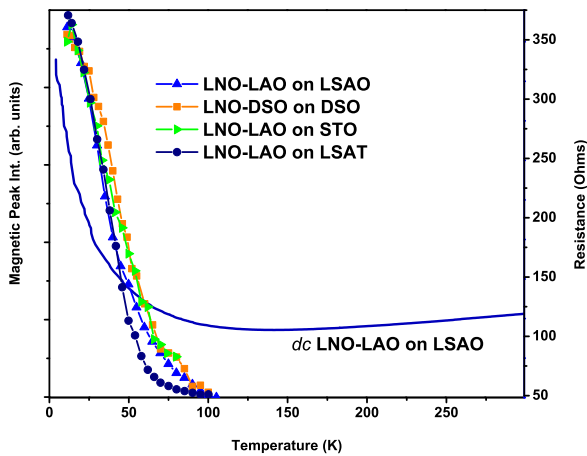


**Figure 4.35** The temperature dependence of the peak at  $\mathbf{Q}_{SDW}$  compared to the resistance of a LNO-LAO SL on LSAO.

The question about CO in the LNO based SLs is one which was partially addressed during this thesis. The main findings done so far are summarized in Fig. 4.36. In an effort to further characterize the low-temperature ground state, we measured the intensities of Bragg reflections with wave vector  $\mathbf{Q}_{CO} = (\frac{1}{2}, \frac{1}{2}, \frac{1}{2})$  as a function of photon energy close to the Ni  $K$ -resonance at several temperatures. Previously, commensurate CO was detected on NNO films grown under tensile-strain conditions [88, 133], as discussed on page 45. We have reproduced the same lineshape in the low-temperature insulating state of a reference film NNO on an STO substrate, which also imposes tensile strain (Fig. 4.36(a) top). The maximum of the resonant peak decreases with increasing temperature. In panel (b), the electronic modulation amplitude (defined as the peak maximum normalized by the off-resonance intensity) is compared to the off-resonant intensity of the structural peak. Both the electronic and structural amplitudes show an order-parameter-like temperature dependence consistent with the metal-to-insulator transition observed in the resistance curve shown as a red line Fig. 4.36(b). However, a clear difference to the results reported in Ref.’s [88, 133] is a remaining energy-dependent peak at  $\mathbf{Q}_{CO}$  above the  $T_{MIT}$ . We attribute this to structural differences between our film and the one of Ref.’s [88, 133] which we observe in non-resonant diffraction studies [11].

To obtain a qualitative understanding of the spectra, we have done first principles calculations as follows [8]. We considered LNO structures with a charge disproportionation into

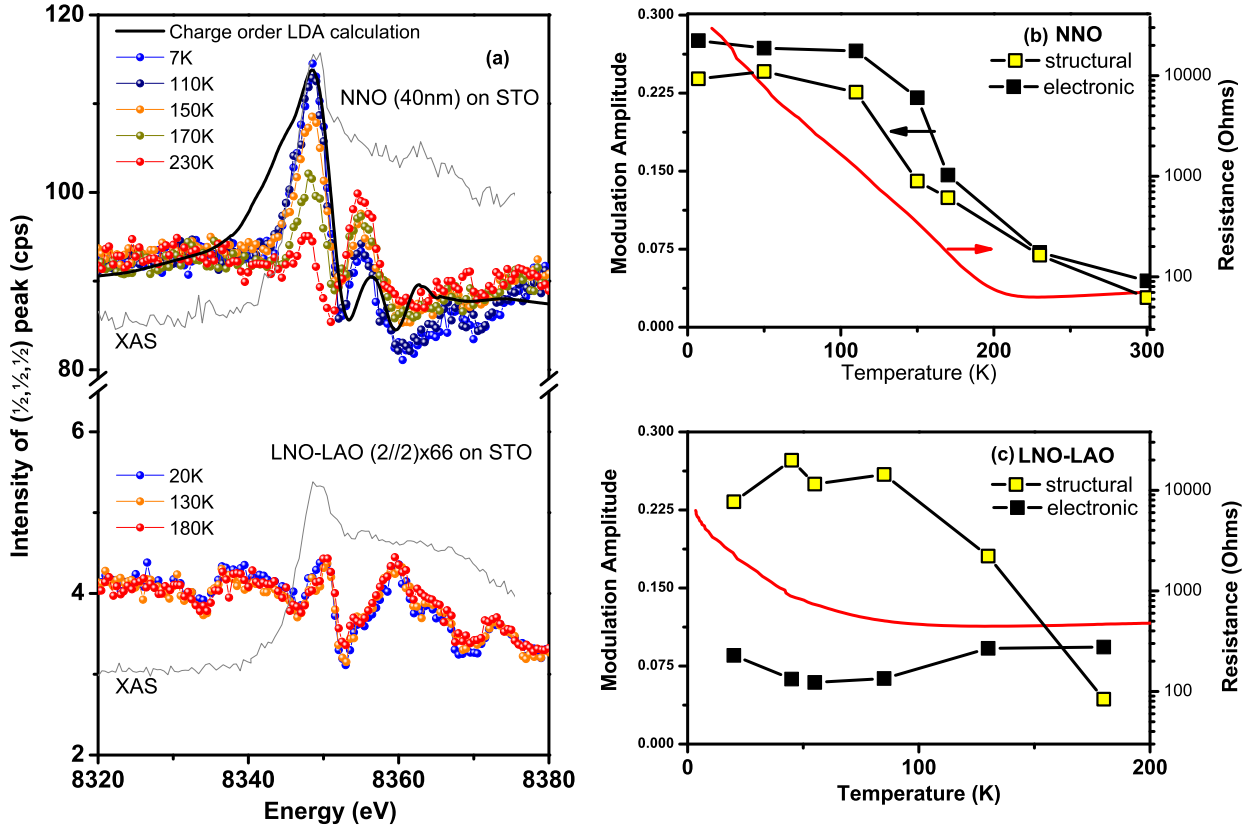


**Figure 4.36** The discussion about the CO in NNO and the LNO SL on STO.

two inequivalent Ni sites with valence states  $3-\delta$  and  $3+\delta$ , along with a corresponding modulation of the Ni-O bond lengths and distortions induced by rotation of the oxygen octahedra with different Glazer patterns and bond angles. These calculations were performed using the WIEN2k code based on the full-potential (linearized)-augmented-plane-wave plus local orbitals method within density functional theory in the generalized gradient approximation [8]. These calculations yield the imaginary component of  $\sigma$  around the Ni  $K$ -edge for each structure. The real part of  $\sigma$  was obtained using the Kramers-Kronig transformation. With these results, the diffraction spectra were then calculated using the matrix formalism implemented in the ReMagX program [69]. The model lineshape, shown in Fig. 4.36(a) (upper panel), are in decent agreement with the low temperature data. The modulation at temperatures above  $T_{MIT}$  may arise from either a residual charge disproportionation and/or from  $\text{NiO}_6$  octahedral tilts, driven by different strain conditions which relax the  $Pbnm$ -extinction rule at  $Q_{CO}$ . In such case, the lower symmetry phase will result in non-zero off-diagonal terms in  $\sigma$ . A schematic of the two different sites is shown in Fig. 4.37. It also depicts examples of the resulting matrix  $\Im(\sigma)$ .

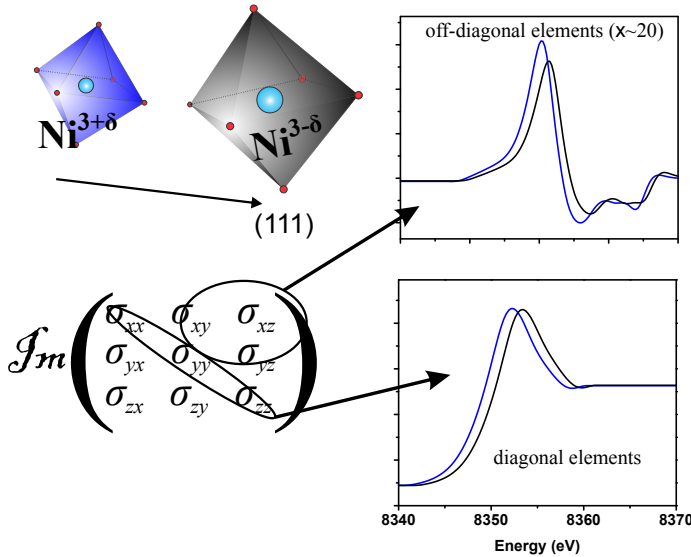


**Figure 4.37** A schematic of the results of charge disproportionation and octahedral tilts where two Ni sites have different  $\sigma$  tensors. The off-diagonal terms are generated by the tilts and have smaller amplitude than the diagonal terms, whose asymmetry arises from a different core potential at disproportionate sites.

In contrast, the LNO SL on STO, with a weaker overall intensity at  $\mathbf{Q}_{CO}$ , shows a different behavior (Fig. 4.36(a), bottom). While the structural amplitude decreases with increasing temperature, the electronic modulation does not change with temperature (Fig. 4.36(c)). This might suggest a precursor structural transition that, in the case of LNO SLs, does not lock-in the electronic CO transition. In other words, the structural modulations are not connected to the change in conductance. However, the weak changes in structural intensity can also be related to the phase transition of STO [112] and/or alignment issues which could not be fine-tuned during the experiment. Modeling the “wiggly” lineshape for this sample as well as for the NNO film at high temperatures remains a part of the outlook.

The temperature dependent structural amplitude of Fig. 4.36(c) tempts us to attribute the dimensionality-induced MIT to a structural change in LNO. However, the LNO SL on LSAO (whose lattice structure is characterized by the same space group  $I2/c$  but a smaller octahedral tilt amplitude [8]) defies this connection. In this case, no diffraction signal is detectable at  $\mathbf{Q}_{CO}$  above background level at all temperatures. These observations would agree with the suggestion of [99, 100] where the SDW amplitude is the primary order parameter in these systems, and a secondary CDW can be suppressed depending on details of the lattice structure. From these observations, compressive strain may effectively provide conditions for a suppressed CO.

Finally, the nickelates can be epitaxially integrated with other oxides exhibiting ferromagnetic metallic or insulating states through atomically sharp interfaces. Along with the control options for the SDW polarization and the secondary CO we have identified, and the possibility of *in-situ* monitoring of SDW and CDW order by resonant x-ray diffraction, our discovery provides interesting new perspectives for spintronic devices, in particular for the possible application of spin-transfer torque effects on spin valves containing metallic AFM systems [134]. In analogy to Ref. [114] where exchange bias between nickelates and manganites was observed, a possible design is shown in Fig. 4.38. However, in this case the design would comprise a half-metallic manganite layer and an AFM-metallic nickelate layer. The former could be LCMO. The latter could be LNO or PNO, which has shown a metallic behavior when grown on compressive strain [11]. A spin-polarized current applied in the FM-ordered state of the manganite can pass into the AFM-metallic nickelate layer and exert

a spin-transfer torque on the Ni ions. This could conceivably alter in the spiral state of the nickel. Thus, dynamically manipulating the orientation of the spins in a spin-valve-like heterostructure would offer intriguing perspectives to the spintronics community.

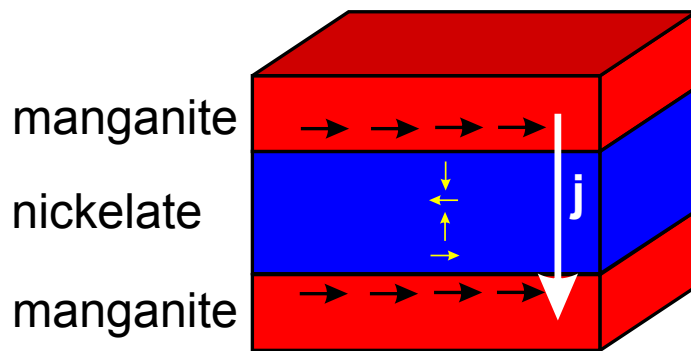


**Figure 4.38** A simple design of a heterostructure combining a FM-metal with a nickelate in a AFM-metal phase. The spin-polarized current generated in the manganite may exert a spin-transfer torque on the magnetic spiral of the Ni, which could lead to a change in their polarization.



# Chapter 5

## The Cuprates: A Charge Density Wave

Superconductivity (SC), a prime jewel of condensed matter physics, was discovered in simple metals in 1911. It took physicists several decades to better understand the phenomenon, when the BCS theory was developed and granted the Nobel prize to Bardeen, Cooper and Schrieffer in 1972. And just when physicists were convinced that the upper limit in the transition temperature ( $T_c$ ) cannot be breached, along came the cuprates. Discovered in 1986 by Müller and Bednorz, they still challenge physicists with fundamental questions.

This chapter will present and discuss the evidence of incipient charge density wave (CDW) order found throughout this PhD project in the  $\text{YBa}_2\text{Cu}_3\text{O}_{6+x}$  (YBCO) system, including single crystals and YBCO-based heterostructures. It includes a brief introduction to cuprate physics, serving to motivate the importance of the present study.

### 5.1 Properties of bulk YBCO

#### The crystal structure

As in many TMO materials, details of the crystal structure are crucial. The superconducting cuprates have a crystal structure deriving from the perovskite  $\text{CaTiO}_3$  structure, discussed on page 3. However, the fundamental building block of cuprates are closely spaced,  $\text{CuO}_2$  planes, separated by  $\sim 6\text{-}8 \text{ \AA}$ . Thus, the  $\text{ABO}_3$  cell is split into AO and  $\text{BO}_2$  layers. The families of superconducting cuprates can be obtained by stacking  $\text{CuO}_2$  planes between charge reservoir layers with family-dependent chemical composition. This effectively results in a 2-dimensional system, which can be observed in anisotropic measurements of different kinds [135]. A general schematic of this characteristic is shown in Fig. 5.1.

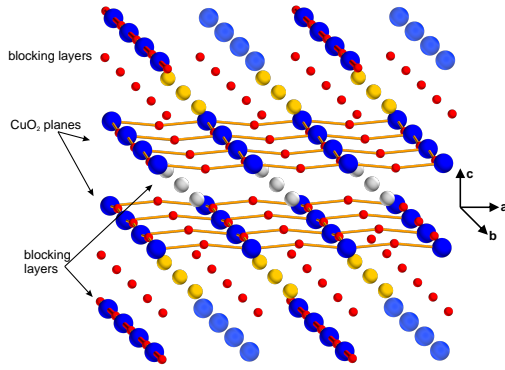


**Figure 5.1** The basic building block in all superconducting cuprates are the  $\text{CuO}_2$  planes, which are isolated between blocking layers, which are different for all families.

YBCO is a member of the so-called  $123$ -cuprate family. The unit cell, shown in Fig. 5.2, contains two adjacent  $\text{CuO}_2$  layers, separated by  $2.85 \text{ \AA}$ . The Y-ion sits between these two layers, ensuring their 2-dimensional nature. The  $\text{BaO} + \text{CuO}_x$  block follows the  $\text{CuO}_2$  plane double-stack, separating them by about  $8.5 \text{ \AA}$ .

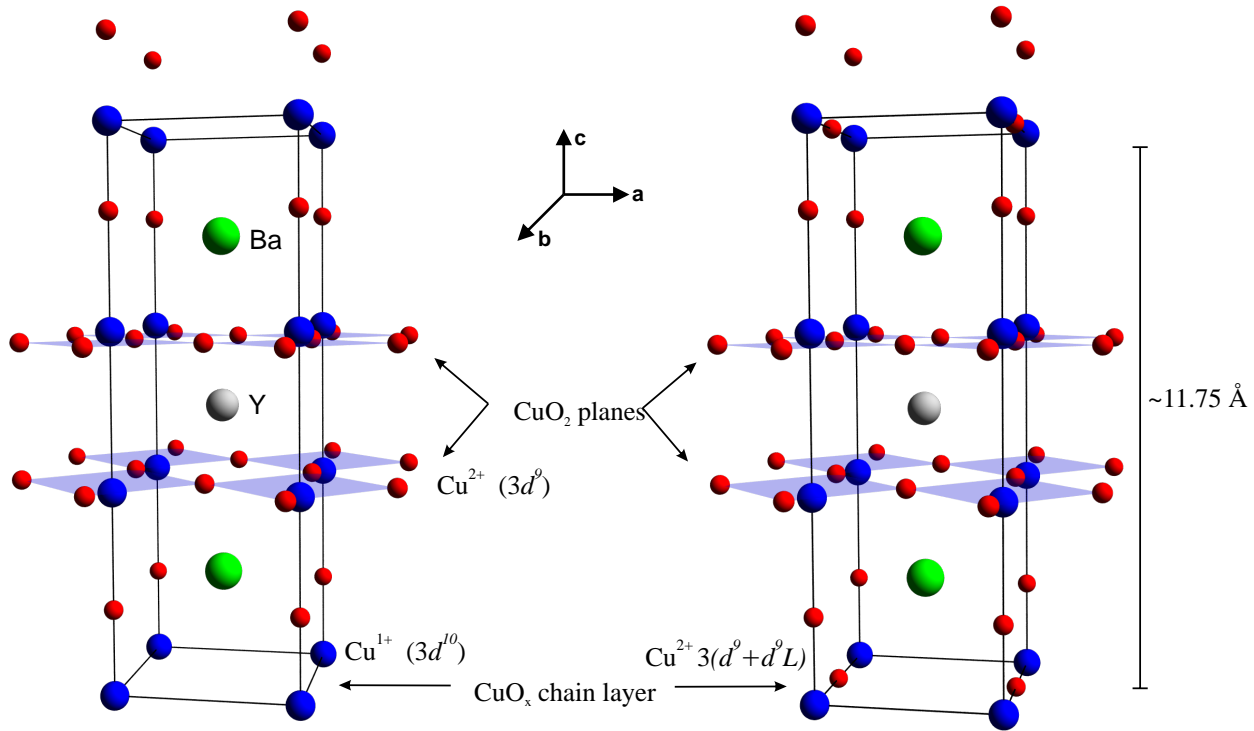


**Figure 5.2** The unit cell for  $\text{YBCO}_{6+x}$  for  $x = 0$  (left) and  $x = 1$  (right). Two adjacent  $\text{CuO}_2$  planes, separated by  $2.85 \text{ \AA}$  conform a bilayer unit. The added oxygen is located along the  $\text{CuO}_x$  chains which run along the crystallographic  $b$ -direction, which transitions from a tetragonal  $P4/mmm$  phase (left) to an orthorhombic  $Pmmm$  structure (right). The degree of orthorhombicity increases with  $x$ . Figure based on Ref. [136].

A close look at Fig. 5.2 will reveal a unique characteristic of the YBCO system. Within one unit cell, there are two different Cu-O environments. Aside from the ions lying within  $\text{CuO}_2$  planes, 1-dimensional chains of Cu-O run along the crystallographic  $b$ -axis. These chains fill up as the excess of oxygen  $x$  varies from 0 to 1 and have important consequences on the structure of YBCO.

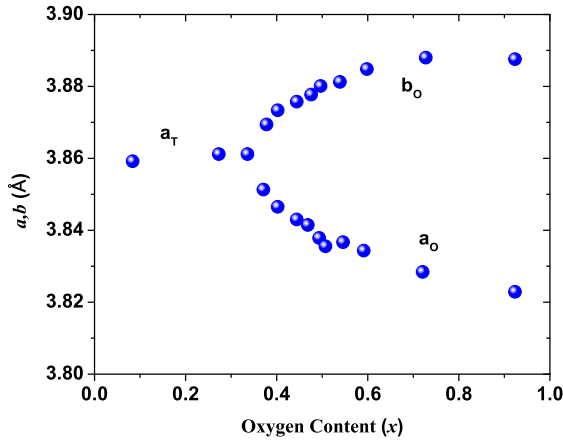


**Figure 5.3** The disproportionation of the  $a, b$  lattice constants of  $\text{YBCO}_{6+x}$  increases with the excess oxygen  $x$ . The crossover from a tetragonal to orthorhombic structure takes place at  $x \sim 0.33$ . Image reproduced from [136].

The parent compound  $\text{YBCO}_6$  has a tetragonal  $P4/mmm$  structure, with  $a = b = 3.86 \text{ \AA}$  and  $c = 11.78 \text{ \AA}$ . As the oxygen ions are introduced, their preferential aligning along the  $b$ -axis results in a uniaxial length distortion along that direction. After  $x \sim 0.33$ ,  $\text{YBCO}_{6+x}$  evolves into an orthorhombic structure ( $Pmmm$ ), with increasing  $a-b$  disproportionation until  $x = 1$ , as shown in Fig. 5.3. No structural phase transitions occur below room temperature, i.e. in the temperature ranges of interest to this study.

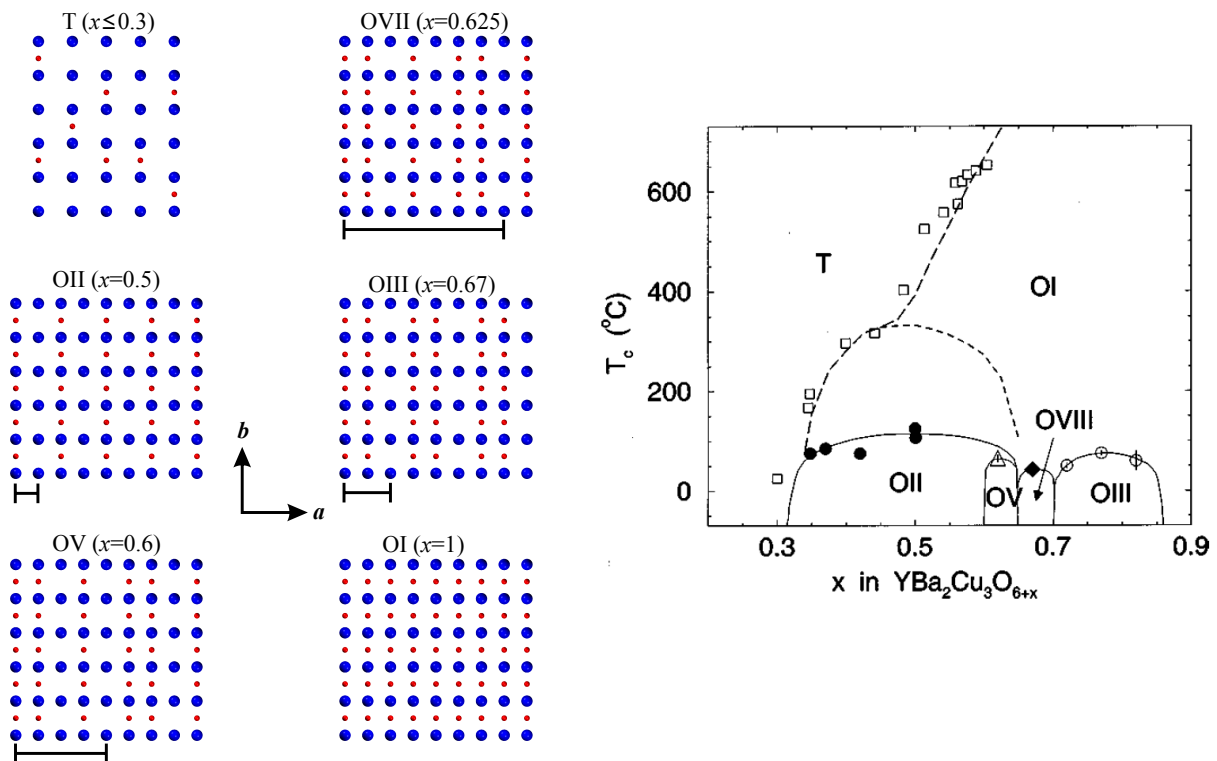


**Figure 5.4** The several oxygen-ordered phases of the chains in  $\text{YBCO}_{6+x}$  are shown, with Cu ions in blue and O in red. Depending on the content  $x$ , the superstructures along  $a$  can be  $N$ -fold (with  $N=1,2,3,5,8$ ), and the super unit cell is shown underneath each case. No superstructure exists in the tetragonal phase. Figure based on [137, 138].

The Cu-O chains can have yet another implication on the structure of  $\text{YBCO}_{6+x}$ . Within the orthorhombic phase, special annealing treatments can lead the Cu-O chains to order

into  $b$ -axis-oriented arrays of Cu-O and Cu-empty sites [137, 138]. This results in a periodic superstructure visible along the  $a$ -axis, shown in Fig. 5.4. The period of this superstructure, which depends on the amount of oxygen  $x$ , serves to classify the different phases. Their nomenclature follows the notation *ortho*-N (or ON), where the roman numeral N stands for the N-fold periodicity along the  $a$ -axis. The structural coherence length of these ordered chains can be very good, reaching its best value in the OII phase.

### XAS: the valence states of the Cu ions

The different Cu sites in the unit cell of YBCO can be distinguished by their valence states. Planar  $\text{CuO}_2$  has a  $d^9$  oxidation state while the CuO chains have changing valence states between  $\text{Cu}^{1+}$  and  $\text{Cu}^{2+}$  as the excess of oxygen  $x$  varies from 0 to 1. These yield several final states for the XAS process [139–142]. Fig. 5.5 shows typical spectra for different samples of  $\text{YBa}_2\text{Cu}_3\text{O}_{6+\delta}$  around the  $L_3$  absorption line: a  $2p_{3/2} \rightarrow 3d$  transition. In it, three features can be identified, which correspond to three different final states, as follows. The first and most intense of all features, at photon energy of 931.5 eV, corresponds to  $2p^63d^9 \rightarrow 2p^53d^{10}$  transition, filling up the valence states of the Cu ions that live in the planes. Since the  $3d$  shell has one single hole in the  $d_{x^2-y^2}$  level the transition has such an in-plane symmetry. In other words, for light polarized along the  $c$ -axis this absorption peak weakens. Such feature in the XAS is generic and present for all the cuprate families at any doping level. The feature at 934.4 eV corresponds to the monovalent  $\text{Cu}^{1+}$  states that the empty chains possess ( $2p^63d^{10}(sp)^0 \rightarrow 2p^53d^{10}(sp)^1$ ), similar to XAS measurements of monovalent  $\text{Cu}_2\text{O}$  [141]. Since this transition pertains to empty chains, this feature is absent in fully oxygenated  $\text{YBCO}_7$ .

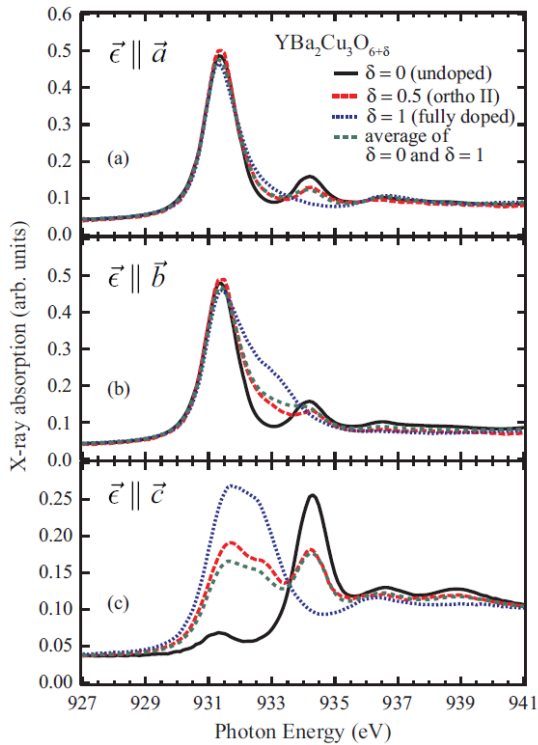


**Figure 5.5** XA spectra measured for several doping levels and light polarizations, taken from [139].

An additional shoulder emerges upon introducing excess oxygen to the chains. At 933 eV

this energy corresponds to transitions of the kind  $2p^63(d^9 + d^9\bar{L}) \rightarrow 2p^53(d^9 + d^{10}\bar{L})$ . This implies a strong hybridization between the Cu orbitals and the ligand oxygen ions. These states correspond to the copper ions along the Cu-O chains and can probe the oxygen content comparatively. In untwinned samples with well ordered chains, such a feature will vanish with light polarized along the  $a$ -axis. Although the chains only exist in YBCO, other cuprates may also show this feature (albeit weaker) since the doping similarly alters the valence state of the  $\text{CuO}_2$  planes.

### Hole doping YBCO

The properties of  $\text{YBCO}_{6+x}$  can be tuned by introducing positive charge carriers, holes, into the  $\text{CuO}_2$  planes. In general, hole doping a cuprate parent compound is achieved by altering the valence state of blocking layers, which transfers the excess charge into the  $\text{CuO}_2$ -planes.  $\text{YBCO}_{6+x}$  accommodates the charge by introducing excess oxygen into the CuO chains [143]. Since the chains can be well-ordered, this doping mechanism makes the  $123$ -family the least disordered one of the cuprates.

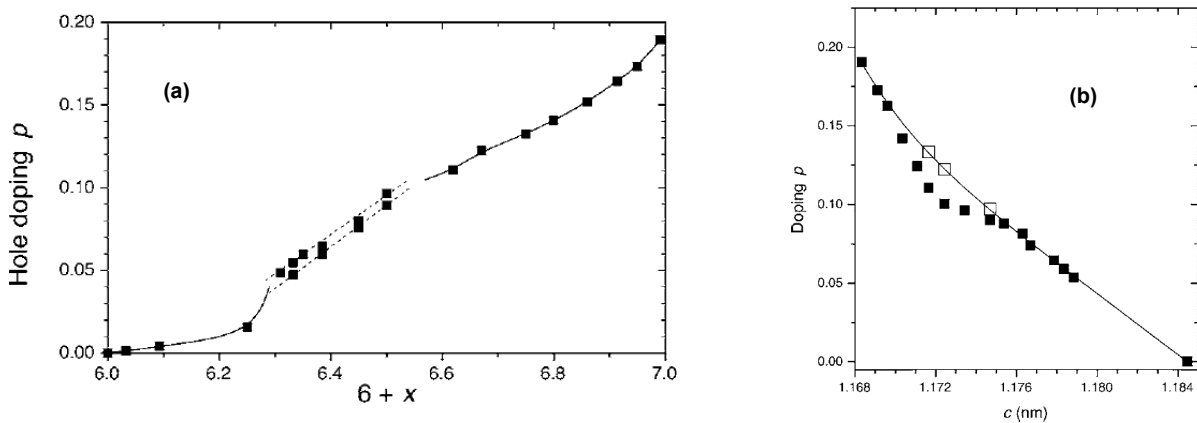


**Figure 5.6** (a) The hole count  $p$  per  $\text{CuO}_2$  unit dependence on the oxygen content  $x$ . (b) The relationship between the  $c$ -axis lattice constant and doping. Figure reproduced from [143].

The hole count dependence on the oxygen content  $x$  is shown in Fig. 5.6(a). For  $x \lesssim 0.25$ , a critical fragment length of 3 Cu ions connected by 2 oxygen ligands must be exceeded in order to trigger doping into the  $\text{CuO}_2$ -planes, which leads to the flat dependence [144]. The onset of the orthorhombic distortion at around the same  $x$ -value (Fig. 5.3) corroborates the formation of longer chain fragments, which coincides with the initiation of transfer of holes into the planes and to the onset of SC. Fig. 5.6(b) shows how the oxygen content affects the  $c$ -axis lattice constant. More oxygen anions contract the unit cell along the vertical direction. Thus, the  $c$ -lattice parameter can generally be used to monitor the doping level. Since the oxygen content in  $\text{YBCO}_{6+x}$  cannot exceed  $x = 1$  and  $\text{YBCO}_7$  is only slightly overdoped, further doping is done by substituting the Y ion by controlled amounts of Ca [145].

## The phase diagram

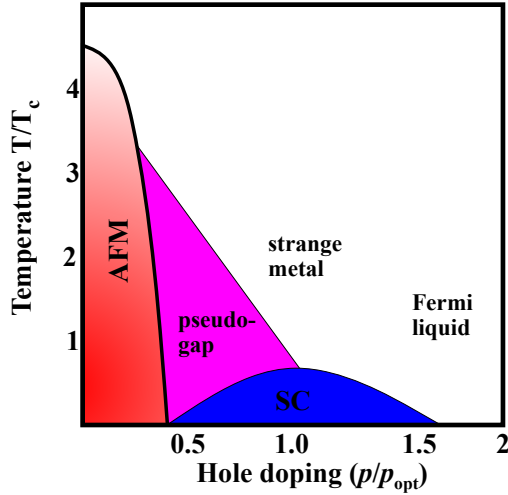


**Figure 5.7** A general schematic of a doping vs.  $T_c$  phase diagram of the cuprates. From an AFM parent compound, doping leads to a SC state at optimal level ( $p_{opt}$ ), passing through the pseudogap phase. In the overdoped regime, the system is well-described by Fermi liquid theory. Image reproduced from Ref. [146].

The doping vs. temperature phase diagram of the SC cuprates is one of the most enigmatic problems in modern condensed matter physics. The generic schematic of a cuprate phase diagram is shown in Fig. 5.7. Albeit slightly different for different families, they all show the same general features.

The low-temperature, undoped parent compound of YBCO is an AFM Mott insulator with a Néel temperature in the order of  $T_N=400$  K [147–150]. The superexchange coupling in the plane is larger than out of the plane, as observed in the modulated  $l$ -dependence of the AFM peak at  $(\frac{1}{2}, \frac{1}{2}, l)$  investigated by neutron scattering [148]. The magnetic moments lie mostly in the plane, directed along the Cu-O bond direction, and show a small in-plane anisotropy between the two orthogonal directions [151].

Doping the system with holes destroys the long-range AFM order and leads to a SC ground state with a gap showing  $d$ -wave symmetry (Fig. 5.9(a)). Empirically, the doping dependence of the superconducting critical temperature is often described using the following formula [143]:

$$T_c = T_c^{max}(1 - 82.6(p - p_{opt})^2).$$

In the underdoped regime, SC sets in at low temperatures with increasing  $T_c$ . However, the formula breaks down in YBCO<sub>6+x</sub> for doping levels near  $p \sim 0.12$  or  $x \sim 0.6$ , forming the “plateau” shown in Fig. 5.8. Among the most likely origins of the plateau<sup>1</sup>, observed in other cuprate families as well, is the formation of charge and/or spin ordered phases at the same doping levels, which are believed to be in competition with SC [152]. This notion was hitherto challenged by the absence of a charge or spin ordered state around the plateau in YBCO.

<sup>1</sup>Others discussed in Ref. [149]

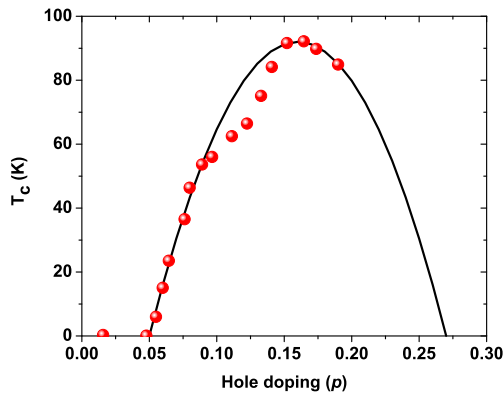


**Figure 5.8** A comparison between the empirical model of the SC dome and the actual values of  $T_c$  for  $\text{YBCO}_{6+x}$  reveals a set of doping levels where the model does not fit the data. This is known as the “plateau”. Figure reproduced from Ref. [143].

At high doping levels ( $p \gtrsim 0.16 - 0.20$ ) the normal state out of which superconductivity emerges is often considered as a good Fermi liquid. It shows a hole-like Fermi surface (FS) with  $1+p$  holes per Cu ion [146, 153, 154], a  $T^2$  dependence of the resistivity [155], and obeying the Wiedemann-Franz law [156].

### The pseudogap

As it turns out, however, the normal state from which SC emerges is not always conventional, and is particularly puzzling in the underdoped region [146, 150, 157–159]. The term “pseudogap”, coined by Sir Nevill Mott in his seminal treatment of metal-insulator transitions [160], refers to a loss of low-energy excitations, i.e. a reduction of available states near the Fermi level in a metal. In the cuprates, a consequence of such a loss of states was first observed by nuclear resonance experiments on  $\text{YBCO}_{6+x}$ . A reduction in the dynamic [161] and static [162] spin susceptibilities were observed below  $T^* > T_c$  (although at different temperatures<sup>2</sup>), in contrast to a temperature-independent Pauli susceptibility expected for a Fermi-liquid metal. These observations fueled speculation that the pairing mechanism of the SC cuprates was stemming from AFM correlations, in analogy to the spin-singlet formation leading to a loss in susceptibility at  $T_c$  in conventional SC. Inelastic neutron scattering, another probe coupling to the spin channel, later confirmed a loss of spectral weight of the magnetic resonance peak at low energies at  $T^*$  [163], although not clear-cut for lower doping levels  $x < 0.5$  [149].

Despite the amounting evidence of a gap in the spin channel pointing to a pre-formation of a paired singlet, it was known that any instability could result in the emergence of a gap. These instabilities could be AFM correlations or charge density waves (CDW), as incidentally one of the pioneering theories of pseudogap states was developed for 1-dimensional CDW systems [164]. Furthermore, the implications the “spin gap”<sup>3</sup> would have on the electronic charge lead the way to explore this phenomenon with probes which couple directly to the charge. Among these were optical conductivity and  $dc$ -resistivity. The former probe showed a drop in the  $c$ -axis, frequency-dependent conductivity below a certain frequency  $\omega_{gap}$  in the order of 75 meV, at temperatures lower than  $T^*$  [157, 158]. Interestingly, the in-plane response showed an increase in the conductivity, suggesting a lowering of the scattering rate by partial removal of states with high cross-section. This anisotropy was confirmed in the  $dc$ -resistivity, which showed the changes at a  $T^*$  roughly coinciding with NMR [158].

<sup>2</sup>The actual value of  $T^*$  can vary substantially depending on the probing tool.

<sup>3</sup>Not to be confused with the spin gap observed in the low-energy excitation spectrum [149, 165, 166].

Angle-resolved photo emission experiments (ARPES) done on cleave-favorable cuprate compounds also contributed evidence of the pseudogap. The experiment yielded an estimated gap value, and more importantly, its symmetry. Tracking the position of the gap along  $k$ -space, the FS was monitored through the crossover between regimes in the phase diagram. It showed symmetry properties similar to the SC gap where it vanishes along certain directions in  $k$ -space due to its  $d$ -wave symmetry [167]. However, instead of fading out only at the nodal points, available states remained along portions of the FS coming from the overdoped side, eventually ending in a complete loss of antinodal quasi-particle spectral weight when approaching the Mott insulating state. These segments along the FS are known as “Fermi arcs” (FAs) (Fig. 5.9). Disconnected portions of the FS are not easy to account for in current theoretical frameworks, which only predict continuous or closed (pockets) contours [146]. This has led to a discussion of whether the FAs are parts of a coherent, closed and pocket-like FS or whether they are indeed a discontinuous phase separation in momentum space between gapped and non-gapped electrons at certain  $k$ 's. Recent measurements of quantum oscillations point towards the existence of closed loops in a real FS [168, 169], and will be discussed later on.

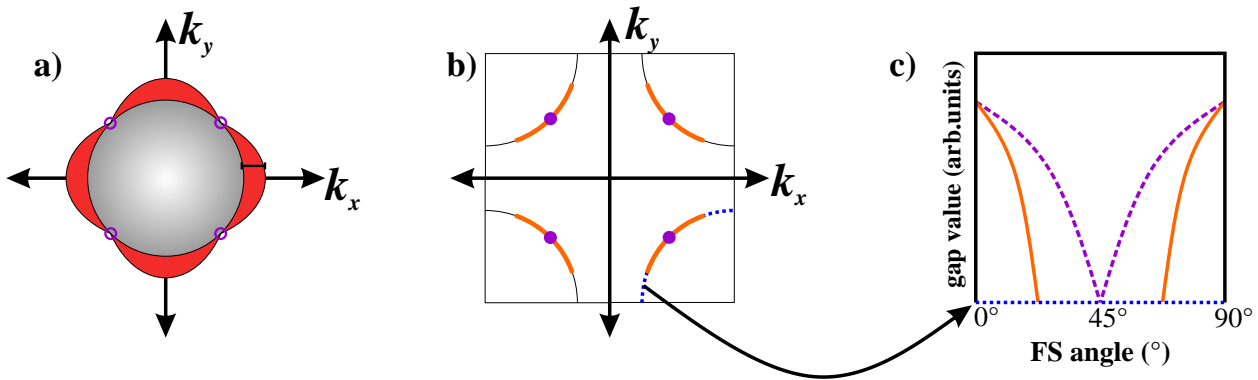


**Figure 5.9** (a) The gap ( $\Delta$ ) symmetry of the  $d$ -wave SC state in the cuprates. As opposed to a spherical  $s$ -wave scenario, the gap has nodes where it vanishes (purple open circles), along the  $(\pi, \pi)$  direction. (b) A schematic of the hole-like FS in the overdoped regime (solid black lines), the nodes in the SC gap (solid purple circles) and the Fermi arcs developed within the pseudogap (solid orange lines). (c) A schematic of the gap values in the SC (dotted purple lines) and pseudogap (solid orange lines) state as function of the angle along the FS, as indicated by dotted blue lines in panel (b). Image adapted from [159].

Today, there are two leading interpretations which attempt to explain the pseudogap phenomenon [146, 157, 158]. On the one hand, there is the notion of a “precursor” state to SC. In this sense, the pseudogap seen by ARPES and other techniques see a “leading-edge” peak below the Fermi level set in at  $T^*$  and eventually become a coherent quasiparticle peak in the SC state at  $T_c$ . Scientists supporting this view believe the SC state is merely the onset of coherent pairing coming from the incoherently paired state: the pseudogap.

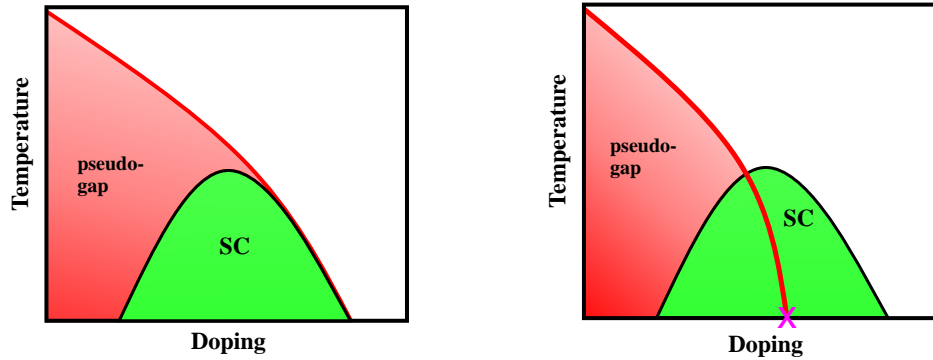


**Figure 5.10** The two scenarios proposed to explain the pseudogap phenomenon. The left panel shows the precursor picture, where the SC state is merely present when the gap excitations gain coherence, thus the pseudogap extends always above the SC dome. On the right, the competing phase picture implies the presence of a QCP (marked by a pink x) where a symmetry broken state sets in at  $T=0$  K. The position of this QCP in terms of doping in the phase diagram is also controversial and is probably material dependent.

The second viewpoint is that of a competing phase. In this notion, the idea is that a quantum critical point (QCP) at  $T=0$  K marks the border between a broken symmetry state and a normal state. These correlations extend into higher temperatures and lead to the FS reconstruction observed by many techniques. Addressed in more detail in the following section, such idea is compelling due to the observation of charge and/or spin ordered states in certain families of cuprates, but hitherto lacked universal acceptance due to the fact that such long-range charge order has eluded the YBCO family.

### Charge order in cuprates

Unidirectional “stripes” of charge and spin density waves have been observed in perovskite manganites [170],  $214$ -nickelates [171–173], and isostructural cuprates, suggesting a possible affinity of the underlying mechanism. However, their integration into the SC phase diagram of the cuprates has been the center of an intensive discussion. Since the literature is rather extensive, the main scope of this section will be restricted to content relevant to the study carried out in this thesis. More information (in particular details of spin order) can be found in Ref.’s [149, 150, 152, 174–178], from which the following section was summarized.

The AFM magnetic structure of undoped cuprates consists of spins living in the  $\text{CuO}_2$  planes with a staggered “spin-up spin-down” superstructure, with a 2-dimensional wave vector  $Q_{AFM}^{2D} = (\frac{1}{2}, \frac{1}{2})$ . For doping levels above the undoped phase, there are several manifestations of local, incommensurate and dynamic forms of magnetic order, which seem to be strongly dependent on the material. In some compounds the single AFM Bragg peak splits into four spots, displaced from  $Q_{AFM}$  by a certain  $\delta$ . These new  $Q$ -vectors arise from a spin modulation which is locally commensurate, but jumps by a phase  $\pi$  at periodic arrays of domain walls. The convolution of these two periodicities (AFM and spin flip at the domain walls), results in a SDW with  $Q_{SDW_x} = (\frac{1}{2} + \delta, \frac{1}{2})$  and  $Q_{SDW_y} = (\frac{1}{2}, \frac{1}{2} + \delta)$ . The domain walls host the dopant holes and form *charged* rivers with an additional sinusoidal modulation. The CDW peaks appear at  $Q_{CDW_x} = (h + 2\delta, k)$  and  $Q_{CDW_y} = (h, k + 2\delta)$ . A schematic of a stripe ordered lattice is shown in Fig. 5.11.

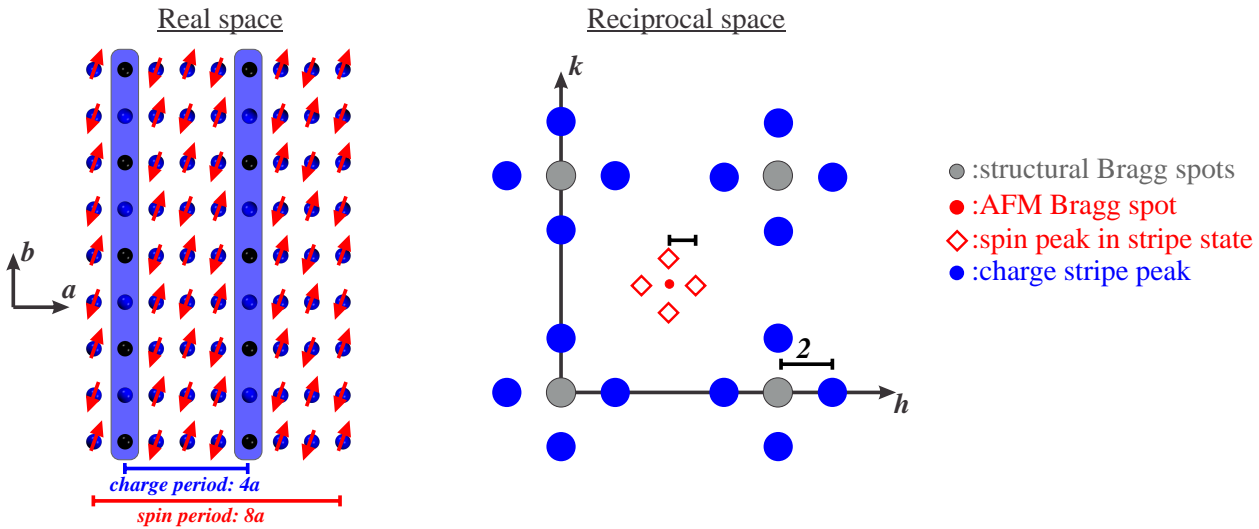


**Figure 5.11** A schematic of the stripe phase, shown for the commensurate case of  $p = \frac{1}{8}$  for simplicity. On the left, the real space picture is described, where the doped holes (shown as alternating black/blue spheres) reside within the domain walls (shown as blue rectangles). If one hole lives per  $\text{CuO}_2$  unit, then the period of the charged stripes corresponds to the doping level. The locally AFM spin structure is interrupted by these charged walls, changing the phase of the spin modulation, resulting in a double-sized magnetic super-cell. On the right, the reciprocal space picture, where four charge peaks appear around each Bragg spot, with  $2\delta = 0.25$  for this doping. The AFM Bragg spot splits into four incommensurate peaks around it in the stripe phase.

Birgeneau *et al.* [179] first observed incommensurate, dynamic magnetic fluctuations in the compound  $\text{La}_{2-x}\text{Sr}_x\text{CuO}_4$  (LSCO) by inelastic neutron scattering. Later on, Tranquada *et al.* [152] set out to investigate if the “ $\frac{1}{8}$ -anomaly”, where the SC state is dramatically suppressed at doping  $p = \frac{1}{8}$  [180], is connected to these fluctuations. Attempting to stabilize these fluctuations, they chose to work with Nd-substituted LSCO (LNSCO), a system in a low-temperature tetragonal (LTT) structural phase which had been identified as an ingredient to enhance of the  $\frac{1}{8}$ -anomaly [181]. With an onset temperature well below the LTT phase transition and pinned by the LTT lattice to a commensurate value of  $\delta = \frac{1}{8}$ , the static spin stripes they discovered emerged as solid evidence of a competing phase.

Subsequent neutron experiments further confirmed and expanded these observations. The Yamada plot in Fig. 5.12 shows  $\delta$ 's dependence on doping [182], where we note the occurrence of static stripes in LSCO at higher doping levels. A comparison of inelastic scattering signals between LNSCO at  $p = 0.12$  and LSCO at  $p = 0.15$  (optimally doped) shows low-energy fluctuations of the SDW stripe state above the SC state in the latter. It was also found that these fluctuations are governed by scaling laws which are typical of the vicinity of a QCP [174, 183].

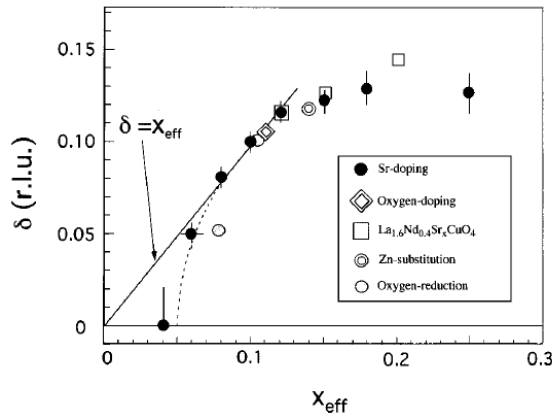


**Figure 5.12** The Yamada plot shows the dependence of the stripes' incommensurability  $\delta$  on the doping in 214-cuprates. Figure reproduced from Ref. [182].

However informative and conclusive the observation of SDW stripes using (elastic and inelastic) neutron scattering were, they were only able to detect the spin and nuclear channel. Thus, the conclusion of a coexisting CDW was based on the symmetry arguments described in Fig. 5.11. It was then up to a scattering technique coupling to the valence charge to first directly show the charge order. Abbamonte *et al.* carried out seminal RSXS experiments and found CDW order in  $\text{La}_{2-x}\text{Ba}_x\text{CuO}_4$  (LBCO) with  $p = 0.125$  [178] at  $Q_{CDW} = (\frac{1}{4}, 0, L)$ . The  $L$ -dependence revealed a rod-like feature, suggesting a weak coupling between subsequent layers, maximizing at half-integer values. This observation suggested a  $90^\circ$  rotation of the stripe orientation at every layer, consistent with Coulomb energy minimization and features of the LTT phase which stabilizes the stripes.

Measurements at the Cu  $L$ -edge are mostly sensitive to the lattice displacements of the Cu ions. However, tuning the photon energy to the O  $K$ -edge can directly probe the disproportionation of doped carriers since the dopant holes reside in the ligand O atoms. There are two XAS peaks around the O  $K$ -edge shown in Fig. 5.13. The first one at  $\sim 528$  eV corresponds to transitions into the doped hole levels, labeled in the reference as the mobile carrier peak (MCP). The second peak at 530 eV is from transitions into the upper Hubbard band (UHB). So the authors exploited the phase  $Q_{CDW}$  at the MCP which directly quantifies the doped charge in the ligand. They extracted an estimate of the charge modulation, yielding a peak-to-trough modulation of  $\sim 0.06$  holes. The value, however, is strongly tied to the charge layout model used, and thus can be controversial [174]. Nonetheless, the confirmation of a “spatially modulated correlated Mott state” is deemed very instructive.

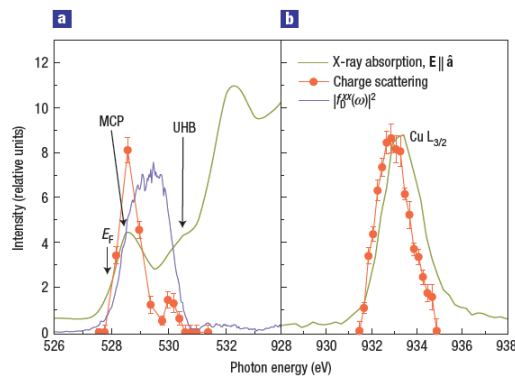


**Figure 5.13** The study of the CDW resonance around (a) the O  $K$ -edge and (b) the Cu  $L_{3/2}$ -edge. Figure reproduced from Ref. [178].

The onset of the CDW in LBCO coincided with the LTT phase of LBCO ( $\sim 60$  K), which made it hard to disentangle the transitions. Therefore, Fink and collaborators turned to perform similar RSXS experiments on Eu-substituted LSCO: LESCO [175,176] which has a higher LTT transition temperature ( $T_{LTT}$ ). The authors found the charge stripe phase to set in at  $\sim 70$  K, well below  $T_{LTT}$  at 125 K and above spin correlations detected at lower temperatures [184]. The series of transitions with  $T_{LTT} > T_{CDW} > T_{SDW}$  suggests that structural phases are, at most, weakly driving the CDW state [176]. Some authors believe that stripe order could be driven by AFM correlations, which set in at higher temperatures [174].

A doping series conducted by the same team revealed a similar behavior of the charge stripe modulation to the Yamada plot, shown in Fig. 5.14. It showed that the charge ordered phase has a dome-like trend in the phase diagram, possibly linking it to underlying electronic mechanisms instead of purely structural, and that the coherence length of the CDW is probably linked to the proximity to the commensurate  $\frac{1}{8}$ -state instead of random dopant potentials.

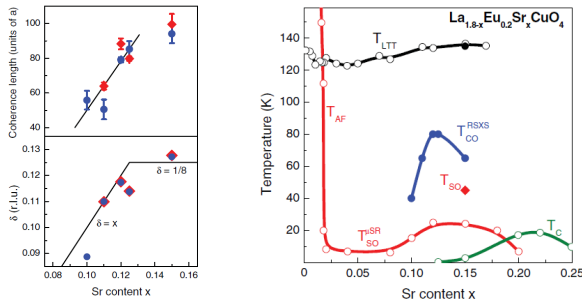


**Figure 5.14** The doping dependence of the onset of charge order ( $T_{CDW}$ ) in LESCO, taken from Ref. [175].

In summary, x-ray and neutron studies show different temperature dependencies and onset temperatures. This suggests that the charge order drives the spin order, and that the former is not necessarily connected with the LTT phase. In the stripe phase, the charge and spin order are connected by the relation  $\delta_{spin} = \delta_{charge}/2$ . In the  $214$ -family, the dependence of  $p$  vs.  $\delta$  behavior appears to rule out the possibility of FS nesting as the driving mechanism, where  $\delta$  would decrease with increasing doping (the vector joining the segments near the antinodal regions decreases with doping). Finally, we note that other techniques have contributed to addressing the presence of charge ordered states. Muon spin rotation, magnetic resonance, transport measurements and surface techniques like STM have been applied to the appropriate families and are discussed elsewhere [174].

Despite the thorough literature addressing ordered phases in cuprates, the question of its role in the phase diagram is still an open one [174]. Does the stripe order compete or collaborate with SC? Do they coexist? If so, can an external parameter tune this interplay? These and other questions are compounded by the apparent lack of universality among the cuprates, in particular YBCO. Recently, the observation of anisotropic, quasistatic, incommensurate spin (possibly non-stripe) order in underdoped YBCO [185,186] has sparked the notion of a new phase at  $T=0$  K, leading to an electronic nematic state. Whether this corresponds to a new type of stripe phase coupled to an unobserved charge order or to a more complex spiral structure remains to be discovered. For doping levels where stripes occur in LSCO, spin excitations in YBCO are gapped, showing no sign of static magnetism.

### Evidence of Fermi surface reconstruction in underdoped YBCO

With its low chemical and structural disorder, the lack of observed charge order in YBCO troubled the discussion of charge order universality in cuprates. However, recent years saw amounting evidence of a FS reconstruction in the underdoped region which suggested an underlying ordering phenomenon [146, 168, 169, 187–189].

Evidence of quantum oscillations were first found in the  $\text{YBCO}_{6.5}$  compound under applied magnetic field of up to 62 T by Doiron-Leyraud and coworkers [168]. These results vindicated the presence of a FS in the underdoped regime. The oscillation frequency shown in Fig. 5.15(c) further suggested a reconstruction into a FS with pockets as small as  $\sim 2\%$  of the Brillouin zone, considerably smaller than the FS of the overdoped region and at odds with the size predicted by Luttinger's theorem. From their results, they suggested the formation of closed elongated pockets centered in the nodal directions, possibly connected to the Fermi arcs seen by ARPES. This schematic is shown in Fig. 5.15(a-b). It shows the difference in the FS between the two doping regimes of the phase diagram, and the proposed closed FS pocket in the underdoped case. Although they could not conclude whether this reconstruction is a feature driven by the inherent O-II structure of  $\text{YBCO}_{6.5}$  or if it is a real feature of the cuprates, the study inspired important subsequent results.

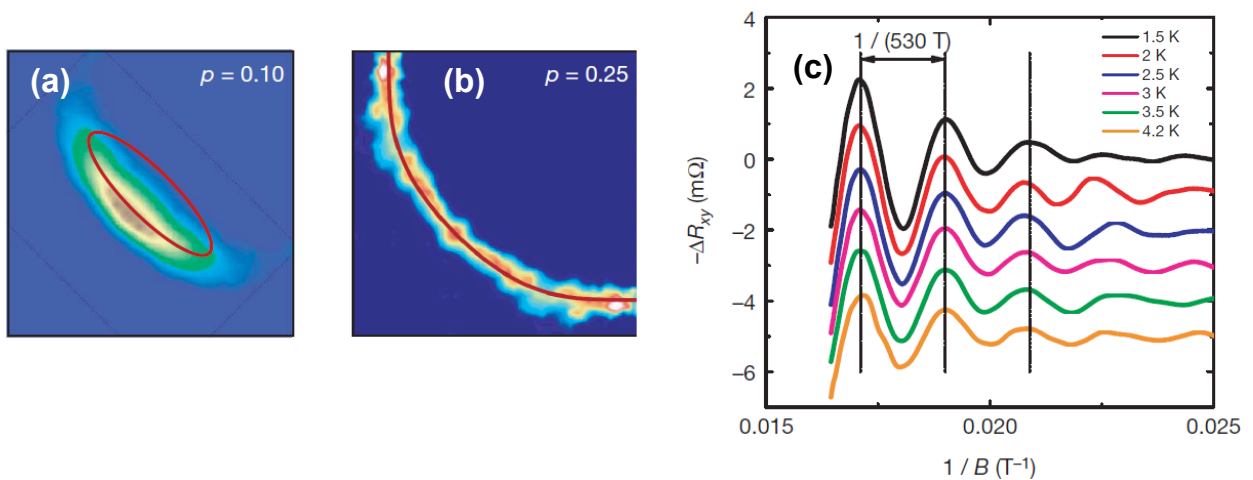


**Figure 5.15** A schematic of the FS of (a) underdoped and (b) overdoped YBCO showing the suggested scenario of an elongated FS pocket (red ellipse) accounting for the observed Fermi arc feature and the hole-like FS of the overdoped regime. (c) The Hall resistance oscillations from which the size of the FS is extracted. Reproduced from Ref. [168]

In these results [169, 188], the authors found that for several doping levels, the sign of the Hall resistance turns negative at temperatures around 50 K. As a measure of the charge carrier type, a negative Hall coefficient suggested the presence of *electron* charge carriers in a FS with mixed hole-electron character. This result is equally remarkable as the finding of a FS itself, as it may call to question the models available which presume the physics in the cuprates to be mostly governed by holes [146, 187]. Furthermore, the same research team extended their interpretation to include stripe order when they compared the observed Hall resistance [188] and Seebeck coefficient [189] of YBCO with the  $214$ -cuprate family. In both cases, the hallmark of a reconstructed FS sets in at temperatures correlated with the onset

of stripe order in the  $214$ -family. This suggested a similar case of a CDW-SDW breaking symmetry, possibly a QCP at  $T=0$  K in both families. However, the marked difference in the spin dynamics of the two families particularly in doping levels around the plateau questions the interpretation (with YBCO showing a gapped spin excitations while the  $214$ -family has static magnetic order). This implies, therefore, that were YBCO prone to a CDW instability, it would probably be unlocked from the spin channel. And as the question about the exact fermiology of underdoped cuprates remains open, some have proposed a mixed  $\mathbf{Q}$  scenario where hole and electron pockets are present and lead to an ordered state acting exclusively on the charge response [190].

In 2011, nuclear magnetic resonance (NMR) studies revealed the presence of a charge density wave order in  $\text{YBCO}_{6.54}$  under applied magnetic field of up to  $\sim 30$  Tesla [191]. With the observation of a splitting of the spectra assigned to the Cu sites in the  $\text{CuO}_2$  planes sitting underneath full CuO chains, below temperatures of around 50K (similar to the temperatures where the Hall coefficient turned negative in previous results), the research group claimed the presence of charge order in the planes. The observed hyperfine shift was explained by accounting for varying charge densities on different sites. The fact that the splitting is strongly field dependent lead the authors to conclude that the charge order competes with the SC state. Furthermore, their model proposed a uniaxial CDW, along  $a$ , with period of 4 unit cells, in analogy to the stripe ordered  $214$ -family with doping  $p = \frac{1}{8}$ , but found no evidence of spin order accompanying the CDW. Thus, a spinless, charge ordered state was finally found in YBCO. But the question of why is this state not visible to x-rays still remained.

## 5.2 CDW order in YBCO single crystals

We now turn to the results obtained during this PhD project regarding the confirmation of CDW order in underdoped YBCO single crystals using RSXS. The investigation began with the observation of an  $\mathbf{Q}$ -dependent intensity anomaly in the elastic line of inelastic x-ray scattering (RIXS) spectra taken by our collaborators in Milan, Italy, shown in Fig. 5.16(a). Besides identifying the peak, the RIXS data was crucial to identify that the order phenomenon was charge rather than spin, as shown in Fig. 5.16(b). To confirm and deepen this observation, particularly at odds with previous reports [139], the samples were taken to the elastic (REXS) diffractometer of the UE46 beamline at BESSY, and thus became an integral part of this PhD project. These results will be summarized in the following section. They can also be found in Refs. [192–194]. Shortly after the first announcement of these findings, Ref. [195] confirmed the CDW using high energy x-ray scattering.

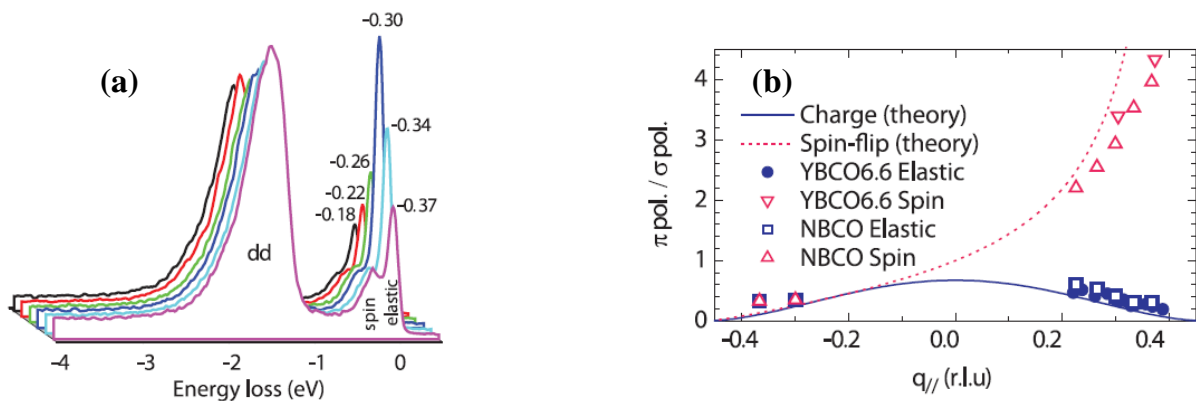


**Figure 5.16** (a) A  $\mathbf{Q}$ -dependent intensity anomaly was first observed in the elastic line of RIXS spectra of  $\text{YBCO}_{6.6}$ , which was later confirmed using REXS at the UE46 beamline in Berlin, during this PhD project. (b) The RIXS data confirmed a charge rather than spin ordered state. Figure taken from Ref. [192].

### Alignment and $\mathbf{Q}$ -dependence

We begin our discussion of a wide range of results surrounding the investigation of CDW order in YBCO with a detailed description of the scattering geometry and technical details of the experiment. Figure 5.17 shows a top view schematic of the scattering geometry where the peak is maximized. The YBCO single crystals were mounted with the  $[001]$  and  $[100]$  crystal axes in the scattering plane. The  $[010]$  direction can be accessed by rotating the sample by  $90^\circ$ . The incoming beam's polarizations ( $\sigma$  and  $\pi$ ) are also shown in the figure. As we will later see, the CDW peak has an elongated dispersion along  $(00l)$ . This implies that different scattering angles can be used to access parts of the rod. The scattering angles shown in the left panel of Fig. 5.17 are ones where the peak intensity was maximized.

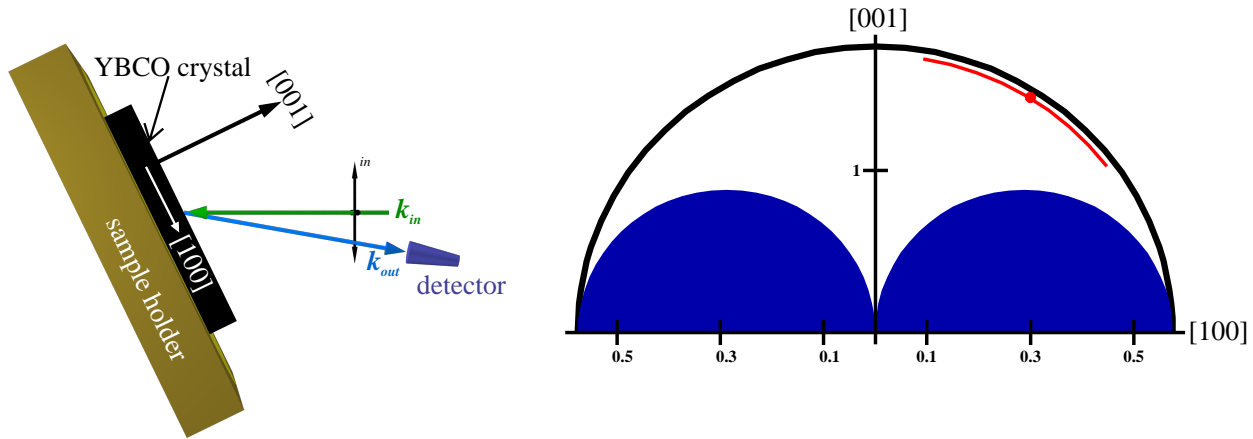


**Figure 5.17** (left) The top view schematic of the scattering geometry used in the investigation of CDW order in YBCO single crystals. The peak was found with incoming (green arrow) angle of  $\theta \sim 116^\circ$  and scattering angle (blue arrow and detector schematic)  $2\theta \sim 167^\circ$  (the largest angle accessible before blocking the incoming beam). (right) The schematic reciprocal space (RS) of YBCO for photon energy of 931.4 eV. A red spot indicates the position in RS for the given angles of the left panel. The red streak indicates the movement of rocking curve.

Following the discussion around Fig. 3.13, we turn to translate into the region in reciprocal space accessible at the Cu  $L_3$ -edge ( $\sim 930$  eV), shown in the right panel of Fig. 5.17. Underdoped YBCO has an orthorhombic unit cell structure with in-plane lattice constants  $a = 3.83$ ,  $b = 3.88$ . While the  $c$ -lattice parameter can visibly change when altering the doping level [143],  $a$  and  $b$  remain essentially the same throughout the doping range of interest in the phase diagram. Fig. 5.17 shows the resulting region in reciprocal space. The red dot corresponds to the scattering conditions shown in the left panel, and the red streak displays the movement of a typical rocking curve scan ( $\Delta\omega \equiv \pm 10^\circ$ ) used mostly throughout this thesis.

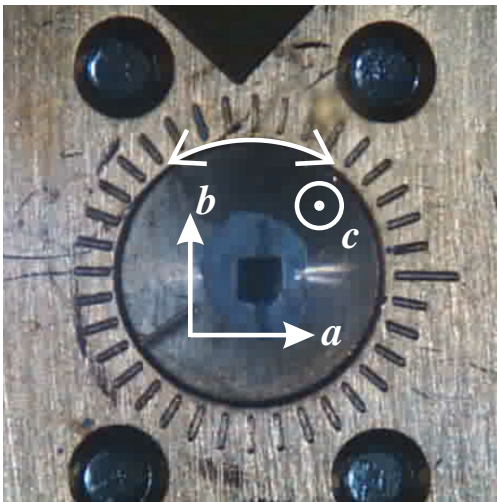


**Figure 5.18** A photograph of the YBCO<sub>6.6</sub> single crystal mounted at the diffraction chamber at UE46-PGM1 at BESSY. The crystal axes shown were determined using conventional x-ray diffraction.

The sample alignment is guided by two reflections which are needed to define the orientation matrix [196]. For the first reflex, we searched for the nominal (002) peak of YBCO by changing the incoming photon energy to 1070 eV. This wavelength not only brings the

reflex into the Ewald sphere, but it requires a scattering angle  $2\theta \sim 167^\circ$ . This angle is very close to one required for the investigation of the CDW. Thus, we ensure alignment under the closest conditions of the actual experiment. To define the perpendicular direction (100) or (010), the samples were pre-aligned using a conventional x-ray diffractometer, allowing unambiguous identification of the  $a$  and  $b$  crystallographic axes. In addition, fine tuning of the azimuthal direction was done once the CDW peak was found, by manually rotating the azimuth  $\pm 12^\circ$  in steps of  $\sim 3^\circ$ . A representative photograph of the mounted sample during such procedure is shown in Fig. 5.18.

To confirm the elastic intensity enhancement that was observed in the RIXS spectra, rocking curve scans were done on a (97%) detwinned crystal of  $\text{YBCO}_{6.6}$ . The results of such scans are shown in Figure 5.20. In a very exciting outcome, a clear peak is observed centered around  $\mathbf{Q}_{CDW}^K = 0.315$  rlu and  $\mathbf{Q}_{CDW}^H = 0.305$  rlu. Although with a slight difference in the position of the peak, scans along both in-plane directions  $a$  and  $b$  display equal intensity, showing an isotropic behavior of the CDW order. In the following discussion, the same behavior was seen in both directions, thus we refer generically to  $\mathbf{Q}_{CDW}$  unless noted. Before elaborating further on the peak observed, a few words will be said about the background signal. Particularly on resonance, the background's shape is a result of an intricate combination of systematic effects, including most prominently fluorescence, making it difficult to interpret quantitatively. On a qualitative account, the rocking curve scans we performed, shown in Fig. 5.17, span up to  $40^\circ$ , so variations of  $\sim 1\text{-}2\%$  in the background are expected. Particularly on the far side ( $\theta \sim 135^\circ$ ,  $2\theta = 167^\circ$ ), grazing angles for both the incoming and take-off beam approach the sample horizon, substantially decreasing the resonant fluorescence background via self-absorption. To analyze the peak, a proper background subtraction procedure must be done. In most cases, the high-temperature scans, when the peak has vanished, were taken and used to extract the background of the low temperature data.

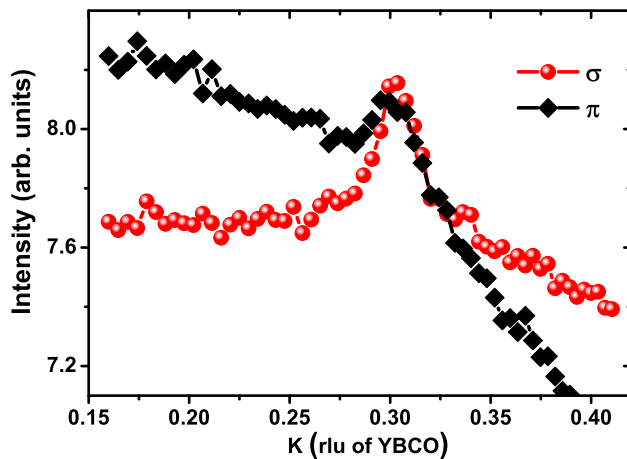


**Figure 5.19** The dependence of the CDW peak on incoming light polarization.

Figure 5.19 shows the polarization dependence of the scattered intensity, alternating between  $\pi$  and  $\sigma$ . In the case of charge scattering, pertinent here, the difference between the two channels arises only from the fact that the available Cu  $3d$  states have a planar  $d_{x^2-y^2}$  symmetry. Thus, while the  $\pi$  channel's projection to the  $xy$ -plane is reduced by a factor  $(\sin(\theta) \sin(\beta))^2$  (with  $\beta$  the take-off angle with respect to the surface), the  $\sigma$  channel is not affected by the scattering geometry (see Eq. 3.13 and Fig. 3.8). Therefore, the polarization

used throughout this investigation is  $\sigma$ , seen in Fig. 5.17 as the arrow coming out of the paper.

Figure 5.20(b) shows the peak as measured on the positive (Fig. 5.17) and negative side of RS. Similar intensities were recorded on both sides, but in the following, the positive side was chosen in order to have normal incidence on the sample. Figure 5.20(c) shows the raw data of the peak intensities' for different scattering angles  $2\theta$ , shifted vertically for clarity. For all cases, the peak is centered around the same  $Q$ -value, suggesting a rod-like elongation shown in Figure 5.20(d), which is a map of the background subtracted scans. Such a dispersion is expected from the 2-dimensional nature of the scattering from the YBCO planes. The slight decrease in intensity at smaller  $l$ -values shown in Figure 5.20(e) is qualitatively consistent with the intrinsic  $l$ -dependence centered at half-integer values due to finite inter-layer coupling, as shown in [195, 197]. In addition, the increasingly shallow take off angle can suppress the scattered intensity by self-absorption effects. The optimized conditions to study the reflex involve the highest possible  $2\theta$  angle. We also attempted to do straight  $h$ -scans rather than (curved) rocking curves, but the clearest intensity contrast is seen in the latter method. We attribute this effect to the electronic noise polluting the diode when the detector arm is in motion. Being a peak of only  $\sim 6\%$  rise over the background, this noise becomes relevant. Therefore, rocking curve scans were done throughout this investigation.

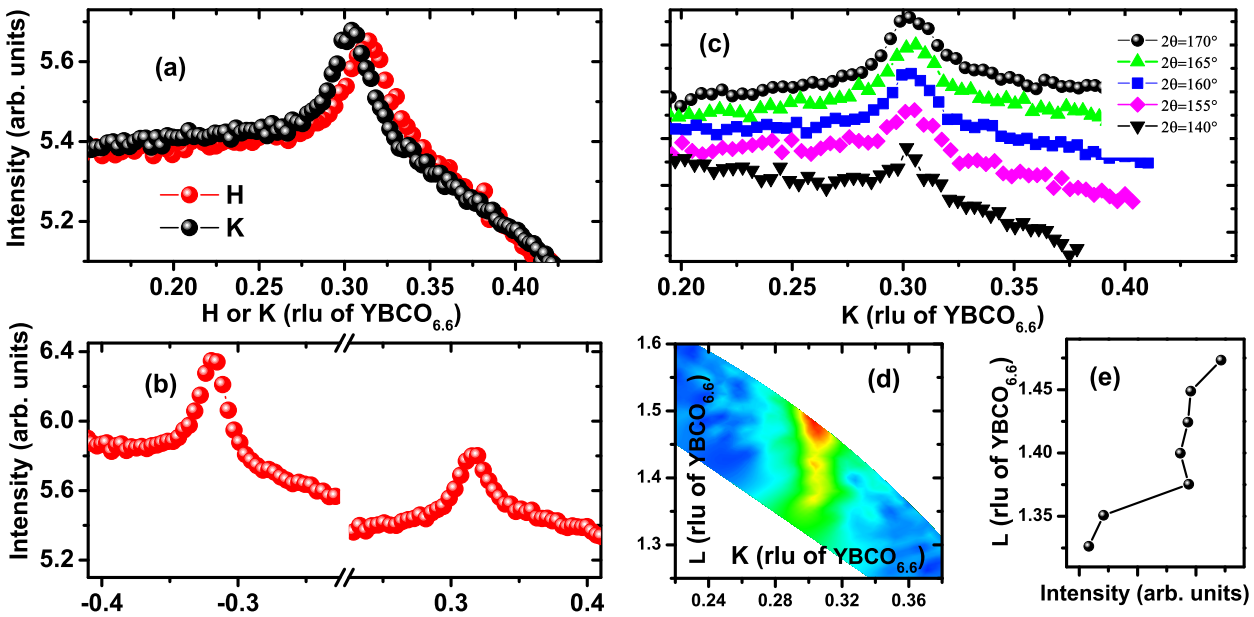


**Figure 5.20** (a) The result of scans around the scattering conditions shown in Fig. 5.17 for untwinned  $\text{YBCO}_{6.6}$ , revealing a peak centered around  $Q_{CDW}^K = 0.315$  rlu and  $Q_{CDW}^H = 0.305$  rlu, with equal intensity shown when scanning along both in-plane directions. (b) The peak is evident in the positive and negative  $Q$  sides. (c-e) The  $l$ -dependence of the peak.

### Energy dependence

A thorough energy dependence was necessary to fully understand the origin and nature of the CDW intensity observed so far. Due to the rather low intensity of the peak above the background ( $\sim 6\%$ ) compared to the high fluorescence yield at resonance above the non-resonant background ( $\sim 400\%$ ), a conventional energy scan fixed at  $Q_{CDW}$  will be strongly

dominated by the fluorescence background and thus misleadingly resonant at 931.5 eV. Even the contrast between an energy scan on  $\mathbf{Q}_{CDW}$  versus off  $\mathbf{Q}_{CDW}$  is not sufficient to yield quantitative description. Therefore, to carry out a reliable quantitative study, a series of rocking curves were taken at each energy. Later, the peak intensity is found by subtracting the background. This procedure yields a reliable description of the peak intensity as function of photon energy across a strong resonance<sup>4</sup>.

Figure 5.21(a) shows the results of the analysis of such a series of scans. With representative raw data for several energies shown in the inset, the blue solid circles in the main panel show the dependence of the peak at  $\mathbf{Q}_{CDW}$  on incoming photon energy. Overlaid to it is a black solid line representing the XAS taken in the TEY mode. We recall from Fig. 5.5 that each of the different Cu sites in the unit cell of YBCO has a different resonance energy. The CDW peak clearly resonates at 931.5 eV, distinguishably away from 933 eV, entirely ruling out that the resonant scattering originates in the Cu sites in the CuO chains. Therefore, utilizing the site selectivity offered by RSXS, we concluded the CDW order lives in the CuO<sub>2</sub> planes.

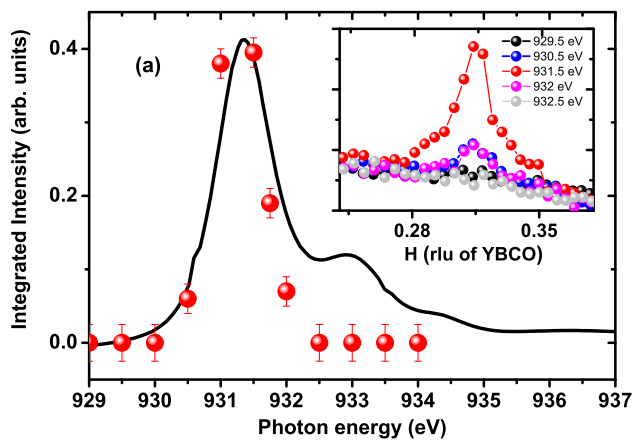


**Figure 5.21** The energy dependence of the reflex at  $\mathbf{Q}_{CDW}$  (solid blue circles) compared to the XAS spectrum (black line). The inset shows the raw data for several labeled energies.

### Temperature dependence

Using the versatility and flexibility of a REXS chamber as compared to a RIXS setup, the temperature dependence of the scattered intensity at  $\mathbf{Q}_{CDW}$  was investigated thoroughly at the UE46-PGM1 station. The temperature dependent experiments were carried out in similar fashion to the nickelates, where the sample height was scanned at every temperature to certify that the beam struck the sample at the same position. Moreover, the CDW properties were monitored at several sample positions. All the scans revealed the same feature, confirming the homogeneity of the sample and of the CDW order phase. Fig. 5.22(a) displays the normalized integrated intensity of the peak as a function of the sample temperature. The onset temperature is between 120-150 K, difficult to quantify exactly due to the background subtraction issues. The peak intensity grows upon cooling down, until it reaches a maximum at around 60 K. At this point, coinciding with the transition temperature into the SC state, the intensity begins to decrease as temperature is cooled down. The inset of panel (a) shows raw data for some representative temperatures.

<sup>4</sup>In general, a fixed- $\mathbf{Q}$  energy scan only works when the peak intensity-background ratio is  $\sim 5$  times larger than the fluorescence-background ratio.

In an equally striking result, the peak's width also reveals a remarkable temperature dependence. Fig. 5.22(b) shows how the peak's full width at half maximum (FWHM), obtained from the peak analysis done at every temperature, behaves as a function of temperature. A minimum of the FWHM at  $T_c$  shows a divergence of the CDW order's correlation length  $\xi$  of up to  $\sim 18$  unit cells ( $\equiv \sim 69 \text{ \AA}$ ), calculated from the expression  $\xi = \frac{a}{2\pi \times \text{FWHM}}$ . At each side of  $T_c$ , the correlation length decreases to a value of  $\xi \sim 58 \text{ \AA}$  at lowest accessible temperature (10 K), and on the high side of  $T_c$  until the peak vanishes. In contrast to the non-temperature dependent behavior of the stripe order below  $T_c$  in the  $214$ -family [176, 178, 198], the case of CDW in  $\text{YBCO}_{6.6}$  strongly suggests a fluctuating rather than static order.

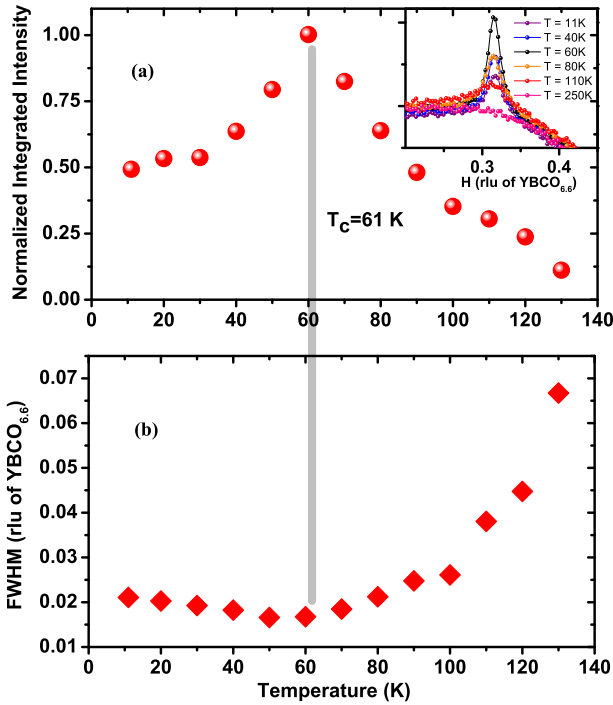


**Figure 5.22** (a) The temperature dependence of the integrated intensity of the reflex at  $\mathbf{Q}_{CDW}$ , normalized to the maximum value measured at around  $T_c$ . The inset shows raw data for several temperatures. (b) The temperature dependence of the FWHM.

### The case of $\text{YBCO}_{6.55}$

The discovery of a CDW in  $\text{YBCO}_{6.6}$  described above answered some fundamental questions about the physics of underdoped cuprates, but also opened new queries concerning the marriage with previous results from different techniques. In the paper where the RIXS data was published [192], a major question remained open. As Figure 3 in the paper shows, RIXS scans along the  $a$ -direction for O-II ordered crystals revealed no CDW intensity. However, this is the doping where the NMR results have suggested a uniaxial CDW along  $a$  under applied field [191].

To address this seemingly contradictory scenario, we turned to carefully explore the presence of a CDW in excellent quality single crystals of  $\text{YBCO}_{6.55}$ . Using the same scattering geometry, we first tested the hypothesis of a CDW along  $a$ , without applied magnetic field. To our advantage, a well ordered O-II sample will show a reflex in the  $(\frac{1}{2}, 0, l)$  position, which proves useful to align the second in-plane reflection after the (002). Furthermore, albeit it essentially is a structural peak, it is expected to resonate at the energy of 933 eV, since it originates in the CuO chains. Fig. 5.23 shows a series of scans along the  $a$  direction taken at

different photon energies. Indeed a strong reflection is visible at  $(\frac{1}{2}, 0, 0.78)$ , which resonates at 933 eV, attesting to the excellent sample quality. The peak also serves to fine tune the azimuthal alignment, in contrast to the oxygen disordered YBCO<sub>6.6</sub> crystal. However, a close look at smaller  $\mathbf{Q}$ -value at photon energy 931 eV reveals a small peak above the background at  $\mathbf{Q}_{CDW}^H = 0.315$  rlu, as shown in the inset of Fig. 5.23. Unlike the O-II peak which is very sensitive to azimuthal rotations, we found the CDW peak does not vary when rotating  $\psi$  by  $\pm 3^\circ$  around the nominal value. This suggests a shorter in-plane correlation of the CDW compared to the rigid ortho order. Resulting in a modulation of  $\sim 3.2$  lattice units, the present data clarifies the NMR model proposed for a period 4 modulation. The weakness of the feature compared to the case of YBCO<sub>6.6</sub> may explain why the original RIXS scans were unsuccessful in finding the reflex. Moreover, the sample quality and treatment was found to be of high importance during these experiments. It took several attempts to discover that a thorough polishing of the sample surface is needed shortly before the experiment to ensure a clean surface (and with a small penetration depth of the soft xrays, this is highly relevant).

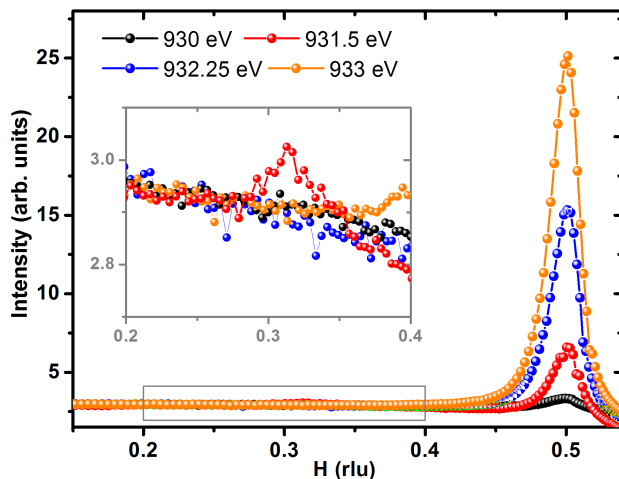


**Figure 5.23** Rocking curve scans along the  $a$  direction of a YBCO<sub>6.55</sub> crystal at different photon energies, showing excellent O-II order with a peak resonating at 933 eV. The inset shows a zoom-in of the scan around  $\mathbf{Q}_{CDW}$ .

Although at odds with the NMR model, it is encouraging to verify the presence of a CDW using a scattering technique. With the technique's reliability and versatility, we set out to test another important hypothesis of NMR investigation. In that proposal, the CDW was suggested to be uniaxial along  $a$ . In that case, no intensity is expected when scattering along  $b$ . Fig. 5.24(a) shows a comparison of rocking curve scans along both in-plane directions. It reveals yet another discrepant result to the NMR: not only is there a visible peak along the  $b$ -direction, but it carries about 4 times more intensity than along  $a$ . In addition, there is a larger difference in  $\mathbf{Q}$ -values than observed previously, with  $\mathbf{Q}_{CDW}^K = 0.325$  rlu. The correlation lengths are slightly different  $\xi_a \sim 48$  Å and  $\xi_b \sim 82$  Å, which along  $b$  is larger than in YBCO<sub>6.6</sub> and YBCO<sub>6.75</sub> [193], presumably due to the lower disorder in the well oxygen-ordered samples. The peak anisotropy probably arises from the strong commensurate potential from the ordered CuO chains which weakens the incommensurate CDW. Fig.'s 5.24(b-c) show the peaks' dependence on temperature for both directions. The maximum intensity at  $T_c$  is seen once again in both directions. Likewise, the fluctuating correlation length, diverging close to the SC transition is seen in both directions. These results were simultaneously confirmed using high-energy diffraction in [199].

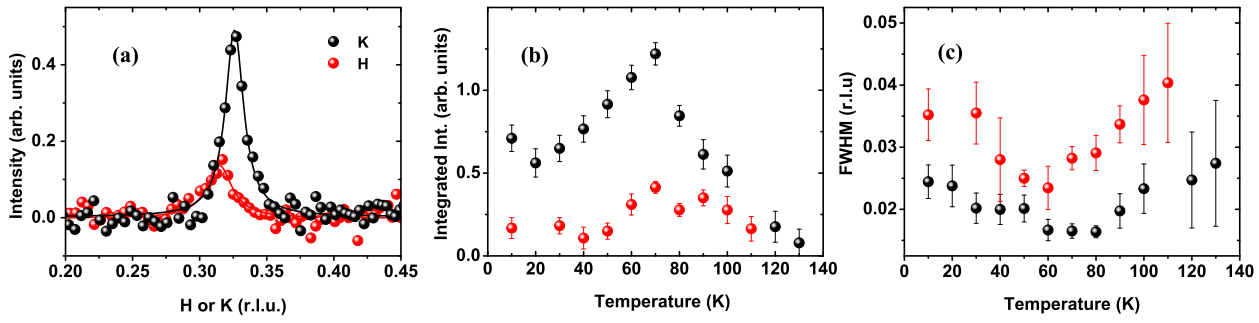


**Figure 5.24** (a) A comparison between scans along  $a$  (red) and  $b$  (black) for  $\text{YBCO}_{6.55}$ , with fitted Lorentzian superimposed as solid lines. The temperature dependence of the integrated intensity (b) and the FWHM (c) for the two directions.

### Magnetic field dependence

Since the NMR experiment of [191] was performed under high magnetic field, reconciling these two approaches requires the REXS experiments to be done under field. To address this issue, we took advantage of the unique capability of applying a magnetic field during scattering experiments offered at the UE46-PGM1 beamline at BESSY, described in detail in 3.3.5. The scattering geometry used to investigate the CDW order in ortho-II YBCO is shown in Fig. 5.25. The opening of the magnet allowed sufficient angular range to be able to sneak intensity past and through to the detector. Ideally, to suppress the SC state, the external field must be applied perpendicular to the surface normal. However, this is not entirely possible inside the limited scattering chamber without later blocking the scattered beam. The best compromise was found when the field direction is tilted  $11.5^\circ$  from the sample normal. Thus, the effective field applied on the superconducting  $\text{CuO}_2$  planes is reduced only by a factor 0.97, low enough to carry out the experiments. The highest magnitude of field obtainable with the magnet is 6 Tesla (T), which remains a limitation for comparison with NMR.

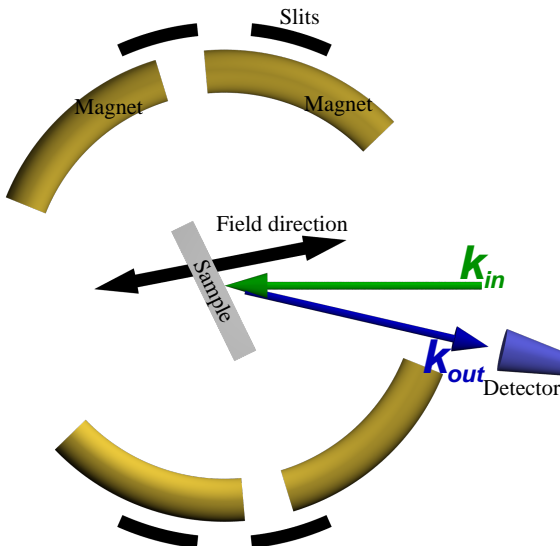


**Figure 5.25** A schematic of the scattering conditions needed to investigate the CDW under field within the high magnetic field scattering chamber.

A thorough summary of the results of investigating the CDW in scattering under applied field is shown in Fig. 5.26. Panel (a) shows the temperature dependent intensity at  $Q_{CDW}^K$

at zero and 6 T. The effect of suppressing the SC state is seen by observing the increase in overall intensity of the CDW peak in below  $T_c$  (shown as a dotted line), while above it the intensities with and without field are equivalent. Likewise, the same behavior trademark of a fluctuating order is seen in the temperature dependence of the FWHM under both extremal fields. Notice the correlation length is higher within the SC state when the field is applied. The lower panels of Fig. 5.26 (c-d) show the behavior under field of  $Q_{CDW}^H$  and  $Q_{CDW}^K$ . Beyond the fact that the modulation vector of the CDW does not change upon applied field (not shown), panel (c) shows that both  $Q_{CDW}^{H,K}$  increase linearly and with the same slope, with no visible crossing of the intensities. The FWHM's dependence on magnetic field also shows the same behavior for both directions, showing how the CDW order tends to higher correlation degree with suppression of the SC state.

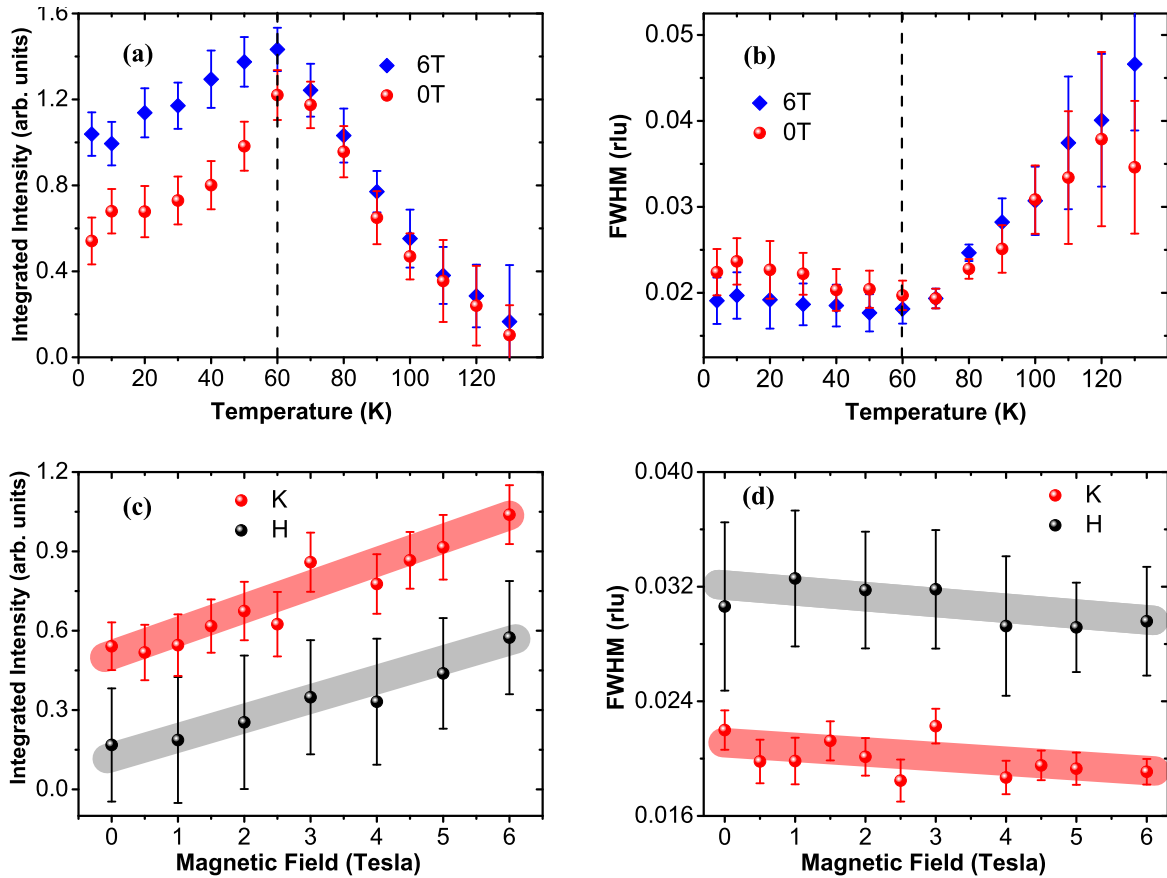


**Figure 5.26** A comparison between the temperature dependence of the intensity (a) and FWHM (b) of  $Q_{CDW}^K$  with 0 and 6 T. The lower panels show the dependence of the intensity (c) and FWHM (d) on the magnitude of the applied field.

### 5.2.1 Discussion and conclusions

With the observation of fluctuations of CDW order in YBCO, all superconducting cuprates have now shown direct evidence of charge order tendency, although sometimes using different techniques. We note here that during the writing stage of this PhD project in a collaboration with other groups, we have identified RSXS evidence of charge order in Bi- and Hg-based, layered cuprates [200, 201]. This bolsters the case supporting ubiquitous charge order in

the superconducting cuprates. In the stripe ordered cuprates, almost gapless spin excitations coexist with the charge order and their modulation periods are connected. In YBCO, however, a CDW peak was detected in doping levels where gapped spin excitations reveal no static magnetic order. The scattering experiments are qualitatively consistent with the suspicion of a FS reconstruction in underdoped YBCO arising from an underlying ordered phase, founded on measurements of quantum oscillations and NMR. Although these experiments are done in high magnetic field that destroy the SC state, the new periodicity revealed by x-ray scattering experiments exists at zero field. This allows to investigate the interplay of the CDW with the SC phase.

The zero-field temperature dependence of the CDW scattered intensity at several doping levels strongly suggests a competition taking place below  $T_c$  between the CDW and the SC state. Furthermore, the temperature dependent correlation length above the SC state (Fig. 5.22) shows evidence of a fluctuating rather than static order. Finally, the reemergence of the CDW peak upon applying an external magnetic field shown in Fig. 5.26 and its discussion, clearly shows how the competition between two ordered states takes place, and how external parameters that suppress one (SC), enhance the other (CDW). A similar scenario of a competing SDW and SC state was suggested for doping levels below  $x < 0.45$  [150, 186], adjacent and close to the doping level investigated here. So how to combine the latter observations? When comparing the intensity of the CDW peak for single crystals of  $\text{YBCO}_{6+x}$  measured along  $\mathbf{Q}_{CDW}^K$ , a decrease in intensity when approaching the SDW phase can be observed (the drop along  $\mathbf{Q}_{CDW}^H$  is even more enhanced), as shown in Fig. 5.27(left). This suggests the destructive influence of the spin correlations on the CDW, the former of which is believed to be in competition with SC [186].

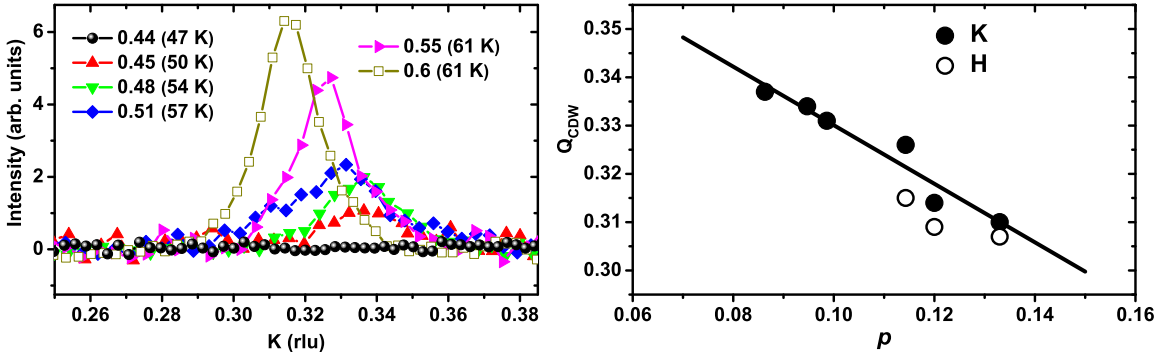


**Figure 5.27** (left) A comparison of the intensity and position of  $\mathbf{Q}_{CDW}^H$  between samples of  $\text{YBCO}_{6+x}$  with varying  $x$ , taken at their respective  $T_c$ , labeled in the legend. (right) The dependence of the modulation vector  $\mathbf{Q}_{CDW}^H$  and  $\mathbf{Q}_{CDW}^K$  as a function of doping. Samples with lower doping do not show a peak along  $H$ . The sample with  $x = 0.75$  was measured at the Canadian Light Source, reported in Ref. [193].

To investigate the (seemingly negative) influence of the spin correlations on the CDW, we studied the presence of CDW order in  $\text{YBCO}_{6.6}$  crystals doped with 2% of spinless zinc (Zn) ions. These ions substitute the Cu ions within the SC planes and are known to locally suppress SC [202] reducing  $T_c$  of our sample to 30 K, slow down the magnetic fluctuations and closing the spin gap [203], and induce incommensurate magnetic order ([204]) similar to the one observed in pure  $\text{YBCO}_{6+x}$  at lower doping levels [149, 150]. The effect of introducing

impurities into a YBCO<sub>6.6</sub> single crystal is observed in Fig. 5.28. Panel (a) shows that while a CDW peak is still present for the Zn-doped sample measured at its  $T_c$ , its intensity is reduced by a factor of  $\sim 4$  with respect to its pristine counterpart. The wavevector of the CDW is not modified by the impurities, which considering the results of Fig. 5.27 makes the case consistent with the fact that the impurities do not modify the doping level, as argued in Ref. [204]. The reduction in intensity and the increase of the FWHM and thus a shorter correlation length is consistent with a picture in which the CDW is suppressed in the vicinity of the Zn-ions, where the spin correlations are stronger. In addition, there is no apparent relation between the modulation vectors of the respective density waves, as shown in Fig. 5.28(b), which compares the background subtracted CDW peak at  $\sim 0.31$  rlu and the incommensurate magnetic diffraction peak, with modulation  $\sim 0.1$  rlu. This supports the observation that the two orders are decoupled, in contrast to the stripe order scenario discussed previously.

Finally, panel (c) of Fig. 5.28 attest to the presence of a competition between the CDW and SC state. In this case, the doped sample does not reduce intensity below  $T_c$  in such evident fashion like the pristine sample does, but the FWHM (inset) does show a minimum at  $T_c$ , once again, suggesting a fluctuating phase, reduced in volume fraction from the presence of a SDW.

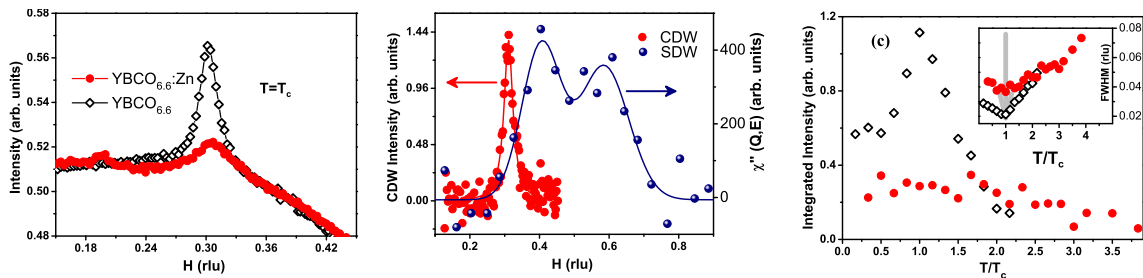


**Figure 5.28** (a) A comparison of the intensity and position of  $Q_{CDW}^H$  between pristine YBCO<sub>6.6</sub> and 2% Zn-doped YBCO<sub>6.6</sub>, taken at their respective  $T_c$ . (b) Overlaid are the CDW and SDW peaks, the latter reproduced from neutron scattering experiments cited in Ref. [204]. (c) A comparison of the respective temperature dependencies between clean and doped YBCO<sub>6.6</sub> of the integrated intensity and FWHM (inset).

Therefore, three main conclusions can be drawn from the collection of observations related to CDW order in single crystal, underdoped YBCO. First, **there exists a CDW in YBCO<sub>6+x</sub> with  $0.45 < x < 0.75$ , with anisotropic modulation and intensity along both in-plane crystal directions  $a$  and  $b$ .** The discrepancy in intensity between  $a$  and  $b$  grows as  $x$  decreases, presumably because of the Coulomb potential of ordered chains and/or a FS with anisotropic properties resulting from it. The  $q$ -vector's dependence on doping as seen in Fig. 5.27(right) is consistent with a FS whose overall size is changing with doping. This supports the second conclusion: **the CDW may be connected to a Fermi surface reconstruction.** This conclusion is in agreement with the amounting evidence of changes in the FS discussed previously. Moreover, we propose that the CDW is an instability of the pseudo-gapped FS, rather than attributing the pseudogap to the CDW phase. The latest RSXS experiments were done on Bi-based cuprates, where the observed CDW modulations can be connected to the fermiology studied by surface-sensitive probes like ARPES and scanning tunneling microscopy. Here, a connection will be made between FS features and the

CDW phenomenon, and will be reported in the next months [200, 201].

The final conclusion is about the interplay of the several ordered states present in the underdoped phase diagram of YBCO. The set of data collected here suggests a strong competition between the SC, SDW, and CDW states. **In the underdoped region of the phase diagram of  $\text{YBCO}_{6+x}$ , close to  $x \sim 0.5$ , there is an proximity of 3 coexisting phases, which are in mutual competition.** This is shown in Fig. 5.29, and explains why the quantum oscillation NMR experiments required high magnetic fields to reveal the effect of a FS reconstruction. This conclusion, once again, is supported by the observation of a suppression of the CDW order in the SC state with magnetic field, as well as by introducing spinless impurities which also locally suppress SC and enhance SDW.

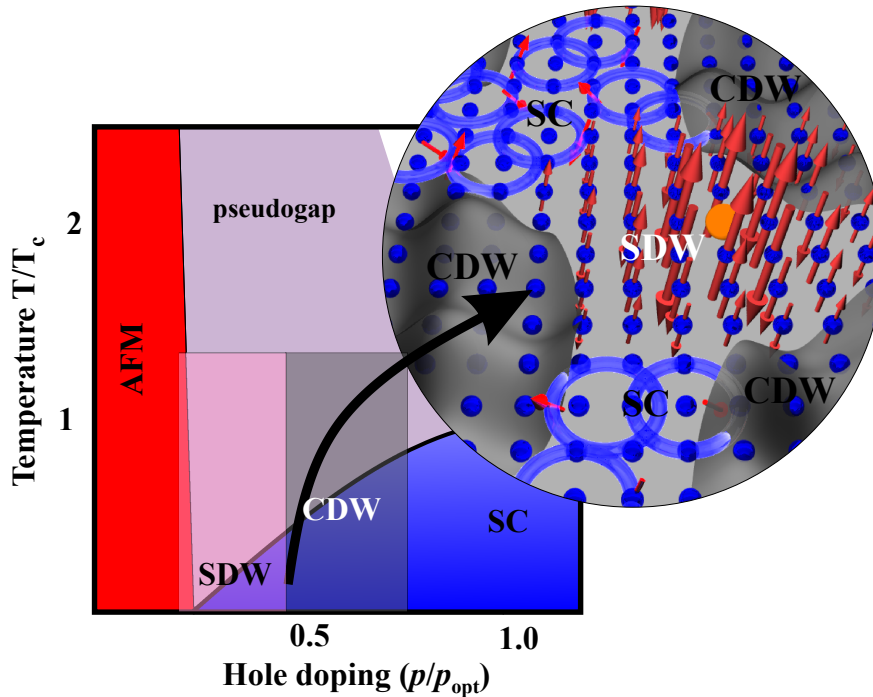


**Figure 5.29** A phase diagram summarizing the conclusions drawn from work done in this thesis about the competition of 3 phases within the  $\text{CuO}_2$  planes of single crystal  $\text{YBCO}_{6+x}$ . In the underdoped regime, close to  $x \sim 0.5$ , there is an proximity of the SC, SDW and CDW phases. The cartoon inset shows how the 3 phases that coexist in the Zn-doped (yellow ion) samples of YBCO compete for the real estate within the  $\text{CuO}_2$  planes.

## 5.3 CDW order in YBCO-LCMO heterostructures

### 5.3.1 Properties of heterostructured YBCO

We now turn to the results of a complimentary project involving YBCO grown into a superlattice (SL), creating layers of it adjacent to  $\text{La}_{2/3}\text{Ca}_{1/3}\text{MnO}_3$  (LCMO). Before discussing the experimental results, we first briefly outline the most important results in the YBCO-LCMO system. For a more thorough introduction to the basic aspects of the system, including the properties of bulk LCMO which motivate this entire class of heterostructures, we refer the reader to Chapter 2, and references therein.

One of the most important results observed in several occasions in the YBCO-LCMO system is a reconstruction of the magnetic profile of LCMO when layered between adjacent YBCO. Using magnetometry and magnetic neutron reflectivity, researchers were able to identify a remarkable change in the magnetization profile of the LCMO, which was attributed to either a suppression of the magnetization in the LCMO [39], or the emergence of an uncompensated ferromagnetic Cu moment in the YBCO layer [38]. In both cases, the appearance of an otherwise forbidden Bragg peak <sup>5</sup> strongly suggested a reconstruction of the magnetic properties at the interface. In the case of Ref. [38], moreover, the suggestion of the magnetism penetrating into the YBCO layer arose from the fitting of the reflectivity, as well as from the observation of the off-specular diffracted neutrons which showed a strong enhancement below  $T_c$  which suggests a mutual interaction between the SC state and the FM moments, which presumably live inside the YBCO.

The discussion between the two models for the magnetic profile of the YBCO-LCMO system remained intense and was further addressed using XAS tools. In work done by J. Chakhalian *et al.* [40], evidence of a FM copper imbalance was found, as seen by a sizeable XMCD signal at the Cu *L*-edge, with a temperature dependence similar to the one at the Mn edge, strongly suggesting an AF coupling through the interface. Moreover, a remarkable effect was seen in the off-specular magnetic neutron reflectivity below  $T_c$ , strongly evidencing the presence of lateral magnetic domains in the SC state. Later, we developed the story further by comparing YBCO interfaced against a FM-metal, LCMO, and a FM-insulator, LMO. Using neutron and soft x-ray reflectivity, we concluded that both scenarios are partially true [41]. While the neutron reflectivity favored the “dead layer” scenario for the YBCO-LCMO SL, the difference between the LCMO and LMO cases suggested that the LCMO close to the interface still has a magnetic moment, probably staggered by AFM interactions that originate at the interface, and was thus called “depleted layer” instead. These interactions are in competition with the conventional FM coupling in LCMO, which result in a complex noncollinear magnetic structure near the interface, presumably with a canted net moment. In this case, the reduced resulting FM moment detected by XMCD and neutron reflectivity is starkly reduced. Furthermore, using magnetic x-ray reflectivity, we determined that the magnetic moments are in the YBCO layers. This was concluded to be driven by an intimate magnetic coupling across the orbitally reconstructed YBCO-manganite interface.

Finally, the origin of the magnetic interactions across the interfaces was addressed using XAS on several different combinations of YBCO-LCMO stackings [42]. By comparing XAS measurements done in the TEY mode, sensitive to only a few nanometers (thus called a

---

<sup>5</sup>The SLs were grown with symmetric thickness of the YBCO and LCMO, thus the even-numbered SL peaks in the reflectivity should be structurally forbidden, as the period ideally introduces a phase shift of  $\pi$ .

surface probe), and fluorescence yield (FY), sensitive to a few ten nanometers (called a bulk probe), on YBCO-LCMO and LCMO-YBCO stackings, the authors identified a shift in the  $L_3$ -edge for the YBCO near the interface. This was attributed to the transfer of charge (electrons) from the LCMO into the YBCO. They estimated the amount of charge per Cu site, citing a value of  $0.2e$ , which even for optimally doped YBCO would bring it well into the AFM insulator phase. Furthermore, they showed that while in bulk YBCO the XAS is highly polarization dependent due to the single hole occupation of the  $d_{x^2-y^2}$  orbital (see Fig.'s 5.5 and 3.8), this linear dichroism was not apparent when looking at the interfacial YBCO. This suggested the presence of unoccupied states of  $d_{3z^2-r^2}$  symmetry, which implied a strong orbital reconstruction. Such a modification of the orbitals was suggested to form from a covalent bonding between the Mn and Cu ions, which is rather novel to occur across such interfaces. The AFM interactions that lead to the magnetic changes across the interface (both into the LCMO and YBCO) arise from this newly formed covalent bonding. The amount of charge transferred into the YBCO and its length scale are still topics of intense discussion. For the most part, this charge transfer is believed to be responsible for the drop in  $T_c$  with respect to bulk YBCO<sub>7</sub>. Although this could in general be attributed to the expelling of oxygen during the growth, it seems apparent that in well-grown samples this is not the case, as we will later show. In conclusion, widespread consensus exists that near the interface with LCMO, the effective doping level of fully oxygenated YBCO is lowered by charge transfer.

### 5.3.2 Experimental results

While the CDW phase in bulk single crystal YBCO is exclusive to the underdoped region of the phase diagram, the transfer of charge at the interface with LCMO will allow fully oxygenated YBCO to search out its phase-space, and could land in a CDW-unstable region. In addition, the LCMO interface could also alter the delicate competition between ordered phases in YBCO. For this reason, we chose to extensively investigate heterostructures of YBCO-LCMO and search for any evidence of a CDW state arising from the reconstruction at the interface. We investigated 3 samples: superlattices (SLs) of varying YBCO thickness and fixed LCMO layer thickness. As shown in Fig. 5.30, these were grown on (001)-oriented STO substrates. The number of layer repetitions varied as to keep the total thickness constant. These were the same samples investigated in the previous report from our group (Ref. [43]), for which the total thickness was in the order of a 300 nm (in that case, to ensure no Raman signal came from the substrate). In this case, as we will later see, the total thickness is of little relevance due to the low penetration depth of the soft x-rays, particularly on resonance.

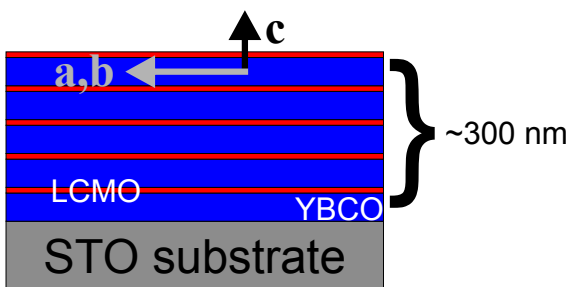


**Figure 5.30** A schematic of the PLD grown, YBCO-LCMO SLs investigated in this work. The layers of LCMO (green) were always 10 nm, while the three YBCO (red) thicknesses were 10 nm, 20 nm, and 50 nm, with a number of repetitions 15, 10 and 5, as to keep the total thicknesses similar.

From the practical and historical perspective, YBCO<sub>7</sub> was chosen due to its highest ability

to retain its stoichiometry during the pulsed-laser deposition as compared to intermediately oxygenated  $\text{YBCO}_{6+x}$  (details of the growth can be found in Ref's. [40,42]). However, careful characterization is needed to ensure that the oxygen content remains maximized ( $x = 1$ ). For this reason, we performed a thorough structural characterization following our expertise in investigating these properties, explained previously in Chapter 2. The results are shown in Fig. 5.31 for the extremal values of the YBCO thicknesses (the same behavior is seen when YBCO is 20 nm thick). The top panels are reciprocal space maps (RSMs) of the SL containing 100 nm of YBCO. On the left, panel (a) shows the vicinity of the substrate (002) peak, with very well defined SL peaks, attesting to the good sample quality. Since YBCO has a  $c$ -axis lattice constant about three times larger than STO (whose Bragg peak is clearly seen with the most intensity) and LCMO, the Bragg peak of YBCO seen in this map is actually the (006). From it, and other Bragg peaks with lower  $l$ -component, the  $c$ -axis lattice parameter of YBCO was determined to be 11.683 Å. This value corresponds reasonably to the bulk value of fully oxygenated YBCO [143]. This was also the lattice constant measured in the RSXS chamber when determining the orientation matrix at 1070 eV. With a comparable penetration depth to the 931.5 eV, this rules out any oxygen deficiencies within the layer probed by RSXS.

In addition, from the right panel (b), we can identify that both the YBCO and LCMO are fully relaxed, with Bragg spots falling on top of the relaxation line (red solid line). In such case, we identify the in-plane lattice constant to be 3.84 Å. We note here that the substrate grid being tetragonal will facilitate YBCO to form twin domains. Therefore, an average between the  $a$  and  $b$  lattice constants is measured. The lower panels of Fig. 5.31 show the corresponding diffraction patterns of the sample with 50 nm of YBCO, yielding similar lattice parameters. We note that these measurements were also carried out at lower temperatures, in particular below  $T_c$  and below the structural transition of STO. No changes in the structure were observed.

Another way to comparatively test the content of oxygen in the YBCO-LCMO SLs is XAS. As discussed previously schematically in Fig. 5.5, in underdoped  $\text{YBCO}_{6+x}$  with  $x \neq 1$ , there are three features present in the XAS around the Cu  $L_3$ -edge. Fig. 5.32 shows a comparison between XAS measurements taken in TEY mode (a) and FY mode (b) between a crystal of  $\text{YBCO}_{6.6}$  (solid blue line) and the YBCO-LCMO SL of 50 nm (solid red line), with light polarized along the in-plane direction, which would pick up the states in the  $\text{CuO}_2$  planes and CuO chains. The main feature around 931.5 eV is common to both systems, but the feature at 933 eV is dramatically suppressed in the SL, while the feature at 934.4 eV is essentially absent. These two peaks correspond to transitions into states that are characteristic of chains with empty oxygen sites, in particular the latter peak. In other words, a full suppression of the smaller features attests to the fact that the chains in the SL are fully oxygenated. We also note that there is a slight difference in the position of the main peak of the YBCO-LCMO SL between the two measurements. Measured in the surface sensitive mode TEY, the main peak is at 931.45 eV, while in the FY spectrum, it lies at 931.6 eV. Although this difference is small, the trend is in agreement with previous reports, where the charge transfer effect was cited as driving the shift in the edge position [42]. In that case, the shift was  $\sim 0.4$  eV, to which the authors estimated an upper limit of the transfer to be 0.2e. In our case, the shift is smaller and thus the charge transfer would imply to be smaller.

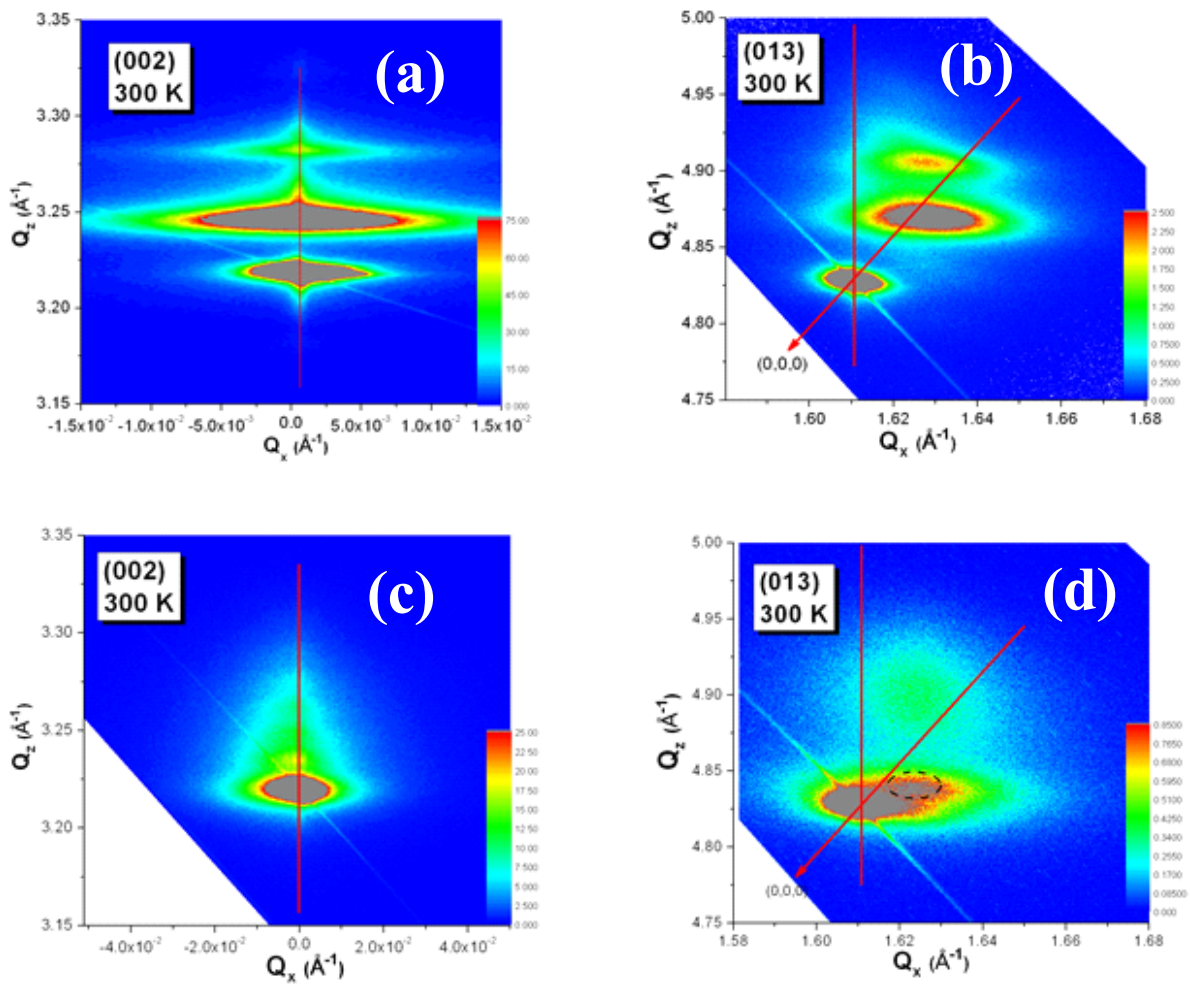


**Figure 5.31** Reciprocal space maps (RSMs) around the (002) (left panels) and (013) (right panels) for SLs with YBCO thickness of 10 nm ((a, b)) and 50 nm ((c, d)).

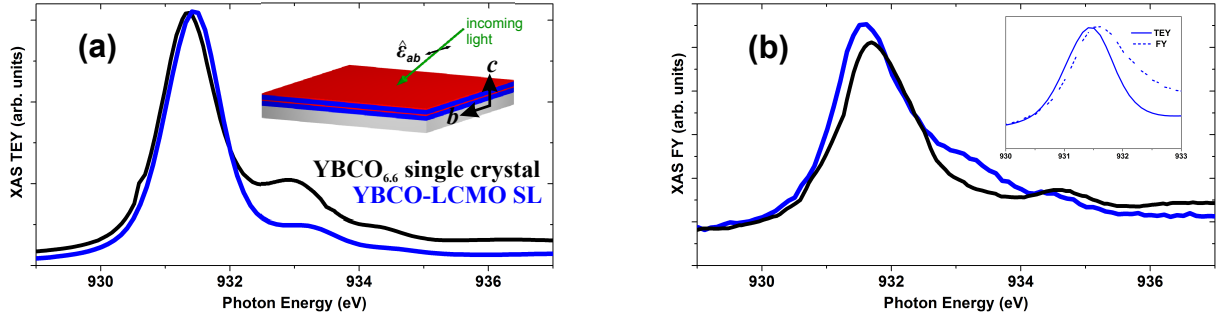


**Figure 5.32** A comparison between the XAS of a single crystal of YBCO<sub>6.6</sub> (blue) and the YBCO-LCMO SL (red), revealing a full oxygen content in the SL. Panel (a) shows the measurement in TEY mode, and panel (b) in FY mode. The inset in (b) shows the difference in the peak position when measuring in both modes.

Finally, the SC and FM transitions were monitored using a VSM-SQUID. While in all cases the Curie temperatures were found to be around 200 K, the SC transitions did vary with YBCO thickness. A summary of the samples measured in this investigation is shown in Table 5.1.

**Table 5.1** YBCO-LCMO SLs investigated in this thesis

Sample	YBCO (nm)	LCMO (nm)	N	$a(b)$ (Å)	$c$ (Å)	$T_c$ (K)
YBCO-LCMO-XX1	10	10	15	3.84	11.68	45
Y-LCM-084C2	20	10	10	3.84	11.68	60
Y-LCMO-ND1	50	10	5	3.84	11.68	82

### Alignment and Q-dependence

Having obtained plentiful experience in finding and characterizing the CDW of YBCO single crystals, the task of searching for CDW order in YBCO-LCMO SLs was rather straightforward. The alignment and scattering of the sample was done similarly to the single crystal case. In this case, the heterostructure has a (001)-surface, so identifying the  $c$ -axis is natural, while the in-plane directions are easily determined by the fact that STO substrates were cut by the manufacturer in a square that coincides with the cubic  $a, b$ -directions. This is shown in Fig. 5.33.

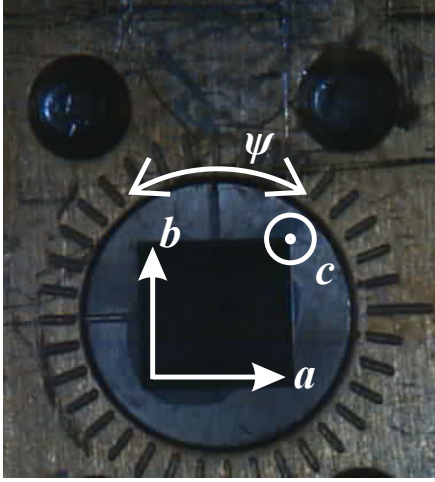


**Figure 5.33** A photograph of the YBCO-LCMO on STO mounted at the diffraction chamber at UE46-PGM1 at BESSY. The crystal axes shown follow the substrate grid, which is cut along the edges by the manufacturer of the substrate.

The scattering geometry used in this experiment, shown in Fig. 5.34, was the same as in the case of YBCO single crystals. The only difference is the fact that YBCO has relaxed and is fully twinned, shown as the equivalency between the (100) and (010) directions. The right of Fig. 5.34 visually shows the effective penetration depth of the soft x-rays by applying a transparency to the segment of the heterostructure which is undetected. On a  $L$ -resonance of  $3d$  transition metals, the penetration depths are found to be in the order of tens of nanometers. In our case, an estimate of the penetration depth at the top of the  $L_3$  white line (931.5 eV) yields a value of  $\sim 35$  nm, while the LCMO has a penetration depth in the order of several hundred of nm, making it transparent at the Cu edge. We note that these values are different to the tabulated values of Henke *et al.* [205], since they do not consider localization which gives rise to strong intensity at the  $L_3$ -edge. The intense absorption edge can decrease the penetration depth even several orders of magnitude. This implies that in this experiment, while most of the material detected is YBCO, only a small portion of the entire heterostructure is probed. In the case of the 50 nm-YBCO SL, only *one* layer of YBCO is probed. Respectively, experiments on the 20 nm-YBCO and 10 nm-YBCO SL capture  $\sim 1.5$  and  $\sim 3$  layers. The effect of going through more interfaces will be discussed later, when addressing the thickness dependence of the CDW peak.

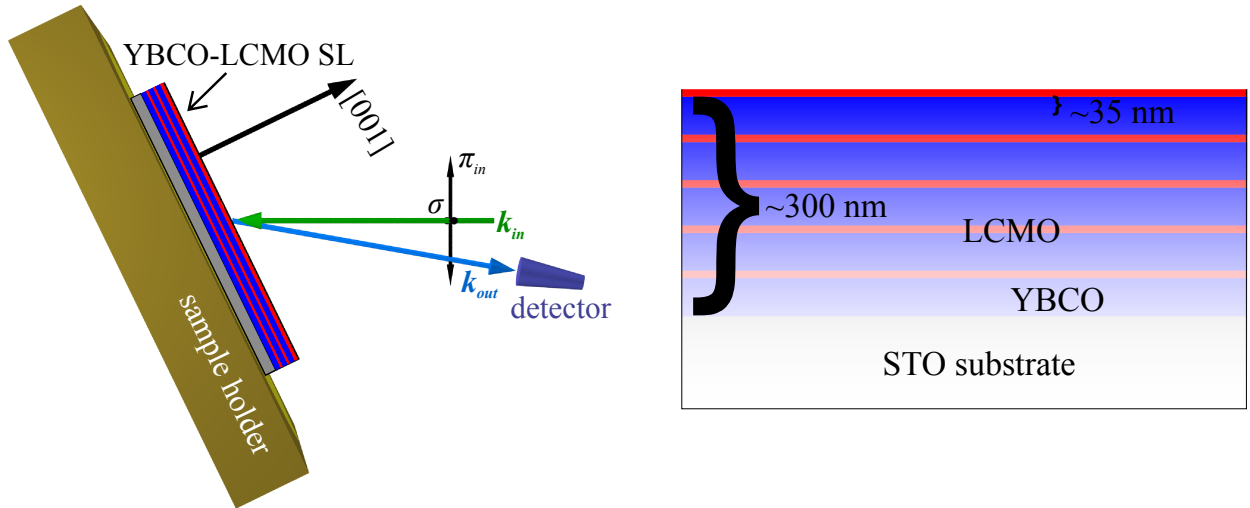


**Figure 5.34** (left) The top view schematic of the scattering geometry used in the investigation of CDW order in YBCO-LCMO SLs. The two in-plane directions are labeled since they are equivalent in YBCO due to twinning. (top) The schematic is reciprocal space (RS) of YBCO for photon energy of 931.4 eV. (right) The penetration depth of the soft x-rays on resonance is about 35 nm, thus only the top layer of the 50 nm-thick YBCO SL is probed.

The results of low temperature scans around the angles shown above, at 931.5 eV, for a 50 nm-thick YBCO-LCMO SL are shown in Fig. 5.35. A clear peak is seen around  $\sim 0.30$  rlu, defining  $\mathbf{Q}_{CDW}$ , much analogous to the case of single crystal YBCO<sub>6.6</sub>, shown in the figure for comparison, taken under the same conditions. In this case, however, the twinned YBCO system results in no difference between both in-plane directions. Moreover, the peak is also broader than in the single crystals, also presumably due to twinning. Recall from Fig. 5.20 that each direction has a slightly different  $\mathbf{Q}$ -vector, so in the twinned case the two directions are averaged out into one, broad, feature. However, quantifying the full intensity of the peak as  $I = (\text{height})(FWHM)^2$ , we obtain comparable values between the 50 nm SL and single crystal. A scan performed at lower detector angles, as shown, also yields a peak at the same  $\mathbf{Q}$ -vector, confirming the same kind of out-of-plane dispersion seen before. In addition, the same polarization dependence as in single crystals was observed.

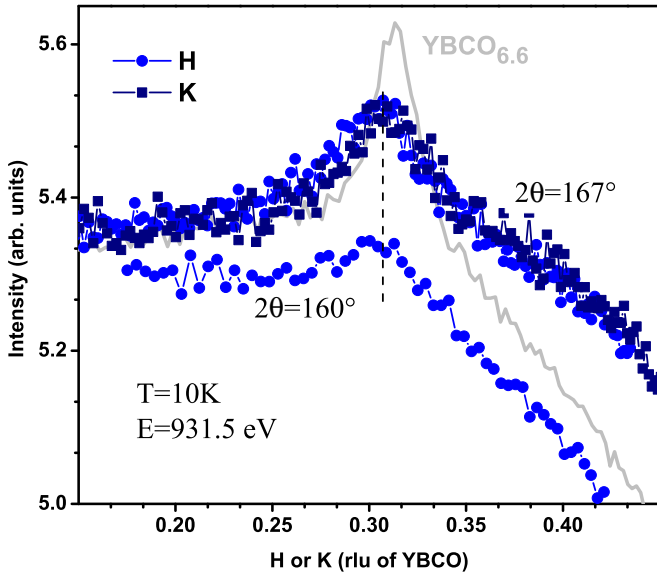


**Figure 5.35** Scans of a 50 nm-thick YBCO SL in both  $h$  and  $k$  directions show a clear peak centered around  $\sim 0.30$  rlu. For comparison, the same scan under the same conditions on a crystal of  $\text{YBCO}_{6.6}$  is shown (solid gray line). In addition, a scan taken at a lower detector angle still reveals the peak.

### Thickness dependence

The peak described above was in fact observed in all three SLs investigated. Now, we turn to examine the thickness dependence of the peak by comparing the three cases in detail. Note, once again, that whilst the amount of YBCO probed in each case is very similar, the thinner layered SLs will require the beam to traverse more interfaces. However, with that in consideration, we present the comparison in Fig. 5.36. Color-coded as labeled in the legend, the figure displays the raw data of all three SLs taken at 10 K. In addition to the low temperature scans, each case is individually compared to its high temperature counterpart data, shown as crosses adjacent to the color-coded scans. In the case of the 10 nm-YBCO SL, the peak is only barely visible as an excess of intensity at around  $Q_{CDW}$ , more easily identified when superimposed with high-temperature scan. The peak’s discernibility increases in the 20 nm-YBCO SL, and further manifests fully in the thickest SL.

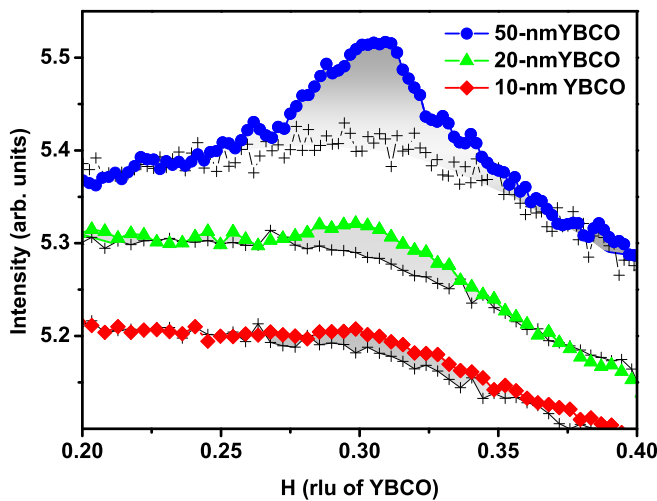


**Figure 5.36** A comparison of scans at 10 K around  $Q_{CDW}$  for all three SLs investigated here. The varying YBCO thickness is labeled in the legend. The color/symbol code introduced here will be used in the following figures of this section. Each set of data is directly compared to the corresponding high-temperature scan, after the peak has vanished.

To better understand the difference between the three SLs investigated, a thorough peak

analysis was done for each case. As Fig. 5.36 shows already, the background in these scans is not a flat, straightforward, easy-to-deal-with shape. So to quantify the intensity and width and identify the position  $Q_{CDW}$  of the peaks, a careful background subtraction procedure was done. In each case, the high-temperature scans were fitted to a 3<sup>rd</sup> order polynomial ( $F(Q) = a_0 + a_1Q + a_2Q^2 + a_3Q^3$ ), such as to have the data fall exactly on the fitted curve. We note that higher order polynomials also yielded satisfactory fits to the background, but for clarity and simplicity, the lowest fitting order was used. Once the background is subtracted, a Lorentzian curve was fitted to the peak without any constraints.

The results of the background-subtracted, fitted Lorentzians is shown in Fig. 5.37. The right panel compares the Lorentzian fits for all three YBCO thicknesses, normalized to their corresponding peak height, following the color/symbol code of Fig. 5.36. On the left panel, a comparison of the obtained results is shown. The solid symbols, referenced to the left vertical axis, reveal the position of  $Q_{CDW}$  for each case. A clear trend of a decreasing modulation length as function of thickness can be readily observed (highlighted by the thick gray line). Moreover, the peak intensity shown by open symbols, calculated as described earlier in this section, is compared on the right vertical axes. In this case, the peak intensity is clearly trending to higher values as the YBCO layer increases, as noted by the dotted gray line. Later in the Discussion, we explain this data in connection to the observation of competing phases in YBCO.

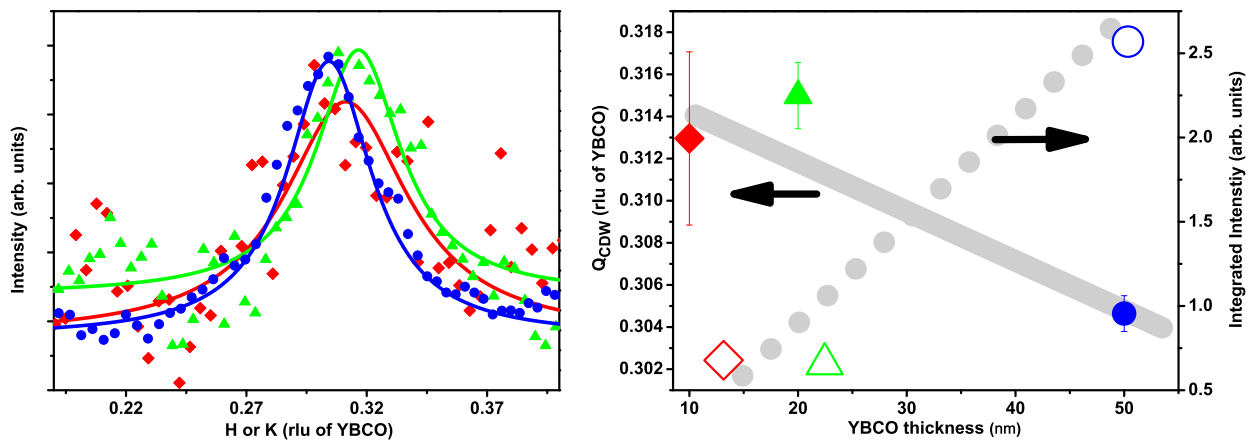


**Figure 5.37** (left) The Lorentzian curves fitted after background subtraction for all three cases. (right) The result of the peak analysis yields a comparison of the position of  $Q_{CDW}$  shown as solid symbols (right vertical axis) and the peak intensity shown as open symbols (left axis).

### Energy dependence

As in the former case of characterizing the CDW peak in single crystal YBCO, we investigated the energy dependence of the peak observed in the YBCO-LCMO system. In this case, there are no ordered CuO chains, or in strict sense, they are fully ordered (O-I order). So there is no oxygen superstructure peak to be ruled out, and the spectroscopy reveals that there are essentially no empty chains. However, to confirm that the peak is indeed of the same origin as in the single crystal case, Fig. 5.38 compares the integrated intensity, following the procedure described above, to the XAS data of the 50 nm-YBCO SL. A clear resonant behavior is seen at 931.5 eV, suggesting the electronic origin of the peak. A comparison of

the energy lineshape between single crystals and SLs reveals no difference, confirming the same origin. The same trend was observed for the other two SLs.

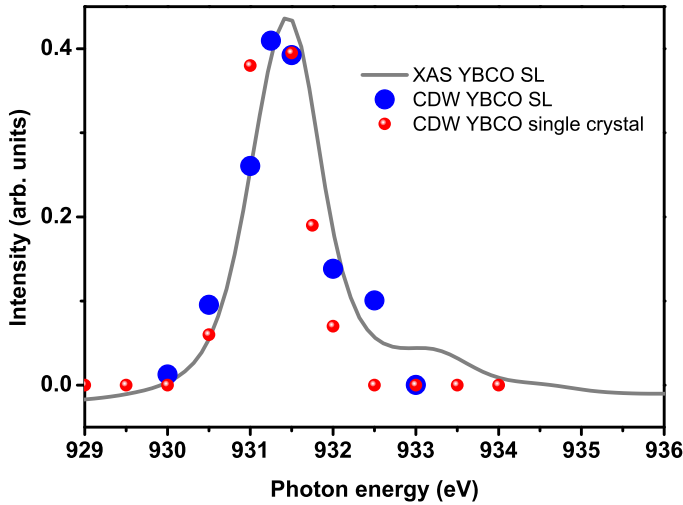


**Figure 5.38** The energy dependence of the reflex at  $Q_{CDW}$  (solid blue circles) compared to the XAS spectrum (black line), for the 50 nm-thick YBCO SL. The same resonant dependence was recorded for the other SLs investigated.

### Temperature dependence

So far, the behavior of the CDW order in YBCO SLs shows close resemblance to the single crystals. However, a remarkable difference is observed in its temperature dependence. The measurements were done in the same fashion as the single crystals, correcting for the sample height at each temperature. The homogeneity of the sample was also tested and found to be pristine, as expected for PLD grown heterostructures. Figure 5.39 shows the result of the peak analysis, as described above, as a function of sample temperature for the 20 nm- and 50 nm-thick YBCO SL, color coded as labeled. As a reference, the data of the YBCO<sub>6.6</sub> single crystal is shown as red crosses, reproduced from Fig. 5.22. The thinner 10 nm-thick YBCO SL shows the same behavior but with a considerably weaker peak. Its analysis is more complicated and thus left out of the discussion. The top panel, first of all, shows the temperature's effect on the integrated intensity of the peak. With an onset temperature of approximately 120 K, similar to single crystals, upon cooling the peak rapidly grows in intensity over the next  $\sim 30$  K, reaching a maximum at around  $\sim 90$  K. Thereafter, cooling further down results in no visible change in the intensity. In other words, there is no anomalous behavior upon entering the SC state. Remarkably, the same “order parameter-” like behavior is observed in all SLs, which have a considerably different  $T_c$ , in stark contrast to the single crystal's drop of the CDW below  $T_c$ .

Even more remarkably, the peak's FWHM, quantifying the correlation length of the order parameter, does not change at all throughout its temperature span, as shown in the lower panel of Fig. 5.39. Albeit with a slightly larger width compared to the single crystal case (shown as well), the CDW order retains the same correlation length upon going through the SC phase transition. This suggests that the CDW order in the YBCO SLs is not fluctuating nor submissible to the SC phase. The peak in this case appears to saturate fully shortly after it sets in, and completely disregards the  $T_c$ .

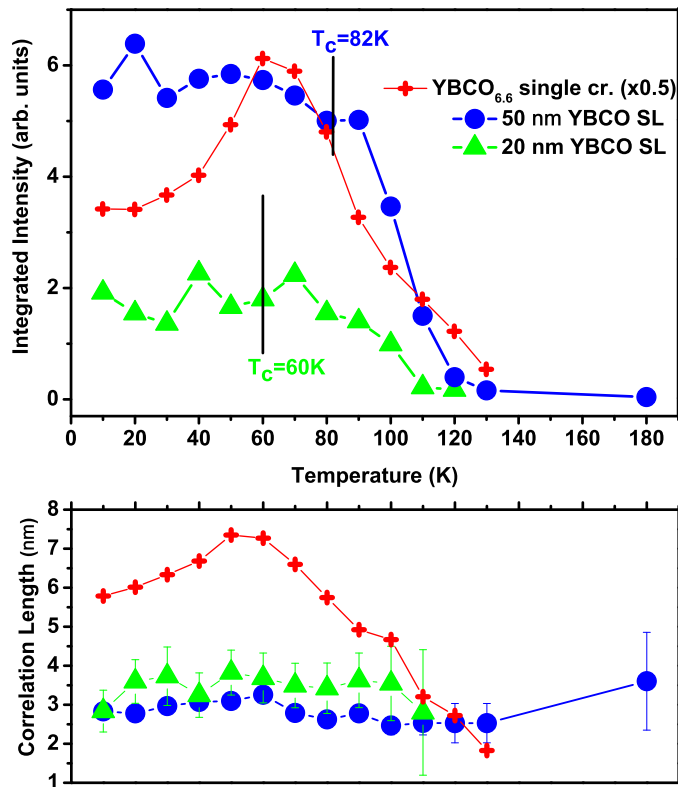


**Figure 5.39** (Top) The temperature dependence of the CDW peak in two labeled YBCO SLs, each with different  $T_c$  as noted, compared to the equivalent data of the YBCO<sub>6.6</sub> crystal (normalized for clarity). (Bottom) The dependence of the peak's width which yields its correlation length for the same two SLs. For comparison, in both panels the data for the YBCO<sub>6.6</sub> (with  $T_c=61$  K) crystal is also shown as red crosses.

### Magnetic field dependence

To further test the saturation level of the CDW peak in YBCO SLs, we performed experiments to investigate the CDW order under applied magnetic field. The scattering geometry utilized is the same as shown in Fig. 5.25. The only major difference in this case is the fact that the interface contains ferromagnetically aligned Mn moments, which are in the order of a few Bohr magnetons [40]. However, these moments lie in the plane, and are thus only somewhat canted when applying a field which is mostly out-of-plane. In addition, the sample was zero-field cooled. Therefore, the presence of additional Mn moments will only marginally add to the effective field felt by the YBCO, rendering the effect it could have comparable to the single crystal case, as shown in Fig. 5.40.

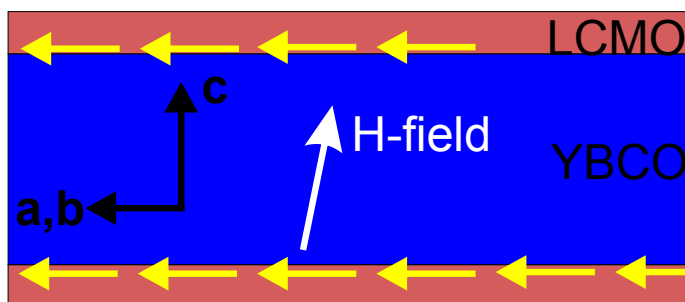


**Figure 5.40** A schematic of the applied field in relation to the YBCO-LCMO interface, indicating the direction of the Mn moments.

In a striking result, however, scans taken at different magnitudes of applied magnetic field at 4 K reveal no increase of the CDW order. Fig. 5.41 shows three background-subtracted scans at different fields, for the case of the 50 nm-thick YBCO SL. In all cases, the same

peak intensity and width was recorded. The inset shows the integrated intensity's non-dependence on applied magnetic field. In contrast once again to the single crystal, the peak at low temperature is fully saturated and will not enhance in intensity upon suppressing the SC state.

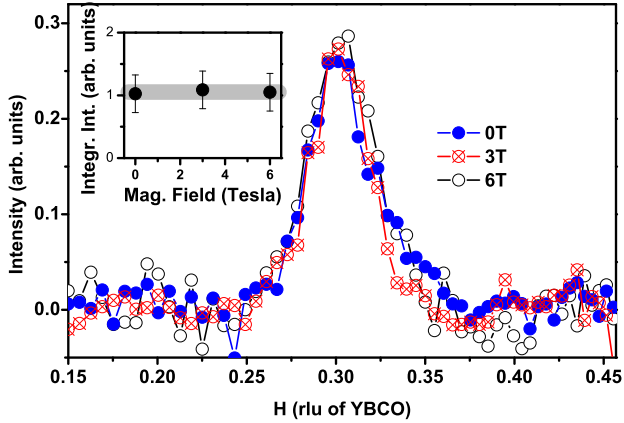


**Figure 5.41** The dependence of the CDW peak on external magnetic field of a 50 nm-thick YBCO SL. The main inset shows the background subtracted peaks at three field magnitudes, labeled in the legend. The inset shows the peaks's independence on applied field.

### 5.3.3 Discussion and conclusions

Now, we turn to discuss the essence of the results observed in the study of CDW order near the interface of optimally doped YBCO-LCMO SLs. The first issue to review is the question of how the YBCO gets to the CDW phase. First of all, during the growth a fully stoichiometric target of YBCO<sub>7</sub> was ablated. To ensure the right chemical environment, the growth process took place under a high oxygen pressure of 0.5 mBar, with the substrate at 750°C. These conditions are optimized to enable the growth of YBCO<sub>7</sub> heterostructures. However, despite the experience we have in creating these heterostructures, retaining the stoichiometry is always a challenge, so there exists the possibility of YBCO expelling oxygen during the growth. Therefore, there are two scenarios that could bring the optimally doped YBCO into the CDW phase, schematically described in Fig. 5.42.

One possible scenario is one of a grown layer of YBCO which is homogeneously oxygen deficient as compared to YBCO<sub>7</sub>. In this case, shown in Fig. 5.42(a), the SC layer is a uniform YBCO<sub>6+x</sub>. A second scenario is that of the charge transfer effect lowering the doping at the interface from  $p_{opt}$  (Fig. 5.42(b)). The extent of this reconstructed area is still under debate but is expected to have an upper limit of a few nm [42, 206], apparently increasing when considering rough interfaces. The characterization we have described in Sec. 5.3.2 suggests in favor of the charge transfer scenario. Furthermore, a close look at the frequency of the Raman phonon which couples to the apical oxygen vibration, highly bulk-sensitive to the oxygen content, is also consistent with a fully oxygenated system, as explained in Ref. [43].

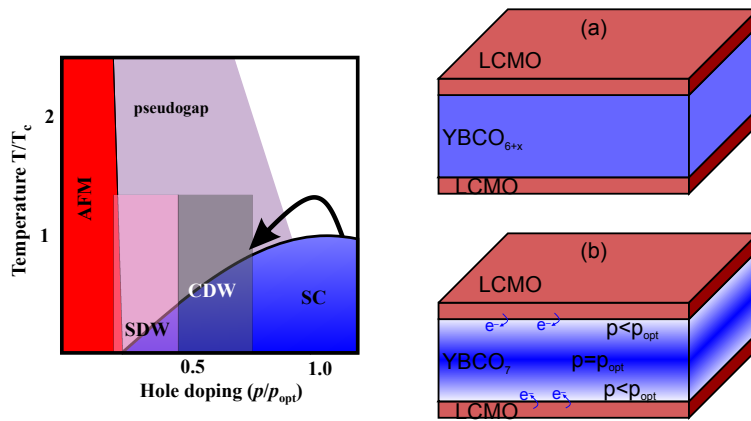


**Figure 5.42** The two scenarios that could result in bringing optimally doped YBCO into the CDW phase near the LCMO interface: (a) the charge transfer of electrons at the interface and (b) the loss of oxygen stoichiometry during the growth, creating a homogeneous layer of oxygen deficient  $\text{YBCO}_{6+x}$ .

The thickness dependence of the CDW characteristics in YBCO SLs contains important information by closely looking at Fig.'s 5.36-5.37 under the light of Fig. 5.27. Previously, we attributed the change in  $Q_{CDW}$  as function of doping to the changes in the size of the FS that presumably occur around these doping levels. The trend of increasing  $Q_{CDW}$  in the superlattices suggests that the doping level is lower, and so the loss of intensity can be also understood as the approximation of the CDW phase to the nearby, competing SDW phase. Although twinning precludes an exact identification  $Q_{CDW}^{H,K}$ , we can estimate the effective doping levels by comparing  $Q_{CDW}$  of the single crystals to the SLs. Fig. 5.43 shows that the 50 nm-SL has  $p \gtrsim 0.14$ ,  $p \sim 0.13$  for the 10 nm-, and  $p \sim 0.125$  for the 20 nm-YBCO SLs.

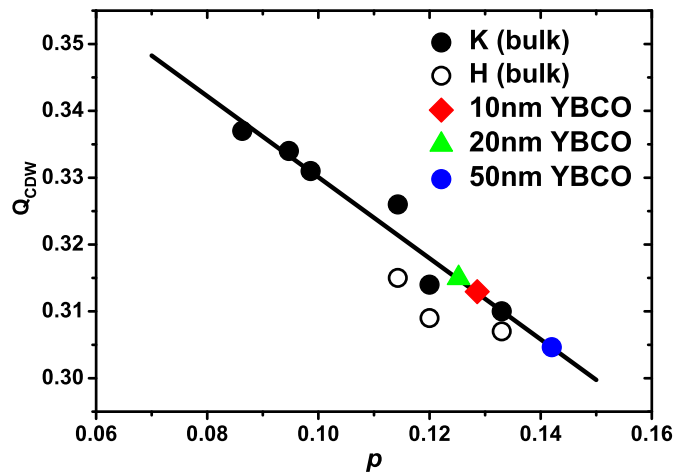


**Figure 5.43** By comparing the values of  $Q_{CDW}$  between single crystals and SLs, an estimate of the doping level in the SLs can be made.

The thickness of the YBCO layer also affects the intensity of the CDW peak. In the layers with  $\lesssim 20$  nm, the proximity to the SDW adjacent to the AFM insulator phase at the interface will reduce the CDW parameter. However, in the SL with 50 nm, the situation allows the CDW to find “breathing area”. A long-range proximity effect presumably extends the CDW ordered phase well into the interior of the layer, resulting in a peak with more intensity. These ideas are summarized in Fig. 5.44.

Perhaps the most striking result in the investigation of YBCO SLs is the temperature dependence of the CDW order. From Fig.'s 5.41-5.39, we conclude that the CDW phase is maximally enhanced in the SL case. In other words, the difference between the two systems

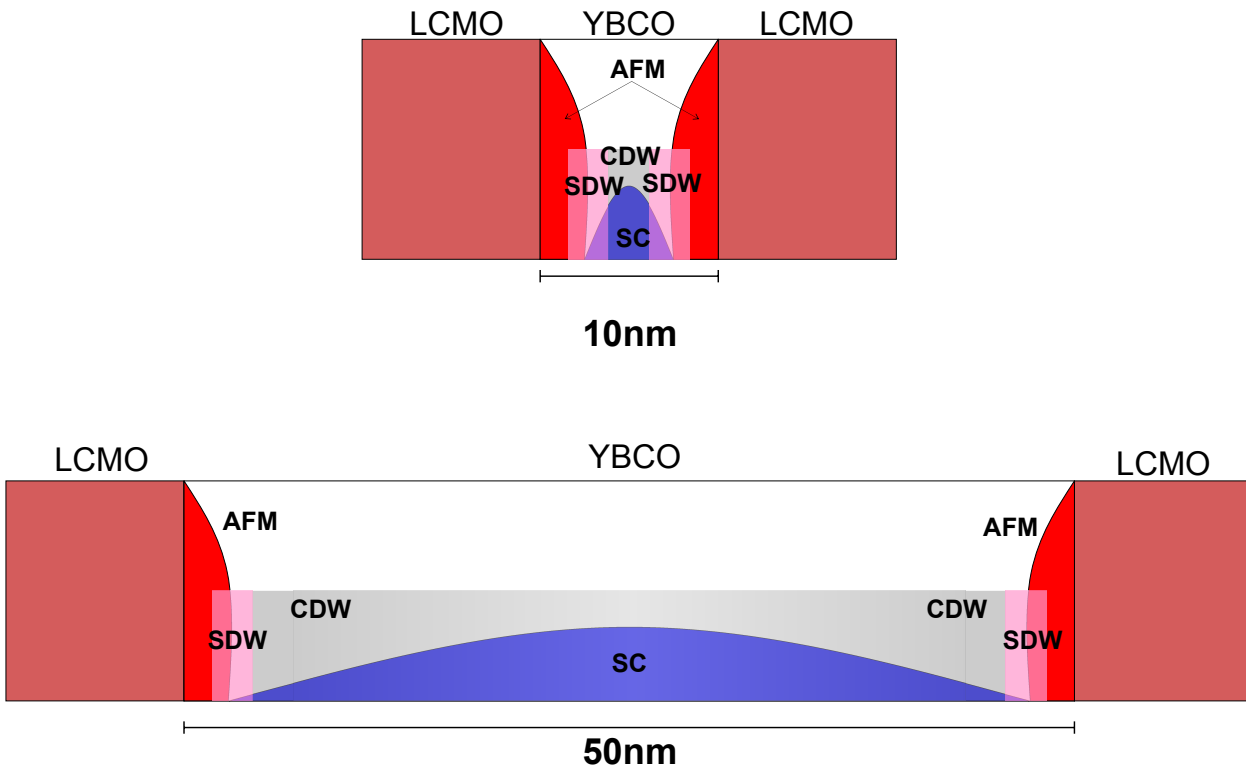


**Figure 5.44** A tomography of the behavior within a layer of YBCO adjacent to LCMO layers which could explain the reduction of CDW intensity with decreasing thickness.

at low-temperatures implies a different mechanism of stabilizing the CDW at the YBCO-LCMO interface. To possibly account for these facts, we discuss several plausible origins. First of all, one wonders how epitaxial strain would anyway alter an incommensurate ordering phenomenon. In this case, however, reciprocal space mapping confirms epitaxial strain of the substrate does not play a role in these heterostructures, since the YBCO is evidently fully relaxed to its bulk lattice parameter.

Second, the magnetization of the LCMO acting on the YBCO can be ruled out on grounds that SQUID measurements confirm the LCMO moments lie in-plane and thus only marginally affect the SC state across the interface (Fig. 5.40), let alone saturate the CDW order parameter at low temperatures without considerably reducing the  $T_c$  with respect to single crystal YBCO<sub>7</sub>. The tendency of Cu to align uncompensated magnetic moments across the interface [38–41] could offer another account. In this case, the exchange “field” generated by the AFM interaction of the Cu moments could locally alter the competition between superconductivity and CDW, allowing the latter to maximize its intrinsic state. Then, applying an external field would only slightly enhance the effective magnetization, leaving the CDW unaffected. However, this notion is challenged by observing how single crystal YBCO behaves under applied field. Fig. 5.45(a) shows the resulting temperature dependence of the CDW-peak for YBCO<sub>6.55</sub> with and without field, measured at the UE46-PGM1 beamline. The maximum applied field of 6 T reduces the  $T_c$  from 62 to  $\sim$ 55 K. In Ref. [195], the authors were able to apply up to 17 T to YBCO<sub>6.67</sub> (hard x-ray diffraction experiments have less limitations to use large magnetic fields). This data is reproduced in panel (b) of Fig. 5.45, normalized to its maximum intensity, which in this case occurs at

$T_c=25$  K. The onset temperature coincides with the zero field investigation (not shown), but the drop below  $T_c$  is less obvious, due to the weakening SC phase. In addition, the roundedness of the phase transition presumably arises from the competition taking place between different order parameters, slowing down the onset of the CDW.

In stark contrast, the temperature dependencies of the two thicker YBCO SLs, normalized to their maximum value at lowest temperature and *not at*  $T_c$ , are shown in Fig. 5.45(b). A field suppressing the SC state in the SL would render a more rounded temperature dependence with a maximum that scales down with decreasing  $T_c$ . Thus, the magnetic interaction across the interface stabilizing the CDW appears unlikely. Despite the difference in  $T_c$  between the samples, the temperature dependencies of the SLs are the same. In contrast to single crystal YBCO, the transition in the SLs is apparently supported by a nucleation effect which allows the CDW phase to enter despite the competition with the SC state.

So if neither the magnetic interactions nor the strain are responsible for the stabilization of the CDW, then what is? An intriguing explanation arises when considering results emanating from our group. In a recent study, Le Tacon *et al.* characterized the CDW order in YBCO<sub>6.6</sub> using non-resonant, hard x-ray, high resolution IXS (with even higher resolution than used in Ref. [192], attainable in the hard x-ray regime), motivated to understand the role of electron-phonon coupling in the superconducting cuprates [197]. In one of the findings of the investigation, the authors found a peak at  $Q_{CDW}$  with minimal energy loss (no more than 1 meV). This quasi-elastic “central peak” has a temperature dependence peaking at  $T_c$ , but more strikingly, it remains present at temperatures well above it. This implies that slowly fluctuating CDW domains, of a few nm in size, are formed at temperatures as high as 150 K, well above the onset seen in RSXS. Such a behavior was observed in other materials which are about to undergo a first order structural phase transition, such as the quintessential perovskite STO reviewed in Ref. [207], and in superconducting Nb<sub>3</sub>Sn [208]. The behavior was attributed to the formation of defect-induced nucleation of domains of the low temperature phase even well above the transition temperature. The nucleation of CDW domains, common to first order phase transitions, is in this case uniquely in competition with the SC phase.

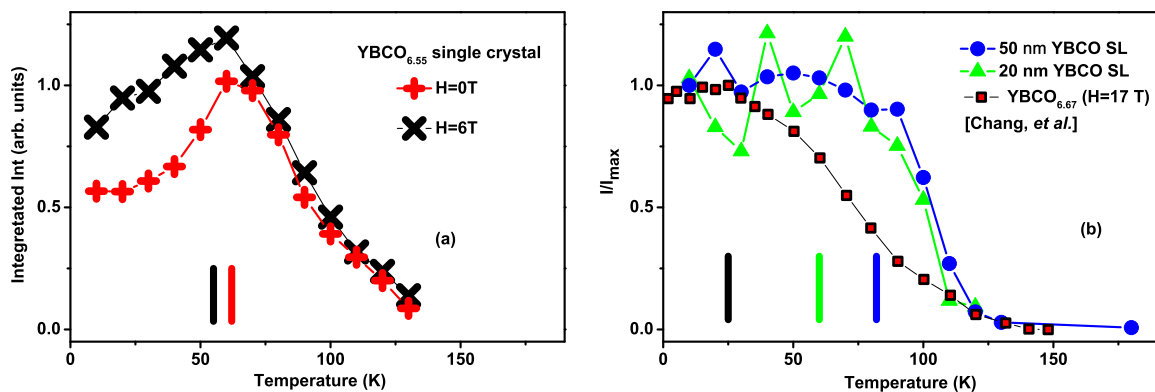


**Figure 5.45** (a) The temperature dependence of the CDW-scattered intensity for a YBCO<sub>6.55</sub> single crystal, without and with external magnetic field, with  $T_c$  of 55 and 62 K, respectively. (b) The comparison of the temperature dependence between the YBCO SLs investigated here and the YBCO<sub>6.67</sub> crystal under 17 T magnetic field of Ref. [195], normalized to their maximum intensity value. The  $T_c$ 's are labeled as color-coded bars (25, 60, 82 K).

The transition to a CDW phase in the YBCO SL is apparently supported by a nucleation effect much stronger than the single crystals, as the temperature dependence of the RSXS signal suggests. The concentration of defects in PLD grown heterostructures is found to be comparable to that of single crystals, by comparing the widths of the structural and CDW peaks. Thus, unless the concentration of defects in the SL is infinitely higher than in single crystal, which would broaden the peaks beyond our detection, a higher defect-induced nucleation in the SL is unlikely. However, there is another “defect” which inherently lives in this class of heterostructures: the interface. An infinite surface truncation, or defect, may be plausible to efficiently nucleate the phase transition. This suggests an intriguing scenario where the interface itself acts as a defect which nucleates the electronic CDW phase. It allows a phase transition to rapidly find its absolute energy minimum, resulting in the temperature dependence displayed above. So, in conclusion, we propose that **the interface between oxides can act as an electronic phase transition nucleator, tipping the balance between competing phases**. In analogy to the famous phrase coined in Herbert Kroemer’s Nobel Prize lecture in the context of semiconductor heterostructures, we conclude by stating that perhaps the interface can be a phase transition nucleator.

# Appendices



# Appendix A

## The Kramers-Kronig Relations

The Kramers-Kronig relations, as described in [209], are given by

$$\begin{aligned} f'(\omega) &= \frac{2}{\pi} \mathbf{P} \int_0^{+\infty} \frac{\omega' f''(\omega)}{(\omega'^2 - \omega^2)} d\omega' \\ f''(\omega) &= -\frac{2\omega}{\pi} \mathbf{P} \int_0^{+\infty} \frac{f'(\omega)}{(\omega'^2 - \omega^2)} d\omega', \end{aligned} \tag{A.1}$$

where  $\mathbf{P}$  is the Cauchy principal value defined for integrals with divergences. Mathematically, the Kramers-Kronig relations are formulated based on Cauchy's theorem which addresses the contour integral shown in Fig. A.1 for an analytical function with both real and imaginary part  $F(z) = f'(z) + \imath f''(z)$  with poles at complex values  $z_0$  which are within the contour.

$$\begin{aligned} F(z_0) &= \frac{1}{2\pi\imath} \oint \frac{F(z)}{(z - z_0)} dz \\ &= \frac{1}{2\pi\imath} \int_{-\infty}^{\infty} \frac{F(z)}{(x - x_0)} dx, \end{aligned} \tag{A.2}$$

where we have required the integral over the upper part of the semicircle to vanish (i.e.  $\lim_{|z| \rightarrow \infty} |F(z)| = 0, 0 \leq \text{Im}(z) \leq \pi$ ). Placing the pole  $z_0$  on the real axis (or letting it approach from the upper half, otherwise the contour would not contain the pole), and taking the average of the second equation of Eq. A.2 and the contour integral around the small semicircle which is 0 (the contour does not contain the pole), i.e.

$$\begin{aligned} F(z_0) &= \left( \frac{1}{2\pi\imath} \int_{-\infty}^{\infty} \frac{F(z)}{(x - x_0)} dx + \frac{1}{2\pi\imath} \oint_{small} \frac{F(z)}{(z - z_0)} dz \right) / 2 \\ &= \frac{1}{\pi\imath} \lim_{\delta \rightarrow 0} \int_{-\infty}^{x_0 - \delta} \frac{F(z)}{(x - x_0)} dx + \int_{x_0 + \delta}^{\infty} \frac{F(z)}{(z - z_0)} dx \\ &= \frac{1}{\pi\imath} \mathbf{P} \int_{-\infty}^{\infty} \frac{F(z)}{(x - x_0)} dx. \end{aligned} \tag{A.3}$$

Splitting the last line of this equation into the real and imaginary parts yields the transformation between the real and imaginary parts of  $F(z)$ , which are the Kramers-Kronig relations.

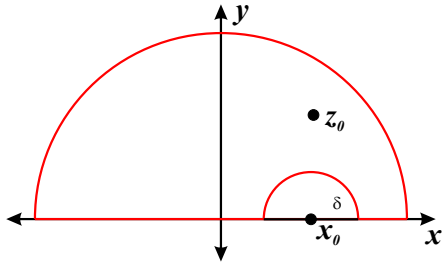


**Figure A.1** The contour integral of Eq. A.2.

In general, these relations will be obeyed by any causal system, i.e. where the effect cannot precede the cause. Mathematically, it is possible to show that if the perturbation is non-existent before it acts and  $F(z)$  is square integrable, the real and imaginary parts of  $F(z)$  will eventually obey the above transformations [209]. This makes the Kramers-Kronig relations relevant to many other interacting systems.

# Appendix B

## Quantization of the Light Field

To understand how to treat the electromagnetic field under the principles of second quantization, we begin by recalling Maxwell's equations in the vacuum:

$$\begin{aligned}\nabla \cdot \mathbf{D} &= \rho \\ \nabla \cdot \mathbf{B} &= 0 \\ \nabla \times \mathbf{E} &= -\frac{\partial \mathbf{B}}{\partial t} \\ \nabla \times \mathbf{H} &= \mathbf{J} + \frac{\partial \mathbf{D}}{\partial t}\end{aligned}\tag{B.1}$$

where we have taken  $\mathbf{B} = \mu_0 \mathbf{H}$ ,  $\mathbf{D} = \epsilon_0 \mathbf{E}$ ,  $\mu_0 \epsilon_0 = 1/c^2$ . Further, we take the Coulomb gauge  $\nabla \cdot \mathbf{A} = 0$ , where we have introduced the vector potential  $\mathbf{A}$  which serves to define the fields as:

$$\begin{aligned}\mathbf{B} &= \nabla \times \mathbf{A} \\ \mathbf{E} &= -\frac{\partial \mathbf{A}}{\partial t}\end{aligned}\tag{B.2}$$

to derive the wave equation of  $\mathbf{A}$  in the Coulomb gauge:

$$\begin{aligned}\nabla^2 \mathbf{A}(r, t) &= \frac{1}{c^2} \frac{\partial^2 \mathbf{A}(r, t)}{\partial t^2} \\ \nabla^2 \mathbf{E}(r, t) &= \frac{1}{c^2} \frac{\partial^2 \mathbf{E}(r, t)}{\partial t^2}.\end{aligned}\tag{B.3}$$

Decomposing  $\mathbf{A}(r, t)$  into its plane wave components arrives at:

$$\mathbf{A}(r, t) = -i \sum_k \sqrt{\frac{\hbar}{2\omega_k \epsilon_0}} (\mathbf{u}_k(r) a_k(t) + c.c.),\tag{B.4}$$

After substituting the Ansatz into Eq. B.3,  $a_k(t) = a_k e^{-i\omega_k t}$  and  $\mathbf{u}_k(r) = \hat{\mathbf{e}}_k \frac{1}{V} e^{i\mathbf{k}_n r}$ , where  $V$  arises as a normalization factor after introducing periodic boundary conditions of a cavity with volume  $V$ . Thus, we arrive at an expression for  $\mathbf{A}$ :

$$\mathbf{A}(r, t) = -i \sum_k \sqrt{\frac{\hbar}{2\omega_k \epsilon_0 V}} \hat{\mathbf{e}}_k (a_k e^{i(k_n r - \omega_k t)} + c.c.).\tag{B.5}$$

Now, following the formalism of quantizing of the energy levels in harmonic oscillator, where the following quantities were introduced:

$$\begin{aligned} a &= \frac{1}{\sqrt{2}}(q + ip) \\ a^\dagger &= \frac{1}{\sqrt{2}}(q - ip), \end{aligned} \tag{B.6}$$

where  $p$  and  $q$  are the momentum and position, respectively, we can see that  $a_k(t)$  and  $a_k^*(t)$  obey the same equations of motion, and so they can be replaced by the operators  $a_k \rightarrow \hat{a}_k$  and  $a_k^* \rightarrow \hat{a}_k^\dagger$ , which obey the commutator relation  $[\hat{a}_{ki}, \hat{a}_{kj}^\dagger] = \delta_{ij}$ ,  $[\hat{a}_{kj}, \hat{a}_{kj}] = 0$  and  $[\hat{a}_{kj}^\dagger, \hat{a}_{kj}^\dagger] = 0$ .

Then, the Hamiltonian of the light can be written as

$$H = \sum_k \hbar\omega_k \left(n_k + \frac{1}{2}\right), \tag{B.7}$$

where we have introduced the number operator  $n_k = \hat{a}_{kj}^\dagger \hat{a}_{kj}$ . Just like in the harmonic oscillator, the operators  $\hat{a}_{kj}^\dagger$  and  $\hat{a}_{kj}$  are the annihilation and creation operators. Thus, any state  $|n_k\rangle$  can be created by acting  $n_k$ -times on the vacuum state:

$$|n_k\rangle = \frac{(\hat{a}_{kj}^\dagger)^{n_k}}{\sqrt{n_k!}} |0\rangle. \tag{B.8}$$

The remanent energy of Eq. B.7 shows that even in the ground state ( $\omega_k = 0$ ), there are fluctuations of energy. These vacuum fluctuations lead to intriguing effects within a cavity like the Casimir effect. For more on the quantization of the light field and the Casimir effect, the reader is referred to Ref. [20] and others therein.

# Appendix C

## Fermi's Golden Rule

In this section, we will derive the transition probability matrix, known as Fermi's Golden Rule, for a quantum mechanical system under a perturbation, paraphrased mostly from [20, 53]. Begin by taking a system with Hamiltonian

$$H\psi = i\hbar \frac{\partial \psi}{\partial t}, \quad (\text{C.1})$$

where the Hamiltonian has the form  $H = H_0 + H'$ , having a  $H_0$  unperturbed system and  $H'$  is a small time-dependent perturbation. The Hamiltonian  $H_0$  has eigenstates and eigenfunctions

$$H_0\psi_n = E_n\psi_n, \quad (\text{C.2})$$

and the eigenfunctions form a complete basis. So, to solve the full Hamiltonian, we introduce the Ansatz of expressing the solution as a linear combination with time-dependent coefficients:

$$\psi(t) = \sum_n a_n(t)\psi_n e^{-iE_n t/\hbar}, \quad (\text{C.3})$$

which we can substitute into the Hamiltonian to arrive at

$$i\hbar \frac{\partial a_k(t)}{\partial t} = \sum_n H'_{kn} a_n(t) e^{i\omega_{kn}t}, \quad (\text{C.4})$$

where  $H'_{kn} = \langle \psi_k | H' | \psi_n \rangle$ , the matrix element connecting states  $n \rightarrow k$ , and  $\hbar\omega_{kn} = E_k - E_n$ , the energy difference between the states. Although it can be solved explicitly for a two-level system, the latter equation must be solved for multiple levels using a perturbation expansion. That is, the  $(p + 1)$ -th order approximation is found from the  $p$ -th order solution:

$$i\hbar \frac{\partial a_k^{p+1}(t)}{\partial t} \approx \sum_n H'_{kn} a_n^p(t) e^{i\omega_{kn}t}, \quad (\text{C.5})$$

while defining the 0-th order approximation to be 0 ( $\frac{\partial a_k^0(t)}{\partial t} = 0$ ).

Consider the first approximation term of a system which is initially in the state  $m$ . For that case  $a_n^0(t) = \delta_{mn}$  because we had imposed the 0-th term to be constant and so no transitions occur. Thus, eqn C.5 can be solved for  $a_k^1(t)$  by integrating

$$i\hbar a_k^1(t) = \int_{-\infty}^t dt' t' H'_{km} a_k^0(t') e^{i\omega_{km}t'}. \quad (\text{C.6})$$

Next, we assume the perturbation to be appear at  $t' = 0$ , and is constant thereafter until time  $t$ . Then, Eq. C.6 can be integrated to give:

$$i\hbar a_k^1(t) = 2H'_{km} e^{i\omega_{km}t/2} \left( \frac{\sin(\omega_{km}t/2)}{\omega_{km}} \right). \quad (\text{C.7})$$

Now, we can calculate the probability of the system to transition from state  $m \rightarrow k$  as

$$P_k(t) = |a_k(t)|^2 = 4/\hbar^2 |H'_{km}|^2 \frac{\sin^2(\omega_{km}t/2)}{\omega_{km}^2}. \quad (\text{C.8})$$

To further evaluate this transition matrix, we consider that there are a number of states allowed within an interval  $d\omega_{km}$ , written as

$$dn = \rho(k) dE_k, \quad (\text{C.9})$$

where we have introduced the density of states  $\rho(k)$  per unit energy interval near  $E_k$ .

So the total transition rate to states near  $k$  is expressed as

$$\begin{aligned} W_k &= \frac{1}{t} \sum_{k'} P_{k'}(t) \implies \frac{1}{t} \int P_{k'}(t) \rho(k') dE_{k'} \\ &= \int \rho(k') dE_{k'} \frac{1}{t} \frac{4}{\hbar^2} |H'_{km}|^2 \frac{\sin^2(\omega_{km}t/2)}{\omega_{km}^2} \\ &= \frac{4}{\hbar} |H'_{km}|^2 \rho(k) \int_{-\infty}^{+\infty} d\omega \frac{1}{t} \frac{\sin^2(\omega t/2)}{\omega^2} \\ &= \frac{2\pi}{\hbar} |H'_{km}|^2 \rho(k), \end{aligned} \quad (\text{C.10})$$

where we have arrived at Fermi's Golden rule. Notice that the function  $\frac{\sin^2(\omega t/2)}{t\omega^2}$  only takes on values at very large  $t$  when  $\omega = 0$ , defining a Dirac delta function, which from the definition  $\hbar\omega_{kn} = E_k - E_n$  implies that the transition will only take place when there is enough energy to carry it through, even if the probability matrix allows it. This ensures energy conservation.

# Appendix D

## Mathematica script to analyze azimuthal dependencies

```
S1 = {x1, y1, z1};
S2 = {x2, y2, z2};
S3 = {x3, y3, z3};
S4 = {x4, y4, z4};
F1 = {{0, S1[[3]], -S1[[2]]}, {-S1[[3]], 0,
  S1[[1]]}, {S1[[2]], -S1[[1]], 0}};
F2 = {{0, S2[[3]], -S2[[2]]}, {-S2[[3]], 0,
  S2[[1]]}, {S2[[2]], -S2[[1]], 0}};
F3 = {{0, S3[[3]], -S3[[2]]}, {-S3[[3]], 0,
  S3[[1]]}, {S3[[2]], -S3[[1]], 0}};
F4 = {{0, S4[[3]], -S4[[2]]}, {-S4[[3]], 0,
  S4[[1]]}, {S4[[2]], -S4[[1]], 0}};
FQ1 = F1 + F2 + F3 + F4;
FQ2 = F1 - F2 + F3 - F4;
FQ4 = F1 + I*F2 - F3 - I*F4;
q = {1, 1, 1};
q = q/Sqrt[q . q];
qperp = {1, -1, 0};
qperp = qperp/Sqrt[qperp . qperp];
kin = Sin[\[Theta]p]*(Cos[\[Phi]]*qperp +
  Sin[\[Phi]]*Cross[qperp, q]) + Cos[\[Theta]p]*q;
kin = FullSimplify[kin/Sqrt[kin . kin]];
kout = Sin[\[Theta]p]*(Cos[\[Phi]]*qperp +
  Sin[\[Phi]]*Cross[qperp, q]) - Cos[\[Theta]p]*q;
kout = FullSimplify[kout/Sqrt[kout . kout]];
\[Epsilon]\[Sigma] = Cross[kin, kout]/Sin[2*\[Theta]p];
\[Epsilon]\[Pi]in = Cross[kin, \[Epsilon]\[Sigma]];
\[Epsilon]\[Pi]out = Cross[kout, \[Epsilon]\[Sigma]];
```

```

FQ4\[Sigma]\[Sigma] = \[Epsilon]\[Sigma].FQ4.\[Epsilon]\[Sigma];
FQ4\[Sigma]\[Pi] = \[Epsilon]\[Pi]out.FQ4.\[Epsilon]\[Sigma];
FQ4\[Pi]\[Sigma] = \[Epsilon]\[Sigma].FQ4.\[Epsilon]\[Pi]in;
FQ4\[Pi]\[Pi] = \[Epsilon]\[Pi]out.FQ4.\[Epsilon]\[Pi]in;
IQ4\[Sigma] =
  FQ4\[Sigma]\[Sigma]\[Conjugate] FQ4\[Sigma]\[Sigma] +
  FQ4\[Sigma]\[Pi]\[Conjugate] FQ4\[Sigma]\[Pi];
IQ4\[Pi] =
  FQ4\[Pi]\[Sigma]\[Conjugate] FQ4\[Pi]\[Sigma] +
  FQ4\[Pi]\[Pi]\[Conjugate] FQ4\[Pi]\[Pi];

```

```

\[Theta]p = (2 \[Pi])/360 35;

```

(\*A dynamical plot module is written which can be compared with the data, while at the same time visually demonstrate where the spins are oriented\*)

```

Manipulate[Show[Plot[Evaluate[
  x1 = m1*Cos[(2 \[Pi])/360 \[Phi]1] Sin[(2 \[Pi])/360 \[Theta]1];
  y1 = m1*Sin[(2 \[Pi])/360 \[Phi]1] Sin[(2 \[Pi])/360 \[Theta]1];
  z1 = m1*Cos[(2 \[Pi])/360 \[Theta]1];
  x3 = -x1; y3 = -y1; z3 = -z1;
  x2 = m2*Cos[(2 \[Pi])/360 \[Phi]2] Sin[(2 \[Pi])/360 \[Theta]2];
  y2 = m2*Sin[(2 \[Pi])/360 \[Phi]2] Sin[(2 \[Pi])/360 \[Theta]2];
  z2 = m2*Cos[(2 \[Pi])/360 \[Theta]2];
  x4 = -x2; y4 = -y2; z4 = -z2;
  IQ4\[Pi]/
  IQ4\[Sigma] /. \[Phi] -> (2 \[Pi])/360 \[Phi]], {\[Phi], -50,
  260}, Frame -> True, PlotRange -> {0, range},
  PlotStyle -> {Thick, Black}],
Graphics[Line[{{90, -1}, {90, 1000}}]],
Graphics[Line[{{180, -1}, {180, 1000}}]],
Graphics[Line[{{270, -1}, {270, 1000}}]],
N[ArcCos[{x1, y1, z1}.{x2, y2,
  z2}/(Norm[{x1, y1, z1}] Norm[{x2, y2, z2}])]]/Degree,
Graphics3D[{Red, Arrowheads[0.1],
  Arrow[Tube[{{0, 0, 0}, 3*{x1, y1, z1}}, 0.04]], Red,
  Arrowheads[0.1], Arrow[Tube[{{0, 0, 0}, 3*{x2, y2, z2}}, 0.04]],
  Black, Arrowheads[0.15],
  Arrow[Tube[{{0, 0, 0}, {0, 0, 3}], 0.05]], , Black,
  Arrowheads[0.15], Arrow[Tube[{{0, 0, 0}, {0, 3, 0}], 0.05]], ,
  Black, Arrowheads[0.15],
  Arrow[Tube[{{0, 0, 0}, {3, 0, 0}], 0.05]]},
Boxed -> False]], {{m1, 1}, 0, 2}, {{m2, 1}, 0,
2}, {{\[Theta]1, 97}, 0, 360}, {{\[Phi]1, 45}, 0,
360}, {{\[Theta]2, 90}, -360, 360}, {{\[Phi]2, 315}, 0,
360}, {{range, 4}, 1, 180]}

```

# Bibliography

- [1] Y. Tokura and N. Nagaosa. Orbital Physics in Transition-Metal Oxides. *Science*, 288(5465):462–468, (2000).
- [2] Y. Tokura. *Colossal Magnetoresistive Oxides*. Gordon and Breach Publishers, (2000).
- [3] S. Maekawa, T. Tohyama, S.E. Barnes, *et al.* *Physics of Transition Metal Oxides*. Springer, (2004).
- [4] E. Dagotto. Complexity in strongly correlated electronic systems. *Science*, 309:257, (2005).
- [5] M. Imada, A. Fujimori, and Y. Tokura. Metal-insulator transitions. *Rev. Mod. Phys.*, 70:1039 – 1263, (1998).
- [6] Y. Tokura. Correlated-electron physics in transition-metal-oxides. *Physics Today*, pages 50 – 55, (July 2003).
- [7] A. M. Glazer. Simple ways of determining perovskite structures. *Acta Crystallographica Section A*, 31(6):756–762, (1975).
- [8] Yi Lu. Structural and electronic properties of perovskite rare-earth nickelate superlattices. Master’s thesis, Universität Stuttgart, (2012).
- [9] T. Hahn. *International Tables of Crystallography*, volume A, Chapter 7. John Wiley and Sons, Ltd., (2006).
- [10] U. Gebhardt. *Strukturelle Relaxation von epitaktischen, dünnen La/Sr-Manganitfilmen in Abhängigkeit von der Schichtdicke*. PhD thesis, Universität Stuttgart, (2006).
- [11] Sangita Baniya. X-ray diffraction from PrNiO<sub>3</sub> thin films. Master’s thesis, Universität Stuttgart, (2012).
- [12] J. (1963) Hubbard. Electron Correlations in Narrow Energy Bands. *Proceedings of the Royal Society of London*, 276(1365):238257, (1963).
- [13] J. Zaanen, G. A. Sawatzky, and J. W. Allen. Band gaps and electronic structure of transition-metal compounds. *Phys. Rev. Lett.*, 55(4):418–421, (Jul 1985).
- [14] N. Ashcroft and D. Mermin. *Solid State Physics*. Thomson Learning Inc., (1976).
- [15] G. Grüner. *Density waves in solids*. Addison-Wesley, (1994).

- [16] G. Grüner. The dynamics of charge-density waves. *Rev. Mod. Phys.*, 60:1129–1181, (1988).
- [17] R. Mott, N.F. and Peierls. *Proc. Phys. Soc. London Ser. A*, 49:72, (1937).
- [18] R. Peierls. *Quantum Theory of Solids*. Oxford University Press, New York, (1955).
- [19] E. Canadell and M.-H Whangbo. Conceptual aspects of structure property correlations and electronic instabilities, with applications to low-dimensional transition-metal oxides. *Chem. Rev.*, 91:965 – 1034, (1991).
- [20] C. Cohen-Tannoudji, B. Diu, and F. Laloe. *Quantum Mechanics*. John Wiley and Sons, Ltd., (2006).
- [21] H.Y. Hwang, Y. Iwasa, M. Kawasaki, *et al.* Emergent phenomena at oxide interfaces. *Nat Mater*, 11:103113, (2012).
- [22] A. J. Millis J. Chakhalian and J. Rondinelli. Whither the oxide interface. *Nat Mater*, 11:92–94, (2012).
- [23] J. Mannhart and D. G. Schlom. Oxide interfaces - an opportunity for electronics. *Science*, 327(5973):1607–1611, (2010).
- [24] J. Chaloupka and G. Khaliullin. Orbital Order and Possible Superconductivity in  $\text{LaNiO}_3/\text{LaMO}_3$  Superlattices. *Phys. Rev. Lett.*, 100(1):016404, (Jan 2008).
- [25] H.Y. Hwang and A. Ohtomo. A high-mobility electron gas at the  $\text{LaAlO}_3/\text{SrTiO}_3$  heterointerface. *Nature*, 427:423–426, (2004).
- [26] N. Reyren, S. Thiel, A. D. Caviglia, *et al.* Superconducting Interfaces Between Insulating Oxides. *Science*, 317(5842):1196–1199, (2007).
- [27] M. Rössle, K. W. Kim, A. Dubroka, *et al.* Electric-Field-Induced Polar Order and Localization of the Confined Electrons in  $\text{LaAlO}_3/\text{SrTiO}_3$  Heterostructures. *Phys. Rev. Lett.*, 110:136805, (2013).
- [28] L. Li, C. Richter, J. Mannhart, and R. C. Ashoori. Coexistence of magnetic order and two-dimensional superconductivity at  $\text{LaAlO}_3/\text{SrTiO}_3$  interfaces. *Nat Ph*, 7:762 – 766, (2011).
- [29] C. Richter, H. Boschker, W. Dietsche, *et al.* Interface superconductor with gap behaviour like a high-temperature superconductor. *Nature*, 502:528 – 531, (2013).
- [30] S. Banerjee, O. Erten, and M. Randeria. Ferromagnetic exchange, spin-orbit coupling and spiral magnetism at the  $\text{LaAlO}_3/\text{SrTiO}_3$  interface. *Nat Phy*, 9:626 – 630, (2013).
- [31] M. Gabay and J. Triscone. Nature physics. *Nat Phys*, 9:610 – 611, (2013).
- [32] A P Ramirez. Colossal magnetoresistance. *Journal of Physics: Condensed Matter*, 9:8171, (1997).

- [33] S-W. Cheong and H. Y. Hwang. *Colossal Magnetoresistive Oxides*. Gordon and Breach Science Publishers, New York, (2000).
- [34] A. J. Millis. Lattice effects in magnetoresistive manganese perovskites. *Nature*, 392:147 – 150, (1998).
- [35] M Cesaria, A P Caricato, G Maruccio, and M Martino. LSMO - growing opportunities by PLD and applications in spintronics. *Journal of Physics: Conference Series*, 292:012003, (2011).
- [36] Z. Sefrioui, D. Arias, V. Peña, *et al.* Ferromagnetic/superconducting proximity effect in  $\text{La}_{0.7}\text{Ca}_{0.3}\text{MnO}_3\text{-YBa}_2\text{Cu}_3\text{O}_{7-\delta}$  superlattices. *Phys. Rev. B*, 67:214511, (2003).
- [37] V. Peña, Z. Sefrioui, D. Arias, *et al.* Coupling of superconductors through a half-metallic ferromagnet: Evidence for a long-range proximity effect. *Phys. Rev. B*, 69:224502, (2004).
- [38] J. Stahn, J. Chakhalian, Ch. Niedermayer, *et al.* Magnetic proximity effect in perovskite superconductor-ferromagnet multilayers. *Phys. Rev. B*, 71:140509, (Apr 2005).
- [39] A. Hoffmann, S. G. E. te Velthuis, Z. Sefrioui, *et al.* Suppressed magnetization in  $\text{La}_{0.7}\text{Ca}_{0.3}\text{MnO}_3\text{-YBa}_2\text{Cu}_3\text{O}_{7-\delta}$  superlattices. *Phys. Rev. B*, 72:140407, (2005).
- [40] J. Chakhalian, J.-W. Freeland, G. Srajer, *et al.* Magnetism at the interface between ferromagnetic and superconducting oxides. *Nat Phys*, 2(4):244–248, (APR 2006).
- [41] D. K. Satapathy, M. A. Uribe-Laverde, I. Marozau, *et al.* Magnetic Proximity Effect in  $\text{YBa}_2\text{Cu}_3\text{O}_7/\text{La}_{2/3}\text{Ca}_{1/3}\text{MnO}_3$  and  $\text{YBa}_2\text{Cu}_3\text{O}_7/\text{LaMnO}_{3+\delta}$  Superlattices. *Phys. Rev. Lett.*, 108:197201, (May 2012).
- [42] J. Chakhalian, J. W. Freeland, H.-U. Habermeier, *et al.* Orbital Reconstruction and Covalent Bonding at an Oxide Interface. *Science*, 318(5853):1114–1117, (2007).
- [43] N. Driza, S. Blanco-Canosa, M. Bakr, *et al.* Long-range transfer of electron-phonon coupling in oxide superlattices. *Nat Mater*, 11:675–681, (2012).
- [44] D. G. Schlom, J. N. Eckstein, E. S. Hellman, *et al.* Molecular beam epitaxy of layered Dy-Ba-Cu-O compounds. *Applied Physics Letters*, 53(17):1660–1662, (1988).
- [45] J. H. Haeni, C. D. Theis, D. G. Schlom, *et al.* Epitaxial growth of the first five members of the  $\text{Sr}_{n+1}\text{Ti}_n\text{O}_{3n+1}$  Ruddlesden-Popper homologous series. *Applied Physics Letters*, 78(21):3292–3294, (2001).
- [46] D. Dijkkamp, T. Venkatesan, X. D. Wu, *et al.* Preparation of Y-Ba-Cu oxide superconductor thin films using pulsed laser evaporation from high  $T_c$  bulk material. *Applied Physics Letters*, 51:619–621, (1987).
- [47] Robert Eason, editor. *Pulsed Laser Deposition of Thin Films*. John Wiley and Sons, Ltd., (2007).

- [48] M. Blume and Doon Gibbs. Polarization dependence of magnetic x-ray scattering. *Phys. Rev. B*, 37:1779–1789, (Feb 1988).
- [49] Isaacs E D McWhan D B Mills D Gibbs D, Harshman D R and Vettier C. Polarization and resonance properties of magnetic x-ray scattering in holmium. *Phys. Rev. Lett.*, 61:1241, (1988).
- [50] J. Fink, E. Schierle, E. Weschke, and J. Geck. Resonant elastic soft x-ray scattering. *Rep. Prog. Phys.*, 76:056502, (2013).
- [51] C. Vettier. Resonant elastic x-ray scattering: Where from? where to? *Eur. Phys. J. Special Topics*, 208:3–14, (2012).
- [52] F. R. Elder, A. M. Gurewitsch, R. V. Langmuir, and H. C. Pollock. Radiation from Electrons in a Synchrotron. *Physical Review*, 71:829–830, (June 1947).
- [53] Jens Als-Nielsen and Des McMorrow. *Elements of Modern X-Ray Physics*. John Wiley and Sons, Ltd., (2001).
- [54] A. Hofmann. *Synchrotron Radiation*. Cambridge, (2004).
- [55] H. Wiedmann. *Synchrotron Radiation*. Springer, (2003).
- [56] D.H. Templeton and L.K. Templeton. Polarized x-ray absorption and double refraction in vanadyl bisacetylacetonate. *Acta Cryst.*, A36:237–241, (1980).
- [57] J. P. Hannon, G. T. Trammell, M. Blume, and Doon Gibbs. X-ray resonance exchange scattering. *Phys. Rev. Lett.*, 61:1245–1248, (Sep 1988).
- [58] P. Carra and B.T. Thole. Anisotropic x-ray anomalous diffraction and forbidden reflections. *Rev. Mod. Phys.*, 66:1509–1515, (1994).
- [59] J. P. Hill and D.F. McMorrow. X-ray resonant exchange scattering: Polarization dependence and correlation functions. *Acta Cryst.*, A52:236–244, ((1996)).
- [60] C.J. Sparks & K. Fischer G. Materlik. *Resonant Anomalous X-Ray Scattering*. Elsevier, (1994).
- [61] F. de Groot and G. van der Laan. Collected works of theo thole: the spectroscopy papers. *Journals of Electron Spectroscopy and Related Phenomena*, 86:25–10, (1997).
- [62] J. Fink, E. Schierle, E. Weschke, and J. Geck. Resonant elastic soft x-ray scattering. *arxiv: 1210.5387*, (2013).
- [63] S.D. Matteo Y. Joly and O. Bunau. Resonant x-ray diffraction: Basic theoretical principles. *The European Physical Journal Special Topics*, 208:21, (2012).
- [64] M. W. Haverkort, N. Hollmann, I. P. Krug, and A. Tanaka. Symmetry analysis of magneto-optical effects: The case of x-ray diffraction and x-ray absorption at the transition metal  $L_{2,3}$  edge. *Phys. Rev. B*, 82:094403, (Sep 2010).

- [65] Maurits Haverkort. Theory of x-ray resonant spectroscopy. Presentation at the UBC-Max Planck Summer School, (2011).
- [66] Sergio di Matteo. Multipole interpretation of resonant elastic x-ray scattering. Presentation at the REXS Conference, (2011).
- [67] B.L. Henke. Atomic scattering factors. <http://henke.lbl.gov/optical-constants/asf.html>.
- [68] K. D. Finkelstein, Qun Shen, and S. Shastri. Resonant x-ray diffraction near the iron  $K$ -edge in hematite ( $\alpha$ - $\text{Fe}_2\text{O}_3$ ). *Phys. Rev. Lett.*, 69:1612–1615, (1992).
- [69] E. Benckiser, M.W. Haverkort, S. Brück, *et al.* Orbital reflectometry of oxide heterostructures. *Nat Mater*, 10:189–193, (2011).
- [70] J. Chakhalian, J. M. Rondinelli, Jian Liu, *et al.* Asymmetric orbital-lattice interactions in ultrathin correlated oxide films. *Phys. Rev. Lett.*, 107:116805, (Sep 2011).
- [71] J. W. Freeland, Jian Liu, M. Kareev, *et al.* Orbital control in strained ultra-thin  $\text{LaNiO}_3/\text{LaAlO}_3$  superlattices. *EPL (Europhysics Letters)*, 96(5):57004, (2011).
- [72] H. Ott, C. Schüßler-Langeheine, E. Schierle, *et al.* Magnetic x-ray scattering at the  $M_5$  absorption edge of ho. *Phys. Rev. B*, 74:094412, (Sep 2006).
- [73] E. Schierle, V. Soltwisch, D. Schmitz, *et al.* Cycloidal order of  $4f$  moments as a probe of chiral domains in  $\text{dymno}_3$ . *Phys. Rev. Lett.*, 105:167207, (Oct 2010).
- [74] W. R. Busing and H. A. Levy. Angle calculations for 3- and 4-circle X-ray and neutron diffractometers. *Acta Crystallographica*, 22(4):457–464, (Apr 1967).
- [75] Tilo Baumbach Ullrich Pietsch, Vaclav Holy. *High-Resolution X-Ray Scattering: From Thin Films To Lateral Nanostructures*. Springer-Verlag, 2nd edition, (2001).
- [76] Alex Frano. X-ray scattering investigations in transition-metal-oxide heterostructures. Master's thesis, Universität Stuttgart, (2010).
- [77] S. Partzsch, S.B. Wilkins, E. Schierle, *et al.* Resonant soft X-ray scattering studies of multiferroic  $\text{YMn}_2\text{O}_5$ . *Eur. Phys. J. Special Topics*, 208:133–139, (2012).
- [78] J. B. Torrance, P. Lacorre, A. I. Nazzal, E. J. Ansaldo, and Ch. Niedermayer. Systematic study of insulator-metal transitions in perovskites  $\text{RNiO}_3$  ( $R=\text{Pr},\text{Nd},\text{Sm},\text{Eu}$ ) due to closing of charge-transfer gap. *Phys. Rev. B*, 45(14):8209–8212, (Apr 1992).
- [79] María Luisa Medarde. Structural, magnetic and electronic properties of perovskites  $\text{RNiO}_3$  ( $R = \text{rare earth}$ ). *Journal of Physics: Condensed Matter*, 9(8):1679, (1997).
- [80] G. Catalan. Progress in perovskite nickelate research. *Phase Transitions: A Multinational Journal*, 81(7):729–749, (2008).
- [81] J.-S. Zhou and J. B. Goodenough. Chemical bonding and electronic structure of  $\text{RNiO}_3$  ( $R = \text{rare earth}$ ). *Phys. Rev. B*, 69:153105, (Apr 2004).

- [82] J. L. García-Muñoz, J. Rodríguez-Carvajal, P. Lacorre, and J. B. Torrance. Neutron-diffraction study of  $RNiO_3$  ( $R=La,Pr,Nd,Sm$ ): Electronically induced structural changes across the metal-insulator transition. *Phys. Rev. B*, 46(8):4414–4425, (Aug 1992).
- [83] J. Rodríguez-Carvajal, S. Rosenkranz, M. Medarde, *et al.* Neutron-diffraction study of the magnetic and orbital ordering in  $^{154}SmNiO_3$  and  $^{153}EuNiO_3$ . *Phys. Rev. B*, 57(1):456–464, (Jan 1998).
- [84] J. L. García-Muñoz, J. Rodríguez-Carvajal, and P. Lacorre. Neutron-diffraction study of the magnetic ordering in the insulating regime of the perovskites  $RNiO_3$  ( $R=Pr$  and  $Nd$ ). *Phys. Rev. B*, 50:978–992, (Jul 1994).
- [85] J. L. García-Muñoz, J. Rodríguez-Carvajal, and P. Lacorre. Sudden Appearance of an Unusual Spin Density Wave At the Metal-Insulator Transition in the Perovskites  $RNiO_3$  ( $R=Pr, Nd$ ). *EPL (Europhysics Letters)*, 20(3):241, (1992).
- [86] J.A. Alonso, M.J. Martínez-Lope, M.T. Casais, J.L. García-Muñoz, and M. T. Fernández-Díaz. Room-temperature monoclinic distortion due to charge disproportionation in  $RNiO_3$  perovskites. *Phys. Rev. B*, 61:17561763, (2000).
- [87] J.A. Alonso, J.L. García-Muñoz, M.T. Fernández-Díaz, *et al.* Charge disproportionation in  $RNiO_3$  perovskites: Simultaneous metal-insulator and structural transition in  $YNiO_3$ . *Phys. Rev. Lett.*, 82:38713874, (1999).
- [88] U. Staub, G. I. Meijer, F. Fauth, *et al.* Direct Observation of Charge Order in an Epitaxial  $NdNiO_3$  Film. *Phys. Rev. Lett.*, 88(12):126402, (Mar 2002).
- [89] Y. Murakami, J. P. Hill, D. Gibbs, *et al.* Resonant X-Ray Scattering from Orbital Ordering in  $LaMnO_3$ . *Phys. Rev. Lett.*, 81(3):582–585, (Jul 1998).
- [90] T.A.W. Beale, G. Beutier, S.R. Bland, *et al.* REXS contribution to electronic ordering investigation in solids. *The European Physical Journal Special Topics*, 208(1):89–98, (2012).
- [91] J. Kokubun and V.E. Dmitrienko. Anisotropic resonant x-ray scattering: Beauty of forbidden reflections. *The European Physical Journal Special Topics*, 208:39–52, (2012).
- [92] M. T. Fernández-Díaz, J. A. Alonso, M. J. Martínez-Lope, M. T. Casais, and J. L. García-Muñoz. Magnetic structure of the  $HoNiO_3$  perovskite. *Phys. Rev. B*, 64:144417, (Sep 2001).
- [93] V. Scagnoli, U. Staub, A. M. Mulders, *et al.* Role of magnetic and orbital ordering at the metal-insulator transition in  $NdNiO_3$ . *Phys. Rev. B*, 73:100409, (Mar 2006).
- [94] V. Scagnoli, U. Staub, Y. Bodenthin, *et al.* Induced noncollinear magnetic order of  $Nd^{3+}$  in  $NdNiO_3$  observed by resonant soft x-ray diffraction. *Phys. Rev. B*, 77:115138, (Mar 2008).

- [95] I. Vobornik, L. Perfetti, M. Zacchigna, *et al.* Electronic-structure evolution through the metal-insulator transition in  $R\text{NiO}_3$ . *Phys. Rev. B*, 60:R8426–R8429, (Sep 1999).
- [96] Bayo Lau and Andrew J. Millis. Theory of the Magnetic and Metal-Insulator Transitions in  $R\text{NiO}_3$  Bulk and Layered Structures. *Phys. Rev. Lett.*, 110:126404, (Mar 2013).
- [97] Shuai Dong and Elbio Dagotto. Quantum confinement induced magnetism in  $\text{LaNiO}_3$ - $\text{LaMnO}_3$  superlattices. *Phys. Rev. B*, 87:195116, (May 2013).
- [98] Danilo Puggioni, Alessio Filippetti, and Vincenzo Fiorentini. Ordering and multiple phase transitions in ultrathin nickelate superlattices. *Phys. Rev. B*, 86:195132, (2012).
- [99] SungBin Lee, Ru Chen, and Leon Balents. Landau theory of charge and spin ordering in the nickelates. *Phys. Rev. Lett.*, 106:016405, (Jan 2011).
- [100] SungBin Lee, Ru Chen, and Leon Balents. Metal-insulator transition in a two-band model for the perovskite nickelates. *Phys. Rev. B*, 84:165119, (Oct 2011).
- [101] P. Hansmann, Xiaoping Yang, A. Toschi, *et al.* Turning a nickelate fermi surface into a cupratelike one through heterostructuring. *Phys. Rev. Lett.*, 103(1):016401, (Jun 2009).
- [102] P. Hansmann, A. Toschi, Xiaoping Yang, O. K. Andersen, and K. Held. Electronic structure of nickelates: From two-dimensional heterostructures to three-dimensional bulk materials. *Phys. Rev. B*, 82:235123, (Dec 2010).
- [103] M. J. Han, C. A. Marianetti, and A. J. Millis. Chemical control of orbital polarization in artificially structured transition-metal oxides:  $\text{La}_2\text{NiXO}_6$  ( $X = B, Al, Ga, In$ ) from first principles. *Phys. Rev. B*, 82(13):134408, (Oct 2010).
- [104] M. J. Han, Xin Wang, C. A. Marianetti, and A. J. Millis. Dynamical Mean-Field Theory of Nickelate Superlattices. *Phys. Rev. Lett.*, 107:206804, (Nov 2011).
- [105] M. Wu, E. Benckiser, M. W. Haverkort, *et al.* Strain and composition dependence of orbital polarization in nickel oxide superlattices. *Phys. Rev. B*, 88:125124, (Sep 2013).
- [106] B. T. Thole and G. van der Laan. Sum rules for magnetic dichroism in rare earth 4  $f$  photoemission. *Phys. Rev. Lett.*, 70:2499–2502, (Apr 1993).
- [107] G. van der Laan. Sum Rules and Fundamental Spectra of Magnetic X-Ray Dichroism in Crystal Field Symmetry. *J. Phys. Soc. Jpn.*, 63:2393–2400, (1994).
- [108] Meng Wu. *Title to be decided*. PhD thesis, Universität Stuttgart, (2014).
- [109] A. V. Boris, Y. Matiks, E. Benckiser, *et al.* Dimensionality control of electronic phase transitions in nickel-oxide superlattices. *Science*, 332(6032):937–940, (2011).
- [110] Jian Liu, S. Okamoto, M. van Veenendaal, *et al.* Quantum confinement of mott electrons in ultrathin  $\text{LaNiO}_3/\text{LaAlO}_3$  superlattices. *Phys. Rev. B*, 83(16):161102, (Apr 2011).

- [111] R. Scherwitzl, S. Gariglio, M. Gabay, *et al.* Metal-Insulator Transition in Ultrathin LaNiO<sub>3</sub> Films. *Phys. Rev. Lett.*, 106(24):246403, (Jun 2011).
- [112] Hideshi Fujishita, Yōichi Shiozaki, and Etsuro Sawaguchi. X-Ray Crystal Structure Analysis of Low Temperature Phase of SrTiO<sub>3</sub>. *Journal of the Physical Society of Japan*, 46(2):581–586, (1979).
- [113] T. Prokscha, E. Morenzoni, K. Deiters, *et al.* The new  $\mu$ E4 beam at PSI: a hybrid-type large acceptance channel for the generation of a high intensity surface-muon beam. *Nucl. Instrum. Methods Phys. Res. A*, 595:317, (2008).
- [114] M. Gibert, P. Zubko, R. Scherwitzl, J. Iniguez, and J.M. Triscone. Exchange bias in LaNiO<sub>3</sub> - LaMnO<sub>3</sub> superlattices. *Nat Mater*, 11:195198, (2012).
- [115] J. Hoffman, I. C. Tung, B. Nelson-Cheeseman, *et al.* Charge transfer and interfacial magnetism in (LaNiO<sub>3</sub>)<sub>n</sub>/(LaMnO<sub>3</sub>)<sub>2</sub> superlattices. *archiv:1301.7295v1*, (2013).
- [116] U. Gebhardt, N. V. Kasper, A. Vigliante, *et al.* Formation and Thickness Evolution of Periodic Twin Domains in Manganite Films Grown on SrTiO<sub>3</sub>(001) Substrates. *Phys. Rev. Lett.*, 98(9):096101, (Feb 2007).
- [117] S. J. May, J.-W. Kim, J. M. Rondinelli, *et al.* Quantifying octahedral rotations in strained perovskite oxide films. *Phys. Rev. B*, 82(1):014110, (Jul 2010).
- [118] S. J. May, C. R. Smith, J.-W. Kim, *et al.* Control of octahedral rotations in (LaNiO<sub>3</sub>)<sub>n</sub>/(SrMnO<sub>3</sub>)<sub>m</sub> superlattices. *Phys. Rev. B*, 83:153411, (Apr 2011).
- [119] H. Heinke. Relaxation and mosaicity profiles in epitaxial layers studied by high resolution X-ray diffraction. *Journal of Crystal Growth*, 135:41–52, (January 1994).
- [120] RC Farrow, MT Asom, KA Jackson, and LC KimIMERLING. SEM Study of Phase-transformation in alpha-Sn Thin Films. *Institute of Physics Conference Series*, (100):259–264, (1989).
- [121] L. X. Cao, T. L. Lee, F. Renner, *et al.* Strain release and twin structure in GdBa<sub>2</sub>Cu<sub>3</sub>O<sub>7- $\delta$</sub>  film on (001) SrTiO<sub>3</sub> and NdGaO<sub>3</sub>. *Phys. Rev. B*, 65:113402, (Feb 2002).
- [122] Yuan-Chang Liang, Hsin-Yi Lee, Heng-Jui Liu, and Tai-Bor Wu. In situ characterization of lattice relaxation of the BaTiO<sub>3</sub>/LaNiO<sub>3</sub> superlattices epitaxially grown on SrTiO<sub>3</sub> substrates. *Journal of Crystal Growth*, 276:534 – 540, (2005).
- [123] Akiji Yamamoto, Mitsuko Onoda, Eiji Takayama-Muromachi, *et al.* Rietveld analysis of the modulated structure in the superconducting oxide Bi<sub>2</sub>(Sr,Ca)<sub>3</sub>Cu<sub>2</sub>O<sub>8+x</sub>. *Phys. Rev. B*, 42:4228–4239, (Sep 1990).
- [124] H Leligny, D Grebille, O Perez, *et al.* A five-dimensional structural investigation of the misfit layer compound [Bi<sub>0.87</sub>SrO<sub>2</sub>]<sub>2</sub>[CoO<sub>2</sub>]<sub>1.82</sub>. *Acta Crystallographica Section B-Structural Science*, 56:173–182, (2000).

- [125] PM DeWolff, T Janssen, and A Janner. The Superspace Groups for Incommensurate Crystal-Structures with a One-Dimensional Modulation. *Acta Crystallographica Section A*, 37(SEP):625–636, (1981).
- [126] Vladimir Y. Butko, Gennady Logvenov, Natasha Bozovic, Zoran Radovic, and Ivan Bozovic. Madelung Strain in Cuprate Superconductors - A Route to Enhancement of the Critical Temperature. *Advanced Materials*, 21(36):3644, (SEP 25 2009).
- [127] T. S. Santos, B. J. Kirby, S. Kumar, *et al.* Delta doping of ferromagnetism in antiferromagnetic manganite superlattices. *Phys. Rev. Lett.*, 107:167202, (Oct 2011).
- [128] R. J. Birgeneau, H. J. Guggenheim, and G. Shirane. Neutron Scattering Investigation of Phase Transitions and Magnetic Correlations in the Two-Dimensional Antiferromagnets  $K_2NiF_4$ ,  $Rb_2MnF_4$ ,  $Rb_2FeF_4$ . *Phys. Rev. B*, 1:2211–2230, (1970).
- [129] D. G. Schlom M. Bernhagen R. Uecker X. Ke, C. Adamo and P. Schiffer. Low temperature magnetism in the perovskite substrate  $DyScO_3$ . *Appl. Phys. Lett.*, 94:152503, (2009).
- [130] G. Catalan, R. M. Bowman, and J. M. Gregg. Metal-insulator transitions in  $ndnio_3$  thin films. *Phys. Rev. B*, 62:7892–7900, (Sep 2000).
- [131] Jian Liu, M. Kareev, B. Gray, *et al.* Strain-mediated metal-insulator transition in epitaxial ultrathin films of  $NdNiO_3$ . *Applied Physics Letters*, 96(23):233110, (2010).
- [132] E. *et al.* Fawcett. Spin density wave antiferromagnetism in chromium alloys. *Rev. Mod. Phys.*, 66:25–127, (1994).
- [133] V. Scagnoli, U. Staub, M. Janousch, *et al.* Charge disproportionation and search for orbital ordering in  $ndnio_3$  by use of resonant x-ray diffraction. *Phys. Rev. B*, 72(15):155111, (Oct 2005).
- [134] A. H. MacDonald and M. Tsoi. Antiferromagnetic metal spintronics. *Philosophical Transactions of the Royal Society A: Mathematical, Physical and Engineering Sciences*, 369(1948):3098–3114, (2011).
- [135] H. Ott. "High- $T_c$  Superconductivity". In *Superconductivity, Volume 2: Novel Superconductors*. Springer, (2008).
- [136] J. D. Jorgensen, B. W. Veal, A. P. Paulikas, *et al.* Structural properties of oxygen-deficient  $YBa_2Cu_3O_{7+\delta}$ . *Phys. Rev. B*, 41:1863–1877, (Feb 1990).
- [137] N.H. Andersen, M Von Zimmermann, T. Frello, *et al.* Superstructure formation and the structural phase diagram of  $YBa_2Cu_3O_{6+x}$ . *Physica C: Superconductivity and its Applications*, 317-318:259–269, (1999).
- [138] M. v. Zimmermann, J. R. Schneider, T. Frello, *et al.* Oxygen-ordering superstructures in underdoped  $YBa_2Cu_3O_{6+x}$  studied by hard x-ray diffraction. *Phys. Rev. B*, 68:104515, (2003).

- [139] D. G. Hawthorn, K. M. Shen, J. Geck, *et al.* Resonant elastic soft x-ray scattering in oxygen-ordered  $\text{YBa}_2\text{Cu}_3\text{O}_{6+\delta}$ . *Phys. Rev. B*, 84:075125, (Aug 2011).
- [140] C. T. Chen, L. H. Tjeng, J. Kwo, *et al.* Out-of-plane orbital characters of intrinsic and doped holes in  $\text{La}_{2-x}\text{Sr}_x\text{CuO}_4$ . *Phys. Rev. Lett.*, 68:2543–2546, (1992).
- [141] M. Grioni, J. F. van Acker, M. T. Czyżyk, and J. C. Fuggle. Unoccupied electronic structure and core-hole effects in the x-ray-absorption spectra of  $\text{Cu}_2\text{O}$ . *Phys. Rev. B*, 45:3309–3318, (1992).
- [142] J. Fink, N. Naecker, E. Pellegrin, *et al.* Electron energy-loss and x-ray absorption spectroscopy of cuprate superconductors and related compounds. *Journal of Electron Spectroscopy and Related Phenomena*, 66:395 – 452, (1994).
- [143] Ruixing Liang, D. A. Bonn, and W. N. Hardy. Evaluation of  $\text{CuO}_2$  plane hole doping in  $\text{YBa}_2\text{Cu}_3\text{O}_{6+x}$  single crystals. *Phys. Rev. B*, 73:180505, (2006).
- [144] J. Zaanen, A. T. Paxton, O. Jepsen, and O. K. Andersen. Chain-Fragment Doping and the Phase Diagram of  $\text{YBa}_2\text{Cu}_3\text{O}_{7-x}$ . *Phys. Rev. Lett.*, 60:2685–2688, (1988).
- [145] J. L. Tallon, C. Bernhard, H. Shaked, R. L. Hitterman, and J. D. Jorgensen. Generic superconducting phase behavior in high- $T_c$  cuprates:  $T_c$  variation with hole concentration in  $\text{YBa}_2\text{Cu}_3\text{O}_{7-\delta}$ . *Phys. Rev. B*, 51:12911–12914, (May 1995).
- [146] Louis Taillefer. Scattering and pairing in cuprate superconductors. *Annual Review of Condensed Matter Physics*, 1(1):51–70, (2010).
- [147] J. M. Tranquada. *Handbook of High-Temperature Superconductivity*, chapter Neutron Scattering Studies of Antiferromagnetic Correlations in Cuprates, pages 257–298. Springer, (2007).
- [148] J. M. Tranquada, G. Shirane, B. Keimer, S. Shamoto, and M. Sato. Neutron scattering study of magnetic excitations in  $\text{YBa}_2\text{Cu}_3\text{O}_{6+x}$ . *Phys. Rev. B*, 40:4503–4516, (1989).
- [149] Vladimir Hinkov. *In-Plane Anisotropy of the Spin-Excitation Spectrum in Twin-Free  $\text{YBa}_2\text{Cu}_3\text{O}_{6+x}$* . PhD thesis, Universität Stuttgart, (2007).
- [150] Daniel Haug. *The Magnetic Phase Diagram of Underdoped  $\text{YBa}_2\text{Cu}_3\text{O}_{6+x}$  studied by Neutron Scattering*. PhD thesis, Universität Stuttgart, (2011).
- [151] P. Burllet, J.Y. Henry, and L.P. Regnault. In-plane magnetic anisotropy in antiferromagnetic  $\text{YBa}_2\text{Cu}_3\text{O}_{6+x}$ . *Physica C: Superconductivity and its Applications*, 296:205–209, (1998).
- [152] J. M. Tranquada, J. D. Axe B. J. Sternlieb, Y. Nakamura, and S. Uchida. Evidence for stripe correlations of spins and holes in copper oxide superconductors. *Nature*, 375:561, (1995).
- [153] M. Platié, J. D. F. Mottershead, I. S. Elfimov, *et al.* Fermi Surface and Quasiparticle Excitations of Overdoped  $\text{Tl}_2\text{Ba}_2\text{CuO}_{6+\delta}$ . *Phys. Rev. Lett.*, 95:077001, (2005).

- [154] A. P. Mackenzie, S. R. Julian, D. C. Sinclair, and C. T. Lin. Normal-state magneto-transport in superconducting  $Tl_2Ba_2CuO_{6+\delta}$  to millikelvin temperatures. *Phys. Rev. B*, 53:5848–5855, (1996).
- [155] Takashi Manako, Yoshimi Kubo, and Yuichi Shimakawa. Transport and structural study of  $Tl_2Ba_2CuO_{6+\delta}$  single crystals prepared by the KCl flux method. *Phys. Rev. B*, 46:11019–11024, (Nov 1992).
- [156] Cyril Proust, Etienne Boaknin, R. W. Hill, Louis Taillefer, and A. P. Mackenzie. Heat Transport in a Strongly Overdoped Cuprate: Fermi Liquid and a Pure  $d$ -Wave BCS Superconductor. *Phys. Rev. Lett.*, 89:147003, (2002).
- [157] M. R. Norman, D. Pines, and C. Kallinc. The pseudogap: friend or foe of high- $T_c$ ? *Advances in Physics*, 54:715 – 733, (2005).
- [158] Tom Timusk and Bryan Statt. The pseudogap in high-temperature superconductors: an experimental survey. *Rep. Prog. Phys.*, 62:61, (1999).
- [159] M.R. Norman and C. Pepin. The electronic nature of high temperature cuprate superconductors. *Rep. Prog. Phys.*, 66:1547–1610, (2003).
- [160] N. F. Mott. Metal-Insulator Transition. *Rev. Mod. Phys.*, 40:677–683, (1968).
- [161] W. W. Warren, R. E. Walstedt, G. F. Brennert, *et al.* Cu spin dynamics and superconducting precursor effects in planes above  $T_c$  in  $YBa_2Cu_3O_{6.7}$ . *Phys. Rev. Lett.*, 62:1193–1196, (1989).
- [162] H. Alloul, T. Ohno, and P. Mendels.  $^{89}Y$  NMR evidence for a fermi-liquid behavior in  $YBa_2Cu_3O_{6+x}$ . *Phys. Rev. Lett.*, 63:1700–1703, (1989).
- [163] P. Bourges. *The Gap Symmetry and Fluctuations in High- $T_c$  Superconductors*, chapter Spin Dynamics in High- $T_c$  Superconducting Cuprates by Inelastic Neutron Scattering Experiments. Plenum Press, (1998).
- [164] P. A. Lee, T. M. Rice, and P. W. Anderson. Fluctuation Effects at a Peierls Transition. *Phys. Rev. Lett.*, 31:462–465, (1973).
- [165] N. B. Christensen, D. F. McMorrow, H. M. Rønnow, *et al.* Dispersive Excitations in the High-Temperature Superconductor  $La_{2-x}Sr_xCuO_4$ . *Phys. Rev. Lett.*, 93:147002, (2004).
- [166] Pengcheng Dai, H. A. Mook, R. D. Hunt, and F. Doğan. Evolution of the resonance and incommensurate spin fluctuations in superconducting  $YBa_2Cu_3O_{6+x}$ . *Phys. Rev. B*, 63:054525, (2001).
- [167] Andrea Damascelli, Zahid Hussain, and Zhi-Xun Shen. Angle-resolved photoemission studies of the cuprate superconductors. *Rev. Mod. Phys.*, 75:473–541, (2003).
- [168] N. Doiron-Leyraud, C. Proust, D. LeBoeuf, *et al.* Quantum oscillations and the Fermi surface in an underdoped high- $T_c$  superconductor. *Nature*, 447:565–568, (2007).

- [169] C. Jaudet, D. Vignolles, A. Audouard, *et al.* de Haas-van Alphen Oscillations in the Underdoped High-Temperature Superconductor  $\text{YBa}_2\text{Cu}_3\text{O}_{6.5}$ . *Phys. Rev. Lett.*, 100:187005, (2008).
- [170] S. Mori, C. H. Chen, and S.-W. Cheong. Pairing of charge-ordered stripes in  $(\text{La,Ca})\text{MnO}_3$ . *Nature*, 392:473–476, (1998).
- [171] S.-H. Lee and S-W. Cheong. Melting of Quasi-Two-Dimensional Charge Stripes in  $\text{La}_{5/3}\text{Sr}_{1/3}\text{NiO}_4$ . *Phys. Rev. Lett.*, 79:2514–2517, (1997).
- [172] J.M Tranquada. Charge stripes and antiferromagnetism in insulating nickelates and superconducting cuprates. *Journal of Physics and Chemistry of Solids*, 59:2150 – 2154, (1998).
- [173] C. Schüßler-Langeheine, J. Schlappa, A. Tanaka, *et al.* Spectroscopy of Stripe Order in  $\text{La}_{1.8}\text{Sr}_{0.2}\text{NiO}_4$  Using Resonant Soft X-Ray Diffraction. *Phys. Rev. Lett.*, 95:156402, (2005).
- [174] Matthias Vojta. Lattice symmetry breaking in cuprate superconductors: stripes, nematics, and superconductivity. *Advances in Physics*, 58(6):699–820, (2009).
- [175] Jörg Fink, Victor Soltwisch, Jochen Geck, *et al.* Phase diagram of charge order in  $\text{La}_{1.8-x}\text{Eu}_{0.2}\text{Sr}_x\text{CuO}_4$  from resonant soft x-ray diffraction. *Phys. Rev. B*, 83:092503, (Mar 2011).
- [176] Jörg Fink, Enrico Schierle, Eugen Weschke, *et al.* Charge ordering in  $\text{La}_{1.8-x}\text{Eu}_{0.2}\text{Sr}_x\text{CuO}_4$  studied by resonant soft x-ray diffraction. *Phys. Rev. B*, 79:100502, (Mar 2009).
- [177] J. Orenstein and A. J. Millis. Advances in the Physics of High-Temperature Superconductivity. *Science*, 288(5465):468–474, (2000).
- [178] P. Abbamonte, A. Rusydi, S. Smadici, *et al.* Spatially modulated 'Mottness' in  $\text{La}_{2-x}\text{Ba}_x\text{CuO}_4$ . *Nat Phys*, 1:155–158, (2005).
- [179] R. J. Birgeneau, Y. Endoh, K. Kakurai, *et al.* Static and dynamic spin fluctuations in superconducting  $\text{La}_{2-x}\text{Sr}_x\text{CuO}_4$ . *Phys. Rev. B*, 39:2868–2871, (1989).
- [180] A. R. Moodenbaugh, Youwen Xu, M. Suenaga, T. J. Folkerts, and R. N. Shelton. Superconducting properties of  $\text{La}_{2-x}\text{Ba}_x\text{CuO}_4$ . *Phys. Rev. B*, 38:4596–4600, (Sep 1988).
- [181] M. K. Crawford, R. L. Harlow, E. M. McCarron, *et al.* Lattice instabilities and the effect of copper-oxygen-sheet distortions on superconductivity in doped  $\text{La}_2\text{CuO}_4$ . *Phys. Rev. B*, 44:7749–7752, (Oct 1991).
- [182] K. Yamada, C. H. Lee, K. Kurahashi, *et al.* Doping dependence of the spatially modulated dynamical spin correlations and the superconducting-transition temperature in  $\text{La}_{2-x}\text{Sr}_x\text{CuO}_4$ . *Phys. Rev. B*, 57:6165–6172, (1998).

- [183] G. Aeppli, T. E. Mason, S. M. Hayden, H. A. Mook, and J. Kulda. Nearly Singular Magnetic Fluctuations in the Normal State of a High- $T_c$  Cuprate Superconductor. *Science*, 278:1432–1435, (1997).
- [184] M. Hücker, G.D. Gu, J.M. Tranquada, *et al.* Coupling of stripes to lattice distortions in cuprates and nickelates. *Physica C: Superconductivity*, 460:170 – 173, (2007).
- [185] V. Hinkov, D. Haug, B. Fauque, *et al.* Electronic Liquid Crystal State in the High-Temperature Superconductor  $\text{YBa}_2\text{Cu}_3\text{O}_{6.45}$ . *Science*, 319(5863):597–600, (2008).
- [186] D Haug, V Hinkov, Y Sidis, *et al.* Neutron scattering study of the magnetic phase diagram of underdoped  $\text{YBa}_2\text{Cu}_3\text{O}_{6+x}$ . *New Journal of Physics*, 12(10):105006, (2010).
- [187] Sudip Chakravarty. From complexity to simplicity. *Science*, 319:735, (2008).
- [188] D. LeBoeuf, N. Doiron-Leyraud, J. Levallois, *et al.* Electron pockets in the Fermi surface of hole-doped high- $T_c$  superconductors. *Nature*, 450:533, (2007).
- [189] F. Laliberte, J. Chang, N. Doiron-Leyraud, *et al.* Fermi-surface reconstruction by stripe order in cuprate superconductors. *Nature Comm.*, 2:432, (2011).
- [190] N. Harrison and S. E. Sebastian. Protected Nodal Electron Pocket from Multiple- $\mathbf{Q}$  Ordering in Underdoped High Temperature Superconductors. *Phys. Rev. Lett.*, 106:226402, (2011).
- [191] T. Wu, H. Mayaffre, S. Kraemer, *et al.* Magnetic-field-induced charge-stripe order in the high-temperature superconductor  $\text{YBa}_2\text{Cu}_3\text{O}_y$ . *Nature*, 477:191–194, (2011).
- [192] G. Ghiringhelli, M. Le Tacon, M. Minola, *et al.* Long-Range Incommensurate Charge Fluctuations in  $(\text{Y,Nd})\text{Ba}_2\text{Cu}_3\text{O}_{6+x}$ . *Science*, 337(6096):821–825, (2012).
- [193] A. J. Achkar, R. Sutarto, X. Mao, *et al.* Distinct Charge Orders in the Planes and Chains of Ortho-III-Ordered  $\text{YBa}_2\text{Cu}_3\text{O}_{6+\delta}$  Superconductors Identified by Resonant Elastic X-ray Scattering. *Phys. Rev. Lett.*, 109:167001, (Oct 2012).
- [194] S. Blanco-Canosa, A. Frano, T. Loew, *et al.* Momentum-Dependent Charge Correlations in  $\text{YBa}_2\text{Cu}_3\text{O}_{6+\delta}$  Superconductors Probed by Resonant X-Ray Scattering: Evidence for Three Competing Phases. *Phys. Rev. Lett.*, 110:187001, (May 2013).
- [195] J. Chang, E. Blackburn, A. T. Holmes, *et al.* Direct observation of competition between superconductivity and charge density wave order in  $\text{YBa}_2\text{Cu}_3\text{O}_{6.67}$ . *Nat Phys*, (2012).
- [196] S. A. Stepanov, E. A. Kondrashkina, R. Köhler, *et al.* Dynamical x-ray diffraction of multilayers and superlattices: Recursion matrix extension to grazing angles. *Phys. Rev. B*, 57(8):4829–4841, (Feb 1998).
- [197] M. Le Tacon, A. Bosak, S. M. Souliou, *et al.* Inelastic X-ray scattering in  $\text{YBa}_2\text{Cu}_3\text{O}_{6.6}$  reveals giant phonon anomalies and elastic central peak due to charge-density-wave formation. *Nat. Phys.*, (2013).

- [198] S. B. Wilkins, M. P. M. Dean, Jörg Fink, *et al.* Comparison of stripe modulations in  $\text{La}_{1.875}\text{Ba}_{0.125}\text{CuO}_4$  and  $\text{La}_{1.48}\text{Nd}_{0.4}\text{Sr}_{0.12}\text{CuO}_4$ . *Phys. Rev. B*, 84:195101, (Nov 2011).
- [199] E. Blackburn, J. Chang, M. Hücker, *et al.* X-ray diffraction observations of a charge-density-wave order in superconducting ortho-II  $\text{YBa}_2\text{Cu}_3\text{O}_{6.54}$  single crystals in zero magnetic field. *Phys. Rev. Lett.*, 110:137004, (Mar 2013).
- [200] R. Comin, A. Frano, M. Yee, *et al.* Charge ordering driven by Fermi-arc instability in underdoped cuprates. *Science*, 343:390–392, (2013).
- [201] E.H. da Silva Neto, P. Aynajian, A. Frano, *et al.* Ubiquitous Interplay between Charge Ordering and High Temperature Superconductivity in Cuprates. *Science*, 343:393–396, (2013).
- [202] C. Bernhard, J. L. Tallon, C. Bucci, *et al.* Suppression of the Superconducting Condensate in the High- $T_c$  Cuprates by Zn Substitution and Overdoping: Evidence for an Unconventional Pairing State. *Phys. Rev. Lett.*, 77:2304–2307, (1996).
- [203] H. Alloul, P. Mendels, H. Casalta, J. F. Marucco, and J. Arabski. Correlations between magnetic and superconducting properties of Zn-substituted  $\text{YBa}_2\text{Cu}_3\text{O}_{6+x}$ . *Phys. Rev. Lett.*, 67:3140–3143, (1991).
- [204] A. Suchaneck, V. Hinkov, D. Haug, *et al.* Incommensurate Magnetic Order and Dynamics Induced by Spinless Impurities in  $\text{YBa}_2\text{Cu}_3\text{O}_{6.6}$ . *Phys. Rev. Lett.*, 105:037207, (2010).
- [205] B.L. Henke, E.M. Gullikson, and J.C. Davis. X-ray interactions: photoabsorption, scattering, transmission, and reflection at  $E=50\text{--}30000$  eV,  $Z=1\text{--}92$ . *Atomic Data and Nuclear Data Tables*, 54(2):181–342, (1993).
- [206] T. Y. Chien, L. F. Kourkoutis, J. Chakhalian, *et al.* Visualizing short-range charge transfer at the interfaces between ferromagnetic and superconducting oxides. *Nat. Comm.*, 4:2336, (2013).
- [207] R. A. Cowley. The phase transition of strontium titanate. *Phil. Trans. R. Soc. Lond. A*, 354(1720):2799–2814, (1996).
- [208] J. D. Axe and G. Shirane. Inelastic-Neutron-Scattering Study of Acoustic Phonons in  $\text{Nb}_3\text{Sn}$ . *Phys. Rev. B*, 8:1965–1977, (1973).
- [209] G.B. Arfken and H.J. Weber. *Essential Mathematical Methods for Physicists*. Harcourt Academic Press, 5th edition, (2001).

# List of Publications

1. A. Frano, S. Blanco-Canosa, E. Schierle, Y. Lu, M. Wu, G. Cristiani, H. U. Habermeier, E. Benckiser, E. Weschke, M. Le Tacon, and B. Keimer, *Interfacial Charge Density Wave Order in Cuprate-Manganite Superlattices*. In preparation.
2. A. Frano, E. Benckiser, M. Wu, Y. Lu, M. Castro-Colin, A. V. Boris, E. Detemple, W. Sigle, P. van Aken, G. Cristiani, G. Logvenov, H.U. Habermeier, P. Wochner, B. Keimer, and V. Hinkov. *Layer Selective Control of the Lattice Structure in Oxide Superlattices*. Adv. Mater. DOI: 10.1002/adma.201303483 (2013).
3. A. Frano, E. Schierle, M. W. Haverkort, Y. Lu, M. Wu, S. Blanco-Canosa, U. Nwankwo, A. V. Boris, P. Wochner, R. Feyerherm, E. Dudzik, J. Stremper, G. Cristiani, H. U. Habermeier, G. Logvenov, V. Hinkov, E. Benckiser, E. Weschke, and B. Keimer. *Orbital Control of Noncollinear Magnetic Order in Nickelate Heterostructures*. Phys. Rev Lett. **111**, 106804 (2013).
4. R. Comin, A. Frano, M. Yee, Y. Yoshida, H. Eisaki, E. Schierle, E. Weschke, R. Sutarto, F. He, A. Soumyanarayanan, Y. He, M. Le Tacon, I.S. Elfimov, J. Hoffman, G.A. Sawatzky, B. Keimer, and A. Damascelli. *Charge Order Driven by Fermi-Arc Instability in Underdoped Cuprates*. Science **343**, 390 (2013).
5. E. da Silva Neto, P. Aynajian, A. Frano, R. Comin, E. Schierle, E. Weschke, A. Gyenis, J. Wen, J. Schneeloch, Z. Xu, S. Ono, G. Gu, M. Le Tacon, and A. Yazdani. *Ubiquitous Interplay between Charge Ordering and High-Temperature Superconductivity in Cuprates*. Science **343**, 393 (2013).
6. M. Wu, E. Benckiser, M. W. Haverkort, A. Frano, Y. Lu, U. Nwankwo, S. Brück, P. Audehm, E. Goering, S. Macke, V. Hinkov, P. Wochner, G. Christiani, S. Heinze, G. Logvenov, H.-U. Habermeier, and B. Keimer. *Strain and Composition Dependence of Orbital Polarization in Nickel Oxide Superlattices*. Phys. Rev. B. **88**, 125124 (2013).
7. S. Blanco-Canosa, A. Frano, T. Loew, Y. Lu, J. Porras, G. Ghiringhelli, M. Minola, C. Mazzoli, L. Braicovich, E. Schierle, E. Weschke, M. Le Tacon, and B. Keimer. *Momentum-Dependent Charge Correlations in  $YBa_2Cu_3O_{6+\delta}$  Superconductors Probed by Resonant X-Ray Scattering: Evidence for Three Competing Phases*. Phys. Rev. Lett. **110**, 187001 (2013).
8. M. Rössle, K.W. Kim, A. Dubroka, P. Marsik, C. N.Wang, R. Jany, C. Richter, J. Mannhart, C.W. Schneider, A. Frano, P. Wochner, Y. Lu, B. Keimer, D. K. Shukla, J. Stremper, and C. Bernhard. *Electric-Field-Induced Polar Order and Localization*

- of the Confined Electrons in LaAlO<sub>3</sub>/SrTiO<sub>3</sub> Heterostructures.* Phys. Rev. Lett. **110**, 136805 (2013).
9. A. J. Achkar, R. Sutarto, X. Mao, F. He, A. Frano, S. Blanco-Canosa, M. Le Tacon, G. Ghiringhelli, L. Braicovich, M. Minola, M. Moretti Sala, C. Mazzoli, Ruixing Liang, D. A. Bonn, W. N. Hardy, B. Keimer, G. A. Sawatzky, and D. G. Hawthorn. *Distinct Charge Orders in the Planes and Chains of Ortho-III-Ordered YBa<sub>2</sub>Cu<sub>3</sub>O<sub>6+δ</sub> Superconductors Identified by Resonant Elastic X-ray Scattering.* Phys. Rev. Lett. **109**, 167001 (2012).
  10. G. Ghiringhelli, M. Le Tacon, M. Minola, S. Blanco-Canosa, C. Mazzoli, N. B. Brookes, G. M. De Luca, A. Frano, D. G. Hawthorn, F. He, T. Loew, M. Moretti Sala, D. C. Peets, M. Salluzzo, E. Schierle, R. Sutarto, G. A. Sawatzky, E. Weschke, B. Keimer, L. Braicovich. *Long-Range Incommensurate Charge Fluctuations in (Y,Nd)Ba<sub>2</sub>Cu<sub>3</sub>O<sub>6+x</sub>.* Science **337**, 821 (2012).
  11. D. K. Satapathy, M. A. Uribe-Laverde, I. Marozau, V. K. Malik, S. Das, Th. Wagner, C. Marcelot, J. Stahn, S. Brück, A. Ruhm, S. Macke, T. Tietze, E. Goering, A. Frano, J.-H. Kim, M. Wu, E. Benckiser, B. Keimer, A. Devishvili, B. P. Toperverg, M. Merz, P. Nagel, S. Schuppler, and C. Bernhard. *Magnetic Proximity Effect in YBa<sub>2</sub>Cu<sub>3</sub>O<sub>7</sub>/La<sub>2/3</sub>Ca<sub>1/3</sub>MnO<sub>3</sub> and YBa<sub>2</sub>Cu<sub>3</sub>O<sub>7</sub>/LaMnO<sub>3+δ</sub> Superlattices.* Phys. Rev. Lett. **108**, 197201 (2012).
  12. E. Detemple, Q. M. Ramasse, W. Sigle, G. Cristiani, H.-U. Habermeier, E. Benckiser, A. V. Boris, A. Frano, P. Wochner, M. Wu, B. Keimer and P. A. van Aken. *Polarity-Driven Nickel Oxide Precipitation in LaNiO<sub>3</sub>-LaAlO<sub>3</sub> Superlattices.* Appl. Phys. Lett. **99**, 211903 (2011).
  13. A. V. Boris, Y. Matiks, E. Benckiser, A. Frano, P. Popovich, V. Hinkov, P. Wochner, M. Castro-Colin, E. Detemple, V. K. Malik, C. Bernhard, T. Prokscha, A. Suter, Z. Salman, E. Morenzoni, G. Cristiani, H.-U. Habermeier, B. Keimer. *Dimensionality Control of Electronic Phase Transitions in Nickel-Oxide Superlattices.* Science **332**, 937 (2011).
  14. E. Benckiser, M.W. Haverkort, S. Brück, E. Goering, S. Macke, A. Frano, X. Yang, O.K. Andersen, G. Cristiani, H.U. Habermeier, A.V. Boris, I. Zegkinoglou, P. Wochner, H.J. Kim, V. Hinkov, B. Keimer. *Orbital Reflectometry of Oxide Heterostructures.* Nature Materials **10**, 189 (2011).

# Acknowledgements

Without question, the most profound lesson I learned throughout this PhD is the importance of collaboration and teamwork. Together we are stronger. As part of a diverse and extensive group, I would like to thank my teammates.

First, I thank Bernhard Keimer for his teachings, supervision, and support throughout the 5 years spanning my Master's and PhD, and for the vision of establishing the collaboration with the Helmholtz Center in Berlin. To Alan Tennant, for accepting the collaboration and to Stefan Eisebitt for supervising as well as Mario Dähne for chairing my thesis defense at TU Berlin.

In Berlin, I sincerely thank Eugen Weschke and Enrico Schierle for (almost literally) giving me a home at BESSY. Your patience, trust, and support seamlessly complemented the vast knowledge you gave me. In your chamber, every scattered photon is worth counting.

In Stuttgart, I would like to thank the workgroup I am honorably part of. I am particularly grateful to Eva Benckiser for the eternal patience and everlasting support, Prof. Yi Lu for your teachings, Meng Wu for all the fun beam times, Martin Bluschke for the walks back to the S-Bahn at 7am, Peter Wochner for teaching me how to scatter x-rays, Maurits Haverkort for teaching me *why* scatter x-rays, Santi Blanco-Canosa for letting me call every 2 minutes with questions, to Mathieu Le Tacon for letting me tag along the YBCO ride, Vladimir Hinkov for always believing in me, Toshinao Loew and Juan Porras for excellent YBCO crystals, Georg Cristiani for designing the sample holders and along with Hanns-Ulrich Habermeier, and Gennady Logvenov for the great heterostructure samples.

To both new and old member's of Bernhard Keimer's department: Sangita Baniya, Friederike Wrobel, Uba Nwankwo, Sebastian Macke, Alexander Boris, Christopher Dietl, Gerd Friemel, Alex Charnukha, Stephan Heinze, Nadir Driza, Luqman Mustafa, Junghwa Kim, Darren Peets, Giorgi Ghambashidze, Matthias Hepting, Giniyat Khalliulin, George Jackeli, Jiří Chaloupka, Dmitri Efremov, Timofei Larkin, Yulia Matiks, Matteo Minola, Manfred Ohl, Benjamin Bruha, Ayman Akil, Daniel Pröpper, Armin Schulz, Michaela Souliou, Agnes Szoekfalvi-Nagy, Hoyoung Jang, Dmytro Inosov, Michael Schulz, Heiko Uhlig, Youngje Um, Peter Yordanov, Daniel Haug, Martin Rahlenbeck, Ioannis Zegkinoglou, Philippe Leininger, Claudia Hagemann, and Sonja Balkema, I thank you for providing such a pleasant and inspiring environment of collaboration.

I would like to thank Ralf Feyerherm and Esther Dudzik for support at the MAGS beamline, Jörg Stempfer and Sonia Francoual for support at the P09 beamline at DESY, Miguel Castro-Colin and Miguel Mantilla for support with the diffraction experiments at ANKA, Ronny Sutarto and Feizhou He for support at the CLS.

I sincerely thank Giacomo Ghiringhelli, Lucio Braicovich and Claudio Mazzoli for allowing me to complement your RIXS measurements, and Riccardo Comin, Andrea Damascelli,

George Sawatzky, and (recently) Eduardo da Silva Neto for hosting me at UBC and inviting me to take part in fruitful collaborations. Also, thank you Matthias Rössle and Christian Bernhard at Universtät Fribourg for the collaboration on LAO/STO.

To my beautiful friends in Germany: Berna (wassup berns?), Carlos (el broody), Carola (3 Jahre mich ertragen), Carolina (men!!), Fred (mon frère), Fede (my trainer), Humberto (plaa), Hendrik/Karl/Lina/Joaquín (la familia más linda), Maia (mi profesora de francés), Marjorie (my therapist), Nicole (calm down!!), Tom (William S. Burroughs) and Volker (the Superfluid Vacuum Theory) thank you for an amazing time and support through all these years. To Bianca for teaching me how to persevere armed only with the love of life... for always believing and never forgetting.

Finalmente, este logro de mi vida no sería posible sin el apoyo incondicional no obstante lo atrevidos y extraordinarios que han sido mis sueños, por lo que agradezco de todo corazón a Dios, a mis padres Luis and Fatima, a mis hermanos Daniel, Luis y Wendy así mismo a Teles, Diego y Alex Loera, a mis abuelas Mamichiqui y Lela (Q.E.P.D.).

It's all part of a plan, where circles are meant to close and the music keeps playing. It never stops.